# IBRACON

**IBRACON Structures and Materials Journal**
Revista IBRACON de Estruturas e Materiais

# IBRACON Structures and Materials Journal
Revista IBRACON de Estruturas e Materiais

# Contents

**Cover:** Parametric Tower

**Courtesy:** Marcela Noronha P. de O. e Sousa

# Aims and Scope

## Aims and Scope

The IBRACON Structures and Materials Journal (in Portuguese: Revista IBRACON de Estruturas e Materiais) is a technical and scientific divulgation vehicle of IBRACON (Brazilian Concrete Institute), published every two months. Each issue has 12 to 15 articles and, possibly, a technical note and/or a technical discussion regarding a previously published paper. All contributions are reviewed and approved by professionals with recognized scientific competence in the area. The IBRACON Structures and Materials Journal is an open access Journal, free of charges for authors and readers.

## Objectives

The IBRACON Structures and Materials Journal´s main objectives are:

- Present current developments and advances in concrete structures and materials.
- Make possible the better understanding of structural concrete behavior, supplying subsidies for a continuous interaction among researchers, producers, and users.
- Stimulate the development of scientific and technological research in the areas of concrete structures and materials, through papers peer-reviewed by a qualified Editorial Board.
- Promote the interaction among researchers, constructors and users of concrete structures and materials and the development of Civil Construction.
- Provide a vehicle of communication of high technical level for researchers and designers in the areas of concrete structures and materials.

## Submission Procedure

The procedure to submit and revise the contributions, as well as the formats, are detailed in the Journal Website (ismj.org).

The papers and the technical notes are revised by at least two reviewers indicated by the editors. Discussions and replies are accepted for publication after a review by the editors and at least one member of the Editorial Board. In case of disagreement between the reviewer and the authors, the contribution will be sent to a specialist in the area, not necessarily linked to the Editorial Board. Conflict of interests is carefully handled by the Editors.

## Contribution Types

The Journal will publish original papers, short technical notes, and paper discussions. Original papers will be accepted if they are in accordance with the objectives of the Journal and present quality of information and presentation. A technical note is a brief manuscript. It may present a new feature of research, development, or technological application in the areas of Concrete Structures and Materials, and Civil Construction. This is an opportunity to be used by industries, companies, universities, institutions of research, researchers, and professionals willing to promote their works and products under development.

A discussion is received no later than 3 months after the publication of the paper or technical note. The discussion must be limited to the topic addressed in the published paper and must not be offensive. The right of reply is granted to the Authors. The discussions and the replies are published in the subsequent issues of the Journal.

The submission file should be in accordance with the paper template available at the Journal Website. It is recommended that the length of the papers does not exceed 25 pages. Where available, URLs for the references should be provided.

The IBRACON Structures and Materials Journal will conduct the review process for manuscripts submitted in English. Titles, abstracts, and keywords are presented in English, and in Portuguese or Spanish. Articles and technical notes are peer-reviewed and only published after approval of the reviewers and the Editorial Board.

Once accepted, an article is typeset according to the journal layout. The author will be required to review and approve the galleys before publishing. At this stage only typesetting errors will be considered.

## Internet Access

The IBRACON Structures and Materials Journal Webpage is available at http://ismj.org.

## Sponsors

The funds for the maintenance of the Journal are currently obtained from the IBRACON. The Journal is not supposed to be maintained with funds from private sponsorship, which could diminish the credit of the publications.

## Photocopying

Photocopying in Brazil. Brazilian Copyright Law is applicable to users in Brazil. IBRACON holds the copyright of contributions in the journal unless stated otherwise at the bottom of the first page of any contribution. Where IBRACON holds the copyright, authorization to photocopy items for internal or personal use, or the internal or personal use of specific clients, is granted for libraries and other users registered at IBRACON.

## Copyright

## IBRACON

## Disclaimer

Papers and other contributions and the statements made, or opinions expressed therein are published on the understanding that the authors of the contribution are the only responsible for the opinions expressed in them and that their publication does not necessarily reflect the views of IBRACON or of the Journal Editorial Board.

# Editorial Board

# IBRACON Structures and Materials Journal
## Revista IBRACON de Estruturas e Materiais

ORIGINAL ARTICLE

# Assessment of design codes for the in-service behaviour of steel-concrete composite slabs

*Avaliação dos códigos de projeto para o comportamento em serviço de lajes mistas de aço-concreto*

Lucas Antônio Morais Oliveira[a] (iD)
Tainá Mascarenhas Borghi[a] (iD)
Yury Ouriques Rodrigues[a] (iD)
Ana Lucia Homce de Cresce El Debs[a] (iD)

[a] Universidade de São Paulo – USP, Escola de Engenharia de São Carlos, Departamento de Engenharia de Estruturas, São Carlos, SP, Brasil

**Abstract:** Steel-concrete composite slabs, also known as steel decking floor slabs or popularly as steel decks® have recent development and are advancing in Brazilian construction. There are relatively few researches about the long-term effects on composite slabs, and it has been identified that they can be significant in the evolution of deflections, mainly due to the effects of non-uniform shrinkage. However, there are no Brazilian references on the subject and Brazilian Code ABNT NBR 8800:2008 does not indicate any procedure for its evaluation. This paper presents a study on the serviceability limit state of excessive deflection with the application of two simplified approaches: Eurocode 4:2004 (European code) and AS/NZS 2327:2017 (Australian code), also comparing them against experimental results by the authors and literature. Due to the impermeability of the soffit face promoted by the steel decking, the occurrence of non-uniform shrinkage is a relevant aspect. As a consequence, the deflections were underestimated by Eurocode 4. At the same time, the simplified approach of AS/NZS 2327, which explicitly takes into account the non-uniform shrinkage, presented good accuracy when compared to the experimental values. Finally, authors indicate the use of more robust prediction models for the evaluation of deflections in composite floors.

**Keywords:** composite structures, profiled steel decking, instantaneous and long-term deflections, creep and non-uniform shrinkage, cracking concrete.

**Resumo:** As lajes mistas, também chamadas de lajes com fôrma de aço incorporada e popularmente como steel deck®, apresentam desenvolvimento relativamente recente no Brasil e têm ganhado espaço na construção civil. Existem poucas pesquisas sobre os efeitos diferidos no tempo em lajes mistas e têm-se identificado que estes podem ser significativos na evolução das flechas, sobretudo devido aos efeitos da retração não-uniforme. No entanto, não há referências nacionais e a ABNT NBR 8800:2008 não indica qualquer consideração de análise estrutural na sua avaliação. O presente trabalho apresenta um estudo sobre esse estado limite de serviço, com aplicação e comparação de duas abordagens de avaliação simplificadas: Eurocode 4:2004 e AS/NZS 2327:2017, comparando-as ainda com resultados experimentais dos autores e da literatura. Reforça-se que devido à impermeabilidade da face inferior promovida pela fôrma de aço, a ocorrência da retração não-uniforme é um aspecto relevante. Como resultado, a previsão das flechas foi subestimada no modelo Eurocode 4, quando comparado com a abordagem da AS/NZS 2327. Os resultados mostram que a abordagem simplificada da AS/NZS 2327, que leva em conta explicitamente a ocorrência da retração não-uniforme, apresentou boa acurácia quando comparada com os valores experimentais. Dessa forma, indica-se o uso de modelos de previsão mais robustos na avaliação das flechas desse sistema de pisos.

**Palavras-chave:** estruturas mistas, fôrma de aço incorporada, flechas imediatas e diferidas no tempo, fluência e retração não-uniforme, fissuração do concreto.

*L. A. M. Oliveira, T. M. Borghi, Y. O. Rodrigues, and A. L. H. C. Debs*

# 1 INTRODUCTION

Steel-concrete slabs are composed of a steel sheeting and concrete filling and take advantage of the best characteristics of both materials. Lightness of steel profile and its high tensile strength are added to the excellent compression strength of concrete, relatively inexpensive material with low-maintenance, robustness and fire resistance. In this way, construction favors economy, speed, flexibility, high quality, sustainability and aesthetics. The use of composite slabs as a structural solution is promising and increasingly advantageous, being highlighted here some applications of this system in Brazil, as illustrated in Figure 1.
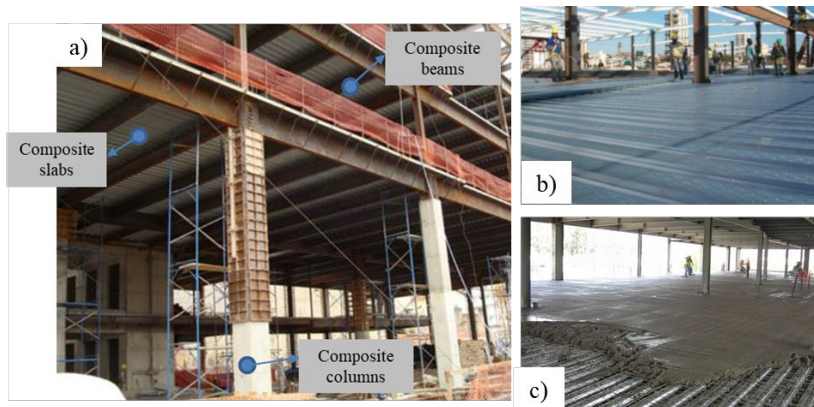


**Figure 1.** Steel-concrete composite structures: solution in composite floors. a) Composite structures in Real Hospital Português, Pernambuco (Brazil) [1]. b) Steel decking installation and c) Casting of slab concrete [2]

The composite behaviour is achieved when profiled steel sheeting is capable of transferring the longitudinal shear at the interface between steel and the concrete. The natural adhesion between steel and concrete is not sufficient to guarantee the composite behaviour, so mechanical and friction bonding mechanisms are also included. It is emphasised that the critical failure mode for composite slabs is commonly the longitudinal shear, characterising as partial interaction between components.

The structure should be attending all the ultimate limit states (ULS), both at normal- and under fire-situation. Altogether, the composite slabs must also attend the serviceability limit states (SLS) of excessive deflection, cracking and vibrations.

Given the slenderness of the composite floors, the excessive deflections are usually the primary check for the in-service conditions. Abdullah [3] points out that bending failure is not a dominant design criterion, because the interaction between steel and concrete is generally incomplete and the serviceability state of excessive deflections commonly limits the span of the slab.

The exact calculation of the deflection is highly complex due to the interdependence of the numerous variables and uncertainties involved. In this way, proposals for simplified methods for the deflection evaluation are presented by normative codes, being addressed here the approaches of Eurocode 4:2004 [4] and AS/NZS 2327:2017 [5] (Australian Standard / New Zealand Standard).

Recent researches on time-dependent deflections of composite slabs have been carried out. Some of the findings have been incorporated into the AS/NZS 2327 [5]. Must be advertised the contributions of Ranzi et al. [6] [7], Gholamhoseini [8] [9], Al-deen et al. [10].

This paper presents the results of an exploratory experimental program developed in Brazil, evaluating long-term deflections for a simply-supported steel-concrete composite slab under in- service conditions. Since Brazilian code ABNT NBR 8800:2008 [11] does not indicate any procedure for this calculation, the approaches of Eurocode 4 (EC4) and AS/NZS 2327 are presented and discussed. The procedures are used to predict the deflection and compared to the experimental result.

## 2 BEHAVIOUR OF STEEL-CONCRETE COMPOSITE SLABS

The use of profiled steel decking, usually cold-formed profiles, has special functions: at first, they serve as formwork for the slab, supporting the loads during concrete casting and also act as a work platform. During the composite phase, they act as the positive reinforcement (part or total), play the role of horizontal diaphragm, distribute the deformations due to shrinkage and avoid excessive concrete cracking. Steel sheeting has advantages such as lightness when handled and installed, the possibility of dispensing shoring for the slab besides ease passage of ducts and installations. Finally, the system results in high speed of construction and waste reduction.

Figure 2 shows the scheme of the profiled sheeting types used in composite slabs. Usually, in trapezoidal forms (a) the mechanical connection is obtained employing mosses. In re-entrant forms (b) and clip-pan or L (c) form, the friction connection occurs due to the microscopic irregularities of the surface-associated to normal pressures (concrete confinement), with possible use of dents on the surface. In Brazil, the steel decking found on the market is the trapezoidal type.



|  a) Trapezoidal type | b) Re-entrant type | c) Clip-pan ou L type |
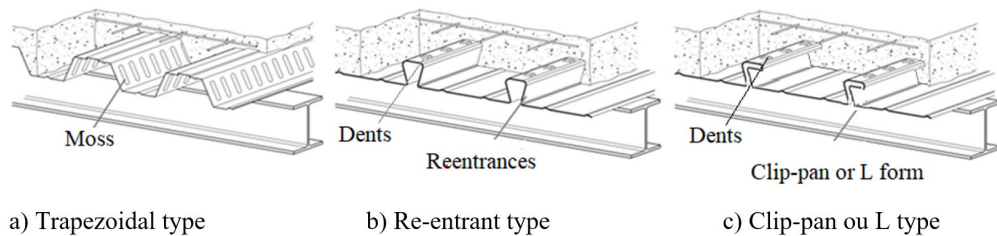
**Figure 2.** Steel decking types for composite slabs

The main trapezoidal profiles available in Brazil have ribs between 45 to 75 mm of height, and they can be a competitive solution for spans from 2 to 4 meters, using secondary beams. In this condition, it is common to dispense shoring and, consequently, obtaining good agility in the construction. This system can be used in residential and commercial buildings, hospitals, schools, garages, bridges and industrial buildings.

Usually, manufacturers of the steel decking provide tables for the design of each profile and steel thickness. There one can find the maximum span without shoring for single, double and triple spans or structural balances, for each total height of slab. In general, for a given span, total thickness and height of the slab is defined, with the maximum load capacity

Present paper has focused on evaluating the in-service behaviour of composite slabs. However, the design of the slab is based on the resistance to the various ultimate limit states, headlining the longitudinal shear and, only later, on the verification of the in-service deflection.

Based on the knowledge of the concrete structures and for the understanding of the total deflections, it is vital to mention its division in two parts: the instantaneous deflection and time-dependent deflection. The first occurs as an accommodation due to the deformation of the materials. The second arises over time, under the action of long-term loads (concrete creep) and the concrete shrinkage. Furthermore, the cracking of the concrete changes the deformation profile of the sections, reduces their rigidity and contributes to the increase of deflection.

The exact deflection calculation depends on numerous variables, being very complex and turning impossible its use in routine design. Temperature and humidity, curing conditions and slab exposure condition, age of the concrete, loading history, compression reinforcement rate, dead load and live loads, among others, can affect the results, such as the uncertainties involved in the models of evaluation of creep and shrinkage concrete.

An important fact is the occurrence of non-uniform shrinkage of concrete due to the impermeability of the soffit slab, given the presence of the steel decking (seen in Figure 1 and 2). In this regard, underline the studies by Bradford et al. [12], Gilbert et al. [13]; Ranzi et al. [6]; Gilbert [14], Al-deen and Ranzi [15], Al-deen et al. [10] and Gholamhoseini [8] [9].

The phenomenon of non-uniform shrinkage significantly influences the evolution of time-dependent deflection and requires new analysis procedures, as highlighted by Gholamhoseini [8] [9]. Ranzi [16] proposed a simplified methodology for the assessment of in-service behaviour of steel-concrete slabs, already incorporated by the Australian code AS/NZS 2327 [5].

All experimental programs on the evaluation of the in-service deflection found [8]–[10] the occurrence of total interaction between steel and concrete, with no significant relative slips between the materials. The application of usual

homogenisation on the cross-section proved to be coherent for the evaluation of the deflection, giving very accurate results. Furthermore, the more important factor affecting the predictions was the adoption of a non-uniform shrinkage profile. If the behaviour with partial interaction may occur due to variability of profiles steel decking in the global market, the basic article by Bradford [17] is indicated, which presents an analytical formulation with consideration of the time-dependents effects of concrete and partial interaction.

## 3 DEFLECTION BY SIMPLIFIED APPROACHES

The in-service behaviour of composite slabs is usually calculated by the classical method, with adaptations of the Euler-Bernoulli beam hypotheses and elastic-linear constitutive law. The equations consider the static balance, compatibility of deformations and constitutive laws of the materials. Limitation of the concrete stress values at most 40% of the compressive strength of concrete [18]. It uses the section homogenisation procedure for the structure with steel-concrete composite cross-section.

Total interaction is assumed with no occurrence of relative slips between steel and concrete. It was the typical situation presented under service condition as observed in the results of the experimental tests. The guidelines for deflection prediction in composite steel-concrete slabs are presented from the point of view of the Eurocode 4 [4] approaches and the Australian model AS/NZS 2327 [5].

### 3.1 Deflection by Eurocode 4:2004 calculation

Eurocode 4 [4] approach is the main one for deflection checking in technical manuals and books, as Johnson [19] and Dujmovic, Andrioic and Lukavevic [20]. Although the method does not explain the shrinkage effects, it indicates neglecting shrinkage effects in its clause EC4 [4] 9.8.2(3). The deflection under service conditions due to loading must be calculated using elastic and kinematic Euler-Bernoulli analysis with the following hypotheses:

- The longitudinal deformations of concrete and steel in any cross-section of the steel form are proportional to the distance of the neutral line fibre of the composite section. Plane sections remain plane after flexural bending;
- The stresses are proportional to the deformations in both concrete and steel;
- The entire steel cross-section must be used, except when reduced by holes;
- Usually, a reduced elasticity modulus is used for the consideration of concrete creep;
- The second moment of area used in the deflection calculations must be considered as the average of the uncracked and cracked concrete in the composite section.

EC4 [4] presents the evaluation of the effect of creep deformation, adopting the simplified procedure as presented for the composite beams, dividing the modulus of elasticity of the concrete by 2 in Equation 1 (Eurocode 4:2004). As a comparison, the British Standard BS 5950: 1994 [21] (replaced by EC4) indicates for the calculation a consideration of a weighted average for both short- and long-term effects, according to Equation 2 (BS 5950:1994).

$$E'_{cm} = \frac{1}{2} \cdot E_{cm} \tag{1}$$

$$E'_{cm} = \frac{1}{2} \cdot \left( E_{cm} + \frac{E_{cm}}{3} \right) = \frac{2}{3} \cdot E_{cm} \tag{2}$$

Regarding the second moment of area of the concrete in the steel-concrete composite section, the average presented by the cracked section ($I_{cr}$) and uncracked section ($I_{uncr}$) is adopted, to take into account the occurrence of concrete cracking, according to Equation 3.

$$I_m = \frac{I_{uncr} + I_{cr}}{2} \tag{3}$$

The predicted deflection ($\delta$) for a composite slab simply-supported under uniformly distributed loading ($p_{tot}$), unidirectional span (l), steel decking elastic modulus ($E_{sd}$) and with section homogenisation ($I_m$) based on the steel profile is given by Equation 4.

$$\delta = \frac{5}{384} \cdot \frac{P_{tot} \cdot l^4}{E_{Sd} \cdot I_m} \tag{4}$$

For composite slabs calculated with continuity on intermediate supports, the expressions can be taken based on the elastic-line in the deflection evaluation.

## 3.2 Deflection by AS/NZS 2327:2017 simplified calculation

Proposed in the last update of the Australian Standard AS/NZS 2327 [5] is presented in more detail in Al-deen and Ranzi [15] and Ranzi [16]. It takes into account more explicitly the factors that affect the time-dependent behaviour. The model incorporates the contribution of cracked concrete stiffness, the portions due to creep and non-uniform shrinkage in deflection calculations. Also, it uses elastic and kinematic Euler-Bernoulli analysis.

The code indicates that the procedure applies to the design of composite slabs when the effects of relative slips are considered insignificant. If not attended, end anchorages must be provided; alternatively, the deflection calculations must include these effects.

The deflection due to the loading applied only on the steel formwork must be calculated, taking into account its self-weight and the weight of fresh concrete. Special attention must be given to the occurrence of ponding effects when considering or not increasing the self-weight when not temporary shoring was used. In the composite phase, the instantaneous deflections are calculated after curing due to their self-weight, when removing shoring, if existing, and applying imposed loads.

Total deflection ($\delta_{tot}$) is given by the sum of the instantaneous and time-dependent deflection caused by the permanent loads and the variables loads, effects of creep and shrinkage, given by Equation 5. Figure 3 schematically illustrates the concrete structures deflections plots.
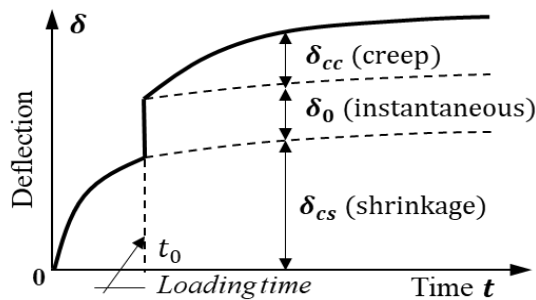


**Figure 3.** Concrete structures deflections plots

$$\delta_{tot} = \delta_0 + \delta_{cc} + \delta_{cs} \tag{5}$$

where:

$\delta_0$ = instantaneous deflection; $\delta_{cc}$ = creep deflection; $\delta_{cs}$ = shrinkage deflection

The guide for the definition and deflection calculation are presented, taking as the theoretical reference of Ranzi [16] and AS/NZS 2327 [5].

### 3.2.1 Instantaneous deflection

The instantaneous deflection ($\delta_0$) that occurs when applying external loads must be calculated using the value of $E_c$ (concrete elasticity module determined at the moment considered) and the value of the second moment of area ($I_{ef}$) in expression of the maximum deflection by elastic line, usually evaluated at mid-span. The material properties for concrete must be those corresponding to the age of the composite slab when external loads are applied for the first time. Simplified process for calculating the value of $I_{ef}$ can be used and must be determined from the values of the position of the cross-sections:

(a) For a simply supported slab, the value at midspan;
(b) In a composite slab with continuity on intermediate supports:
    (i) for an interior span, half the midspan value plus one-quarter of each support value;
    (ii) for end span, half the midspan value plus half the value at the continuous support;
(c) For a cantilever, the value at the support.
    The effective inertia value $I_{ef}$ in each of the indicated cross-section is given (Equation 6).

$$I_{ef} = I_{cr} + \left(I_{uncr} - I_{cr}\right) \cdot \left(\frac{M_{cr}}{M_s}\right)^3 \leq I_{ef,max} \tag{6}$$

where:

$I_{ef,max}$ = maximum effective second moment of area and equal to $I_{uncr}$ ;

$I_{cr}$ = second moment of area of the cracked section (disregarding the contribution of the tensile concrete) and with the steel reinforcement and steel decking homogenised in an equivalent concrete;

$I_{uncr}$ = second moment of area of the uncracked section and with the reinforcement and steel decking transformed into an equivalent concrete area;

$M_s$ = maximum moment in-service;

$M_{cr}$ = cracking moment, given by (Equation 7).

    A highlight is the consideration of the tensile stress caused by the shrinkage in the calculation of the cracking moment. Given the existence of the profiled steel decking, it ends up preventing the free deformation of the concrete, resulting in tensions. The tensile stress resulting from the shrinkage ($\sigma_{cs}$) decreases the flexural tensile strength of the concrete ($f_{ct,f}$).

    The methodology presented by Gilbert and Ranzi [18] was taken as a basis for analysing the cross-sections composed of steel and concrete. According to Ranzi [16], the cracking moment evaluation can be rewritten based on the properties of the composite section and presented in its general form, according to Equations 7-8.

$$M_{cr} = \frac{1}{E_c \cdot \left(\dfrac{R_B}{R_0} - y \cdot \dfrac{R_A}{R_0}\right)} \cdot \left(f_{ct,f} - \sigma_{cs}\right) \geq 0 \tag{7}$$

Where: $\quad R_0 = R_I \cdot R_A - R_B^2 \tag{8}$

    The parcels $R_{A,0}$, $R_{B,0}$ and $R_{I,0}$ represent the axial stiffness, the static moment and the flexural moment, at time $t_0$ without considering time-dependent effects of concrete, given by Equations 9-10-11, respectively. This methodology aims to homogenize the composite section and allows adequate programming in electronic spreadsheets. The terms are calculated with the reference axis at bottom of the slab, defined as seen in Figure 4.

$$R_{A,0} = \sum_{i=1}^{m_c} A_{c(i)} \cdot E_{c(i),0} + \sum_{i=1}^{m_s} A_{s(i)} \cdot E_{s(i)} + A_{sd} \cdot E_{sd} = R_{A,c} + R_{A,s} + R_{A,sd} \tag{9}$$

$$R_{B,0} = \sum_{i=1}^{m_c} B_{c(i)} \cdot E_{c(i),0} + \sum_{i=1}^{m_s} y_{s(i)} \cdot A_{s(i)} \cdot E_{s(i)} + B_{sd} \cdot E_{sd} = R_{B,c} + R_{B,s} + R_{B,sd} \tag{10}$$

$$R_{I,0} = \sum_{i=1}^{m_c} I_{c(i)} \cdot E_{c(i),0} + \sum_{i=1}^{m_s} y_{s(i)}^2 \cdot A_{s(i)} \cdot E_{s(i)} + I_{sd} \cdot E_{sd} = R_{I,c} + R_{I,s} + R_{I,sd} \tag{11}$$

where:

$R_A$ = axial stiffness calculated at time $t_0$ in uncracked condition;

$R_B$ = stiffness associated with the first area moment at time $t_0$ in uncracked condition;

$R_I$ = flexural stiffness calculated at time $t_0$ in uncracked condition.

The subscriptions "c", "sd", "s" references the following components: concrete, steel decking and, steel reinforcement, respectively:

$E$ = elastic modulus;

$A$ = cross-sectional area of the material;

$B$ = first area moment (static moment);

$I$ = second moment of area of the section;

$y_i$ = position of the vertical axis of the steel bars (reinforcement).

The maximum tensile stress induced by shrinkage $(\sigma_{cs})$ in the outer fibre in which the crack occurs, can be calculated by Equations 12-13.

$$\sigma_{cs} = \frac{E_{ef,cs}}{R_{I,cs} \cdot R_{A,cs} - R_{B,cs}^2} \cdot \left[ \left(R_{I,cs} - y \cdot R_{B,cs}\right) \cdot f_{cs1} + \left(R_{B,cs} - y \cdot R_{A,cs}\right) \cdot f_{cs2} \right] - E_{ef,cs} \cdot \left(\varepsilon_{r,cs} - y \cdot \kappa_{cs}\right) \tag{12}$$

$$\begin{bmatrix} f_{cs1} \\ f_{cs2} \end{bmatrix} = E_{ef,cs} \cdot \begin{bmatrix} A_c \cdot \varepsilon_{r,cs} - B_c \cdot \kappa_{r,cs} \\ -B_c \cdot \varepsilon_{r,cs} + I_c \cdot \kappa_{r,cs} \end{bmatrix} \tag{13}$$

where:

$A_c$ = area of the concrete section;

$B_c$ = first moment area of the concrete;

$I_c$ = second moment area of concrete;

$R_{A,cs}$ = axial stiffness at time $t_0$ for uncracked section, using effective module $E_{ef,cs}$;

$R_{B,cs}$ = stiffness associated with the static moment of area at time $t_0$ for uncracked section, using effective module $E_{ef,cs}$;

$R_{I,cs}$ = flexural stiffness at time $t_0$ for uncracked section, using effective module $E_{ef,cs}$;

$\varepsilon_{r,cs}$ = shrinkage deformation at the adopted reference level that defines the non-uniform shrinkage distribution;

$\kappa_{r,cs}$ = curvature that defines the non-uniform concrete shrinkage distribution.

### 3.2.2 Creep deflection

The creep deflection component $(\delta_{cc})$ is determined by multiplying the instantaneous deflection produced by loading $(\delta_{0,i})$ by the creep multiplier $(\alpha_{cc})$, given in Equations 14-15.

$$\delta_{cc} = \delta_{0,i} \cdot \alpha_{cc} \tag{14}$$

$$\alpha_{cc} = \frac{E_c I_{ef}}{E_{ef,cc} I_{ef,cc}} - 1 \tag{15}$$

where:

$E_c$ = value of the static module of concrete at the time of the first loading (or calculated at 28 days if the time of the first loading is not known or expects to be greater than 28 days).

The modulus $E_{ef,cc}$ is given by Equation 16.

$$E_{ef,cc} = \frac{E_c}{1 + \varphi_{cc}} \tag{16}$$

Rev. IBRACON Estrut. Mater., vol. 14, no. 5, e14501, 2021

7/22

$\varphi_{cc}$ = creep coefficient calculated for the concrete at the time of interest for the first loading at time $t_0$, considering the following conditions when calculating the hypothetical thickness $t_h = 2A_g / u_e$. It can be calculated according to the normative codes for structural concrete.

(a) $A_g$ it was assumed equal to the cross-sectional area of the composite slab, therefore, using the actual thickness of the composite slab in the calculation of $A_g$;'

(b) $u_e$ it is taken equal to the width of the slab (assuming, therefore, that concrete drying occurs only from the exposed surface of the slab). For the calculations, the properties for unit width were considered.

$I_{ef}$ = effective second moment of area calculated with Equation 6 using $E_{ef,cc}$ for the concrete static module, for the age evaluated;

$I_{ef,cc}$ = second moment of area calculated according to Equation 6 using $E_{ef,cc}$ for the concrete static modulus for time $t_0$. According to Ranzi [16], it can be assumed that the cracked concrete section corresponds to that identified at time $t_0$ for instantaneous deflection calculation.

The AS/NZS 2327 [5] code still indicates that when $I_{ef,cc}$ is evaluated, the second moment of area associated with the cracked section can be determined based on the cracked geometry identified for the short-term tests.


### 3.2.3 Shrinkage deflection

The non-uniform shrinkage profile is due to the presence of the steel decking, which turns the underside impermeable. The linear gradient adopted is an approximation of the real gradient, introduced to simplify the calculations. The conditions specified for the hypothetical thickness are based on the fact that the shrinkage gradient was calibrated based on shrinkage profiles induced by concrete slabs exposed on both sides with the same slab's thickness.

In the simplified method, the shrinkage profile used in the induced deflection calculation due to the shrinkage and cracking moment can be based on a linear gradient shrinkage distribution with deformation of $\eta_{b,k} = 0,2\varepsilon_{cs}$ on the bottom face of the slab and $\eta_{t,k} = 1,2\varepsilon_{cs}$ on the top face slab (exposed surface). Which $\varepsilon_{cs}$ is the concrete shrinkage strain. Figure 4 shows the reference for deformation and curvature shrinkage.
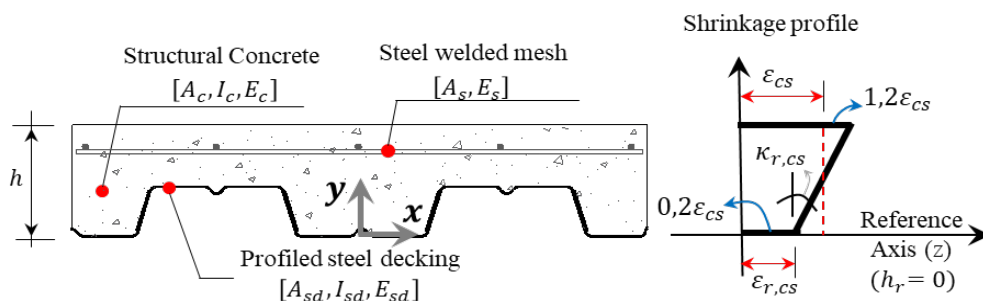


**Figure 4.** Linear shrinkage gradient and reference axis system.

$$\varepsilon_{r,cs} = \frac{(h - h_r) \cdot \eta_{t,k} + h_r \cdot \eta_{b,k}}{h} \cdot \varepsilon_{cs,k} \tag{17}$$

$$\kappa_{r,cs} = \frac{(\eta_{t,k} - \eta_{b,k})}{h} \cdot \varepsilon_{cs,k} \tag{18}$$

The reference strain value $\varepsilon_{cs}$ can be calculated according to the normative codes for structural concrete and adopts a hypothetical thickness equal to the thickness of the slab. The linearly varied non-uniform profile can be given by the reference strain $\varepsilon_{r,cs}$ (Equation 17) and by the curvature given by the ratio of the difference between deformation on the top and bottom face by the height of the slab section (Equation 18).

For simply-supported slab, schematically shown in Figure 5, due to the restriction of the free shrinkage by the steel decking, appearance of normal eccentric stress, an internal moment is generated due to the $M_{cs}$. The shrinkage deflection can be expressed by the curvature ($\kappa$) given that are directly proportional to flexural moment ($M(z) = \kappa EI$). The component $\delta_{cs}$ is calculated using the curvature and its span ($l$) by Equation 19.
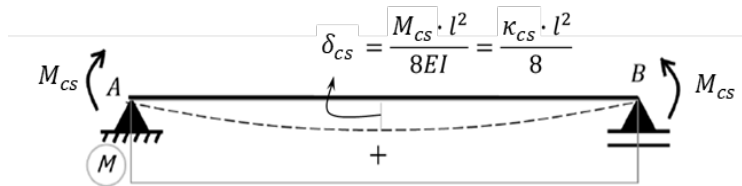


**Figure 5.** Simply-supported beam model with moments at the ends

$$\delta_{cs} = \frac{\kappa_{cs} \cdot L^2}{8} \tag{19}$$

The shrinkage deflection component ($\delta_{cs}$) must be determined for long-term analysis, considering the effects expressed by the shrinkage curvature induced, according to Equations 20-21, respectively.

$$\kappa_{cs} = (1 - \gamma_{cs}) \cdot \kappa_{cs,cr} + \gamma_{cs} \cdot \kappa_{cs,uncr} \tag{20}$$

$$\gamma_{cs} = \left(\frac{M_{cr}}{M_s}\right)^2 \leq 1 \tag{21}$$

where:
$\kappa_{cs,uncr}$ = shrinkage curvature for an uncracked cross-section considering the effective modulus of elasticity $E_{ef,cs}$ for the concrete;
$\kappa_{cs,cr}$ = shrinkage curvature for a cracked cross-section considering the effective modulus of elasticity $E_{ef,cs}$ for the concrete.
$E_{ef,cs}$ is given by Equation 22.

$$E_{ef,cs} = \frac{E_c}{1 + 0,55 \cdot \varphi_{cc}} \tag{22}$$

The curvature $\kappa_{cs}$ is determined based on the weighting of the effects of the cracked ($\kappa_{cs,cr}$) and uncracked section ($\kappa_{cs,uncr}$). They can be determined for the composite slab cross-section according to the procedure by Equations 23-24, respectively.

$$\kappa_{cs,uncr} = \left[\frac{R_{B,cs,uncr}}{R_{0,cs,uncr}} \quad \frac{R_{A,cs,uncr}}{R_{0,cs,uncr}}\right] \cdot E_{ef,cs} \cdot \left[\begin{array}{c} A_{c,uncr} \cdot \varepsilon_{r,cs} - B_{c,uncr} \cdot \kappa_{r,cs} \\ -B_{c,uncr} \cdot \varepsilon_{r,cs} + I_{c,uncr} \cdot \kappa_{r,cs} \end{array}\right] \tag{23}$$

$$\kappa_{cs,cr} = \left[\frac{R_{B,cs,cr}}{R_{0,cs,cr}} \quad \frac{R_{A,cs,cr}}{R_{0,cs,cr}}\right] \cdot E_{ef,cs} \cdot \left[\begin{array}{c} A_{c,cr} \cdot \varepsilon_{r,cs} - B_{c,cr} \cdot \kappa_{r,cs} \\ -B_{c,cr} \cdot \varepsilon_{r,cs} + I_{c,cr} \cdot \kappa_{r,cs} \end{array}\right] \tag{24}$$

The second moment of area of the sections can be obtained by the stiffness of the section from a reference axis, using Equations 25-26.

$$I_{uncr} = \frac{R_I \cdot R_A - R_B^2}{R_A \cdot E_c}$$
(25)

$$I_{cr} = \frac{R_{I,cr} \cdot R_{A,cr} - R_{B,cr}^2}{R_{A,cr} \cdot E_c}$$
(26)

where:
$I_{uncr}$ = second moment of area of the homogenised uncracked section;
$I_{cr}$ = second moment of area of the homogenised cracked section;
$R_{A,cr}$ = axial stiffness calculated at time $t_0$ for cracked section;
$R_{B,cr}$ = stiffness associated with the static moment of the area at time $t_0$ for cracked section;
$R_{I,cr}$ = flexural stiffness at time $t_0$ for cracked section.

Attention to the clear differences between the two simplified approaches for the deflection calculations. The Brazilian Standard NBR 8800:2008 [11] does not indicate a method for evaluating deflection in composite slabs. Usually, Eurocode 4 [4] is used. The detailed development of an example using the simplified method presented previously to evaluate the total deflection of the experimental test performed by the authors is presented. It is considered an infinite time of 10,000-days, in which, all the deformations due to the effects of concrete shrinkage and creep have occurred.

## 4 EXPERIMENTAL DATA AND CHARACTERISTICS OF COMPOSITE SLABS

The long-term experimental test with composite steel-concrete slab was developed at the São Carlos School of Engineering with a duration of 134 days. The composite slab consisted of steel decking profile MD55 [22] trapezoidal type with a nominal thickness of 0.80 mm. Table 1 presents the properties of the profiled steel decking MD55, based on unit width and design thickness, disregarding the zinc layer protection thickness of 0.04 mm. Figure 6 shows the composite slab cross-section.

**Table 1.** Properties of MD55 trapezoidal steel decking

| Profile Steel Decking | Thickness $(t_{sd})$ | Cross Section Area $(A_{sd})$ | Centroid Height $(h_{sd})$ | Second moment of area $(I_{sd})$ |
|---|---|---|---|---|
| MD55 | 0.76 mm | 975 mm²/m | 27.5 mm | 565,550 mm⁴ / m |

The concrete was composed of natural aggregates of the basaltic gravel and river sand, and cement CPII-Z-32. The compressive strength was $f_{cm} = 31.12$ MPa, flexural tensile strength $f_{ct.f} = 3.54$ MPa and elastic modulus $E_c = 30.00$ GPa, at 28 days. Used welded steel mesh with a $\phi$ 4.2 mm c/150 mm (92 mm² / m) at 30 mm from the top face. The steel decking presents an elastic modulus $E_{Sd} = 204.00$ GPa and the steel welded mesh $E_s = 191.00$ GPa.
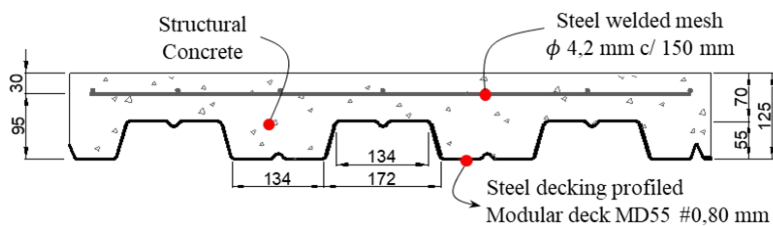


**Figure 6.** Cross-section of composite slabs (measured in *mm*)

Rev. IBRACON Estrut. Mater., vol. 14, no. 5, e14501, 2021

10/22

The prototype of the composite slab had a total height of 125 mm and a total span of 3,200 mm, with an effective span of 3,000 mm. The structural system was under simply-supported condition. Figure 7a shows the static configuration and the in-service loading, consisting of two parts: the slab self-weight (2.40 kN/m²) and the imposed load (2.26 kN/m²). Figure 7b shows the experimental test that consisted of loading distributed uniformly by concrete prisms on the slab. The slab had a 7-day wet curing process.

For the quasi-permanent load combination (long-term SLS), the imposed load represents a permanent load parcels due finishes and partitions (1.06 kN/m²) and long-term live load (1.20 kN/m²) due $\psi_2 \cdot Q_k$, where partial factor load $\psi_2 = 0.30$ and live load $Q_k = 4.00$ kN/m² (office areas).

The deflection measurements started at the age of 8-days after concrete casting, with the removal of the shoring placed in the mid-span. Dial gauges were arranged in the middle span. After removing the shoring, the measured instantaneous deflection due to self-weight was 0.35 mm. At 28 days, deflection reached 2.00 mm. On that same date, an imposed load was applied, simulating in-service loadings.
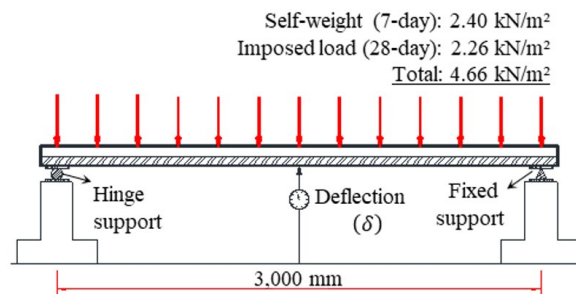


a) Static configuration of test



b) Composite slab under service loading

**Figure 7.** Long-term experimental test in composite slab

The instantaneous deflection resulting from the imposed loads was 0.65 mm. The deflection at the end of the experiment was 4.47 mm. The total instantaneous deflection was 1.00 mm, while the time-dependent deflection was 3.47 mm, at the age of 134 days.

The temperature and relative air humidity were monitored at the test site, with averages of 21.5ºC and 58.2%, respectively. The coefficients of variation were 10.7% and 18.8%, respectively. It is essential to highlight the lateral sealing of the slabs with the use of waterproofing mortars in order to simulate the real situation regarding the drying process that influences the shrinkage phenomenon.

Visual inspections identified no cracks. The existence of dial gauges confirmed the absence of relative slips at the ends of the composite slab assessed for the in-service evaluation.

The deflections obtained for the tested composite slab were compared to the predictions given by EC4 [4] and AS/NZS 2327 [5] and a discussion on the accuracy of models is presented.

# 5 RESULTS OF THE DEFLECTION CALCULATIONS

## 5.1 Eurocode 4 approach

Based on the characteristics and properties of the composite slab, a procedure for the deflection calculation is presented. Figure 8 presents the deflection $(\delta_{tot})$ predicted by EC4 for the composite slab, seen Equation 4.



$$\delta_{tot} = \frac{5}{384} \cdot \frac{p_{total} \cdot l^4}{E_{Sd} I_{cm}}$$

$$\delta_{tot} = \frac{5}{384} \cdot \frac{4.66 \ kN/m \cdot (3{,}000 \ mm)^4}{204{,}000 \ N/mm^2 \cdot 7{,}846{,}800 \ mm^4} = \mathbf{3.07 \ mm}.$$

**Figure 8.** Static system of the simply-supported composite slab

In the expression, total load ($p_{tot}$) considered self-weight plus imposed load, span was 3.000 mm, and material properties were steel modulus properties ($E_{Sd}$) and weighted average second moment of area ($I_m$), whose calculation is showed below. The modular ratio n considered the long-term effects with reduced modulus according to Equation 27:

$$n = \frac{E_{Sd}}{E_c'} = \frac{E_{Sd}}{0{,}5 \cdot E_c} = \frac{204{,}000}{0{,}5 \cdot 30{,}000} = 13.6. \tag{27}$$

From the slab cross-section, an equivalent T section is adopted for unit width, schematically shown in Figure 9. The value of $b_m$ is given by Equation 28.
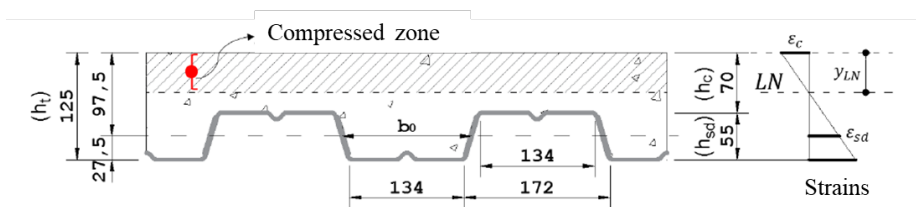


**Figure 9.** Composite slab slab variables and measures

$$b_0 = \frac{172 + 134}{2} = 153 \ mm \Rightarrow b_m = \frac{b}{b_s} \cdot b_0 = \frac{1000}{306} \cdot 153 = 500 \ mm \ / \ m \tag{28}$$

Second moment of area of the uncracked section, $I_{uncr}$, for unit width b (Equation 29).

$$I_{uncr} = \frac{b \cdot h_c^3}{12 \cdot n} + \frac{b \cdot h_c}{n} \cdot \left( y_u - \frac{h_c}{2} \right)^2 + \frac{b_m \cdot h_{Sd}^3}{12 \cdot n} + \frac{b_m \cdot h_p}{n} \cdot \left( h_{total} - y_u - \frac{h_{Sd}}{2} \right)^2 + A_{Sd} \cdot \left( y_{Sd} - x_u \right)^2 + I_{Sd} = 10{,}337{,}783 \ mm^4 \ / \ m. \ \left( \text{on steel modulus} \right) \tag{29}$$

In which $y_{uncr}$ is the position of the neutral axis in the uncracked section (Equation 30).

$$y_{uncr} = \frac{b \cdot \frac{h_c{}^2}{2} + b_m \cdot h_{Sd} \cdot \left(h - \frac{h_{Sd}}{2}\right) + n \cdot A_{Sd} \cdot y_{Sd}}{b \cdot h_c + b_m \cdot h_{Sd} + n \cdot A_{Sd}} = 57.67 \, \text{mm}. \tag{30}$$

Second moment of area of the cracked section, $I_{cr}$, for $b = 1,000 \, \text{mm}$ (Equation 31):

$$I_{cr} = \frac{b \cdot y_c{}^3}{3 \cdot n} + A_p \cdot (y_{Sd} - y_c)^2 + I_{Sd} = 5,355,816 \, \text{mm}^4/\text{m}. \tag{31}$$

The neutral axis position of the cracked section to the top of the slab $y_{cr}$ is by Equation 32.

$$y_{cr} = \frac{\Sigma A_i \cdot z_i}{\Sigma A_i} = \frac{n \cdot A_p}{b} \left( \sqrt{1 + \frac{2 \cdot b \cdot d_{Sd}}{n \cdot A_{Sd}}} - 1 \right) = 39.29 \, \text{mm}. \tag{32}$$

The average value of second moment of area ($I_{cm}$) for cracked ($I_{cr}$) and uncracked ($I_{uncr}$) section is (seen Equation 3):

$$I_{cm} = \frac{I_{uncr} + I_{cr}}{2} = \frac{10,337,783 + 5,355,816}{2} = 7,846,800 \, \text{mm}^4/\text{m}. \tag{}$$

The expression of predicted deflection takes into account the cracking effects with average second moment of area and is based on the reduction in half of the concrete's modulus of elasticity.

## 5.2 Prediction of AS/NZS 2327 approach

According to the experimental test and considered evaluation approach, the composite slabs have the followings deflections components:

• Instantaneous deflections: due self-weight $(\delta_{0,8d})$ and imposed load $(\delta_{l,28d})$;

• Time-dependent deflections: due creep component: imposed load $(\delta_{cc,l})$ e shrinkage component: $(\delta_{cs})$.

Based on the equations presented in **Section 3.2**, each component is calculated. Table 2 presents a summary of them.

**Table 2.** Data for analysis using section rigidities at $t_0$

| Input data | Unit | Concrete (c) Uncracked section | Concrete (c) Cracked section | Steel Decking (sd) | Steel mesh (s) |
|---|---|---|---|---|---|
| *Cross-section area (A)* | $\text{mm}^2/\text{m}$ | 97,454.4 | 29.933 | 975 | 102 |
| *First area moment (B)* | $\text{mm}^3/\text{m}$ | 7,163,690.7 | 3,293,668 | 26,812.5 | 9695.6 |
| *Second moment of area (I)* | $\text{mm}^4/\text{m}$ | 635,595,091 | 364,648,226 | 1,302,894 | 921,189 |
| *Elastic modulus (E)* | $\text{N}/\text{mm}^2$ | 30,000 | 30.000 | 204,000 | 191,000 |
| Uncracked section: | | $R_{A,0,uncr} = 3,139 \times 10^6 \, \text{N}; R_{B,0} = 2,219 \times 10^8 \, \text{Nmm}; R_{I,0} = 1,948 \times 10^{10} \, \text{Nmm}^2$ | | | |
| Cracked section: | | $R_{A,0,cr} = 1,113 \times 10^6 \, \text{N}; R_{B,0,cr} = 1,058 \times 10^8 \, \text{Nmm}; R_{I,0,cr} = 1,135 \times 10^{10} \, \text{Nmm}^2$ | | | |

The cracking moment for the composite section without taking into account the shrinkage effects is $M_{cr} = 8.34 \, \text{kNm}$. The tensile stress induced by shrinkage is obtained, according to Equations 7, 11, 12. At age 10.000-days, the predicted shrinkage deformation is $\varepsilon_{cs}(\infty, 7) = -548 \cdot 10^{-6}$ and creep coefficient $\varphi(\infty, 28) = 2.48$. Both calculated according to Brazilian code NBR 6118 [23] Annex A recommendations. The stress-induced shrinkage at the bottom face of concrete is $\sigma_{cs} = 0.96 \, \text{MPa}$ and the cracking moment is reduced for $M_{cr,cs(\infty)} = 6.10 \, \text{kNm}$ ($\approx$ -27%).

Rev. IBRACON Estrut. Mater., vol. 14, no. 5, e14501, 2021

13/22

## Instantaneous deflections components

The second moment of area (I) based on the initial stiffness, as there was no cracking, is given by Equation 22. If the section is cracked, Equation 6 is used.

$$I_{uncr} = \frac{1,948 \times 10^{10} \cdot 3,139 \times 10^6 - \left(2,219 \times 10^8\right)^2}{3,139 \times 10^6 \cdot 30,000} = 126.3 \times 10^6 \, mm^4 \, / \, m \; (on \; concrete \; modulus).$$

The in-service flexural moment at 8-days due self-weight $p_{0,8} = 2.40 \, kPa$ is $M_{s,8} = 2.70 \, kNm < M_{cr}$. The instantaneous deflection is $\delta_{0,8d} = 0.67 \, mm$. In-service flexural moment at 28-days, plus imposed load ( $p_{1,28} = 2.26 \, kPa$ ) produces $M_{s,8} = 5.02 \, kNm < M_{cr}$. The second part of the instantaneous deflection is $\delta_{0,28d} = 0.63 \, mm$. The total instantaneous deflection is $\delta_{0,tot} = 1.30 \, mm$.

## Creep deflection component

The total creep deflection component for imposed load $\left(\delta_{cc,sob1,\,\infty}\right)$ is given by Equations 14 and 15. The effective creep module for the imposed load, with creep coefficient $\varphi(\infty,8) = 2.48$ is $E_{ef,cc} = 8,618 \, MPa$. The effective inertias $I_{ef}$ and $I_{ef,cc}$ are calculated with modules $E_c$ and $E_{ef,cc}$, respectively, taking into account the possibility of cracking and, consequently, tension-stiffening effects. Calculating the inertia for effective creep modulus ( $E_{ef,cc}$ ), one obtains $I_{ef} = 164 \times 10^6 \, mm^4 \, / \, m$. Therefore, $\alpha_{cc,sob1(\infty)} = 1.68$ and $\delta_{cc,\infty} = 0.63 \, mm \cdot 1.68 = 1.06 \, mm$. The creep deflection component is $\delta_{cc} = 1.06 \, mm$.

## Shrinkage deflection component

The total shrinkage deflection component ( $\delta_{cs,\infty}$ ) is determined based on the curvature induced by $\kappa_{cs}$ shrinkage. The effective concrete modulus for shrinkage $E_{ef,cs}$ is calculated according to Equation 19 and the reference shrinkage deformation $\varepsilon_{r,cs,\infty}$ and curvature $\kappa_{r,cs,\infty}$, as shown in Figure 2. Given the non-occurrence of cracking in the cross-section, uncracked inertia of the concrete was used. Table 3 presents the data summary for obtaining the curvatures due to non-uniform shrinkage.

**Table 3.** Data summary for non-uniform shrinkage parameters

| | | |
|---|---|---|
| $E_{ef,cs} = 12,687 \, MPa;$ | $A_{c,uncr} = 97,454.4 \, mm^2;$ | $R_{A,cs,uncr} = 1453.5 \times 10^6 \, N;$ |
| $\varepsilon_{r,cs,\infty} = -110 \cdot 10^{-6} \, mm \, / \, mm;$ | $B_{c,uncr} = -7,163,691 \, mm^3;$ | $R_{B,cs,uncr} = -980.9 \times 10^8 \, Nmm;$ |
| $\kappa_{r,cs,\infty} = -4.38 \, mm^{-1};$ | $I_{c,uncr,r} = 635.6 \times 10^6 \, mm^4;$ | $R_{0,cs,uncr} = 2725.4 \cdot 10^{18} \, N^2 mm^2.$ |

The curvature of the composite slabs section is obtained according to Equation 20.

$$\kappa_{cs,uncr,\infty} = \left[\frac{R_{B,cs,uncr}}{R_{0,cs,uncr}} \quad \frac{R_{A,cs,uncr}}{R_{0,cs,uncr}}\right] E_{ef,cs} \left[\begin{array}{c} A_{c,uncr} \cdot \varepsilon_{r,cs} - B_{c,uncr} \cdot \kappa_{r,cs} \\ -B_{c,uncr} \cdot \varepsilon_{r,cs} + I_{c,uncr} \cdot \kappa_{r,cs} \end{array}\right] = -4.95 \cdot 10^{-6} \, mm^{-1}.$$

The maximum long-term shrinkage deflection is given by Equation 20.

$$\delta_{cs(\infty)} = \frac{\kappa_{cs} \cdot L^2}{8} = \frac{4.95 \cdot 10^{-6} \cdot 3,000^2}{8} = 5.57 \, mm.$$

Rev. IBRACON Estrut. Mater., vol. 14, no. 5, e14501, 2021

14/22

Therefore, the deflection by AS/NZS 2327 [5] calculation has a final predicted value of instantaneous component equal $\delta_{0,tot} = 1.30\,\mathrm{mm}$ and the long-term component of $(\delta_{cc} + \delta_{cs}) = 6.63\,\mathrm{mm}$. The total deflection predicted is the sum of all components $\delta_{tot}\,(\delta_0 + \delta_{cc} + \delta_{cs}) = 7.93\,\mathrm{mm}$. The non-uniform shrinkage being the most representative component, which for the slab calculation represented 70% of the total deflection predicted.

## 6 DISCUSSIONS OF THE AUTHOR'S EXPERIMENTAL RESULTS

The Brazilian code NBR 8800 [11] includes in its Annex Q normative guidelines for composite steel-concrete slabs. For serviceability criteria, it states that the maximum deflection must be less than the ratio of the theoretical span $L_F/350$, considering only the effect of the live loads. However, it does not provide any indication for deflection evaluations. The international codes Eurocode 4 [4] and AS/NZS 2327 [5] provide further guidance, highlighting the usual limitation of $L_F/250$ for actions by the quasi-permanent combination.

The results presented by the two evaluation approaches for the same in-service loading were 3.07 mm and 7.93 mm, respectively, for the EC4 [4] and AS/NZS 2327 [5] approaches for total deflection. A significant difference between them, with the Australian approach considering the time-dependent effects, and presenting higher values of deflection than the Eurocode 4 approach.

The deflection predicted for the imposed load has a value corresponding to 48.5% (1.49 mm) of the total deflection (3.07 mm) for the Eurocode 4 [4] approach. In the AS/NZS 2327 [5] approach, instantaneous deflection is 0.63 mm and the creep deflection 1.06 mm (total 1.69 mm). Shrinkage deflection occurs without the influence of loadings.

The AS/NZS 2327 [5] approach shows good accuracy compared to the experimental results. The shrinkage strain and creep coefficient were calculated based on the model of Annex A of the Brazilian Standard ABNT NBR 6118:2014 [23]. Figure 10 shows the results for experimental data and theoretical predictions by AS/NZS 2327 [5] over time and the deflection value with EC4 [4] approach.

The evolution of the long-term deflection can be observed, reaching an asymptote in a long-time of the effects of shrinkage and creep concrete. An age 10.000-days was taken for the comparative analysis. For the test age of 134 days with the imposed load, the instantaneous deflection is observed in the jumps (Figure 10). The final experimental deflection was 4,40 mm, compared to the analytical-theoretical prediction of 4.54 mm, (Experimental / Predicted) equals 0.97.

Table 4 shows the results of the experimental and theoretical analysis using the simplified approach of the code AS/NZS 2327 [5].

**Table 4.** Results of experimental and theoretical deflection by AS/NZS 2327 approach

| Measured | Instantaneous deflection (Inst.) | | | Long-term deflection (L.T.) | | | Total deflection (Inst.+L.T.) | Ratio (Inst.)/(LT) |
|---|---|---|---|---|---|---|---|---|
| | *Self-weight (1)* | *Imposed Load (2)* | *Total* | *8-28 days* | *29-134 days* | *Total* | | |
| **Experimental** | 0.35 | 0.65 | 1.00 | 1.65 | 1.82 | 3.47 | **4.47** | 3.47 |
| **Predicted** | 0.67 | 0.63 | 1.30 | 0.97 | 2.30 | 3.27 | **4.57** | 2.52 |
| **Ratio Exp./Pred)** | 0.52 | 1.03 | 0.77 | 1.76 | 0.79 | 1.06 | **0.98** | - |

Compared to the instantaneous deflection, there is (Exp. = 1.00 mm / Pred. = 1.30 mm), a ratio of 0.77. For the instantaneous deflection component due imposed load, we have (Exp. = 0.65 mm / Pred. = 0.63 mm), a ratio of 1.03. The long-term deflection showed an experimental value of 3.47 mm, against an analytically predicted value of 3.27 mm (Exp./Pred. = 1.06). The long-term deflection predicted is 2.52 times larger than the instantaneous deflection at this age (134-days). In this way, the approach is more accurate in predicting deflections.
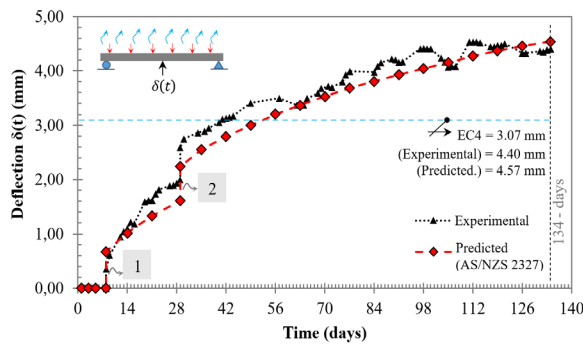
*(*) Activities: (1) Removal of temporary shoring ;(2) Loading application – imposed load*

**Figure 10.** Results of experimental test for composite slabs and predicted deflections by simplified method AS/NZS 2327 [5]

Compared to the instantaneous deflection, there is (Exp. = 1.00 mm / Pred. = 1.30 mm), a ratio of 0.77. For the instantaneous deflection component due imposed load, we have (Exp. = 0.65 mm / Pred. = 0.63 mm), a ratio of 1.03. The long-term deflection showed an experimental value of 3.47 mm, against an analytically predicted value of 3.27 mm (Exp./Pred. = 1.06). The long-term deflection predicted is 2.52 times larger than the instantaneous deflection at this age (134-days). In this way, the approach is more accurate in predicting deflections.

For the extrapolation of data, as shown for the presented example, the final deflection at age 10,000-days is 6.63 mm. For the age of 134-days, the occurred deflection represents around 50% of the long-term effects. Thereby even a test with relatively short duration allows reassuring the need of taking into account the long-term effects for more accurate analysis.

## 7 RESULTS AND DISCUSSIONS OF THE LITERATURE EXPERIMENTAL

In order to obtain a complete picture of design code deflection calculation for steel-concrete composite slabs, experimental results from the literature were also considered in this study. These studies include experimental tests of 12 simply-supported slabs.

Al-Deen et al. [10] tested 2 composite slabs, with a span of 3,000 mm and slab thickness of 180 mm, without imposed load. They used a clip-pan profile steel decking and normal concrete. The duration was 239 days. Gholamhoseini [8][9] tested 10 slabs, with a span of 3,100 mm and slab thickness of 150 mm, 2 without and 8 with an imposed load. Each five slabs used one trapezoidal type steel decking and normal concrete. The duration test evaluated varied in 197-251 days.

Table 5 shows the summary of specimens evaluated. The Slabs ID brings the original names by the authors. The self-weight and imposed load are presented in kPa.

**Table 5.** Simply-supported composite slabs: long-term experimental results in literature

| Author(s) | Slab ID | Profiled Steel Decking | Span (mm) | Slab Thickness (mm) | Self-weight (kPa) | Imposed Load (kPa) | Duration test (days) |
|---|---|---|---|---|---|---|---|
| Al-deen et al. [10] | CS1 | Condeck HP55[a] [24] | 3000 | 180 | 4.40 | None | 239 |
| | CS2 | | | | | None | |
| Gholamhoseini [8] [9] | 1LT-70-0 | Filders KF70[b] [25] | 3100 | 150 | 3.00 | None | 247 |
| | 2LT-70-3 | | | | | 3.40 | |
| | 3LT-70-3 | | | | | 3.40 | |
| | 4LT-70-6 | | | | | 6.00 | |
| | 5LT-70-6 | | | | | 6.00 | 197 |
| | 6LT-40-0 | Filders KF40[c] [25] | 3100 | 150 | 3.20 | None | 244 |
| | 7LT-40-3 | | | | | 3.40 | |
| | 8LT-40-3 | | | | | 3.40 | 251 |
| | 9LT-40-6 | | | | | 6.40 | |
| | 10LT-40-6 | | | | | 6.40 | |

[a] Profile steel decking clip-pan type: 0.75 mm Stramit Condeck HP55 [24]
[b, c] Profile steel decking trapezoidal type: 0.75 mm KF40 and KF70 [25]

Rev. IBRACON Estrut. Mater., vol. 14, no. 5, e14501, 2021

16/22

The characteristics of the composite slabs, as geometrical and materials properties are summarised in Table 6. These works brought the characteristics of the steel decking, loads and environmental conditions and, characteristics of the concrete, elastic modulus and flexural tensile strength.

These twelve composite slabs were used to compare experimental results to the provisions by AS/NZS 2327 [5]. The slabs of Al-deen et al. [10] and Gholamhoseini [8] [9] were referred to the Australian Standard AS 3600:2018 [26] for concrete creep and shrinkage models, since they were designed considering local materials and conditions.

The composite slabs were uncracked for the given load. In the occurrence of cracking, the effects of creep and shrinkage on the deflection shall increase, considering the reduction in the stiffness of the cracked cross-sections.

**Table 6.** Characteristics of the composite slabs in literature
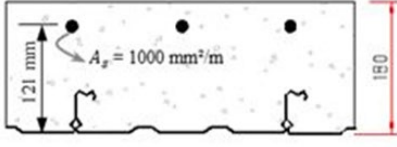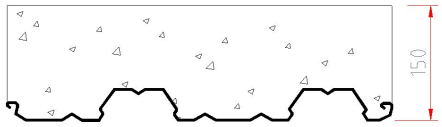
| Composite Slab | Steel decking | Concrete |
|---|---|---|
| **• CS1 [10]** | **Profile: Clip-pan Condeck HP55** | **Normal concrete** |
|  | Steel thickness: *0.75 mm* | *Compressive strength:* $f_{c28} = 27.30\,\text{MPa}$ |
| | Centroid height (bottom face): *15.3 mm* | *Elastic modulus:* $E_c = 26.40\,\text{GPa}$ |
| **• CS2 [10]** | Steel area: *1,211* $\text{mm}^2/\text{m}$ | |
|  | Second moment: $I_s = 488,000$ $\text{mm}^4/\text{m}$ | *Flexural tensile strength:* $f_{ct,f} = 3.13\,\text{MPa}$ |
| | Elastic modulus: $E_s = 200\,\text{GPa}$ | |
| **• LT-70 [8] [9]** | **Profile: Trapezoidal KF70** | **Normal concrete** |
| | Steel thickness: *0.75 mm* | *Compressive strength:* $f_{c28} = 28.00\,\text{MPa}$ |
|  | Centroid height (bottom face): *27.7 mm* | *Elastic modulus:* $E_c = 30.725\,\text{GPa}$ |
| | Steel area: *1.100* $\text{mm}^2/\text{m}$ | *Flexural tensile strength:* $f_{ct,f} = 3.50\,\text{MPa}$ |
| | Second moment: $I_s = 584,000$ $\text{mm}^4/\text{m}$ | |
| | Elastic modulus: $E_s = 212\,\text{GPa}$ | |
| **• LT-40 [8] [9]** | **Profile: Trapezoidal KF40** | **Normal concrete** |
| | Steel thickness: *0.75 mm* | *Compressive strength:* $f_{c28} = 35.50\,\text{MPa}$ |
|  | Centroid height (bottom face): *14.0 mm* | *Elastic modulus:* $E_c = 28.20\,\text{GPa}$ |
| | Steel area: *1.040* $\text{mm}^2/\text{m}$ | *Flexural tensile strength:* $f_{ct,f} = 3.80\,\text{MPa}$ |
| | Second moment: $I_s = 269,000$ $\text{mm}^4/\text{m}$ | |
| | Elastic modulus: $E_s = 193\,\text{GPa}$ | |

Figure 11 show experimental results compared with deflection calculation by code AS/NZS 2327 [5] approach in the simply-supported composite slabs in long-term tests. In comparison, the values of the deflection calculated using the EC4 [4] model are shown. The first 4 slabs are subject only to their self-weight. The others 8 slabs have testing pairs and have imposed loads in the order of the self-weight and double it.

Rev. IBRACON Estrut. Mater., vol. 14, no. 5, e14501, 2021

17/22

A good accuracy between experimental and predicted long-term deflections was observed (Figure 11) with obtained ratio (Exp./Pred.) ranging between (0.88 - 1.14) as presented in Table 7, with average equal 0.99 and coefficient of variation (c.o.v) of 9.6%. The long-time deflection calculation adopted the procedure shown in **Section 3.2**. This simplified method proposed by AS/NZS 2327 [5] used materials and geometric properties from tests presented in the literature and performed by authors to compare the predicted deflections to the measured ones.

Table 7 provides a comparative evaluation of the results at the end of the performed tests considering measured values and deflections predicted by the AS/NZS 2327 [5] approach. A second comparison considers the final deflections for long-time at $t_\infty$ given by AS/NZS 2327 [5], BS5950 [21] and Eurocode 4 [4] models, using reduced elasticity modulus of concrete with $2/3E_{cm}$, $1/3E_{cm}$ and $1/2E_{cm}$, respectively, for each tested slab. Figure 12 summarizes the comparative results of the deflections evaluations.
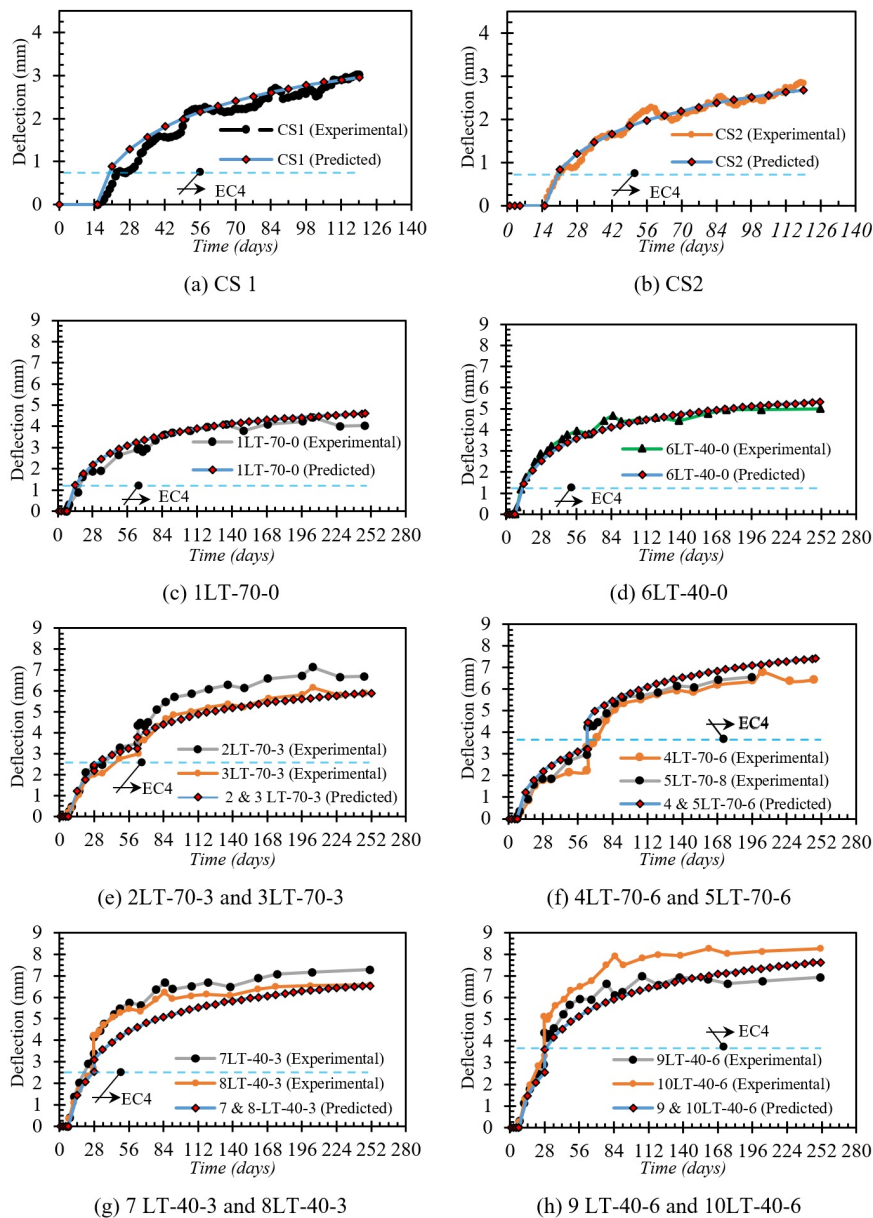


**Figure 11.** Comparisons between experimental and theoretical predicted (AS/NZS 2327) deflections of simply-supported composite slabs in long-term tests

L. A. M. Oliveira, T. M. Borghi, Y. O. Rodrigues, and A. L. H. C. Debs

**Table 7.** Deflection calculation using design codes compared to experimental tests results

| Slabs ID | Imposed Load / Self-weight | Deflections at the end of test (t) | | | Final predicted deflection | | | | |
|---|---|---|---|---|---|---|---|---|---|
| | | Tests Results (mm)[(1)] | AS/NZS 2327 (mm)[(2)] | Ratio* (1)/(2) | AS/NZS 2327 ($t_\infty$) (mm)[(3)] | BS5950 (2/3$E_{cm}$) (mm)[(4)] | ($E_{cm}$/3) (mm)[(5)] | EC4 ($E_{cm}$/2) (mm)[(6)] | Ratio** (3)/(6) |
| CS1 | None | 3.02 | 2.96 | (1.02) | 5.17 | 0.67 | 1.05 | 0.81 | (6.38) |
| CS2 | | 2.85 | 2.68 | (1.06) | 4.48 | 0.65 | 0.99 | 0.78 | (5.74) |
| 1LT-70-0 | | 4.04 | 4.60 | (0.88) | 6.11 | 1.01 | 1.56 | 1.22 | (5.01) |
| 6LT-40-0 | | 4.99 | 5.33 | (0.94) | 7.24 | 1.04 | 1.58 | 1.24 | (5.84) |
| 2LT-70-3 | 1.13 | 6.70 | 5.87 | (1.14) | 7.40 | 2.15 | 3.33 | 2.60 | (2.85) |
| 3LT-70-3 | | 5.86 | | (1.00) | | | | | |
| 7LT-40-3 | 1.06 | 7.30 | 6.55 | (1.11) | 8.75 | 2.14 | 3.27 | 2.56 | (3.42) |
| 8LT-40-3 | | 6.57 | | (1.00) | | | | | |
| 4LT-70-6 | 2.00 | 6.76 | 7.41 | (0.91) | 10.86 | 3.03 | 4.69 | 3.65 | (2.98) |
| 5LT-70-6 | | 6.58 | 7.08 | (0.93) | | | | | |
| 9LT-40-6 | | 6.94 | 7.63 | (0.91) | 10.06 | 3.11 | 4.75 | 3.73 | (2.70) |
| 10LT-40-6 | | 8.26 | | (1.08) | | | | | |
| Presented | 0.94 | 4.40 | 4.57 | (0.98) | 7.93 | 2.54 | 3.86 | 3.07 | (2.58) |
| | | | Average = 0.99 * | | Average = 5.74 / C.O.V = 9.8% (No imposed load) ** | | | | |
| | | | C.O.V = 9.6% * | | Average = 2.90 / C.O.V = 11.1% (With imposed load) ** | | | | |

* Ratio between experimental results[(1)] and predicted deflection by AS/NZS 2327[(2)] at end age of test (t).

** Ratio between total deflection AS/NZS 2327 at infinite time ( $t_\infty$ )[(3)] and EC4 approach[(6)]
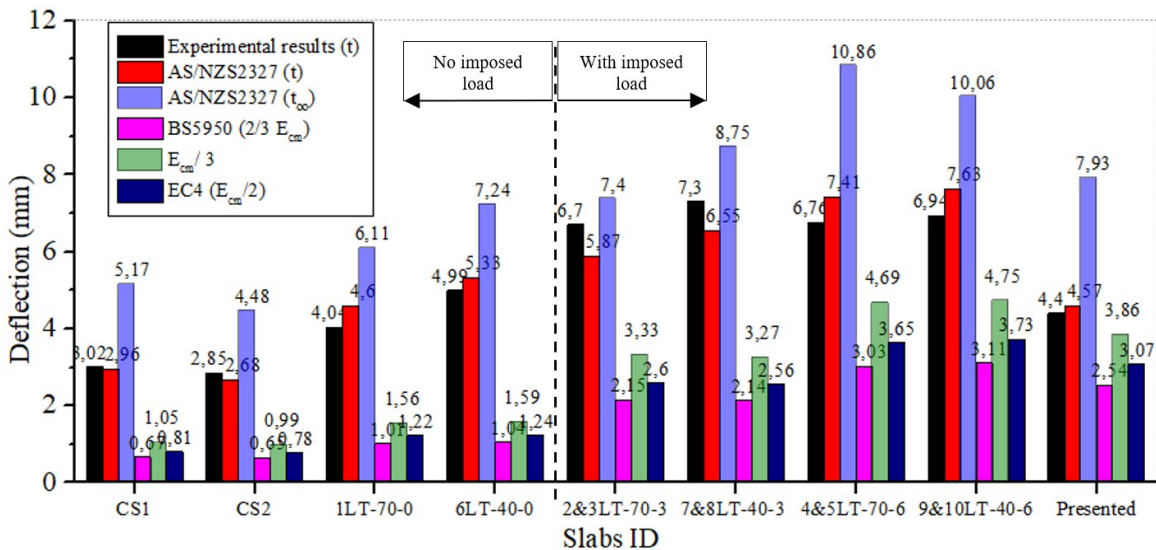


**Figure 12.** Comparisons between experimental results (*black color*) and theoretical predictions deflections of simply-supported composite slabs in long-term tests

The final predicted deflections by the analysed codes for the first four studied slabs, with no imposed load, presented a massive difference between obtained values, being 5.01-6.38 (average = 5.74 and C.O.V = 9.8%) lower for the Eurocode model [4] regarding the AS/NZS approach [5]. For the other eight slabs, plus the one presented by the authors, with imposed load representing 0.94-2.00 of the self-weight, the results showed that for the in-service loading, the predictions of the Eurocode 4 model were 2.58-3.42 (average = 2.90 and C.O.V = 11.1%) lower than the AS/NZS 2327 [5] model. Figure 12 clarifies that strategy of reduced elastic modulus of concrete is not adequate, even using values such as its third part. The deflection component due to the shrinkage was the most expressive contribution for that difference.

Rev. IBRACON Estrut. Mater., vol. 14, no. 5, e14501, 2021

19/22

The mean values practiced in the market were represented by the evaluated composite slabs of 3 m span and 125 to 180 mm in height of slab, and composed with profile steel decking with 40-75 mm and steel thicknesses of 0.75 mm – 1.00 mm. The analyses indicate that for simply supported slabs, the in-service assessment that considered the shrinkage and creep effects enabled results consistent with experimental results in tested time. Based on this first comparation and when performing the extrapolation for a long useful life of the structure to the AS/NZS 2327 model, the values of the EC4 model using different reduced modulus of elasticity of concrete underestimate the evaluations for the total deflections.

Due to the significance of the shrinkage deflection, it may prevail against the $L_F/350$ for the live loads. Shrinkage deflection happens regardless of the live loads. However, it is related to the cracking, which can be increased by the greater magnitude of the loads.

For the Brazilian market, an outstanding point is the in-service checks for slabs with lattice joists using the ArcelorMittal *Trelifácil* system [27] (Figure 13) or steel-bars truss (Wang et al. [28]). The use of this steel form leads to a non-uniform shrinkage, similarly to composite slabs, indicating the application of the methodology for total deflections calculations.



a) Bottom slab with juxtaposed panels [26]             b) T*relifácil* lattice slab [26]

**Figure 13.** *Trelifácil* system with steel formwork on slab soffit face [27]

AS/NZS 2327 [5] also indicates that the application of surface treatments or the installation of floor coverings can influence and reduce the ability of concrete to dry from its upper face. In these cases, it is possible to reduce the drying shrinkage component used in the deflection calculations reflecting the reduction in drying that occurs from the slab surface, as long as the solution adopted becomes part of the structural design specifications.

# 8 CONCLUSIONS

This paper discussed the deflection evaluation of the serviceability limit state (SLS) for steel-concrete composite slabs, which are presented as a solution for floors in buildings and bridges. Some relevant aspects are highlighted:

- The presentation and comparison of the two main approaches for assessing the deflections demonstrated the difference in complexity and consideration of the variables in the calculations.
- The approach recommended by AS/NZS 2327 [5] showed a total deflection $\delta_{tot} = 7.93\ mm$ against $\delta_{tot} = 3.07\ mm$ of Eurocode 4 [4] approach, for the tested slab. So, the first was 2.58 times larger.
- Shrinkage deflection component does not depend directly on the applied load, representing for the numerical example, 70% of the total deflection. Therefore, it appears that this analysis is essential.
- Given the experimental analysis of the simply-supported composite slab, it was possible to investigate the time-dependent effects over 134-days. It was found that Eurocode 4 underestimated the total deflection, while the AS/NZS 2327 model shows to be accurate compared to the experimental results.
- At the age of 134-days, it is estimated that 50% of the time-dependents effects have occurred, showing the importance of considering the long-term effects already in the initial ages of buildings. This fact corroborates the application in steel and composite structures, which have a reduced construction time and more immediate use.
- The good accuracy of the simplified approach by AS/NZZS 2327 [5] was evaluated for Brazilian composite slabs, as well as Al-deen et al. [10] and Gholamhoseini [8] [9] Australian slabs;

- For the experimental results with simply-supported composite slabs under in-service conditions, the calculated final deflections showed that Eurocode 4 [4] can underestimate the values around 2.58-3.42 times, compared to AS/NZS 2327 [5]. Most expressive deflection component was due to shrinkage.
- As a suggestion for future investigations, it recommended the evaluation: of long-term deflection of continuous composite slabs; higher in-service loadings and; the influence of the slabs surface finishing on the effect of drying shrinkage and, consequently, on the time-dependent behaviour of composite slabs.

Therefore, the advance in materials and studies to improve the interaction between steel decking and concrete, obtaining larger spans and/or loads indicate the need of using more representative models. Considering cracking and long-terms effects, such as non-uniform shrinkage and creep in the correct assessment of the in-service behaviour of the composite slabs is progressively more necessary.

## ACKNOWLEDGEMENTS

## REFERENCES

[1]  D. A. Souza, "Steel-concrete composite structures", in *56 Brazilian Concr Congr*, Natal, 2014 (in Portuguese).

[2]  Techne Fast Construction, "Steel-concrete composite slabs system" (in Portuguese). (accessed Nov 1, 2020). Available: http://techne.pini.com.br/engenharia-civil/179/construcao-rapida-sistema-misto-que-dispensa-parcial-ou-totalmente-287917-1.aspx

[3]  R. Abdullah, "Experimental evaluation and analytical modelling of shear bond in composite slabs", PhD dissertation, Virginia Polytech. Inst. and State University, Blacksburg, 2004.

[4]  The European Union, *Eurocode 4 – Design of Composite Steel and Concrete Structures – Part 1-1: General Rules for Buildings*, EN 1994-1-1:2004.

[5] Australian Standard/New Zealand Standard, *Composite Structures – Composite Steel-Concrete Construction Buildings,* AS/NZS 2327:2017.

[6]  G. Ranzi, G. Leoni, and R. Zandonini, "State of the art on the time-dependent behaviour of composite steel-concrete structures," *J. Construct. Steel Res.*, vol. 80, pp. 252–263, 2013a, http://dx.doi.org/10.1016/j.jcsr.2012.08.005.

[7]  G. Ranzi, S. Al-Deen, L. Ambrogi, and B. Uy, "Long-term behaviour of simply-supported post-tensioned composite slabs," *J. Construct. Steel Res.*, vol. 88, pp. 172–180, 2013b., http://dx.doi.org/10.1016/j.jcsr.2013.05.010.

[8]  A. Gholamhoseini, "Long-term deformation of composite concrete slabs," *Concr. Aust.*, vol. 38, no. 4, pp. 25–32, 2014a., http://dx.doi.org/10.1080/13287982.2016.1238531.

[9]  A. Gholamhoseini, "Time-dependent deflection of composite concrete slabs," *ACI Struct. J.*, vol. 111, no. 4, pp. 765–776, 2014b., http://dx.doi.org/10.14359/51686629.

[10] S. Al-Deen, G. Ranzi, and B. Uy, "Non-uniform shrinkage in simply-supported composite steel concrete slabs," *Steel Compos. Struct.*, vol. 18, no. 2, pp. 375–394, 2015., http://dx.doi.org/10.12989/scs.2015.18.2.375.

[11] Associação Brasileira de Normas Técnicas, *Projeto de Estruturas de Aço e de Estruturas Mistas de Aço e Concreto de Edifícios*, ABNT NBR 8800:2008, 2008.

[12] M. Bradford, R. I. Gilbert, R. Zeuner, and G. Brock, "Shrinkage deformations of composite slabs with open trapezoidal sheeting," *Procedia Eng.*, vol. 14, pp. 52–61, 2011, http://dx.doi.org/10.1016/j.proeng.2011.07.006.

[13] R. I. Gilbert, M. A. Bradford, A. Gholamhoseini, and Z. T. Chang, "Effects of shrinkage on the long-term stress and deformations of composite concrete slabs", *Eng Struct.*, vol. 40, pp. 9-19, 2012,  https://doi.org/10.1016/j.engstruct.2012.02.016.

[14] R. I. Gilbert, "Time-dependent stiffness of cracked reinforce and composite concrete slabs," *Procedia Eng.*, vol. 57, pp. 19–34, 2013, http://dx.doi.org/10.1016/j.proeng.2013.04.006.

[15] S. Al-Deen and G. Ranzi, "Effects of non-uniform shrinkage on the long-term behavior of composite steel-concrete slabs," *Int. J. Steel Struct.*, vol. 15, no. 2, pp. 415–162, 2015, http://dx.doi.org/10.1007/s13296-015-6012-7.

[16] G. Ranzi, "Service design approach for composite steel-concrete floors," *P I Civil Eng-Str B.*, vol. 171, no. 1, pp. 38–49, 2017, https://doi.org/10.1680/jstbu.16.00196.

[17] M. A. Bradford, "Generic modelling of composite steel-concrete slabs subjected to shrinkage, creep and thermal strains including partial interaction", *Eng Struct.*, vol. 32, no. 5, pp. 1459–1465, 2010, https://doi.org/10.1016/j.engstruct.2010.01.024.

[18] R. I. Gilbert and G. Ranzi, *Time-Dependent Behaviour of Concrete Structures*, Nova York: Spon Press, 2011.

[19] R. P. Johnson, *Composite Structures of Steel and Concrete: Beams, Slabs, Columns, and Frames for Buildings, vol. 1* , 3rd ed. London: Blackwell Scientific Publications, 2013.

[20] D. Dujmovic, B. Androic, and I. Lukacevic, *Composite Structures According to Eurocode 4: Worked Examples*. Croatia: Ernst & Sohn, 2015.

[21] British Standard. *Structural Use of Steelwork in Buildings – Part 4: Code of Practice for Design of Composite Slabs with Profiled Steel Sheeting*, BS5950-4, 1994.

[22] Modular Sistemas Construtivos, *Modular Deck MD 55*, Dourados, MS: Modular Sistemas Construtivos, 2018 (in Portuguese).

[23] Associação Brasileira de Normas Técnicas, *Projeto de Estruturas de Concreto – Procedimento*, ABNT NBR 6118:2014, 2014.

[24] Stramit Condeck HP, *Composite Slab System, Product Technical Manual*, Queensland, Australia: Stramit Condeck HP, 2012.

[25] Fielders Australia Kingflor, *Composite Steel Formwork System Design Manual*, Marleston, Australia: Fielders Australia Kingflor, 2008.

[26] Australian Standard/New Zealand Standard, *Concrete Structures*, AS/NZS 3600:2018, 2018.

[27] ArcelorMittal. "Trelifácil®: much easier to build slabs", São Paulo, SP: ArcelorMittal, 2017 (in Portuguese). 2017 (accessed Nov 1, 2020). Available: http://blog.arcelormittal.com.br/trelifacil-muito-mais-facilidade-para-construir-lajes/

[28] Q. Wang, G. Ranzi, Y. Wang, and Y. Geng, "Long-term behaviour of simply-supported steel-bars truss slabs recycled coarse aggregate," *Constr. Build. Mater.*, vol. 116, pp. 335–346, 2016, http://dx.doi.org/10.1016/j.conbuildmat.2016.04.150.

# IBRACON Structures and Materials Journal
## Revista IBRACON de Estruturas e Materiais

ORIGINAL ARTICLE

# Thermal numerical analysis of steel and steel and concrete composite columns in a fire situation aimed at the evaluation of the simplified method of ABNT NBR 14323:2013

*Análise numérica térmica de pilares de aço e mistos de aço e concreto em situação de incêndio visando a avaliação do método simplificado da ABNT NBR 14323: 2013*

Mariana Lavagnolli Rossi[a]  (iD)
Yagho de Souza Simões[a]  (iD)
Jorge Munaiar Neto[a]  (iD)
Alessandra Lorenzetti de Castro[a]  (iD)

[a] Universidade de São Paulo – USP, Escola de Engenharia de São Carlos - EESC, Departamento de Estruturas, São Carlos, SP, Brasil

**Abstract:** The design of steel and steel and concrete composite columns in a fire situation is directly linked to the reduction of strength and stiffness, among other properties, which are manifested in response to rising temperatures. The normative codes that deal with the design of these elements under the action of fire consider the thermal action based on heating on the four faces of the column, an aspect that does not cover most cases in buildings due to the presence of walls. In this context, given the importance of the correct determination of the thermal field for design purposes, as well as given the simplification adopted by the normative codes, the present work deals exclusively with a study basically aimed at obtaining a representative thermal field for purposes of thermo-structural verification of steel and steel and concrete composite columns. With the focus on the analysis of cases that differ from the prescribed configurations in standards, purely thermal numerical models are proposed, validated through experimental results, whose analyses show an evident reduction in temperature in the steel column when encased with concrete, and with even greater evidence when additionally inserted into walls as a compartmentalizing element. To verify the simplified method proposed by ABNT NBR 14323: 2013, comparative analyses between the numerical thermal fields and obtained by the standardized model were carried out for steel and steel and concrete composite cross sections. For the isolated steel columns, as expected, the normative method proved to be consistent, but conservative when it came to columns inserted into walls. In relation to the composite columns, the results obtained indicate the need for adjustment in the standards for purposes of determining the thermal field and, consequently, of design these elements.

**Keywords:** steel and concrete composite columns partially encased, steel columns, walls, fire, fire resistance.

**Resumo**: O dimensionamento de pilares de aço e mistos de aço e concreto em situação de incêndio está diretamente atrelado à redução da resistência e da rigidez, entre outras propriedades, as quais se manifestam em resposta à elevação da temperatura. Os códigos normativos que tratam do dimensionamento desses elementos sob ação do fogo consideram a ação térmica com base em aquecimento nas quatro faces do pilar, aspecto que não abrange a grande maioria dos casos nas edificações em função da presença de paredes. Nesse mesmo contexto, dada a importância da correta determinação do campo térmico para fins de dimensionamento, bem como dada a simplificação adotada pelos códigos normativos, o presente trabalho se volta exclusivamente a um estudo basicamente direcionado à obtenção de campo térmico representativo para fins de verificação termoestrutural de pilares de aço e mistos. Tendo como foco principal a análise de casos que diferem das configurações prescritas em normas, são propostos modelos numéricos puramente térmicos validados por meio de resultados experimentais, cujas análises constatam uma evidente redução da temperatura no pilar de aço quando revestido com concreto, e ainda com maior evidência quando adicionalmente inseridos em paredes enquanto elemento de compartimentação. De modo a verificar o método simplificado proposto pela ABNT NBR 14323:2013, análises comparativas entre os campos térmicos

numérico e obtido pelo modelo normatizado foram realizadas para seções transversais de aço e mistas de aço e concreto. Para os pilares de aço isolados, como esperado, o método normativo se mostrou consistente, porém conservador quando voltado a pilares inseridos em paredes. Em relação aos pilares mistos, os resultados obtidos sinalizam a necessidade de ajuste nas prescrições normativas para fins de determinação de campo térmico e, consequentemente, para fins de dimensionamento desses mesmos elementos.

**Palavras-chave:** pilares mistos de aço e concreto parcialmente revestidos, pilares de aço, paredes, incêndio, resistência ao fogo.

# 1 INTRODUCTION

Concrete and steel are widely used in civil construction. The perception of the efficient work developed individually by these materials allowed the appearance of composite elements of steel and concrete, which started to be used to bond the advantages brought by both materials.

Among the countless advantages of using steel and concrete composite structures, good fire resistance is worth mentioning. According to Correia and Rodrigues [1], concrete, due to its lower thermal conductivity and higher specific heat when compared to steel, increases the fire resistance of metallic elements, since it acts as a protective coating against thermal action, in addition to contributing structurally. Still in relation to this association, steel reduces the effects of cracking and spalling in concrete. According to Simões et al. [2], concrete increases the fire resistance of the purely steel element, because by reducing the average temperature of the set, it can present a resistant capacity for a longer time.

Currently, the rules that address the design of steel and composite columns partially encased in a fire situation are the Brazilian standard ABNT NBR 14323 [3] and Eurocode 3 and 4 Part 1-2 [4], [5], but they only include the scenario where the columns are subjected to heating on all faces of the cross section. However, in current structures most, or almost all, of the columns are inserted into walls, so that, in a fire situation, they present a different structural behavior than when isolated.

The presence of the wall in contact with the column generates a thermal gradient in its cross section since one side of the column is subject to thermal action, and the other is not, promoting the formation of curvature in the structural element and, consequently, additional bending moments from the phenomenon called Thermal Bowing [6].

Rocha [7] points out that, although there are scientific studies in the experimental and numerical spheres regarding columns subjected to thermal gradients, there are few studies regarding the influence of walls on the thermal behavior of these elements, as they seek to simulate the differential heating of the columns originated from masonry, through thermal protection of some faces of the columns, as performed in Dwaikat and Kodur [8], Dwaikat et al. [9], Agarwal et al. [10].

Most works deal with purely steel columns and, exceptionally, steel and concrete composite columns. In this context, some studies assess the influence of partially or fully encasing or filling steel columns with concrete under fire situations. The benefits of this material in both the fire resistance and structural behavior can be identified [1, 2, 11]. When associated with masonry walls, research is even more scarce, thus emphasizing the importance of the present study.

Considering the above, the present work seeks to study the influence of the filler concrete between the flanges and the masonry wall in determining the thermal field developed in the cross section of steel and steel and concrete composite columns partially encased inserted into walls, in situations of fire. Although the present text focuses only on the analysis of temperature levels, this analysis is of fundamental importance for the purposes of design since the thermal field is determinant in a thermo-structural context.

For this purpose, thermal numerical models developed with the aid of ABAQUS are proposed, whose numerical results are validated through experimental results presented in Rocha [7], allowing evaluations in relation to the temperature field and the thermal gradient presented by these elements under high temperatures. In a complementary way, but not less important, comparisons will also be made between the temperature evolution of steel and steel and concrete composite columns with that achieved when applying the simplified methods of ABNT NBR 14323 [3] and Eurocode 3 and 4 Part 1-2 [4], [5].

## 2 EXPERIMENTAL REFERENCE ANALYSIS

As previously mentioned, the present work is based on results of prototypes related to the experimental program presented in Rocha [7], whose characteristics are described in Table 1. For purposes of identifying the columns, the nomenclature used adopts the type of steel profile (HEA 220), the relative position of the web of the metal profile in relation to the walls (parallel or orthogonal), the thickness of the ceramic block used for the construction of the wall (11 cm or 15 cm) and the presence or absence of concrete coating (CONC). The columns that received the thermal action on the four faces also receive the term ISO for identification purposes.

**Table 1.** Characteristics of the columns used in the numerical modeling.

| Number | Reference | HEA Profile | Web orientation | Block thickness | Presence of concrete |
|--------|-----------|-------------|-----------------|-----------------|----------------------|
| 1 | H220-PAR-T15 | 220 | Parallel | 15 cm | - |
| 2 | H220-ORT-T15 | 220 | Orthogonal | 15 cm | - |
| 3 | H220-CONC-PAR-T15 | 220 | Parallel | 15 cm | Yes |
| 4 | H220-CONC-ORT-T15 | 220 | Orthogonal | 15 cm | Yes |
| 5 | H220-CONC-PAR-T11 | 220 | Parallel | 11 cm | Yes |
| 6 | H220-CONC-ORT-T11 | 220 | Parallel | 11cm | Yes |
| 7 | H220-ISO | 220 | - | - | - |
| 8 | H220-CONC-ISO | 220 | - | - | Yes |

The steel and steel and concrete composite columns, both with HEA 220 profile, had a length of 2940 mm. In relation to the composite columns, the concrete inserted between the profile flanges had a characteristic resistance to compression equal to 30 MPa, which was reinforced longitudinally with bars with a diameter equal to 20 mm, as well as transversely with stirrups with a diameter equal to 8 mm spaced every 150 mm. All reinforcements had a yield strength equal to 500 MPa. The dimensions of the cross section can be seen in Figure 1. In the experiments, the walls were made using ceramic blocks and mounted separately from the columns, presenting the same length in relation to the columns and arranged 1200 mm on each side.



**(a)**                    **(b)**
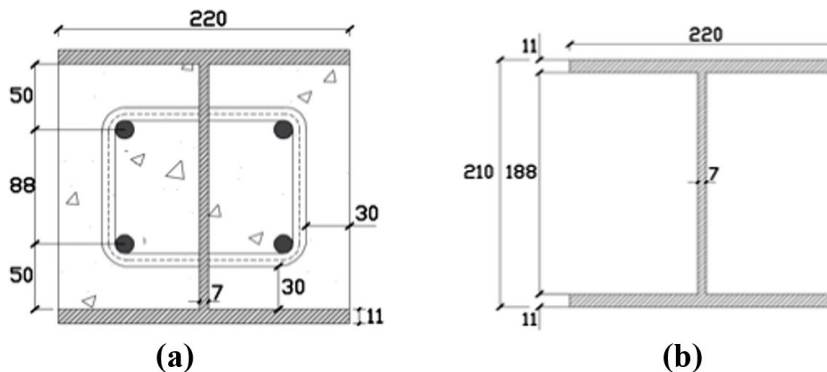
**Figure 1.** Geometric characteristics of the studied columns, considering as cases of interest: (a) steel and concrete composite, and (b) Purely steel.

The columns were inserted in a three-dimensional constraint structure in order to simulate the columns inserted in a real structure. The structural elements were heated using a modular electric oven made up of three modules, two of which are 1.0 m high and the other 0.5 m and for that reason, only 2.5 m of the central part of the columns were heated.

The presentation of the results and the validation of the proposed models were made with reference to the section (central), as it has the highest temperature among the others and also did not suffer the influence of the less heated extremities. Thus, this region presents the greatest degradation of its mechanical properties, which negatively affects the thermo-structural behavior of the columns.

# 3 NUMERICAL ANALYSIS CARRIED OUT IN THERMAL CONTEXT

## 3.1 General aspects regarding the numerical strategy adopted

The proposed numerical models sought to evaluate the influence of the filler concrete and walls on the thermal field generated in steel and steel and concrete composite columns in a fire situation. According to Rocha [7], the experimental analysis of columns attached to the walls has many peculiarities that hinder the numerical modeling of this set, which is why the strategies adopted are described below.

The numerical modeling was performed with the ABAQUS code 6.18 version, which is based on the Finite Element Method. To represent the steel profiles finite shell elements (DS4) were used, the filler concrete and masonry walls were reproduced with solid elements (C3D8), while the steel reinforcements present in the concrete were modeled with bar elements (T3D2). The identification of the finite element by ABAQUS for each structural component is shown in Table 2, in which quadratic finite elements with a size of 30 mm were adopted.

The walls were reproduced by means of a "macro-modeling" and represented as a massive block with dimensions representative of the experimental model, that is, 50 cm for each side of the column (corresponding to the region heated by the oven), and with block thickness varying between 11 and 15 cm. According to Lourenço [12], this strategy presents good efficiency and still allows to consider the masonry blocks and mortar joints as a unique element of homogeneous properties.

Figure 2 shows the cross section of the columns H220-CONC-ORT-T11 and H220-CONC-PAR-T11. The other models were built in a similar way, changing only the dimensions of the cross section, the thickness of the compartmentalization elements and the presence or not of masonry and concrete.



| | |
|---|---|
| H220-CONC-ORT-T11 | H220-CONC-PAR-T11 |
| **(a)** | **(b)** |
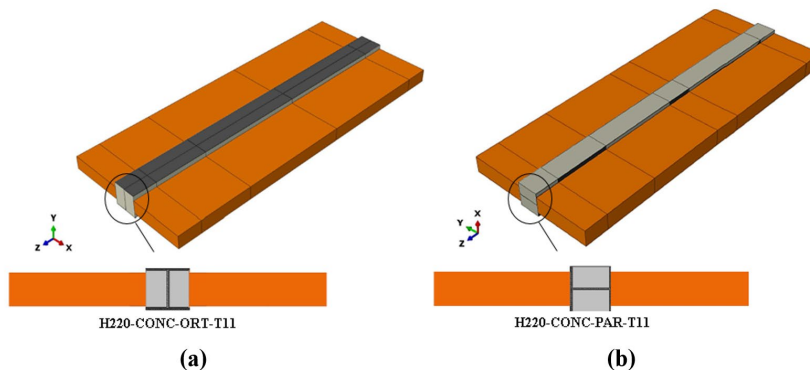
**Figure 2.** Representation of the thermal models for the columns: a) H220-CONC-ORT-T11; b) H220-CONC-PAR-T15.

## 3.2 Boundary conditions and material properties

The columns were modeled with the heating curves of the gases obtained in the experimental tests, emphasizing that these curves were not coincident with the standard fire curve defined by ISO 834-1 [13]. Regarding the boundary conditions of a thermal modeling, the three phenomena of heat exchange (convection, radiation and conduction) between the environment and the element were used, along with their respective coefficients and the active regions.

Regarding the modeling of columns inserted into walls, the exposed and non-exposed sides were considered in the construction of the thermal model. Concerning the exposed face, the Brazilian standard ABNT NBR 14323 [3] considers the convection coefficient equal to 25 W/m²ºC and the emissivity of 0.7 for the steel and concrete surfaces, while for the non-exposed side to fire it does not make reference to which values to adopt. Eurocode 1 Part 1-2 [14], in turn, allows two options to be considered: one can consider the effects of convection and radiation together by means of a convection coefficient equivalent to 9 W/m² ° C, or admit these phenomena separately, so that the convection coefficient is equal to 4 W/m²ºC with the emissivity value dependent on the material used.

With regards to the thermal properties used for the materials under analysis, for steel and concrete, those described by ABNT NBR 14323 [3] were used, while for the walls, information was used according to Cadorin [15], which are: 840 J/kg°C for specific heat and 1600 kg/m³ for specific mass.

## 3.3 Validation of the numerical model in thermal context

During the processing of the numerical thermal models for the purposes of calibration and validation, it is worth mentioning that the results obtained were not satisfactory using normative concepts as emissivity. Therefore, based on Simões et al. [2], [16], sensitivity analyses for emissivity were developed to obtain more representative values for the same parameter. Table 2 presents the parameters that best represented the experiments in Rocha [7]. The value adopted for the emissivity of steel on the exposed side was 0.8, differing from that recommended by the European normative code, which is 0.7. Nevertheless, this change can be accepted, since the scenario of the gas oven used in the experimental tests is different from an actual fire. Since the European normative codes do not specify values for unexposed surfaces, it was adopted those values that best described the thermal numerical model, which were 0.6 for steel surfaces and 0.7 for concrete and wall surfaces.

**Table 2.** Parameters adopted for calibration of the thermal numerical model.

| Surface | Exposed side | | Non-exposed side | |
| | Emissivity | Convection Coefficient W·m²/°C | Emissivity | Convection Coefficient W·m²/°C |
|---|---|---|---|---|
| Steel | 0.8 | 25 | 0.6 | 4 |
| Concrete | 0.7 | 25 | 0.7 | 4 |
| Wall | 0.7 | 25 | 0.7 | 4 |

Figure 3 shows the validation of the proposed thermal modeling for some of the analysed columns, from the comparison between numerical and experimental temperature evolution curves in the section located at half height of the column, according to Rocha [7]. In the same figure, it is possible to visualize the positions of the thermocouples in each of the studied columns, whose nomenclature used for the reading points was established as TX, where X represents the reading point of the central section of the column.

In general, it is noted that the maximum temperature difference found, between numerical and experimental results, resulted in around 50ºC for the columns presented. Based on the curves presented in Figure 3, and highlighting that for the other mentioned column the same similarity was observed, it is possible to consider the numerical strategy adopted here as consistent, making it possible to use it for additional and specific analyses in a purely thermal context for the columns under analysis.



**NUM: Numerical Result     EXP: Experimental Result**
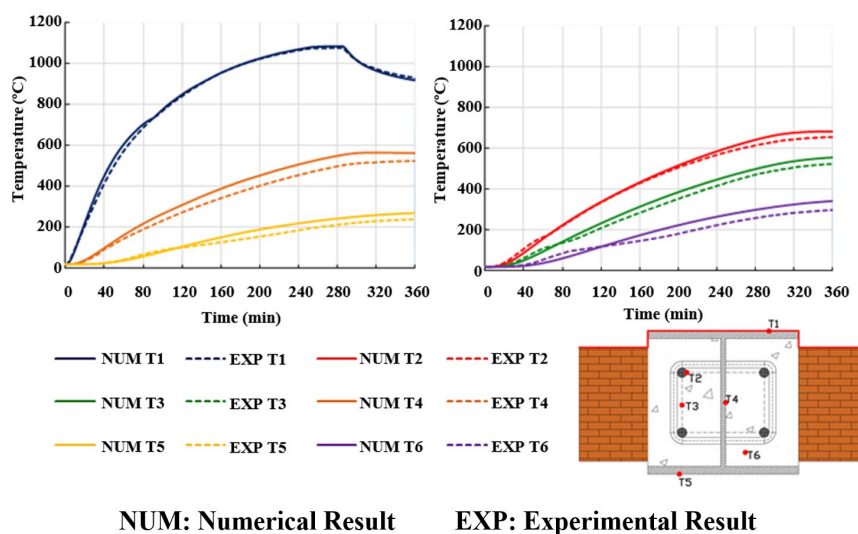
**Figure 3.** Comparison of numerical models and experimental results: H220-CONC-ORT-T11.

# 4 INFLUENCE OF THE FILLER CONCRETE AND MASONRY WALL IN THE THERMAL FIELD OF COLUMNS

Based on the proposed numerical strategy, according to item 3.3, as well as considering its consistency as results, studies will be carried out focused on the concrete and wall influences on the thermal behavior of the columns. As the idea is also to verify results obtained through the concepts of ABNT NBR 14323 [3], unlike the temperature curves adopted for the purpose of consistency analysis, as per item 3.1, the columns were modeled using the standard fire curve defined by ISO 834-1 [13], and with the thermal parameters recommended by the mentioned Brazilian standard, when available.

The studies presented in the items that follow aim to evaluate the influence of masonry walls and the filler concrete in the temperature field developed in the steel profile, which is why points located in predefined locations of the cross section will be studied in all the columns to carry out comparative analyses. Figure 4 shows the indication of the thermocouples considered in the columns analyzed here, remembering that the position of these in the columns H220- CONC-ORT-T11 and H220-CONC-PAR-T11 is identical to that of the columns H220-CONC-ORT-T15 and H220 -CONC-PAR-T15, respectively.



a) H220-ISO     b) H220-ORT-T15     c) H220-PAR-T15

d) H220-CONC-ISO     e) H220-CONC-ORT-T15     f) H220-CONC-PAR-T15
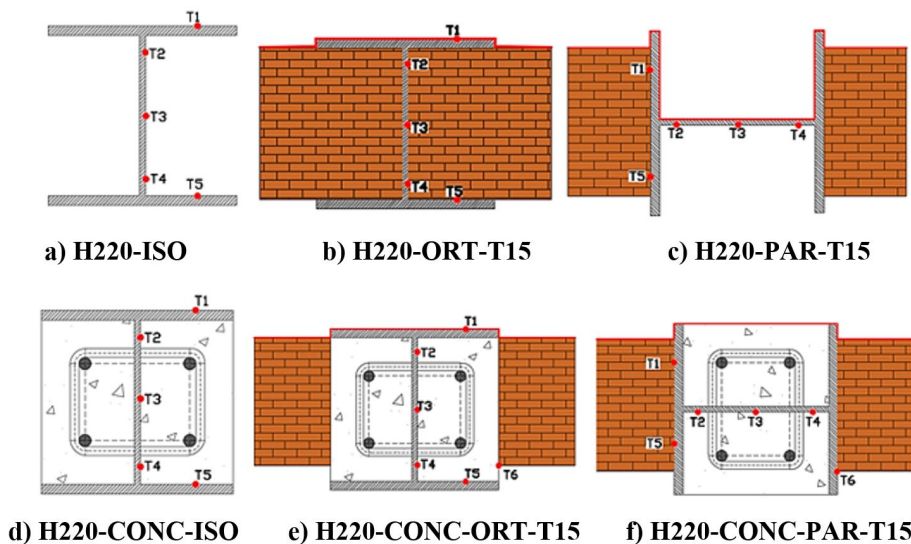
**Figure 4.** Positioning of thermocouples in the cross section of the columns under study.

## 4.1 Evaluation of the influence of the filler concrete

As a starting point, the influence of filler concrete on steel profiles subject to fire is analyzed. Figure 5 shows the representation of the thermal numerical models H220-ISO and H220-CONC-ISO, based on their symmetry, which present the temperature field developed in the cross section of the structural element for the instant equal to 120 minutes.

It is observed, through Figure 5, a difference in behavior between the two types of structural design. Immediately, it is possible to notice that, although the metal profile flange is exposed to fire in both situations, in the case of the steel and concrete composite column the temperature field becomes milder as it advances with depth, as expected.

Additionally, Figure 6 shows the evolution of temperatures for the steel and steel and concrete composite columns isolated during 120 minutes, in which a temperature reduction of 200ºC is identified on the flange exposed to fire (T1/T5 thermocouple) in 30 minutes of exposure of the composite column, even though both flanges were in contact with the thermal action. With an increase in the duration of the thermal action, the same difference decreased due to the heat transfer phenomena.
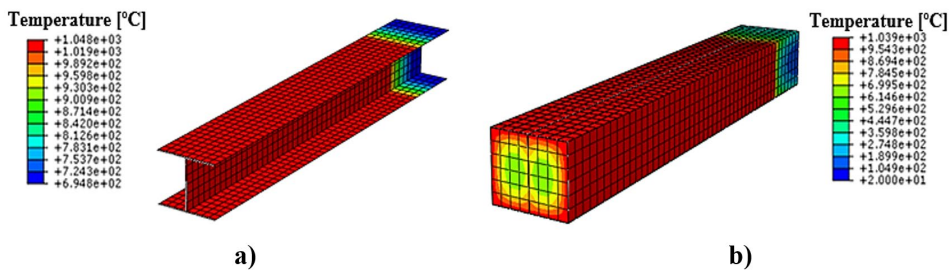
**Figure 5.** Thermal field for the columns: (a) H220-ISO e (b) H220-CONC-ISO.

Regarding the web of the steel profile, at both points evaluated the temperature difference is even greater, around 400ºC and 600ºC at 30 minutes when comparing the temperatures in the T2 and T3 thermocouples, respectively. This aspect can be justified because the concrete works efficiently as a thermal insulator due to its thermal properties, such as low thermal conductivity, high specific heat, as well as forming more robust elements that hinder the propagation of heat.
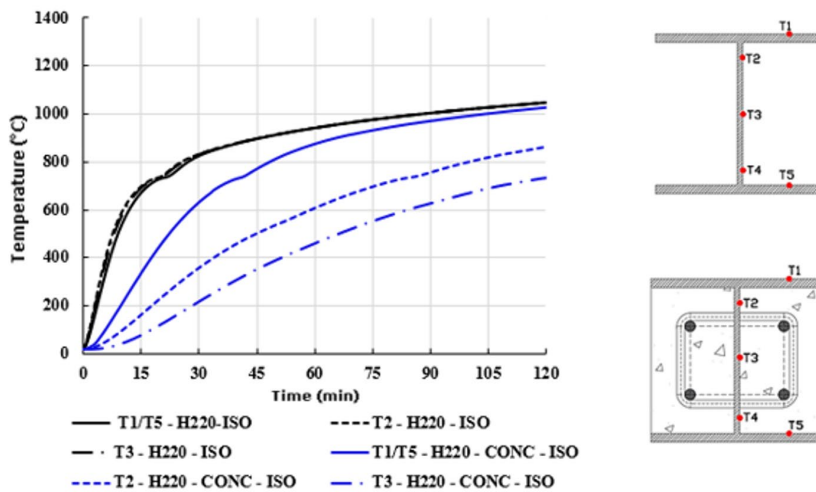


**Figure 6.** "Temperature vs time" curve for steel and composite H220-ISO columns.

## 4.2 Evaluation of the influence of masonry walls

Subsequently to the analysis of the influence of the filler concrete, the influence of the masonry walls on the thermal field of the purely steel columns was carried out. Figure 7 shows the temperature field formed in the cross section of the columns H220-ORT-T15 and H220-PAR-T15. In a general view, it is possible to verify the difference of the thermal field presented in the steel profile, because while the H220-ORT-T15 column presents a gradient along the web, in the H220-PAR-T15 column, this differential heating occurs around the flange.
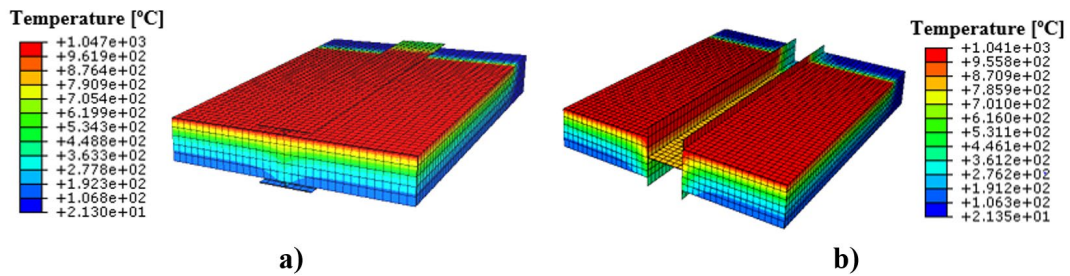
**Figure 7.** Columns thermal field: (a) H220-ORT-T15; (b) H220-PAR-T15.

Figures 8 and 9 show the temperature distribution at points arranged on the web and on the flange, respectively, for the H220-ISO isolated steel columns and H220-ORT-T15 and H220-PAR-T15 columns inserted into walls. Similarly to what was identified as the influence of the filler concrete, as expected as well, there is a reduction in temperature in the steel profile with walls compared to the isolated column, since their presence, as partitioning, prevents the incident heat directly in the metallic profile, resulting in less heating and less marked reduction of its mechanical properties.

The insertion of the wall, according to the H220-ORT-T15 column, reduced the temperature of the steel profile flange (T5 thermocouple) by approximately 800 ºC compared to the same profile without any thermal barrier at 60 minutes of exposure. Regarding the web, points T2 and T4, regions more and less heated, showed reductions close to 300ºC and 700 ºC, respectively, for the same time periods.

With respect to the H220-PAR-T15 column, the web (T2/T3/T4 thermocouples) showed a reduction of 200 ºC at 120 min compared to the isolated steel column. The flange, for that same time, reduced its temperatures at points T1 and T5 (more and less heated regions, respectively) by values close to 100 ºC and 500 ºC. This decrease was inferior to the previous case, the H220-ORT-T15 column, since one of the faces of the web and part of the flanges, in this type of structural design, is directly in contact with the flames, which makes its heating faster.

For the H220-ORT-T15 column, the formation of a thermal gradient along the web is observed. The region most exposed to fire (Thermocouple T1) is at a temperature close to 1050 ºC, while the T5 thermocouple, which is farthest from the thermal action, is close to 170 ºC in 120 min, allowing the identification of a thermal gradient close to 880 ºC. Regarding the H220-PAR-T15 column, while heating, it is possible to notice that the web heats up evenly, while the flange has a thermal gradient depending on the position of the walls in that region. The temperature difference between the most heated points (thermocouple T1) and the least heated points (thermocouple T5) results in around 463ºC at 120 minutes. Therefore, this column presents a more uniform heating compared to the H220-ORT-T15 column, suggesting a thermo-structural behavior similar to that of the isolated columns.
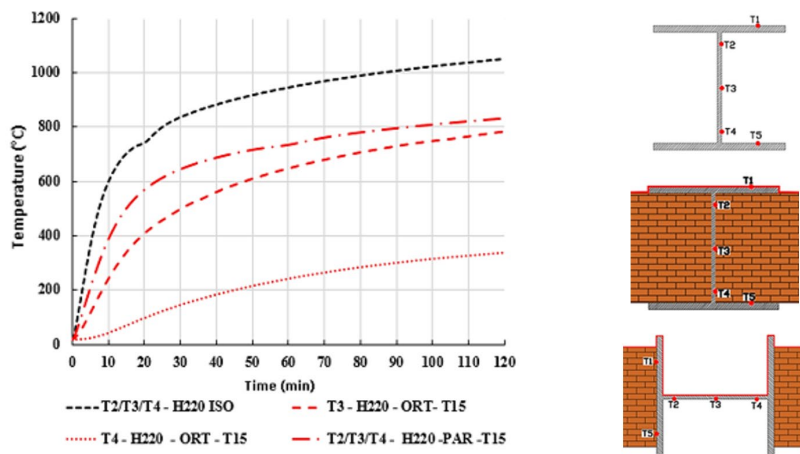


**Figure 8.** Curve referring to temperature as a function of time for isolated steel columns and steel columns inserted into walls, in contact with the flanges or with the web.

Rev. IBRACON Estrut. Mater., vol. 14, no. 5, e14502, 2021

8/16
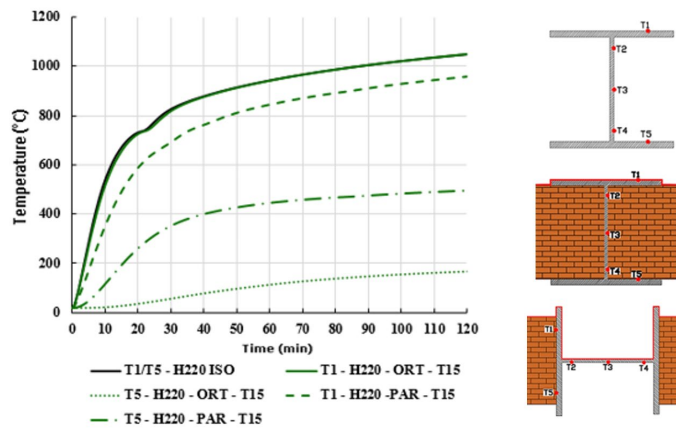
**Figure 9.** Curve referring to temperature as a function of time for isolated steel columns and steel columns inserted into the wall, in contact with the flanges or with the web.

After the separate analyses of the filler concrete and masonry walls, what follows is an analysis aimed at studying the simultaneous influence of concrete and wall on steel columns. First, the thermal field of the steel and concrete composite columns, H220-CONC-ORT-T15 and H220-CONC-PAR-T15, can be visualized, through Figure 10.
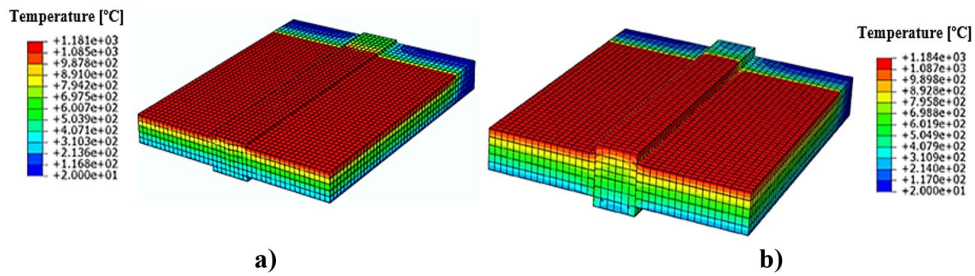


**Figure 10.** Columns thermal field: a) H220-CONC-ORT-T15 e b) H220-CONC-PAR-T15.

In general, the differential heating mode presented by these columns is similar to the models shown in Figure 7. The H220-CONC-ORT-T15 column has a thermal gradient along the web, while on the H220-CONC-PAR-T15 column the differential heating takes place around the flange with a different intensity as generated temperature field. The temperature differences for these elements, during the 120-minute warm-up, occur according to Figures 11 and 12.

In all cases, the temperatures of the composite columns inserted into walls are lower when compared to the steel columns analyzed previously, since in these elements there are two materials acting as a thermal barrier, in this case, the concrete and the masonry walls. In the case of composite columns, the concrete acts as a thermal insulator of the steel profile, preventing the direct flow of heat in the element. In the purely metallic column, the thermal barrier consists of the masonry wall itself, which is in direct contact with the web or flange of the metallic profile, which consequently provides heat diffusion difficulty.

In this sense, in relation to the columns with the web orthogonal to the surface of the wall, in the region of the most heated flange (T1), the temperature difference between the composite and steel columns at 30 min was approximately 150ºC, reducing to about 50ºC at 120 minutes. This small difference is justified by the fact that the thermal action acts directly on the steel profile flange, which facilitates the transmission of heat by the element.
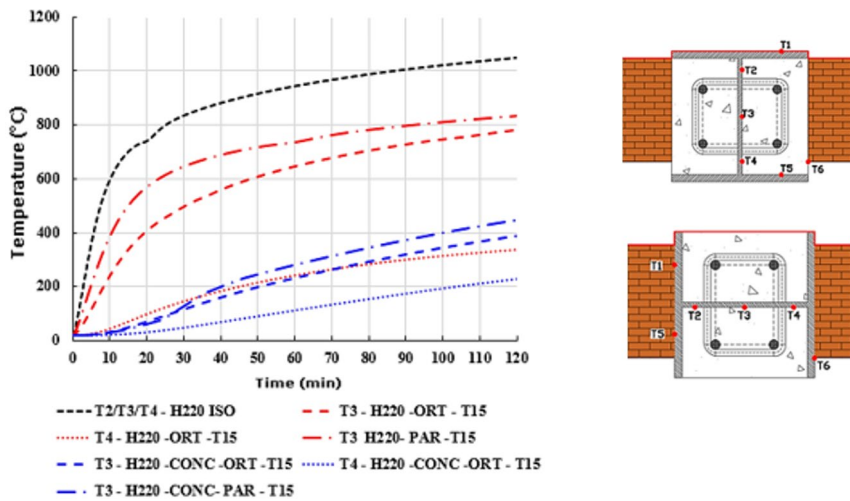
**Figure 11.** Curve for temperature versus time for columns (WEB).
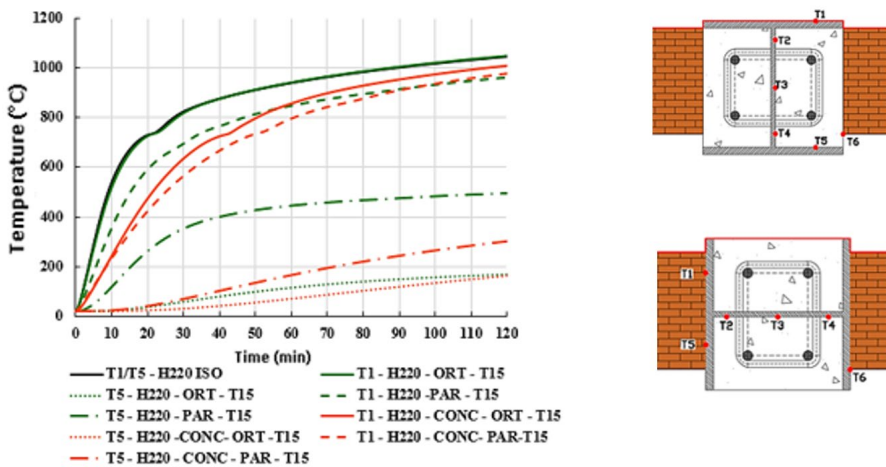


**Figure 12.** Curve for temperature versus time for columns (FLANGE).

In the case of columns with a web parallel to the wall surface, the thermal action against the steel profile is completely changed in the composite columns, because the web and part of the steel profile flange directly receive the heat from the flames. Thus, according to Figures 11 and 12, the temperatures of the most heated (thermocouple T1) and least heated (thermocouple T5) regions, referring to the flange, showed temperature reductions of about 150°C and 300°C, respectively, compared to the steel columns inserted into walls at 30 minutes of exposure. Regarding heating the web for these columns (T3), there was a reduction of approximately 500°C in the first 30 minutes of exposure.

Regarding the H220-CONC-ORT-T15 column, which has a thermal gradient along the web, it is noted that the region most exposed to fire (Thermocouple T1) has a temperature equal to 1010°C, while the T5 thermocouple, further from the thermal action, has 162°C in 120 min of exposure. In this sense, it was possible to observe a thermal gradient equal to 848 °C, a value close to that found for the H220-ORT-T15 column. This similarity of results is due to the configuration of the structural elements. In both cases, the heat acts directly on one of the steel profile flanges and the web is protected, either by concrete or by the wall.

Regarding the H220-CONC-PAR-T15 column, the thermal gradient developed along the flanges, with a temperature difference between the most heated (T1) and least heated (T5) points around 677°C at 120 minutes, whose value it is more expressive when compared to that found for the H220-PAR-T15 column, since the composite column has the presence of concrete between the flanges, which ends up protecting the components of the steel profile, hindering the propagation of heat and increasing, consequently, the thermal gradient.

# 5 EVALUATION OF NORMATIVE MODELS TO OBTAIN TEMPERATURE IN STEEL AND COMPOSITE PROFILES

This item evaluates the simplified method recommended by Brazilian standards ABNT NBR 14323 [3] and European Eurocode 3 and 4 Part 1-2 [4], [5] for calculating temperature in steel and concrete composite profiles partially encased when subjected to the action of fire. The purpose of this analysis is to compare the results of the thermal numerical models proposed here with those obtained through the application of normative theoretical methods. Such comparison has representativeness since the thermal numerical models were validated based on experimental results.

The normative method for determining the temperature in purely steel profiles, whether isolated or inserted into walls, was evaluated. As a result, it was concluded that it was satisfactory for columns with heating on all four sides, considering that the numerical and normative temperatures were close. In the case of columns inserted into walls, as expected, the standard proved to be quite in favor of safety, with differences between the average and normative numerical temperatures above 600 ºC.

As the focus of this work is on the steel and concrete composite columns, the application of the simplified method for this structural design is described in detail below. For the case of steel and concrete composite columns partially encased in a fire situation, ABNT NBR 14323 [3] and Eurocode 4 Part 1-2 [5] present a specific method to determine their fire resistance. First, the temperature of each component of the cross section is found as a function of the required time of fire resistance (TRRF) and then used for the calculation of the normal resistant force.

The mentioned normative codes establish criteria for the application of this calculation procedure, which are related to the cross section of the composite elements (height, width and longitudinal reinforcement rate). They are presented in item B.3.2.1 of ABNT NBR 14323 [3] and are described below:

a) height of the cross section between 230 mm and 1100 mm, with a minimum of 300 mm in the case of TRRF equal to or greater than 90 min;

b) cross-section width between 230 mm and 500 mm, with a minimum of 300 mm in the case of TRRF equal to or greater than 90 min;

c) rate of steel longitudinal reinforcement in relation to the concrete area from 1% to 6%.

As illustrated in Figure 1a, the dimensions of the cross section of the composite columns of this study showed values very close to the intervals established by the method guidelines, with differences in height and width between 4% and 8%, respectively. Considering the small difference found, by hypothesis it was considered reasonable to apply the normative calculation procedure described in Annex B of ABNT NBR 14323 [3] to obtain the temperature of the columns in a fire situation.

The mentioned standard divides the cross section of the columns into four components, namely: steel profile flanges, steel profile web, concrete between the flanges and longitudinal reinforcement. In this sense, each component must be evaluated based on its mechanical properties in a fire situation according to the TRRF.

The following also shows the average, maximum and minimum numerical temperatures for the four regions of the composite columns isolated and inserted into walls for TRRF equal to 30, 60, 90 and 120 minutes. These values are compared with those determined by the theoretical method proposed by the current standard. It is important to highlight that the normative codes do not include a calculation methodology to determine the temperature evolution in composite columns inserted into walls, that is, they are limited to composite columns with thermal action on their four faces (uniform heating). Despite this, the method was evaluated for all situations.

## 5.1 Analysis of the temperature of the steel profile flanges

ABNT NBR 14323 [3], in its item B.3.2.2.1, presents Equation 1 to determine the average temperature in the steel profile flanges, given in function of the section mass factor (ratio between the perimeter exposed to the fire, u, and the gross cross-sectional area of the profile ($A_g$)), initial temperature ($\theta_{0,t}$) and empirical coefficient ($k_t$), the last two being obtained through the same standard as a function of TRRF values.

$$\theta_{f,t} = \theta_{0,t} + k_t \left( u/A_g \right) \tag{1}$$

Table 3 presents the temperature values obtained by the numerical and normative models for the steel and concrete composite column with heating on all sides, which is named H220-CONC-ISO. The results point to a good agreement

Rev. IBRACON Estrut. Mater., vol. 14, no. 5, e14502, 2021

11/16

between the presented values, with maximum difference between the numerical models and normative method of approximately 10%.

**Table 3.** Comparison of theoretical temperatures and numerical model on steel profile flanges for composite columns with uniform heating.

| TRRF (min) | 30 | 60 | 90 | 120 |
|---|---|---|---|---|
| Normative | 730 | 858 | 919 | 987 |
| H220-CONC-ISO | 657 | 880 | 973 | 1027 |

Regarding the composite columns inserted into walls, Table 4 shows the average, maximum and minimum temperatures obtained in the numerical models. We chose to present these three possibilities in view of the thermal gradient that appears in the cross section due to the differential heating of the column.

It is possible to verify the low similarity of the average numerical values of the temperature in relation to the normative ones. In some cases, there was a difference in the thermal field above 400°C at 120 minutes of heating, indicating a certain conservatism of the referred standard. In contrast, the maximum temperature values of the numerical model were the ones that best approximated the temperature values obtained by the proposed normative method.

**Table 4.** Temperatures obtained in the numerical model on the steel profile flanges for the composite columns inserted into walls.

| Columns | TRRF (min) | 30 | 60 | 90 | 120 |
|---|---|---|---|---|---|
| Normative | | 730 | 858 | 919 | 987 |
| H220-CONC-ORT-T11 | Average | 331 | 461 | 527 | 576 |
| | Maximum | 637 | 864 | 957 | 1012 |
| | Minimum | 26 | 57 | 98 | 139 |
| H220-CONC-ORT-T15 | Average | 332 | 463 | 536 | 586 |
| | Maximum | 634 | 857 | 954 | 1010 |
| | Minimum | 30 | 69 | 118 | 162 |
| H220-CONC-PAR-T11 | Average | 197 | 354 | 462 | 541 |
| | Maximum | 631 | 847 | 949 | 1008 |
| | Minimum | 93 | 205 | 284 | 337 |
| H220-CONC-PAR-T15 | Average | 186 | 337 | 442 | 524 |
| | Maximum | 568 | 798 | 912 | 979 |
| | Minimum | 76 | 166 | 244 | 302 |

## 5.2 Analysis of the temperature of the steel profile web

For the web of the steel profile, ABNT 14323 [3] does not refer to the calculation methodology to determine its temperature. However, in order to dimension the normal plastification force in a fire situation, item B.3.2.3.2 presents Equation 2 for calculating the yield resistance of this region, which is a function of the steel yield resistance at room temperature ($f_y$), the height of the composite section ($d_c$) and the $H_t$ value that is obtained by the Brazilian standard for each TRRF.

$$f_{y,\theta,w} = f_y \sqrt{1 - (0.16(\frac{H_t}{d_c})}$$

(2)

From Equation 2, by hypothesis, a reduction factor was determined for the yield resistance of rolled steel ($f_{y,\theta,w}$), which corresponds to the portion that multiplies the steel yield resistance at room temperature ($f_y$). Thus, an analogy was made with values provided by Table 1 of item 5.1.1.2 of ABNT NBR 14323 [3], which corresponds to a reduction coefficient for the mechanical properties of steel.

Due to the presence of concrete, the column with heating on all sides presents a thermal gradient along the web. Therefore, Table 5 shows the average, maximum and minimum temperature values in the numerical model and the theoretical values obtained when applying the normative concepts.

Rev. IBRACON Estrut. Mater., vol. 14, no. 5, e14502, 2021

12/16

From this table, it is possible to verify that the numerical average values for the web temperature of the steel profile are reasonably represented by the normative values, although with differences close to 20%. In relation to the maximum temperatures, the normative values showed great differences in comparison to the numerical model, whereas for the minimum numerical temperatures, the norm was consistent.

**Table 5 -** Comparison of the temperatures obtained in the numerical model with the normative values for the steel profile web for the isolated composite column.

|  | TRRF (min) | 30 | 60 | 90 | 120 |
|---|---|---|---|---|---|
| Normative |  | 465 | 544 | 622 | 710 |
| | Average | 370 | 612 | 760 | 864 |
| H220-CONC-ISO | Maximum | 576 | 815 | 932 | 998 |
| | Minimum | 228 | 466 | 632 | 736 |

In the case of columns inserted into walls, for comparison purposes, the average, maximum and minimum temperatures were also analyzed in the numerical models for columns with the web orthogonal to the wall. As for columns with a parallel web, this variation was not considered, since the web of the steel profile has practically no thermal gradient during the heating process.

As can be seen in Table 6, the average numerical temperatures of the web, regardless of the orientation of the steel profile in front of the wall, showed significant differences in relation to the theoretical values, with differences greater than 300ºC at 120 minutes of heating. Regarding the maximum and minimum values, there was practically no agreement with the normative values. It is worth mentioning that, as well as obtained for the steel profile flange, the conservatism of the standard for determining the temperature in the profile web was observed when considering the average temperature of the composite column.

**Table 6.** Comparison of the temperatures obtained in the numerical model with the normative values for the steel profile web of the composite columns inserted into walls.

| Columns | TRF (min) | 30 | 60 | 90 | 120 |
|---|---|---|---|---|---|
| Normative |  | 465 | 544 | 622 | 710 |
| | Average | 121 | 236 | 320 | 387 |
| H220-CONC-ORT-T11 | Maximum | 561 | 777 | 890 | 954 |
| | Minimum | 32 | 72 | 164 | 162 |
| | Average | 120 | 234 | 318 | 386 |
| H220-CONC-ORT-T15 | Maximum | 560 | 770 | 886 | 951 |
| | Minimum | 35 | 82 | 134 | 181 |
| H220-CONC-PAR-T11 | - | 89 | 217 | 327 | 416 |
| H220-CONC-PAR-T15 | - | 103 | 227 | 328 | 412 |

## 5.3 Analyses focused on the temperature of the concrete between the steel profile flanges

For the determination of the average temperature in the concrete, ABNT NBR 14323 [3] disregards an external layer ($b_{c,fi}$), for each TRRF, the thickness of which is provided by the item B.3.2.4.1 of the referred rule, which uses the mass factor of the composite section for its determination. This procedure allows you to identify which region the normative code is calculating the temperature for. Therefore, this value will be used to calculate the temperatures in the numerical models to compare with the normative values.

Regarding the normative temperature, it is also determined in function of the mass factor of the composite section, as well as the TRRF. It is important to mention that average temperature values in the concrete were determined by linear interpolation, according to ABNT NBR 14323 [3] in its item B.3.2.4.2.

For the case of the composite column with heating on all sides, Table 7 presents the values of the concrete temperatures obtained by the normative method and by the numerical model. It was found that the normative temperatures adequately represented the average numerical temperatures, only up to 60 min of exposure. For TRRF equal to 90 and 120 min, the standard presented lower values than the numerical ones with maximum differences above 20%.

**Table 7.** Comparison of the temperatures obtained in the numerical model with the normative values for the concrete between the flanges of the columns with heating on all sides.

| | TRRF (min) | 30 | 60 | 90 | 120 |
|---|---|---|---|---|---|
| Normative | | 240 | 346 | 434 | 484 |
| H220-CONC-ISO | Average | 158 | 361 | 529 | 658 |
| | Maximum | 254 | 489 | 658 | 774 |
| | Minimum | 141 | 331 | 496 | 625 |

Concerning the columns inserted into walls, Table 8 shows the comparative study. In general, the normative results were superior to the average and minimum numerical results, being considered, in this aspect, conservative. On the other hand, when comparing them with the maximum numerical values, there was a very considerable difference with the norm, presenting smaller values.

## 5.4 Temperature analysis in the longitudinal reinforcement

ABNT NBR 14323 [3] establishes in its item B.3.2.5 that to obtain the temperature of the longitudinal reinforcements it is necessary, first, to calculate the geometric mean ($u_{sm}$) of the distances $u_1$ and $u_2$, which correspond to the value of the distances between the bars centroid to the external faces of the concrete. From this, through of this same item of the standard, the reduction factor ($k_{ys,\theta}$) of the reinforcement yield resistance as a function of the TRRF is determined.

**Table 8.** Comparison of the temperatures obtained in the numerical model and the theoretical values for the concrete between the flanges of the columns inserted into walls.

| Columns | TRRF (min) | 30 | 60 | 90 | 120 |
|---|---|---|---|---|---|
| Normativo | | 240 | 346 | 434 | 484 |
| H220-CONC-ORT-T11 | Average | 66 | 157 | 240 | 315 |
| | Maximum | 681 | 891 | 593 | 685 |
| | Minimum | 25 | 54 | 104 | 154 |
| H220-CONC-ORT-T15 | Average | 49 | 127 | 200 | 272 |
| | Maximum | 646 | 860 | 692 | 777 |
| | Minimum | 25 | 58 | 95 | 120 |
| H220-CONC-PAR-T11 | Average | 50 | 134 | 389 | 474 |
| | Maximum | 763 | 904 | 677 | 776 |
| | Minimum | 29 | 75 | 178 | 234 |
| H220-CONC-PAR-T15 | Average | 73 | 190 | 345 | 429 |
| | Maximum | 758 | 903 | 579 | 678 |
| | Minimum | 25 | 48 | 90 | 217 |

With the reduction factor calculated, the temperature of the reinforcement is determined from Table 1 of item 5.1.1.2 of the standard, which considers for each value found of the reduction factor, a corresponding temperature for the longitudinal reinforcement of CA-50 class.

For the four-sided heating column, Table 9, the temperature results in the numerical model were not well represented by the normative values. In all cases, the theoretical temperatures were lower than the numerical ones, and the smallest difference was above 20% (120 min).

**Table 9.** Comparison of the temperatures obtained in the numerical model and the theoretical values for longitudinal reinforcement of the columns with heating on all faces.

| TRRF(min) | 30 | 60 | 90 | 120 |
|---|---|---|---|---|
| Normative | 212 | 411 | 567 | 676 |
| H220-CONC-ISO | 360 | 603 | 757 | 859 |

In the case of columns inserted into walls, as shown in Table 10, the values of the average numerical temperature for this region were lower in relation to the values obtained by the normative method. Regarding H220-CONC-ORT-11 and H220-CONC-ORT-T15 columns, the biggest differences in relation to average temperatures were approximately 461ºC and 350ºC at 120 minutes of heating, respectively. In contrast, for the columns H220-CONC-PAR-11 and H220-CONC-PAR-T15, this difference was less than 230ºC.

**Table 10.** Comparison of the temperatures obtained in the numerical model and the theoretical values for longitudinal reinforcement of the columns inserted into walls.

| Columns | TRRF (min) | 30 | 60 | 90 | 120 |
|---|---|---|---|---|---|
| Normative | | 212 | 411 | 567 | 676 |
| H220-CONC-ORT-T11 | Average | 65 | 158 | 170 | 215 |
| | Maximum | 96 | 231 | 339 | 430 |
| | Minimum | 33 | 85 | 148 | 212 |
| H220-CONC-ORT-T15 | Average | 88 | 177 | 258 | 326 |
| | Maximum | 153 | 305 | 420 | 509 |
| | Minimum | 24 | 50 | 95 | 142 |
| H220-CONC-PAR-T11 | Average | 171 | 316 | 422 | 503 |
| | Maximum | 302 | 527 | 670 | 773 |
| | Minimum | 39 | 105 | 174 | 233 |
| H220-CONC-PAR-T15 | Average | 36 | 269 | 369 | 447 |
| | Maximum | 248 | 443 | 579 | 678 |
| | Minimum | 36 | 94 | 158 | 217 |

## 6 CONCLUSIONS

This article presented numerical analyses carried out in a thermal context, using the ABAQUS computational package, considering eight steel and steel and concrete composite columns. Of those two were isolated steel columns and six were steel columns inserted into 11 and 15 cm thick walls, to evaluate the thermal field developed in the structural elements.

When comparing similar positions of steel columns and steel and concrete composite columns, it was possible to note a reduction in temperature in the latter elements as a consequence of the concrete properties (low thermal conductivity and high specific heat). In relation to the composite columns inserted into walls, results indicate that the thermal field started to be reduced by the contribution of both concrete and the compartmentalization element. Regarding the thermal gradients presented by the columns inserted into walls, it is perceived a greater value for the cases in which the columns present the web orthogonal to the wall surface.

In addition to assessing the influence of the compartmentalization element and concrete on the thermal field of the columns, a comparison was made between the temperature evolution of steel and steel and concrete composite columns with that obtained from the application of the simplified methods suggested by ABNT NBR 14323 [3] and Eurocode 3 and 4 Part 1-2 [4, 5]. Regarding steel columns, the simplified method was able to reproduce the evolution of temperatures only for elements with uniform heating on the four faces. However, in the case of steel columns inserted into walls, the normative method proved to be quite in favor of safety when comparing it with the field of average and minimum temperatures of the numerical models.

When evaluating the specific method of the Brazilian standard ABNT NBR 14323 [3] for the case of composite columns, it was found that adjustments are necessary to define a sufficiently satisfactory method for both the isolated columns and those inserted into walls. The simplified method was developed for isolated composite columns. Even so, in these cases, the normative temperature of the concrete for TRRF values above 90 min, as well as the reinforcement temperatures for any TRRF were found to be lower than those from the numerical models. Regarding the flange and the web of the steel profile, the standard was in favor of safety.

Finally, regarding the composite columns inserted into walls, although there is no mention in the current normative codes about the temperature calculation for this structural design, the existing method for isolated composite columns was applied. The results showed that in many cases, the standard was very conservative to the point of showing differences for numerical temperatures above 400 ºC.

Rev. IBRACON Estrut. Mater., vol. 14, no. 5, e14502, 2021

15/16

# REFERENCES

[1] A. J. P. M. Correia and J. P. C. Rodrigues, "Fire resistance of partially encased steel columns with restrained thermal elongation," *J. Construct. Steel Res.*, vol. 67, no. 4, pp. 593-601, Apr 2011. http://dx.doi.org/10.1016/j.jcsr.2010.12.002.

[2] Y. S. Simoes, "F. M. Rocha and J. Munaiar No., "Comparação numérica entre o comportamento termoestrutural de pilares de aço e mistos de aço e concreto parcialmente revestidos em situação de incêndio," *Rev. IBRACON Estrut. Mater.*, vol. 11, no. 4, pp. 876-901, Jul. 2018. http://dx.doi.org/10.1590/s1983-41952018000400012.

[3] Associação Brasileira de Normas Técnicas, *Projeto de estruturas de aço e de estruturas mistas de aço e concreto de edifícios em situação de incêndio*, ABNT NBR 14323, 2013.

[4] European Committee for Standardization, *Eurocode 3 - Design of Steel Structures. Part 1-2: General rules - Structural Fire Design*, EN 1993-1-2, 2005.

[5] European Committee for Standardization, *Eurocode 4 - Design of composite steel and concrete structures. Part 1-2: General rules- Structural Fire Design*, EN 1994-1-2, 2005.

[6] A. J. P. M. Correia, J. P. C. Rodrigues and P. V. Real, "Thermal bowing on steel columns embedded on walls under fire conditions," *Fire Saf. J.*, vol. 67, pp. 53–69, Jul. 2014, http://dx.doi.org/10.1016/j.firesaf.2014.05.001.

[7] F. M. Rocha "Pilares de aço e misto de aço e concreto inseridos em paredes em situação de incêndio," Thesis, Esc. Eng. São Carlos, Uni. São Paulo, São Carlos, Brasil, 2016.

[8] M. M. S. Dwaikat and V. K. R. Kodur, "A simplified approach for evaluating plastic axial and moment capacity curves for beam–columns with non-uniform thermal gradients," *Eng. Struct.*, vol. 32, no. 5, pp. 1423–1436, May 2010. http://dx.doi.org/10.1016/j.engstruct.2010.01.021.

[9] M. M. S. Dwaikat, "V. K. R. Kodur, S. E. Quiel and M. E. M. Garlock, "Experimental behavior of steel beam–columns subjected to fire-induced thermal gradients," *J. Construct. Steel Res.*, vol. 67, no. 1, pp. 30–38, Jan. 2011., http://dx.doi.org/10.1016/j.jcsr.2010.07.007.

[10] A. Agarwal, "L. Choe and A. H. Varma, "Fire design of steel columns: Effects of thermal gradients," *J. Construct. Steel Res.*, vol. 93, pp. 107–118, Feb. 2014., http://dx.doi.org/10.1016/j.jcsr.2013.10.023.

[11] G. M. Kamil, "Q. Q. Liang and M. N. S. Hadi, "Fiber element simulation of interaction behavior of local and global buckling in axially loaded rectangular concrete-filled steel tubular slender columns under fire exposure," *Thin-walled Struct.*, vol. 145, pp. 1–15, Dec. 2019., http://dx.doi.org/10.1016/j.tws.2019.106403.

[12] P. B. Lourenço "Computational strategies for masonry structures," Ph.D. dissertation, Delft Univ. Press, Delft Univ. Tech., Delft, 1996.

[13] International Organization for Standardization. *Fire-resistance tests - Elements of building construct - Part 1: General requirements*, ISO 834, 1999.

[14] European Committee for Standardization. *Eurocode 1 - Actions on structures - Part 1-2: General actions - Actions on structures exposed to fir*e, EN 1991-1-2, 2002.

[15] J. F. Cadorin, "Compartment fire models for structural engineering," Thèse, Doctorat en Sciences Appkiquéés, Faculté de Sciences Applpiques, Uni. Liège, Belgium, 2003.

[16] Y. S. Simoes, F. M. Rocha and J. Munaiar No., "Análises numérica e paramétrica de pilares de aço isolados submetidos a elevadas temperaturas," *Rev. Estrutura Aco*, vol. 8, no. 1, pp. 60–79, Apr. 2019.

# IBRACON Structures and Materials Journal
## Revista IBRACON de Estruturas e Materiais

ORIGINAL ARTICLE

# Influence of concrete strength, fiber content and aspect ratio in the residual flexural strength of steel fiber reinforced self-compacting concrete

*Influência da resistência à compressão do concreto, teor de fibra e fator de forma das fibras, na resistência residual do concreto autoadensável reforçado com fibra de aço*

Matheus Galvão Cardoso[a] ⓘD
Rodrigo de Melo Lameiras[a] ⓘD
Valdirene Maria Silva Capuzzo[a] ⓘD

[a]Universidade de Brasília – UnB, Departamento de Engenharia Civil e Ambiental – ENC, Brasília, DF, Brasil

**Abstract:** Steel Fiber Reinforced Self-Compacting Concrete (SFRSCC) is a material that combines the benefits of self-compacting concrete in the fresh state and the greater durability, with the gains of fiber-reinforced concrete in the hardened state, especially the gains in residual flexural strength. Results are presented in this paper of residual flexural strengths on 48 prenotched prisms conducted in accordance with RILEM TC 162 TDF for the Steel Fiber Reinforced Self-Compacting Concretes (SFRSCC). This article presents equations to estimate residual flexural stresses in SFRSCC. For this, SFRSCC prisms of two compressive strength classes, 20 MPa and 40 MPa, were produced with 3 different types of steel fibers with the contents volume of 0.5% and 1.0%. Based on the test results, equations were proposed to determine the residual flexural stresses established through regression analysis, which were, then, further validated with concretes produced in this work and results available in the literature. The equations found, despite showing an indication of the residual flexural strengths that will be achieved, obtained a relatively high error. In order for the equations to be applied in a technical way, further studies for a larger sample need to be carried out, seeking to optimize the equations.

**Keywords:** steel fiber reinforced self-compacting concrete (SFRSCC), flexural residual strength, three point bending test, hooked end fiber.

**Resumo:** O concreto autoadensável reforçado com fibra de aço (CAARF) é um material que combina os benefícios do concreto autoadensável no estado fresco e a maior durabilidade, com os ganhos do concreto reforçado com fibras no estado endurecido, principalmente os ganhos quanto as resistências residuais à flexão. São apresentados neste trabalho os resultados de ensaios das resistências residuais à flexão de 48 prismas entalhados, conduzidos de acordo com RILEM TC 162 TDF para concreto autoadensável reforçado com fibra de aço (CAARF). Este artigo propõe equações para estimar as resistências residuais à flexão nos CAARFs. Para isso, prismas de CAARFs de duas classes de resistência à compressão, 20 MPa e 40 MPa, foram produzidos com 3 tipos diferentes de fibras de aço com o teor de 0,5% e 1,0% em relação ao volume de concreto. A partir dos resultados dos ensaios, foram propostas equações para determinar as tensões de flexão residuais estabelecidas por meio de análise de regressão, as quais foram, então, validadas com os concretos produzidos neste trabalho e resultados disponíveis na literatura. As equações encontradas, apesar de mostrarem uma indicação das resistências à flexão residuais que serão alcançadas, obtiveram um erro relativamente alto. Para que as equações possam ser aplicadas de forma técnica, novos estudos para uma amostra maior precisam ser realizados, visando otimizar as equações.

**Palavras-chave:** concreto autoadensável reforçado com fibra de aço, tensões residuais de flexão, ensaio de flexão a três pontos, fibra com gancho na ponta.

*M. G. Cardoso, R. M. Lameiras, and V. M. S. Capuzzo*

# 1 INTRODUCTION

The Steel Fiber Reinforced Self-Compacting Concrete (SFRSCC) is an material that combines the benefits of fiber reinforced concrete such as tenacity gain and the ability to withstand residual post-cracking tensile stresses, with the characteristics of self-compacting concrete, such as workability, and the ability to fill and to overcome restrictions without segregating, which eliminates the use of vibration during casting. Several researches has already shown that SFRSCC can be used in segments of tunnels, precast roof elements, beams, sandwich panels, sheet piles, floors and slabs [1]–[7].

The great differential of SFRSCC is related to its residual post cracking flexural strength. A barrier found in the production of SFRSCC is the difficulty in pre-defining the desired post-cracking behavior when determining concrete mixtures. Although there are already some studies that try to determine the influence of fiber volume and its characteristics such as fiber type and compressive strength [8]–[14] in the post-cracking behavior of concrete, the dosage of SFRSCC has been performed, in most times, empirically. The determination of equations that correlate the residual flexural strengths of SFRSCC with the characteristics of concrete and fiber would allow an optimized dosage of this material.

Recently, Domski and Katzer [14] proposed equations to estimate residual strength for common concretes, using the geometric characteristics of the fibers and fiber volume as variables. However, has been verified in some research the great influence of the compressive strength of the matrix on the residual strengths [8], [12], [13].

This work determined new equations to estimate the residual strengths of SFRSCC, inserting the geometric characteristics, the fiber volume content and the compressive strength the matrix as input variables. The determination of equations that allow the estimating residual strength based on the materials used for the production of the SFRSCC can contribute to increase the use of this concrete, considering it will make it possible to perform more rational mixture of this material.

# 2 MATERIALS AND EXPERIMENTAL PROGRAM

The experimental program, carried out at the Laboratories of the Materials and Structures of the University of Brasília, included a total of 48 SFRSCC prisms for 3 point bending tests on prenotched specimens, conducted in accordance with EN 14651 [15]. The materials used in this research were Portland Cement CP II 32 F, a river sand with a maximum diameter of 2.36 mm, a coarse aggregate with a maximum diameter of 9.5 mm, a limestone filler, a superplasticizer admixture (Master Glenium 51) and three types of steel fibers with hooked end.

## 2.1 Steel fibers

Three types of steel fibers with hooked end were used as reinforcement. The properties of the used fibers, according to their manufactures, are presented in Table 1.

**Table 1.** Physical characteristics of the fibers used in the research.

| Fiber Type | Diameter $d_f$ (mm) | Length $l_f$ (mm) | Aspect ratio $l_f/d_f$ | Nominal Young's modulus (MPa) | Nominal unit weight (Kg/m³) |
|---|---|---|---|---|---|
| ST-33/44 | 0.75 | 33 | 44 | 210 | 7850 |
| ST-33/60 | 0.55 | 33 | 60 | 210 | 7850 |
| ST-50/67 | 0.75 | 50 | 67 | 210 | 7850 |

## 2.2 Concrete Mixture

The tests were performed with twelve distinct concrete mixes. The mixes were obtained using the software Betonlab Pro 3, following recommendations proposed by De Larrard and Sedran [16]. They were produced with compressive strength classes equal to 20 MPa and 40 MPa for each fiber. The fiber contents used were 0.5% and 1.0% in relation to the SFRSCC volume (Table 2).

The flow spread of concretes in the fresh state was registered following the recommendations of NBR 15823 [17]. The average value obtained for the flow spread of SFRSCC was equal to 650 mm.

**Table 2 .** Mixes of the SFRSCC produced.

| Mixtures | 20 MPa | | | | | | | 40 MPa | | | | | | |
|---|---|---|---|---|---|---|---|---|---|---|---|---|---|---|
| | REF | ST-33/60 | | ST-50/67 | | ST-33/44 | | REF | ST-33/60 | | ST-50/67 | | ST-33/44 | |
| Fiber Volume (%) | 0.00 | 0.50 | 1.00 | 0.50 | 1.00 | 0.50 | 1.00 | 0.00 | 0.50 | 1.00 | 0.50 | 1.00 | 0.50 | 1.00 |
| Coarse aggregate (G) (kg/m$^3$) | 852 | 844 | 826 | 834 | 802 | 826 | 804 | 852 | 844 | 805 | 834 | 806 | 826 | 803 |
| Sand (S) (kg/m$^3$) | 633 | 627 | 614 | 619 | 596 | 613 | 597 | 633 | 649 | 600 | 641 | 599 | 635 | 597 |
| Cement (C) (kg/m$^3$) | 378 | 382 | 392 | 388 | 398 | 392 | 393 | 498 | 505 | 515 | 513 | 515 | 519 | 520 |
| Limestone Filler (kg/m$^3$) | 242 | 244 | 252 | 249 | 281 | 252 | 287 | 133 | 134 | 177 | 137 | 180 | 138 | 173 |
| Superplasticizer (SP) (kg/m$^3$) | 3.90 | 5.00 | 5.20 | 4.10 | 4.00 | 5.20 | 5.50 | 5.10 | 5.30 | 6.10 | 6.50 | 6.10 | 6.60 | 5.20 |
| Water (W) (kg/m$^3$) | 231 | 234 | 240 | 237 | 244 | 240 | 240 | 231 | 234 | 238 | 237 | 238 | 240 | 241 |

## 2.3 Compressive strength

The compressive strength ($f_{cm}$) of concretes were determined with compressive tests performed on cylinders of 100 mm diameter and 200 mm height casted simultaneously with the three-point bending test specimens. These concrete cylinders were cured for 28 days under laboratory temperature, inside a chamber with humidity control. The compressive strength was obtained based on the procedures given in NBR 5739 [18].

## 2.4 Three point bending test (3PBT)

Four specimens for the three point bending test were produced for each concrete mix, with cross section of 150 mm × 150 mm and length of 550 mm. These specimens are in accordance to the EN 14651 [15]. The specimens were cured for 28 days under laboratory temperature inside a chamber with humidity control. The tests were carried on a press EMIC servo-controlled hydraulic-system. The tests were controlled by the internal displacement transducer of the test machine at a rate of 0.1 mm/min. Each test lasted about 60 minutes and was interrupted when the crack opening reached 6 mm. In the execution of this test, the load was applied in the middle of the specimens' span. The specimens were tested in a three-point bending test with a central notch (25 mm), as illustrated in Figure 1. The crack opening was measured using two linear variable differential transformers (LVDT), one on each of the notch's side, fixed at the base of the specimens.

The acquisition of the test data, i.e., load and crack mouth opening, was performed using a 500 kN HBM load cell and two LVDTs. These devices were connected to a Spider 8 module (model SR30), manufactured by HBM, and controlled by the CATMAN software. This enabled continuous readings of force and displacement. With the results of the crack opening and the load it was possible to obtain the curves that relate the load to the Crack Mouth Opening Displacement (CMOD). The following parameters were calculated: proportionality limit ($f_{ft,L,}$) and residual flexural strength $f_{R.1}$, $f_{R.2}$, $f_{R.3}$, $f_{R.4}$, corresponding to CMOD values equal to 0.5 mm, 1, 5 mm, 2.5 mm and 3.5 mm, respectively.
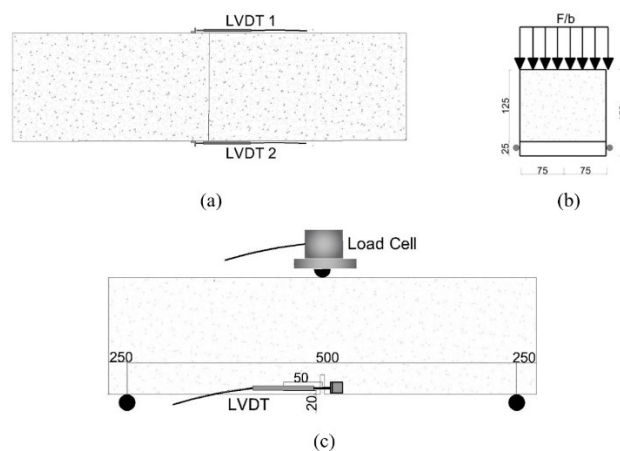
**Figure 1.** Three point bending test setup in accordance with RILEM TC 162 [19]; a: plan view; b: cross section of specimen; c: side view of specimen. Dimensions in mm.

## 2.5 Determination of equations: Linear regression

Based on the results obtained with the three-point bending and compressive strength tests and on the equations proposed by Domski and Katzer [14], a linear regression was performed using the Microsoft Excel 2013 software. Unlike Domski and Katzer [14], who only considered the volume and geometric characteristics of the fiber, the SFRSCC's compressive strength was also inserted as a variable in the equation. Another improvement of the equations found in this work is that they are applicable to self-compacting concrete. As a result, it was obtained equations which correlate the residual flexural strengths $f_{R.1}$, $f_{R.2}$, $f_{R.3}$ and $f_{R.4}$ with the compressive strength of the concrete, the geometric characteristics of the fibers and the volume of fiber adopted.

Each residual flexural strength, $f_{R.1}$, $f_{R.2}$, $f_{R.3}$, $f_{R.4}$, was correlated by means of an equation with the aspect ratio, fiber volume and the square root compressive strength of the concrete. Thus, coefficients were determined that, multiplied by these variables (aspect ratio, fiber volume and square root of the SFRSCC compression strength), provided the SFRSCC residual resistance response.

## 3 RESULTS AND DISCUSSIONS

### 3.1 Compressive Strength

The Figure 2 and Figure 3 show the results obtained in the SFRSCC compressive strength test. Hereinafter the specimens are identified by the following nomenclature "X-YST-Z/W", where: X is the nominal compressive strength, Y is the fiber volume and ST-Z/W is the type of fiber, where Z is the length and W is the aspect ratio of the steel fiber. REF is the concrete without fiber.

Despite the variations found in the different SFRSCC, there were no major changes promoted by the addition of fibers in the compressive strength of the concrete. The same was observed in the concretes produced by Hu et al. [20].

It was observed a decrease in the strength of the 20-MPa concrete when comparing the strength of the concrete with fiber to the reference concrete. However, after performing an ANOVA and Tukey statistical tests, it was verified that the compressive strength of the concrete did not change significantly.
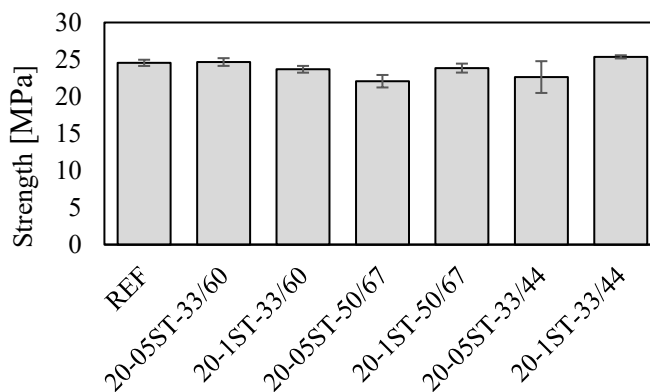


**Figure 2.** Compressive strength for the 20-MPa SFRSCC .

For the 40-MPa Steel Fiber Reinforced Self-Compacting Concretes, shown in Figure 3, it was observed that some mixtures presented a higher strength than that of the reference concrete. This can be explained by the higher cement consumption of these mixes. In the concretes with ST-33/44 fiber, a more evident reduction in compressive strength was observed when compared to other concretes, especially in the case of 1.0% fiber content . After performing an ANOVA and Tukey tests it was found that in the case of the 40-MPa SFRSCC, there was a significant variation in the compressive strength of concrete when fibers were present. The decrease in the strength of concretes using the ST-33/44 fiber can be explained by differences in SFRC mixtures and by its greater tendency to agglomerate.
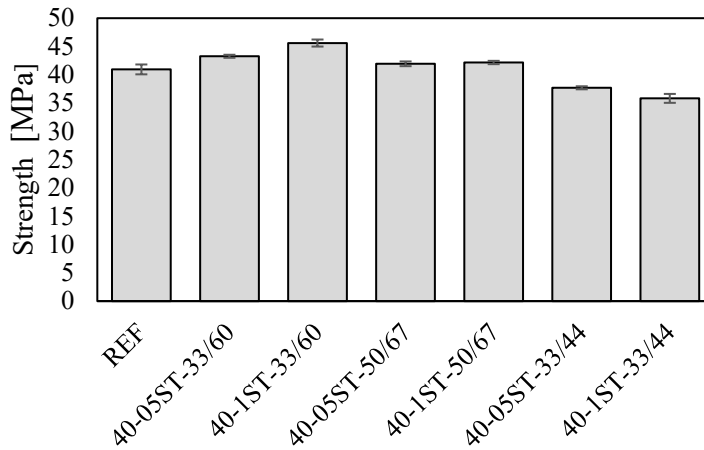
**Figure 3.** Compressive strength for the 40-MPa SFRSCC .

## 3.2 Three point bending tests results

In the three point bending tests in most specimens, a single crack was observed in the rupture, especially in concretes with a smaller fiber volume. Some specimens, in which the fibers offered less reinforcement to the concrete, this crack was almost vertical, as can be seen in Figure 4a. In some isolated cases, the appearance of multiple cracks in the region of application of the load was observed, as can be seen in Figure 4b.
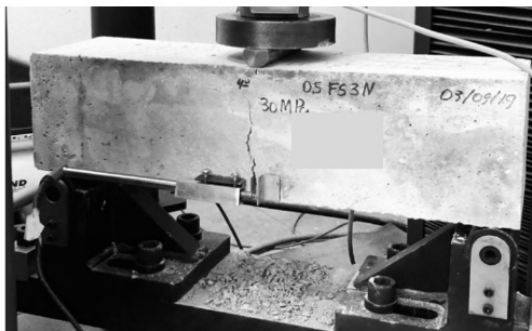


**Figure 4.** Failure mechanisms in specimens of three point bending tests, a: only vertical crack; b: multiple cracks

The average of the load values obtained in the three point bending test, and the envelope formed by the highest and lowest values found, versus CMOD curves are illustrated in Figure 5, Figure 6 and Figure 7. Table 3 shows the parameters that characterize the concrete's post-cracking behavior, showing the mean value and the coefficient of variation found between the samples. It is possible to observe in Figure 5, Figure 6, Figure 7 a significant dispersion of the results, which is common for this type of concrete in view of the impossibility of ensuring that the fibers equally distributed and oriented. This fact was also observed in other studies carried out with concrete reinforced with fibers [19], [21]–[23].

For SFRSCC with ST-33/60 fiber, it was possible to observe that there was a less significant variation between the values found, according to the ANOVA test. The envelope of the results obtained in the four samples of each concrete showed less dispersion from the average. This can be explained by the fact that the concretes produced with this fiber presented more homogeneous properties in the fresh state.

The Figure 5 show the Experimental Load *vs*. CMOD relationships for SFRSCC with the ST-33/60 fiber.
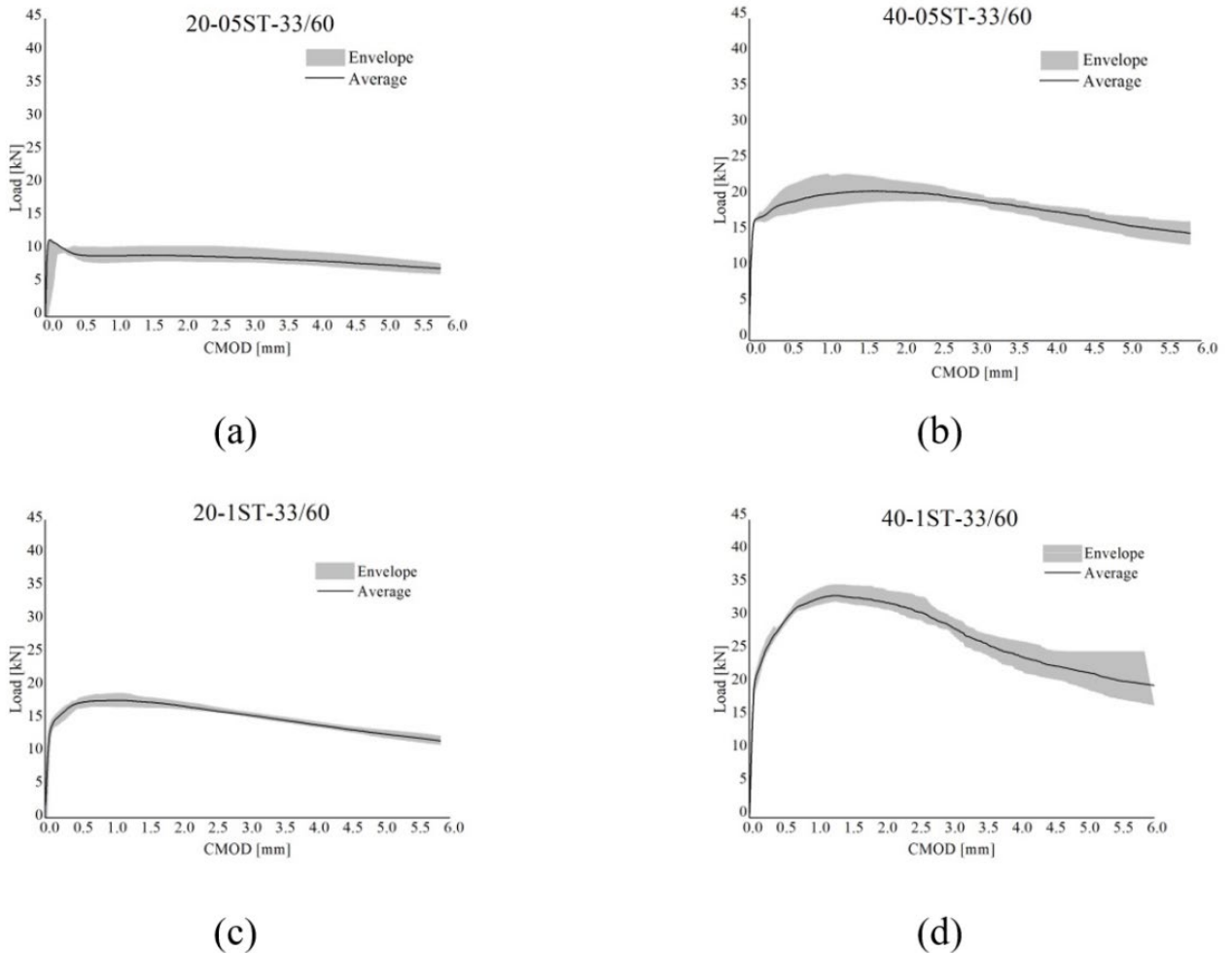
**Figure 5.** Experimental Load *vs.* CMOD relationships for SFRSCC with the ST-33/60 fiber: (a)20-05ST-33/60; (b) 40-05-ST-33/60; (c) 20-1ST-33/60; (d) 40-1ST-33/60.

The Tukey test showed a significant difference between the residual resistances for concretes with the same compressive strength, with varying the fiber content from 0.50% to 1.00%. When the fiber content was fixed and the compressive strength varied from 20 MPa to 40 MPa, there was a significant increase in the residual resistances obtained, as also shown by the Tukey test.

In the 20-05ST-33/60 and 20-1ST-33/60 concretes, as can be seen in Figure 5a and Figure 5c and Table 3, it is possible to observe the increase in residual strengths achieved with the addition of fibers. With the increase in fiber content from 0.5% to 1.0%, an increase of 87.25% in the values of $f_{R.1}$ was observed, rising from 3.06 MPa to 5.73 MPa, and an increase of 67.88% in $f_{R.3}$, which rose from 3.02 MPa to 5.07 MPa. The same was seen in the concretes 40-05ST-33/60 and 40-1ST-33/60 illustrated in Figure 5b and Figure 5d and in Table 3, in which the $f_{R.1}$ increased from 6.17 MPa to 9.42 MPa, resulting in an increase of 52.67%, and the $f_{R.3}$ increased from 6.54 MPa to 9.96 MPa, which represents an increase of 52.29%.

In concretes with the same fiber content, it is possible to observe the impact of the compressive strength in increasing the toughness of the concrete, as can be seen when comparing Figure 5a and Figure 5b and the results of Table 3. Comparing the post-cracking behavior of 20-05ST-33/60 to 40-05ST-33/60, there was an increase of 101.63% in the $f_{R.1}$, while the $f_{R.3}$ increased 116.56%. The same can be seen between the concretes 20-1ST-33/60 and 40-1ST-33/60, in which the $f_{R.1}$ and the $f_{R.3}$ an increase of 64.40% and 96.45%, respectively.

The Figure 6 show experimental load vs. CMOD relationships for SFRSCC with the ST-50/67 fiber.
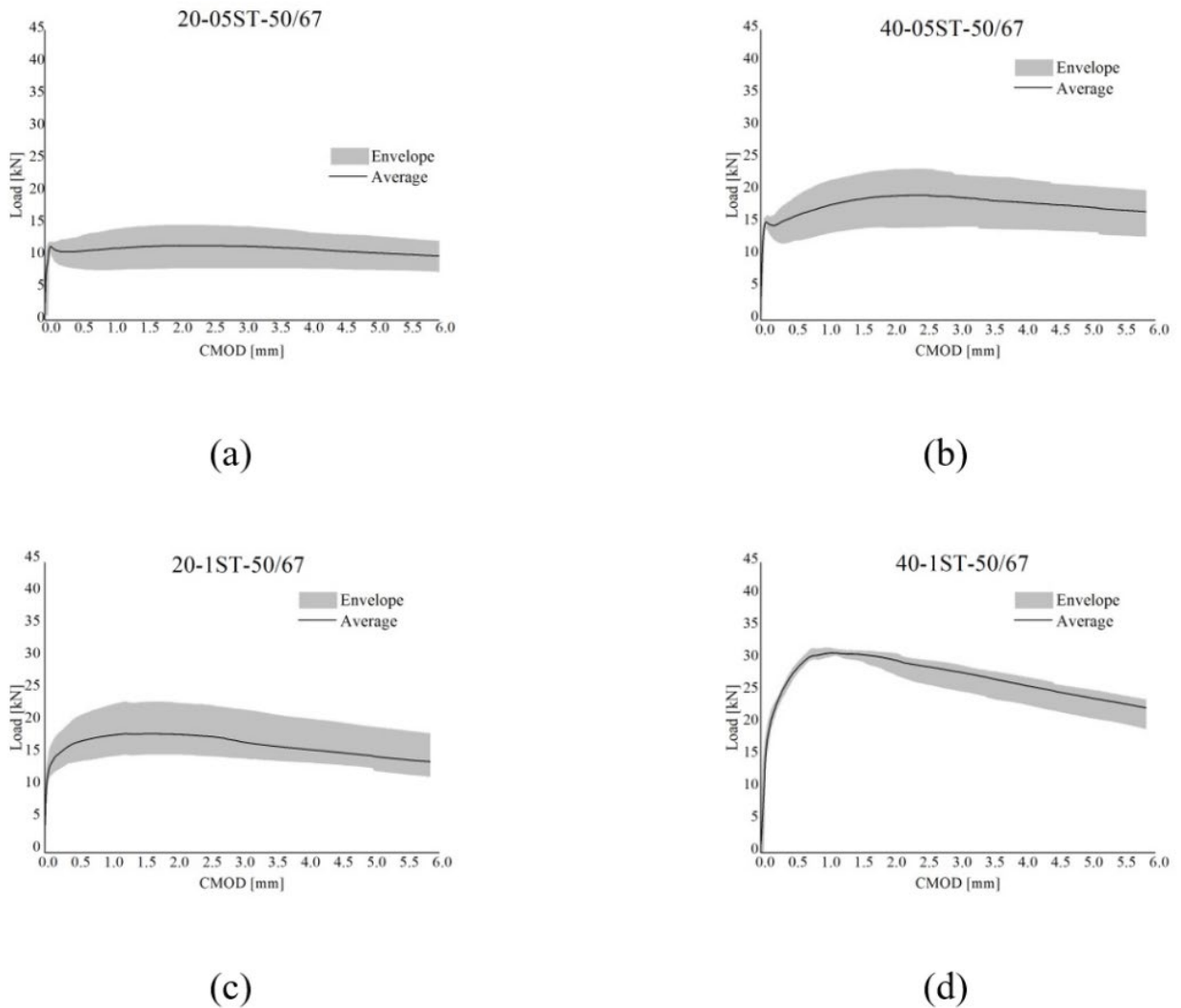
Figure 6. Experimental Load *vs.* CMOD relationships for SFRSCC with the ST-50/67 fiber: (a) 20-05ST-50/67; (b) 40-05-ST-50/67; (c) 20-1ST-50/67; (d) 40-1ST-50/67.

Comparing the 20 MPa concretes with ST-50/67 fibers, shown in Figure 6a and in Figure 6c, the same behavior can be observed, with the addition of fibers resulting in a significant increase in post-cracking strength. The $f_{R.1}$ increased from 3.69 MPa to 5.48 MPa, which is an increase of 48.51%, and the $f_{R.3}$, from 4.05 MPa to 5.77 MPa, which is an increase of 42.47%. For concretes with compressive strength equal to 40 MPa, the $f_{R.1}$ e $f_{R.3}$ increased 62.14% and 37.30% when the fiber content increased from 0.5% to 1.0%, respectively. Comparing the concretes with the same fiber content, varying the compressive strength of the concrete from 20 MPa to 40 MPa for the ST-50/67 fiber, when the fiber volume used was 0.5%, led to a significant gain in the $f_{R.1}$ e $f_{R.3}$, 49.69% and 66.17% respectively. A similar trend, but even more significantly, was verified by comparing the concretes with the resistances with levels of 1.0% of this fiber, where the $f_{R.1}$e $f_{R.3}$ grew 63.32% and 72.62%. Venkateshwaran et al. [12] found a direct relationship between the fiber reinforcement capacity and the matrix strength, as the fiber anchoring capacity offered by the concrete matrix is essential for the fibers to be mechanically activated.

The Figure 7 show experimental load vs. CMOD relationships for SFRSCC with the ST-33/44 fiber.

For the ST-33/44 fiber, the variation of the content from 0.5% to 1.0% in the 20 MPa concrete, as can be seen in Figure 7a and Figure 7c and Table 3, resulted in an increase in $f_{R.1}$ from 2.72 MPa to 4.74 MPa and fR.3 from 2.81 MPa to 4.77 MPa, which represents an increase of 74.26% and 69.75% respectively. In the comparison between 40 MPa concretes with this fiber, shown in Figure 5b and Figure 5d, the $f_{R.1}$ increase of 59,01% and the $f_{R.3}$ increase of 58,40%.
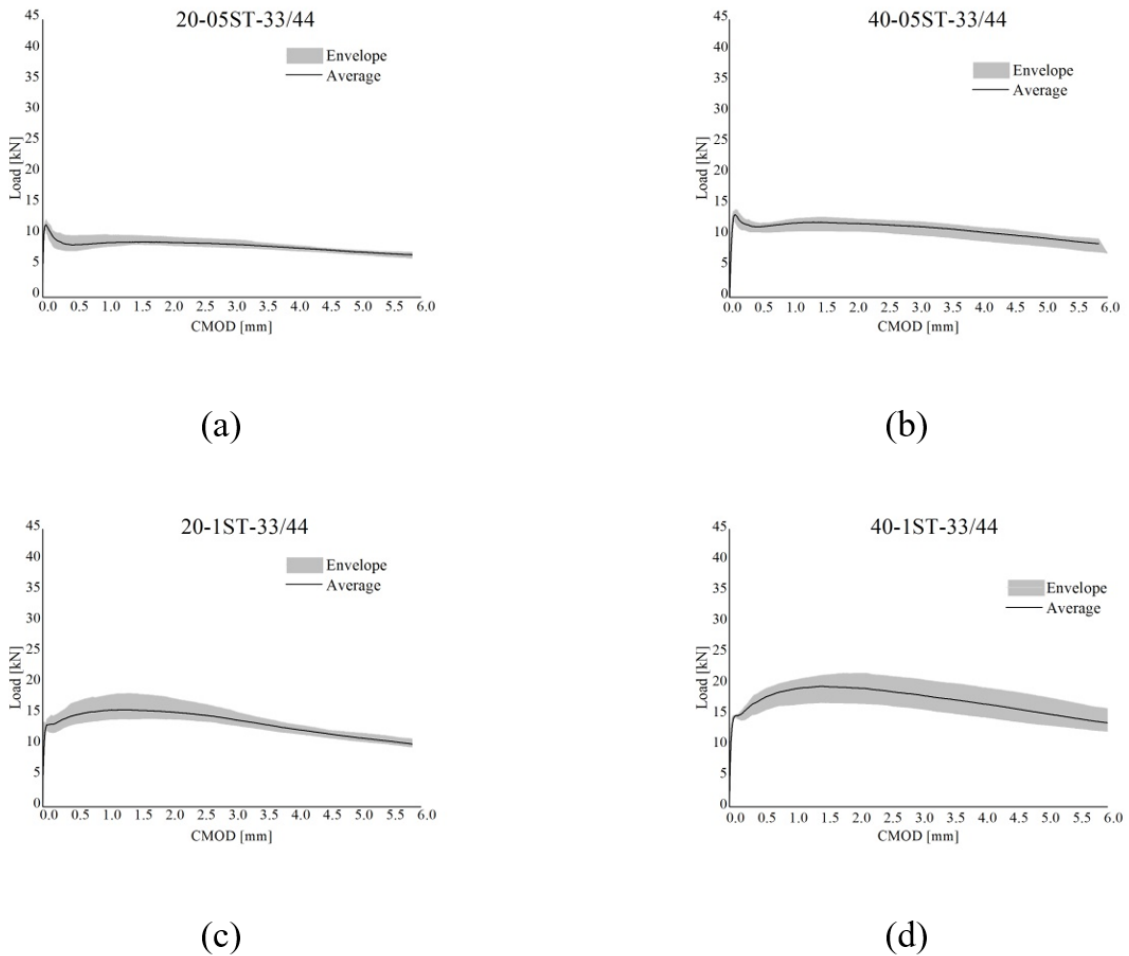
**Figure 7.** Experimental Load *vs.* CMOD relationships for SFRSCC with the ST-33/44 fiber: (a)20-05ST-33/44; (b) 40-05-ST-33/44; (c) 20-1ST-33/44; (d) 40-1ST-33/44

In concretes with this fiber, when the comparison is made for the same fiber contents and varying the compressive strength of the concrete from 20 MPa to 40 MPa, there were increases in $f_{R.1}$ and in $f_{R.3}$, of 34.56% and 33.45% respectively for a 0.5% fiber volume content. In the case of concretes with 1.0% of this fiber, $f_{R.1}$ e $f_{R.3}$ increased 22.78% and 24.53% respectively.

When comparing the ST-33/44 and ST 33/60 fibers, despite having the same length, the ST-33/60 fiber guaranteed higher values of residual resistance to concretes due to their higher aspect ratio. The same was observed by Abbass et al. [24], who found that among concretes with the same compressive strength and fibers of the same length, the aspect ratio will have an impact on the residual flexural strength values achieved. Higher aspect ratios contribute to higher residual flexural strength values.

After comparing the SFRSCC produced with the three types of fiber and performing an analysis of variance and a Tukey test, it was found that the concretes produced with the ST-50/67 fiber and the ST-33/60 fiber, despite the physical differences between the two fibers, showed significantly equal results in residual strength. This was observed for the same fiber contents and equal strength values. Showing the great importance of the aspect ratio of the fibers. These two fibers, despite the differences between their lengths and diameters, have very similar aspect ratios (60 and 67 respectively).

An ANOVA and a Tukey test were performed on the results obtained for concretes produced with the ST-33/44 fiber and for the results obtained for the concretes produced with the ST-50/67 and ST-33/60 fibers. Residual resistances were significantly different. This can be explained by the great difference between the aspect ratios, between the ST 33/44 fiber and the ST-50/67 and ST-33/60 fibers. Chu and Kwan [25] also found that for concrete reinforced with steel fibers that have a higher aspect ratio, the residual strengths obtained were higher.

Rev. IBRACON Estrut. Mater., vol. 14, no. 5, e14503, 2021

8/14

**Table 3.** Residual flexural strength of the concretes determined in the three point bending tests.

| Concrete mix | | $f_{fct,L}$ [MPa] | $f_{ct}$ (0.7*$f_{fct,L}$) [MPa] | Residual Flexural Strength | | | |
|---|---|---|---|---|---|---|---|
| | | | | $f_{R.1}$ [MPa] | $f_{R.2}$ [MPa] | $f_{R.3}$ [MPa] | $f_{R.4}$ [MPa] |
| 20-05ST-50/67 | Avg. | 3.68 | 2.58 | 3.69 | 4.01 | 4.05 | 3.95 |
| | CoV | 4.4% | 4.4% | 20.1% | 24.3% | 24.0% | 23.3% |
| 20-1ST-50/67 | Avg. | 3.97 | 2.78 | 5.48 | 5.89 | 5.77 | 5.28 |
| | CoV | 14.8% | 14.8% | 18.9% | 20.1% | 18.2% | 19.4% |
| 20-05ST-33/60 | Avg. | 3.07 | 2.15 | 3.06 | 3.07 | 3.02 | 2.86 |
| | CoV | 16.9% | 16.9% | 8.5% | 10.5% | 10.8% | 9.8% |
| 20-1ST-33/60 | Avg. | 3.92 | 2.75 | 5.73 | 5.58 | 5.07 | 4.57 |
| | CoV | 10.4% | 10.4% | 4.4% | 4.9% | 5.7% | 7.8% |
| 20-05ST-33/44 | Avg. | 3.76 | 2.63 | 2.72 | 2.86 | 2.81 | 2.66 |
| | CoV | 8.1% | 8.1% | 12.6% | 8.1% | 6.6% | 5.1% |
| 20-1ST-33/44 | Avg. | 4.17 | 2.92 | 4.74 | 5.01 | 4.77 | 4.28 |
| | CoV | 6.6% | 6.6% | 10.3% | 11.6% | 8.6% | 5.8% |
| 40-05ST-50/67 | Avg. | 4.87 | 3.41 | 5.52 | 6.48 | 6.73 | 6.40 |
| | CoV | 3.9% | 3.9% | 9.6% | 11.2% | 10.8% | 10.0% |
| 40-1ST-50/67 | Avg. | 4.07 | 2.85 | 8.95 | 9.84 | 9.24 | 8.65 |
| | CoV | 37.7% | 37.7% | 2.9% | 2.3% | 6.3% | 7.6% |
| 40-05ST-33/60 | Avg. | 5.17 | 3.62 | 6.17 | 6.68 | 6.54 | 6.06 |
| | CoV | 2.4% | 2.4% | 9.0% | 7.9% | 4.7% | 4.1% |
| 40-1ST-33/60 | Avg. | 5.28 | 3.69 | 9.42 | 10.66 | 9.96 | 8.44 |
| | CoV | 10.7% | 10.7% | 1.6% | 3.9% | 5.2% | 4.8% |
| 40-05ST-33/44 | Avg. | 4.10 | 2.87 | 3.66 | 3.88 | 3.75 | 3.54 |
| | CoV | 6.1% | 6.1% | 5.6% | 8.3% | 7.8% | 9.0% |
| 40-1ST-33/44 | Avg. | 4.41 | 3.08 | 5.82 | 6.31 | 5.94 | 5.46 |
| | CoV | 6.2% | 6.2% | 3.6% | 7.9% | 12.5% | 15.2% |

$f_{R.1}$, $f_{R.2}$, $f_{R.3}$, $f_{R.4}$: are the residual flexural strength referring to the crack openings of 0.5 mm, 1.5 mm, 2.5 mm and 3.5 mm, respectively; Avg: average of the values of the 4 specimens; CoV: covariance of the values of the 4 specimens.

## 3.3 Determination of equations

Based on the database of tests performed for the SFRSCC of this work and inspired by the equations of Domski and Katzer [14], new equations were created to estimate the residual flexural strength of self-compacting concrete reinforced with steel fibers, using the Microsoft Excel software.

Equations 1, 2, 3 and 4 represent the residual strengths $f_{R.1}$, $f_{R.2}$, $f_{R.3}$, $f_{R.4}$, which characterize the post-cracking behavior of SFRSCC. These were adjusted with an $R^2$ of 0.91, 0.93, 0.94 and 0,89, respectively. Although $R^2$ did not present such a high value, this fact is common in the measurement of phenomena with dispersed results, as is the case of SFRSCCs.

$$f_{R1} = -0.59 + 0.07\left(\frac{l}{d}\right) + 5,31\left(V_f\right) + 1.44\left(f_c\right)^{0.5} \tag{1}$$

$$f_{R2} = -13.10 + 0.08\left(\frac{l}{d}\right) + 5.65\left(V_f\right) + 1.81\left(f_c\right)^{0.5} \tag{2}$$

$$f_{R3} = -12.33 + 0.08\left(\frac{l}{d}\right) + 4.79\left(V_f\right) + 1.74\left(f_c\right)^{0.5} \tag{3}$$

$$f_{R4} = -10.70 + 0.08\left(\frac{l}{d}\right) + 3.93\left(V_f\right) + 1.51\left(f_c\right)^{0.5} \tag{4}$$

In which:

$f_{R.1}$. $f_{R.2}$. $f_{R.3}$. $f_{R.4}$: are the residual flexural strength referring to the crack openings of 0.5 mm, 1.5 mm, 2.5 mm and 3.5 mm, respectively;

$l$: is the length of the fiber;

$d$:: the fiber diameter;

$V_f$:: is the volume of fiber;

$f_c$: is the concrete compressive strength.

A comparison between the values predicted by the proposed equations and the values experimentally obtained are shown in Table 4.

**Table 4.** Comparison between the values of residual flexural strengths obtained experimentally and the values predicted by the equations.

| Concrete Mix | | Experimentally obtained *vs.* predicted by the equation | | | | | | | |
|---|---|---|---|---|---|---|---|---|---|
| | | $f_{R.1}$ [MPa] | $f_{R.2}$ [MPa] | $f_{R.3}$ [MPa] | $f_{R.4}$ [MPa] | Error $f_{R.1}$ | Error $f_{R.2}$ | Error $f_{R.3}$ | Error $f_{R.4}$ |
| 20-05ST-50/67 | Exp. | 3.69 | 4.01 | 4.05 | 3.95 | 1.13% | 6.53% | 6.75% | 6.44% |
| | Predicted | 3.65 | 3.77 | 3.80 | 3.71 | | | | |
| 20-1ST-50/67 | Exp. | 5.48 | 5.89 | 5.77 | 5.28 | 13.04% | 10.61% | 6.85% | 6.90% |
| | Predicted | 6.30 | 6.59 | 6.19 | 5.68 | | | | |
| 20-05ST-33/60 | Exp. | 3.06 | 3.07 | 3.02 | 2.86 | 11.21% | 13.94% | 15.64% | 17.62% |
| | Predicted | 3.44 | 3.56 | 3.58 | 3.47 | | | | |
| 20-1ST-33/60 | Exp. | 5.73 | 5.58 | 5.07 | 4.57 | 6.02% | 12.75% | 15.03% | 15.80% |
| | Predicted | 6.10 | 6.39 | 5.97 | 5.43 | | | | |
| 20-05ST-33/44 | Exp. | 2.52 | 2.75 | 2.74 | 2.63 | 26.66% | 47.71% | 45.95% | 40.61% |
| | Predicted | 1.99 | 1.86 | 1.88 | 1.87 | | | | |
| 20-1ST-33/44 | Exp. | 4.74 | 5.01 | 4.77 | 4.28 | 2.05% | 6.81% | 11.55% | 11.60% |
| | Predicted | 4.64 | 4.69 | 4.27 | 3.83 | | | | |
| 40-05ST-50/67 | Exp. | 5.52 | 6.48 | 6.73 | 6.40 | 11.29% | 7.57% | 2.59% | 0.23% |
| | Predicted | 6.23 | 7.01 | 6.91 | 6.41 | | | | |
| 40-1ST-50/67 | Exp. | 8.95 | 9.84 | 9.24 | 8.65 | 0.74% | 0.08% | 0.61% | 3.21% |
| | Predicted | 8.88 | 9.83 | 9.30 | 8.38 | | | | |
| 40-05ST-33/60 | Exp. | 6.17 | 6.68 | 6.54 | 6.06 | 5.81% | 1.69% | 1.24% | 1.59% |
| | Predicted | 5.83 | 6.57 | 6.45 | 5.97 | | | | |
| 40-1ST-33/60 | Exp. | 9.42 | 10.66 | 9.96 | 8.44 | 8.27% | 10.28% | 9.38% | 3.44% |
| | Predicted | 8.70 | 9.67 | 9.11 | 8.16 | | | | |
| 40-05ST-33/44 | Exp. | 3.66 | 3.88 | 3.75 | 3.54 | 8.37% | 11.35% | 12.63% | 10.82% |
| | Predicted | 3.99 | 4.38 | 4.30 | 3.97 | | | | |
| 40-1ST-33/44 | Exp. | 5.82 | 6.31 | 5.94 | 5.46 | 9.17% | 8.69% | 7.26% | 3.91% |
| | Predicted | 6.41 | 6.91 | 6.40 | 5.68 | | | | |

As can be seen in Table 4, the results obtained with the equations showed an average error of 10%, when compared to the average value obtained experimentally. Although the error was relatively high, these equations can serve as an initial reference for the residual resistances that will be achieved based on the characteristics of the SFRSCC that will be produced. However, new tests need to be carried out to reduce this margin of error, so the application of the equations become more technically practicable. An exception was the concrete 20-05ST-33/44, for which the equation did not show a good fit, with errors reaching almost 50%.

Rev. IBRACON Estrut. Mater., vol. 14, no. 5, e14503, 2021

10/14

To validate the equations, residual flexural strength estimates were made with data from the Venkateshwaran et al. [12], to verify whether the equations were applicable for other concretes and other materials. The compressive strength of concrete mix and the fibers used by Venkateshwaran et al. [12] in their research are described in Table 5.

Table 5. Properties of hooked steel fiber and compressive strength of concretes mix used by Venkateshwaran et al. [12].

| Concrete Mixture | $f_{c'}$ [MPa] | l [mm] | d [mm] | l/d | Fiber volume content (%) |
|---|---|---|---|---|---|
| M32 | 38.60 | 60 | 0.90 | 66.67 | 0.25 |
| M34 | 37.30 | 60 | 0.90 | 66.67 | 0.50 |
| M36 | 36.00 | 60 | 0.90 | 66.67 | 0.75 |
| M38 | 41.10 | 60 | 0.90 | 66.67 | 1.00 |
| M42 | 38.90 | 60 | 0.90 | 66.67 | 0.25 |
| M44 | 39.70 | 60 | 0.90 | 66.67 | 0.50 |
| M46 | 38.10 | 60 | 0.90 | 66.67 | 0.75 |
| M48 | 39.70 | 60 | 0.90 | 66.67 | 1.00 |

Based on the comparison between the results found experimentally by Venjareshwaran et al. [12] and the results obtained with the equations proposed in this work, using the fibers and concretes described in Table 5, it was possible to verify that the equations showed relatively high errors. However, despite the errors reaching up to 20%, the equations showed that they can serve as a reference for the residual resistances that will be achieved. New tests need to be carried out, in order to optimize the coefficients of the equations, minimizing the errors found.

However, as can be seen in the M32 and M42 concretes mix with 0.25% fiber content, a volume outside the interval to which the regression was performed to obtain the equations (0.50% to 1.00%), errors were very high, reaching almost 50%, overestimating the value of residual flexural strength . The equations were well suited to estimate residual flexural strength when the variation in fiber volume is within the limits of the database used to perform the regression. As the compressive strength and the fiber aspect ratio used by Venjareshwaran et al. [12] were similar to those used in this research, shown in Table 6, it is not possible to draw large conclusions regarding the effects of a compressive strength and fiber resistance with aspect ratio outside the limits of the database.

Table 6. Comparison between the values of residual flexural strengths found experimentally by Venkateshwaran et al. [12] and the predicted by the equations obtained in this work.

| Concrete Mix | | Experimental data obtained by Venkateshwaran et al. (2018) vs. Values predicted by the proposed equations | | | | | | | |
|---|---|---|---|---|---|---|---|---|---|
| | | $f_{R.1}$ [MPa] | Error $f_{R.1}$ | $f_{R.2}$ [MPa] | Error $f_{R.2}$ | $f_{R.3}$ [MPa] | Error $f_{R.3}$ | $f_{R.4}$ [MPa] | Error $f_{R.4}$ |
| M32 | Exp. | 2.38 | 42.66% | 2.69 | 45.00% | 2.76 | 44.92% | 2.74 | 45.17% |
| | Predicted | 4.15 | | 4.89 | | 5.01 | | 5.00 | |
| M34 | Exp. | 5.29 | 0.68% | 6.56 | 7.32% | 7.00 | 16.18% | 6.98 | 19.92% |
| | Predicted | 5.33 | | 6.11 | | 6.03 | | 5.82 | |
| M36 | Exp. | 7.29 | 12.17% | 8.25 | 12.54% | 8.04 | 14.27% | 7.82 | 17.76% |
| | Predicted | 6.50 | | 7.33 | | 7.04 | | 6.64 | |
| M38 | Exp. | 6.82 | 18.99% | 9.39 | 1.02% | 9.51 | 6.28% | 9.17 | 11.23% |
| | Predicted | 8.42 | | 9.49 | | 8.95 | | 8.24 | |
| M42 | Exp. | 3.26 | 22.11% | 4.62 | 6.38% | 4.26 | 15.70% | 3.56 | 29.28% |
| | Predicted | 4.19 | | 4.93 | | 5.05 | | 5.03 | |
| M44 | Exp. | 4.89 | 12.75% | 6.67 | 3.21% | 6.47 | 1.70% | 5.42 | 11.33% |
| | Predicted | 5.60 | | 6.46 | | 6.36 | | 6.11 | |
| M46 | Exp. | 6.16 | 8.71% | 8.11 | 6.11% | 7.21 | 1.72% | 6.08 | 11.90% |
| | Predicted | 6.75 | | 7.64 | | 7.34 | | 6.90 | |
| M48 | Exp. | 9.08 | 9.93% | 9.70 | 4.44% | 8.94 | 2.09% | 7.56 | 9.54% |
| | Predicted | 8.26 | | 9.29 | | 8.76 | | 6.90 | |

Rev. IBRACON Estrut. Mater., vol. 14, no. 5, e14503, 2021

11/14

In order to verify if the equations obtained in this work were able to estimate the residual flexural strengths in SFRSCC with compressive strengths outside the range of this work's database, the predicted residual flexural strengths were calculated using the equations obtained in this paper for some of the concretes produced in Lameiras [26], shown in Table 7, and compared with the experimental results he obtained.

**Table 7.** Properties of hooked steel fiber and compressive strength of concretes mix used by Lameiras [26].

| Concrete Mixture | $f_c$ [MPa] | l [mm] | d [mm] | l/d | Fiber volume content (%) |
|---|---|---|---|---|---|
| 10 | 45.60 | 35 | 0.55 | 63.64 | 0.75 |
| 11 | 56.39 | 35 | 0.55 | 63.64 | 0.75 |
| 12 | 61.23 | 35 | 0.55 | 63.64 | 0.75 |
| 13 | 61.94 | 35 | 0.55 | 63.64 | 0.75 |
| 16 | 60.66 | 35 | 0.55 | 63.64 | 0.75 |
| 17 | 63.46 | 35 | 0.55 | 63.64 | 0.75 |
| 18 | 54.81 | 35 | 0.55 | 63.64 | 0.75 |
| 19 | 64.83 | 35 | 0.55 | 63.64 | 0.75 |

Based on the results described in Table 8, it is possible to observe that none of the concretes fits well in the equations found in this work, showing that they are not applied satisfactorily in concretes with compressive strength outside the range studied in this research, which was 20 MPa at 40 MPa. Mixture 10 presented compressive strength close to the values used in the regressions that provided the equations. However, it also presented high errors, on average of 15%, although smaller when compared to the other concrete mixtures produced by Lameiras [26].

**Table 8.** Comparison between the values of residual flexural strengths found experimentally by Lameiras [26] and with predicted by the equations.

| Concrete Mix | | Experimental data obtained by Lameiras et al. (2015) *vs.* Values predicted by the proposed equations | | | | | | | |
|---|---|---|---|---|---|---|---|---|---|
| | | $f_{R.1}$ [MPa] | Error $f_{R.1}$ | $f_{R.2}$ [MPa] | Error $f_{R.2}$ | $f_{R.3}$ [MPa] | Error $f_{R.3}$ | $f_{R.4}$ [MPa] | Error $f_{R.4}$ |
| 10 | Exp. | 9.21 | 24.95% | 8.11 | 4.03% | 6.82 | 15.84% | 5.70 | 24.35% |
| | Predicted | 7.37 | | 8.45 | | 8.10 | | 7.54 | |
| 11 | Exp. | 8.22 | 2.84% | 7.13 | 27.40% | 5.42 | 42.46% | 4.13 | 52.41% |
| | Predicted | 8.46 | | 9.82 | | 9.42 | | 8.68 | |
| 12 | Exp. | 7.44 | 16.55% | 6.67 | 35.81% | 5.52 | 44.63% | 4.61 | 49.64% |
| | Predicted | 8.91 | | 10.39 | | 9.97 | | 9.15 | |
| 13 | Exp. | 6.82 | 24.05% | 6.25 | 40.33% | 5.38 | 46.45% | 4.69 | 49.15% |
| | Predicted | 8.98 | | 10.47 | | 10.05 | | 9.22 | |
| 16 | Exp. | 6.67 | 24.74% | 5.97 | 42.18% | 5.26 | 46.90% | 4.54 | 50.10% |
| | Predicted | 8.86 | | 10.33 | | 9.91 | | 9.10 | |
| 17 | Exp. | 8.39 | 7.99% | 7.59 | 28.71% | 6.52 | 36.17% | 5.66 | 39.58% |
| | Predicted | 9.12 | | 10.65 | | 10.21 | | 9.37 | |
| 18 | Exp. | 8.36 | 0.63% | 7.47 | 22.42% | 6.40 | 30.70% | 5.59 | 34.37% |
| | Predicted | 8.31 | | 9.63 | | 9.24 | | 8.52 | |
| 19 | Exp. | 6.62 | 28.37% | 6.01 | 44.36% | 5.16 | 50.21% | 4.55 | 46.58% |
| | Predicted | 9.24 | | 10.80 | | 10.36 | | 8.52 | |

Analysing the concretes produced by Venjareshwaran et al. [12] and Lameiras [26], it is possible to verify that the equations are satisfactorily valid when used in concretes fiber content and compressive strength within those in the range of the SFRSCCs studied in this paper. That is, for fiber contents from 0.00% to 1.00%, in SFRSCC with

Rev. IBRACON Estrut. Mater., vol. 14, no. 5, e14503, 2021

12/14

compressive strength from 20 MPa to 40 MPa. When the compressive strength and fiber content were outside these ranges, the errors found in the experimental and analytical comparison were very high.

Analysing the comparison of the predicted residual strengths with the obtained experimentally for the concretes produced by Venjareshwaran et al. [12] and Lameiras [26], it is possible to verify that, when the equations are used in the content of concrete fibers and in the compressive strength within the ranges of the SFRSCCs studied in this work, despite relatively high errors, the equations provided an indication of the residual resistances that have been reached. That is, for fiber contents from 0.50% to 1.00%, in the SFRSCC with compressive strength from 20 MPa to 40 MPa, the equations can be used to estimate the residual strength of concrete based on the materials used in the SFRSCC. However, for a more technical and rational application, further studies need to be carried out in order to optimize the equations and reduce errors.

## 4 CONCLUSIONS

An experimental study was performed to examine the direct residual flexural strengths of Steel Fiber Reinforced Self Compacting Concrete specimens with two compressive strengths, 20 and 40 MPa, and fiber volume factions, 0.50% and 1,00%. The experimental program included tests of 96 specimens: 48 small beams for the three point bending tests and 48 cylindrical specimens for compressive strength test. Variables of the experimental program were the type of fibers, the fiber volume content and concrete strengths. The main conclusions were:

1. Regarding the behavior of concrete in the hardened state, small reductions in compressive strength were observed in 40 MPa concrete with ST-33/44 fibers.
2. The fibers ST-33/60 and ST-50/67 were the ones that led to the greatest increases in residual flexural strength of SFRSCC. This can be explained by the larger form factor of the two fibers (60 and 67), respectively. In the case of the ST-50/67 fiber, the importance of the fiber length can still be emphasized, ensuring greater anchorage in the concrete and, consequently, greater efficiency. The worst result was found for the concrete with ST-33/44 fiber, which can be explained by the fact that the fiber has a shorter length and aspect ratio (44).
3. The proposed equations, obtained based on the experimental data of this work to determine the residual resistance of the SFRSCC, reached an average error of 10% in relation to the experimental results. The errors were relatively high; however, the equations can be adopted to initially estimate residual resistances. However, studies seeking to minimize errors must be carried out.
4. When compared to the results obtained by Venkashwaran et al. [12] it was found that, when the variables (matrix strength, fiber geometric characteristics and fiber volume) are similar to those used in this work, with variations within the ranges adopted in this research, the estimated results had average errors around 10%.
5. When compared to the results obtained by Lameiras [26], it was found that, when the fiber content and the compressive strength of the matrix were outside the varied limits in this study, the errors were high, and it is not possible to use the equations of this work to estimate the residual strengths of these concretes.

## 5 REFERENCES

[1]   S. Grünewald, *Performance-Based Design of Self-Compacting Fibre Reinforced Concrete*. Delft: Delft Univ. Technol., 2004.

[2]   L. Ferrara and A. Meda, "Relationships between fibre distribution, workability and the mechanical properties of SFRC applied to precast roof elements," *Mater. Struct.*, vol. 39, no. 4, pp. 411–420, 2007.

[3]   A. C. Barros, "Avaliação do comportamento de vigas de concreto auto-adensável reforçado com fibras de aço," M.S. thesis, Univ. Fed. Alagoas, Maceió, 2009.

[4]   R. Lameiras, J. Barros, I. B. Valente, and M. Azenha, "Development of sandwich panels combining fibre reinforced concrete layers and fibre reinforced polymer connectors. Part I: conception and pull-out tests," *Compos. Struct.*, vol. 105, pp. 446–459, 2013.

[5]   J. Hedebratt and J. Silfwerbrand, "Full-scale test of a pile supported steel fibre concrete slab," *Mater. Struct.*, vol. 47, no. 4, pp. 647–666, 2014.

[6]   H. Salehian and J. A. Barros, "Assessment of the performance of steel fibre reinforced self-compacting concrete in elevated slabs," *Cement Concr. Compos.*, vol. 55, pp. 268–280, 2015.

[7]   H. Ahmad, "Steel Fibre Reinforced Self-Compacting Concrete (SFRSC) performance in slab application: a review,"*AIP Conf. Proc.*, vol. 1774, 030024, 2016.

[8]   D. Y. Yoo, Y.-S. Yoon, and N. Banthia, "Predicting the post-cracking behavior of normal- and high-strength steel-fiber-reinforced concrete beams," *Constr. Build. Mater.*, vol. 93, pp. 477–485, 2015.

[9]   K. Mak and A. Fam, "Freeze-thaw cycling effect on tensile properties of unidirectional flax fiber reinforced polymers," *Compos., Part B Eng.*, vol. 174, pp. 106960, 2019, http://dx.doi.org/10.1016/j.compositesb.2019.106960.

[10] C. Lin, O. Kayali, E. V. Morozov, and D. J. Sharp, "Influence of fibre type on flexural behaviour of self-compacting fibre reinforced cementitious composites," *Cement Concr. Compos.*, vol. 51, pp. 27–37, 2014.

[11] J. H. Lee, B. Cho, and E. Choi, "Flexural capacity of fiber reinforced concrete with a consideration of concrete strength and fiber contente," *Constr. Build. Mater.*, vol. 138, pp. 222–231, 2017.

[12] A. Venkateshwaran, K. H. Tan, and Y. Li, *Residual Flexural Strengths of Steel Fiber Reinforced Concrete with Multiple Hooked-End Fibers*. Lausanne: International Federation for Structural Concrete, 2018.

[13] W. Abbass, M. I. Khan, and S. Mourad, "Evaluation of mechanical properties of steel fiber reinforced concrete with different strengths of concrete," *Constr. Build. Mater.*, vol. 168, pp. 556–569, 2018.

[14] J. Domski and J. Katzer, "Comprehensive approach to evaluation of mechanical properties of waste aggregate concrete reinforced by steel fiber," *Struct. Concr.*, vol. 21, no. 1, pp. 428–436, 2020, http://dx.doi.org/10.1002/suco.201800271.

[15] International Union of Laboratories and Experts in Construction Materials, Systems and Structures, "Recommendations of RILEM TC 162-TDF: Test and design methods for steel fibre reinforced concrete Design of steel fibre reinforced concrete using the sigma-epsilon method: principles and applications," *Mater. Struct.*, vol. 35, no. 249, pp. 262–278, 2002.

[16] F. De Larrard and T. Sedran. "Formation à BétonlabPro 3: 15 leçonst." IFSTTAR. https://betonlabpro.ifsttar.fr/betonlabpro/formation-a-betonlabpro-3-didacticiel/ (accessed Mar. 5, 2016).

[17] Associação Brasileira de Normas Técnicas, *Concreto Autoadensável*, NBR 15823, 2017.

[18] Associação Brasileira de Normas Técnicas, *Concreto – Ensaio de Compressão de Corpos de Prova Cilíndricos*, NBR 5739, 2018.

[19] J. F. Correal and C. A. Herrána, "Performance of hybrid fiber-reinforced concrete for low-rise housing with thin walls," *Constr. Build. Mater.*, vol. 185, pp. 519–529, 2018.

[20] H. Hu, Z. Wang, F. P. Figueiredo, P. Papastergiou, M. Guadagnini, and K. Pilakoutas, "Postcracking tensile behavior of blended steel fiber-reinforced concrete," *Struct. Concr.*, vol. 20, no. 2, pp. 707–719, 2019.

[21] N. Banthia, F. Majdzadeh, J. Wu, and V. Bindiganavile, "Fiber synergy in Hybrid Reinforced Concrete (HyFRC) in flexure and direct shear," *Cement Concr. Compos.*, vol. 48, pp. 91–97, 2014.

[22] J. Carrillo, J. A. Pincheira, and S. M. Alcocer, "Behavior of low-rise, steel fiber-reinforced concrete thin walls under shake table excitations," *Eng. Struct.*, vol. 138, no. 1, pp. 146–158, 2017.

[23] A. Conforti, F. Minelli, G. Plizzari, and G. Tibert, "Comparing test methods for the mechanical characterization of fiber reinforced concrete," *Struct. Concr.*, vol. 19, no. 3, pp. 656–669, 2017.

[24] W. Abbass, M. I. Khan, and S. Mourad, "Evaluation of mechanical properties of steel fiber reinforced concrete with different strengths of concrete," *Constr. Build. Mater.*, vol. 168, pp. 556–569, 2018.

[25] A. K. H. Kwan and S. H. Chu, "Direct tension behaviour of steel fibre reinforced concrete measured by a new test method," *Eng. Struct.*, vol. 176, no. 1, pp. 324–336, Dec 2018., http://dx.doi.org/10.1016/j.engstruct.2018.09.010.

[26] R. M. Lameiras, "Sandwich structural panels comprising thin-walled SFRSCC and GFRP connectors: from material features to structural behaviour," Ph.D. dissertation, Univ. Minho, 2015.

# IBRACON Structures and Materials Journal
## Revista IBRACON de Estruturas e Materiais

ORIGINAL ARTICLE

# Structural analysis of pile cap as onshore wind turbine foundation

*Análise estrutural de blocos sobre estacas como fundação para aerogerador onshore*

Kaique Yuri Marcio Araújo[a]

Rodrigo Barros[b]

Joel Araújo Nascimento Neto[b]

[a]Instituto Federal de Educação, Ciência e Tecnologia do Rio Grande do Norte – IFRN, Campus Mossoró, Mossoró, RN, Brasil

[b]Universidade Federal do Rio Grande do Norte – UFRN, Programa de Pós-graduação em Engenharia Civil – PEC, Natal, RN, Brasil

**Abstract:** This paper analyzes the structural behavior of reinforced concrete pile caps as onshore wind turbine foundations using eight models based on the finite element method (FEM). The variables adopted are: the type of finite element utilized; the soil representation; and, considering or not the soil under the pile cap base. All materials constituting the models were considered as linear elastic behavior. The results of interest are: reaction in piles; dividing the load between soil and piles; pile cap displacement; normal radial stress and bending moments in the pile cap. The models designed on solid elements and shell elements demonstrated good compatibility between the found values, such as dividing the load between soil and piles. In some models, the numerical analysis showed results against the structural safety of the foundation when the soil under the pile cap is not considered.

**Keywords:** pile cap, wind turbine foundation, structural analysis, finite element method.

Resumo: Este artigo analisa o comportamento estrutural de blocos de concreto armado sobre estacas como fundações de aerogeradores onshore por meio de oito modelos baseados no Método dos Elementos Finitos. Foram adotadas como variáveis: o tipo de elemento finito utilizado; o tipo de representação do solo; e, a consideração ou não da resistência do solo sob a base do bloco. Os materiais foram tratados com modelos constitutivos de comportamento elástico linear. Os resultados de interesse foram: reações nas estacas; divisão do carregamento entre o solo e as estacas; deslocamento do bloco; tensões normais radiais e momentos fletores no bloco. Na comparação entre os modelos em elementos sólidos e elementos de casca foi observado que houve boa compatibilidade entre os valores encontrados, tais como divisão do carregamento entre solo e estacas. Em alguns modelos, as análises numéricas revelaram resultados que podem ser contra a segurança estrutural da fundação, quando não se considera a presença do solo sob a base do bloco.

**Palavras-chave:** bloco sobre estacas, fundação de aerogerador, análise estrutural, método dos elementos finitos.

# 1 INTRODUCTION

The expanding wind energy industry in Brazil has required large size foundation projects, which in most cases are pile caps. The construction of these structural elements demands more than 300 cubic meters of concrete and 20 tons of steel. In this context, a deeper analysis of these RC foundations can collaborate with the improvement of these projects, which are especially relevant for developing the Brazilian energy matrix.

In this regard, the early studies of structural analysis of wind turbines focused on the dynamic analysis of offshore wind turbines and were essential for the calibration of theoretical curves of lift and drag coefficients, such as in Sinclair and Clayton [1].

van der Tempel and Molenaar [2] carried out an analytical study of real situations of offshore wind turbines under the action of waves, based on the theory of dynamic analysis, and concluded that more flexible structures are cheaper, but the dynamics phenomena need to be treated with more attention.

Adhikari and Bhattacharya [3] analyzed the vibration of offshore wind turbines, including the contribution of the foundation. They compared analytical models, analogous to the Euler-Bernoulli beam, with an experimental model, and showed that the natural frequency of the tower decreases with the reduction of the foundation stiffness and with increased axial load.

The improvement of personal computers and the advent of the Finite Element Method (FEM) allowed to carry out analyses with robust numerical models, such as the study of Satari and Hussain [4], which compared the vibration frequency of wind turbines with shallow and deep foundations.

Moura et al. [5] used geotechnical data from a dune soil (from two beaches on the coast of the state of Ceará, Brazil) to estimate the natural vibration frequency of a shallow foundation of 500 kW wind turbine using different analytical methods. In that study, the estimates for natural vibration frequency ranged from 385 to 1529 rpm.

Ribeiro et al. [6] analyzed the fatigue in shallow and deep foundations of wind turbines based on FEM and concluded that the fatigue considerations used in bridge designs can be extended to the design of wind turbine foundations, considering the specific aspects of these structures.

Araújo et al. [7] evaluated spread footing as wind turbines foundation, comparing numerical models built with shell and solid elements, and showed the importance of solid models to analyze stress field of the structural element of the foundations.

Maranhão [8] analyzed the rotational stiffness of a deep foundation (piles) as support for an onshore wind turbine through different finite element numerical models and proposed an analytical model for calculating the rotational stiffness for the type of foundation analyzed.

Within this context, this paper aims to make a comparison between numerical models of circular pile cap, as foundation for onshore wind turbines, by FEM. The focus of this study is to evaluate the compatibility of the structural behavior of pile caps in some models based on FEM, especially when considering the resistance of the soil in contact with the base of the pile cap.

## 1.1 Pile caps for wind turbines

In the design of pile caps, structural engineers usually do not consider the contribution of the pile cap base in contact with soil. However, in cases of large size pile caps, like the bases of onshore wind turbines, the direct load transmission of this element to the ground can be relevant, which becomes a mixed foundation, distributing the loads to the soil both by the base of the pile cap and by the pile group.

The main problem to design pile caps when considering a mixed system, that is, considering the contribution of the soil under the base of the pile cap, regards evaluating its real functioning mechanism, where it is difficult to accurately represent, using analytical models (strut-and-tie or classical beam theory), the complex behavior of this structural system, as well as its physical configuration at rupture.

## STRUCTURAL DESCRIPTION

Static analysis of RC circular pile caps was performed using the ANSYS and SAP2000 software, based on FEM, considering linear elastic behavior of the constitutive material of the models. Twenty-four piles were distributed around the pile cap. The models were developed with and without the soil under the pile cap base.

For the models developed using ANSYS, the soil was represented by a continuous medium, while for the models developed using SAP2000, they were modeled according to the Winkler approach.

When the soil was represented by a continuous medium, it was modeled as a solid with a linear elastic behavior.

According to Velloso and Lopes [9], the Winkler approach establishes that the reactive pressure is proportional to the spring deflection, in a direct relation. What defines the magnitude of this relationship is the so-called "modulus of subgrade reaction", represented by $k_v$.

In this paper, a unique geometry was considered as a reference to design all models created on both the ANSYS and the SAP2000. The pile cap has a diameter (D) of 14.50 m, with 24 piles distributed around a circle with a diameter ($D_{pile}$) of 13.00 m. The pedestal, the central part of the pile cap, has a height (H) of 3.00m and a diameter of 6.00 m.

Rev. IBRACON Estrut. Mater., vol. 14, no. 5, e14504, 2021

2/14

The tilted part of the pile cap has a varying height from (h0) 1.20 m to (h1) 1.80 m, as shown in Figure 1. The pile cap is supported on 24 piles of 41 cm diameter, resulting in a cross-section area of 1,320.25 cm$^2$, and a length of 10.00 m.
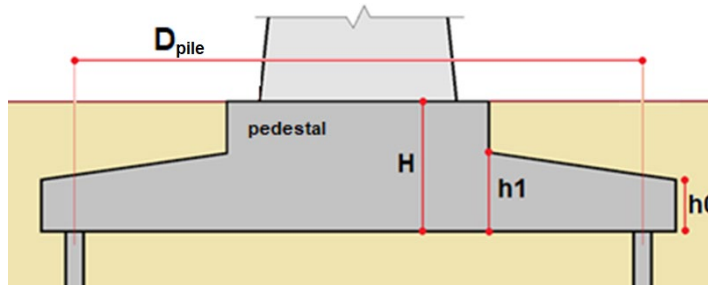


**Figure 1.** Geometry of the pile cap.

The ANS models used piles with polygonal cross section (with an area of 2,126.60 cm$^2$) to make the finite element meshes compatible with the different components of the model, as shown in Figure 2. As a result, it was necessary to reduce the pile modulus of elasticity ($E_{cs,pile}$) 1.61 times (ratio between the pile cross section areas: 2,126.60/1,320.25) to equalize the axial deformations in both cases.
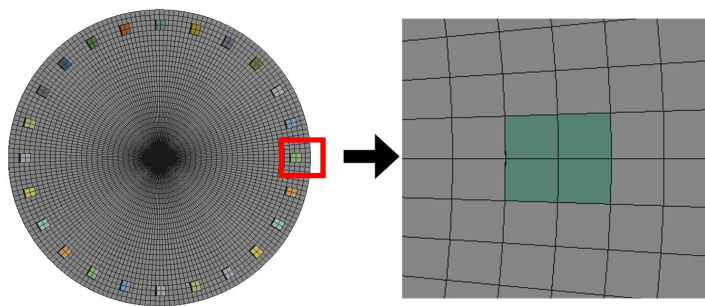


**Figure 2.** Detail of piles with polygonal cross section for all ANS models.

Figure 3 shows the model made on the ANSYS, in which the soil was modeled by a cylindrical soil mass (diameter of 30 m and height of 30 m). Such dimensions were adopted based on Love's proposition [10] for the Boussinesq method, which shows that the addition of vertical stress in the soil at a depth of 2D, induced by a uniformly distributed load (p) in a circular area (of diameter D), is in the order of 0.05p, and the horizontal stress increment spreads radially up to 1.5D from the center of the load. Furthermore, the vertical domain of the soil mass is three times the length of the piles, which is considered reasonable.
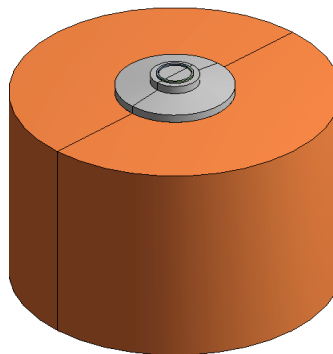


**Figure 3.** Cylindrical soil mass for the ANS-S1, ANS-S2 and ANS-S3 models.

Rev. IBRACON Estrut. Mater., vol. 14, no. 5, e14504, 2021

3/14

For all models, a ring with rigid behavior was used only at the cross section of the pile cap-tower, called in this paper as the "load ring", to minimize the stress concentration due to the loads coming from the wind tower, as well as to represent the high stiffness of the tower wall. This ring is 4.25 m internal diameter and 4.50 m external diameter.

Eight finite elements models were produced for the numerical simulation, all based on the same reference geometry previously presented, four using ANSYS and four using SAP2000. Table 1 summarizes the characteristics of the models, indicating the type of finite element used, as well as the support conditions considered.

**Table 1.** Models' characteristics.

| Models | Software | Finite elements | | |
|---|---|---|---|---|
| | | Pile Cap | Pile | Soil |
| ANS-S0 | ANSYS | Solid | Solid | - |
| ANS-S1 | ANSYS | Solid | Solid | Solid: $E_{soil,1}$ |
| ANS-S2 | ANSYS | Solid | Solid | Solid: $E_{soil,2}$ |
| ANS-S3 | ANSYS | Solid | Solid | Solid: $E_{soil,3}$ |
| SAP-S0 | SAP2000 | Shell | Spring | - |
| SAP-S1 | SAP2000 | Shell | Spring | Elastic Base: $k_{v1}$ |
| SAP-S2 | SAP2000 | Shell | Spring | Elastic Base: $k_{v2}$ |
| SAP-S3 | SAP2000 | Shell | Spring | Elastic Base: $k_{v3}$ |

The concrete parameters were adopted according to the recommendations of the ABNT NBR 6118:2014 [11], where the Poisson's ratio was (v) 0.20 and the secant modulus of elasticity: $E_{cs,pc}$= 27,000 MPa (for C30 concrete), for the pile cap; and, $E_{cs,pile}$= 21,000 MPa (for C20 concrete), for the piles. The pile secant modulus of elasticity was adjusted for the ANS models, considering the cross section was modeled as polygonal shape, to $E_{(cs,pile')}$= 13,043.48 MPa.

For the SAP models, the piles were modeled as elastic supports, with spring coefficient $k_{pile}$ 277,253.41 kN/m, equivalent to a pile of: diameter of 41 cm, length of 10 m and a concrete secant modulus of elasticity of $E_{cs,pile}$= 21,000 MPa. As the objective of this paper is to evaluate the pile cap structural behavior, this simplification was used, which does not consider foundation settlement from the geotechnical element.

Poisson's ratio of v=0.35 was considered for the soil in all models.

For the ANS-S1, ANS-S2 and ANS-S3 models the modulus of elasticity adopted for the soil ($E_{soil}$) is as follows:
- $E_{soil,1}$ = 20 MPa (loose sand);
- $E_{soil,2}$ = 50 MPa (medium sand);
- $E_{soil,3}$ = 100 MPa (dense sand).

The modulus of elasticity for the soil was defined based on the values suggested by Poulos [12], Poulos and Davis [13] and Teixeira and Godoy [14]. Equation 1 was used as proposed by Boussinesq [15], to correlate the modulus of subgrade reaction ($k_v$) with the modulus of elasticity ($E_{soil}$), for the soil. It is worth mentioning that the modulus of subgrade reaction is not a property of the soil, as it depends on the geometry of the foundation.

$$k_v = \frac{2 \cdot E_s}{R \cdot \pi \cdot \left(1 - v^2\right)} \tag{1}$$

Thus, for the SAP-S1, SAP-S2 and SAP-S3 models the modulus of subgrade reaction for the soil ($k_v$) adopted is as follows:
- $k_{v1}$ = 2,000 kN/m³ (loose sand);
- $k_{v2}$ = 5,000 kN/m³ (medium sand);
- $k_{v3}$ = 10,000 kN/m³ (dense sand).

## MODELING AND ANALYSIS

Similar physical and geometric characteristics were adopted for numerical modeling in both software, such as: geometry, loading and mechanical parameters of the concrete. The difference was in the types of finite elements used for the models in each of the software, where solid elements were used on the ANSYS and shell elements on the

SAP2000. It is worth mentioning that only the pile caps modeled with solid elements shows the stress field in three dimensions, which can useful to define a strut-and-tie model.

As the model with shell elements is simpler to make and to process than the model with solid elements, which requires higher computational effort, there was interest in studying the influence of the choice of the finite element type on the results of: reaction in piles; bending moment, pile cap stress and displacement; as well as performing a comparative analysis about the influence of soil modeling as a spring set compared to a model that simulates the continuous medium.

For the ANS models, six and eight nodes solid elements were used to model all components (pile cap, piles and soil). For the ANS-S0 model, there was no soil under the pile cap base. For the ANS-S1, ANS-S2 and ANS-S3 models the soil was modeled as a cylindrical soil mass made with solid elements. For all ANS models, the structural element of the foundation (pile cap + piles) was modeled with solid elements.

Table 2 shows the contact types, as well as their behaviors, available on the ANSYS. Thus, we adopted the contact types for the ANS models as follows: 1) *bonded*: for pile cap-piles and pile cap-loading ring; and, 2) *frictionless*: for soil-pile cap and soil-piles.

**Table 2.** Contact types and behaviors in Ansys.

| Contact types | Behavior | |
|---|---|---|
| | Gap | Sliding |
| Bonded | No | No |
| No Separation | No | Yes, $\mu = 0$ |
| Rough | Yes | No, $\mu = \infty$ |
| Frictionless | Yes | Yes, $\mu = 0$ |
| Frictional | Yes | Yes, $\mu > 0$ |

$\mu$: coefficient of friction (dimensionless scalar value)

For the ANS-S1, ANS-S2 and ANS-S3 models, the axial pile capacity, composed by side friction and end-bearing resistance, was taken as a single resistance at the pile tip to maximize the actions of the pile cap base. This is because if the side friction was considered, the piles would become more rigid and, consequently, they would receive a larger part of the loads, reducing the part that would go directly to the soil under the pile cap base. Thus, a fixed support was defined at the bottom tip of all 24 piles (this situation is possible, for example, when piles are supported on rocks), as well as at the base of the cylindrical soil mass, restricting displacements and rotations.

For the ANS models, a finite element mesh of 25 cm (average spacing between nodes) was used for the pile cap, piles (only in the cross-section plane) and cylindrical soil mass (only under the pile cap). In addition, a mesh of 250 cm vertical space and 100 cm horizontal space was defined for the soil mass around of the pile cap. The same vertical space was used for the piles. Figure 4 shows the details of discretization for the ANS models.
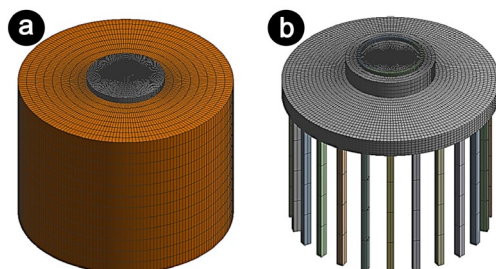


**Figure 4.** Discretization of the ANS models: detail of cylindrical soil mass (a); detail of pile cap (b).

For the SAP models, three and four node shell elements (thin plate type) were used to model the pile cap. The piles were modeled as discrete springs with linear elastic behavior in the vertical direction and set in the horizontal plane. For the SAP-S1, SAP-S2 and SAP-S3 models the soil was modeled as an elastic base, that is, with a group of compression only springs. For all these models, rigid constrains were used in the nodes of the load ring region. For the SAP models, a finite element mesh of 25 cm was utilized, in the radial direction, and varying from 0 to 95 cm in the tangential direction. Figure 5 shows the discretization details for the SAP models.
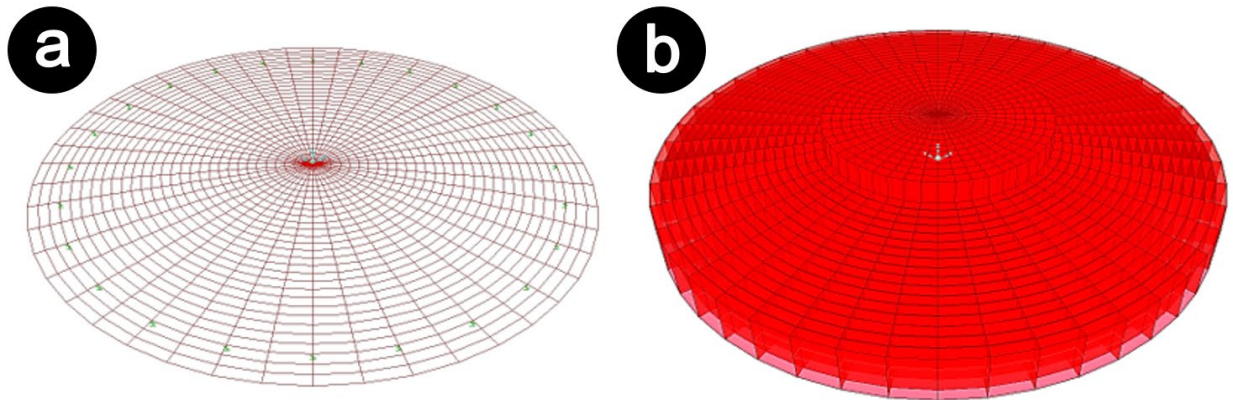
**Figure 5.** Discretization of pile cap for all the SAP models: standard view (a); extruded (b).

For this paper, typical loads of 2 to 3 MW wind turbines were adopted. The loads acting on the foundation are: horizontal force $F_{xy}$ (referring to the result of horizontal forces acting on the XY plane); moment $M_{xy}$ (resulting from the moments acting around X and Y axes) and vertical force $F_z$ due to gravitational loads.

Table 3 presents the characteristic values adopted for the loads acting on the pile cap due to the wind turbine of 86 m rotor diameter and 80 m height (steel tower), as well as the loads that act on it in a power generation situation with extreme wind speed, with a 50-year recurrence period. In addition to these loads, a specific weight of 24 $kN/m^3$ was considered for the pile cap concrete and 16 $kN/m^3$ for the landfill. Thus, the self-weight of the pile cap resulted in 6,826 kN and the landfill weight on it was 1,957 kN.

**Table 3.** Loads acting on the pile cap due to the wind turbine and loads that act on it in a power generation situation with extreme wind speed, with a 50-year recurrence period.

| Type of loads | Operational loads | Extreme loads |
|---|---|---|
| Vertical force - $F_z$ (kN) | 2417 | 2478 |
| Horizontal Force - $F_{xy}$ (kN) | 376 | 622 |
| Moment - $M_{xy}$ (kN·m) | 26918 | 45066 |

Note: The self-weight of the pile cap and the landfill weight are not accounted in the table above.

To simplify the analysis, without damaging the research objectives, all the loads considered (vertical and horizontal force, moment, self-weight and landfill weight) were combined with their characteristic values, that is, with partial factor for loads of $\gamma_{fi} = 1.00$.

The moment considered when the pile cap-tower encountered the block was the total tipping moment ($M_{total}$), which is composed of the sum of the $M_{xy}$ moment and the additional moment caused by the cutting force $F_{xy}$ in relation to the tipping axis of the base, taken as the center of the lower face of the block (O), as shown in Figure 6. Thus, the total moment is given by Equation 2.

$$M_{total} = M_{xy} + F_{xy} \cdot H \tag{2}$$

Applying the values in Equation 2, the total tipping moment results in: $M_{total} = 46,932$ kN·m.
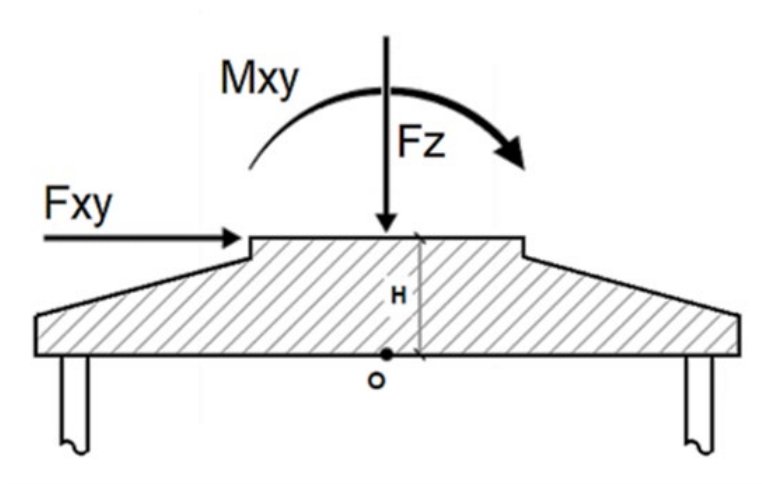
**Figure 6.** Representation of loads transmitted from the wind turbine tower to the pile cap.

The direct action of the horizontal force ($F_{xy}$) was not considered for all models, only considering its tipping effect due to the additional moment ($F_{xy} \cdot H$). This was due to the complexity in calculating the passive earth pressure on the side of the pile cap, as well as the pile cap-soil friction, which would act opposite to the horizontal force. Thus, its application could lead to horizontal reaction in piles that would not be compatible with reality. In addition, the ANS and SAP models present lateral displacement of the pile cap that are very different from each other, due to their particular modeling aspects. That said, the horizontal force was not considered for the sake of a better comparative analysis between all models.

For the SAP models, concentrated loads (representing the action from the tower) were applied on 24 nodes located in the load ring. For the ANS models, the loads were applied directly to the upper surface of the load ring as a distributed load.

The landfill weight was applied as a distributed load over the pile cap (on the surface outside the pedestal), with a value of 14.30 kN/m$^2$.

## 2 RESULTS

Figure 7 shows the numbering defined for the 24 piles, as well as the local axis system (in cylindrical coordinates) used as a reference for all analyses performed in this paper. Axis 3 is in the perpendicular direction to the 1-2 axes plane, in the direction exiting the figure.
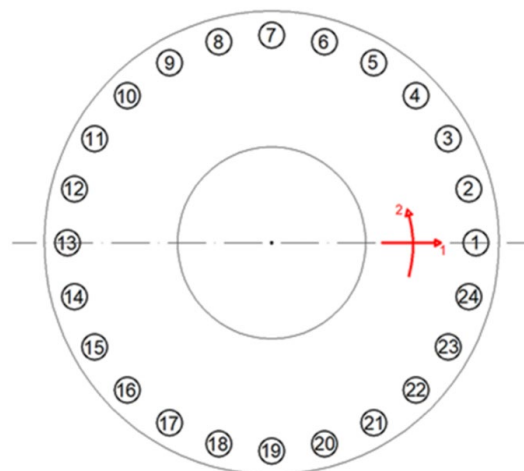


**Figure 7.** Piles numbering and local axis system.

Table 4 presents the results of reaction in piles, obtained for all the models analyzed. The reaction in piles in the "Analytical" column was obtained by an analytical approach, superimposing force and moment applied to the pile cap, using Equation 3, initially proposed by Schiel [16], which is based on the compatibility of displacements, not considering the group effect of the piles. This method is widely used by structural engineers, and recommended by Alonso [17]. It was assumed that the pile cap was infinitely rigid, that the x and y were principal axes and that the piles were all identical and vertical without inclination.

$$R_{pilet,i} = \frac{F_z}{n} + \frac{M_y \cdot x_i}{\sum x_i^2} + \frac{M_x \cdot y_i}{\sum y_i^2} \qquad [3]$$

where:

$R_{pile,i}$ – Vertical reaction in piles for the "i-pile", with $x_i$ and $y_i$ coordinates;

$F_z$ – Resulting vertical force (including the pile cap self-weight and the landfill weight);

$n$ – Number of piles;

$M_x$ – Moment of x-axis;

$M_y$ – Moment of y-axis.

**Table 4.** Reactions in piles obtained by the analytical approach and by the numerical models.

| Pile | Reaction in Piles (kN) | | | | | | | | |
|------|------------|---------|---------|---------|---------|---------|---------|---------|---------|
| | **Analytical** | **ANS-S0** | **ANS-S1** | **ANS-S2** | **ANS-S3** | **SAP-S0** | **SAP-S1** | **SAP-S2** | **SAP-S3** |
| 1 | 1074.70 | 1070.80 | 1014.40 | 936.74 | 830.68 | 1063.41 | 1018.30 | 950.56 | 857.46 |
| 2 | 1054.19 | 1050.30 | 995.04 | 918.95 | 814.98 | 1042.90 | 998.50 | 931.73 | 840.02 |
| 3 | 994.11 | 990.32 | 938.41 | 866.75 | 768.85 | 982.79 | 940.45 | 876.49 | 788.87 |
| 4 | 898.57 | 894.85 | 848.28 | 783.63 | 695.33 | 887.17 | 848.11 | 788.62 | 707.50 |
| 5 | 774.03 | 770.43 | 730.66 | 675.04 | 599.11 | 762.56 | 727.75 | 674.09 | 601.45 |
| 6 | 629.00 | 625.54 | 593.45 | 548.12 | 486.32 | 617.44 | 587.60 | 540.72 | 477.93 |
| 7 | 473.38 | 470.05 | 445.81 | 411.12 | 363.97 | 461.71 | 437.18 | 397.57 | 345.32 |
| 8 | 317.76 | 314.57 | 297.60 | 272.93 | 239.55 | 305.98 | 286.74 | 254.35 | 212.58 |
| 9 | 172.73 | 169.67 | 158.83 | 142.68 | 120.98 | 160.86 | 146.52 | 120.78 | 88.61 |
| 10 | 48.19 | 45.25 | 39.15 | 29.63 | 17.02 | 36.24 | 26.04 | 5.90 | -18.09 |
| 11 | -47.35 | -50.22 | -52.96 | -57.81 | -64.01 | -59.38 | -66.38 | -82.13 | -99.84 |
| 12 | -107.43 | -110.23 | -110.98 | -113.06 | -115.46 | -119.49 | -124.50 | -137.56 | -151.45 |
| 13 | -127.94 | -130.70 | -130.78 | -131.94 | -133.10 | -139.99 | -144.34 | -156.50 | -169.10 |

Figure 8 shows comparisons between the reaction in piles for the corresponding piles in both ANS and SAP models, case by case. This figure presents, as a reference, the reaction in piles obtained by the analytical approach.
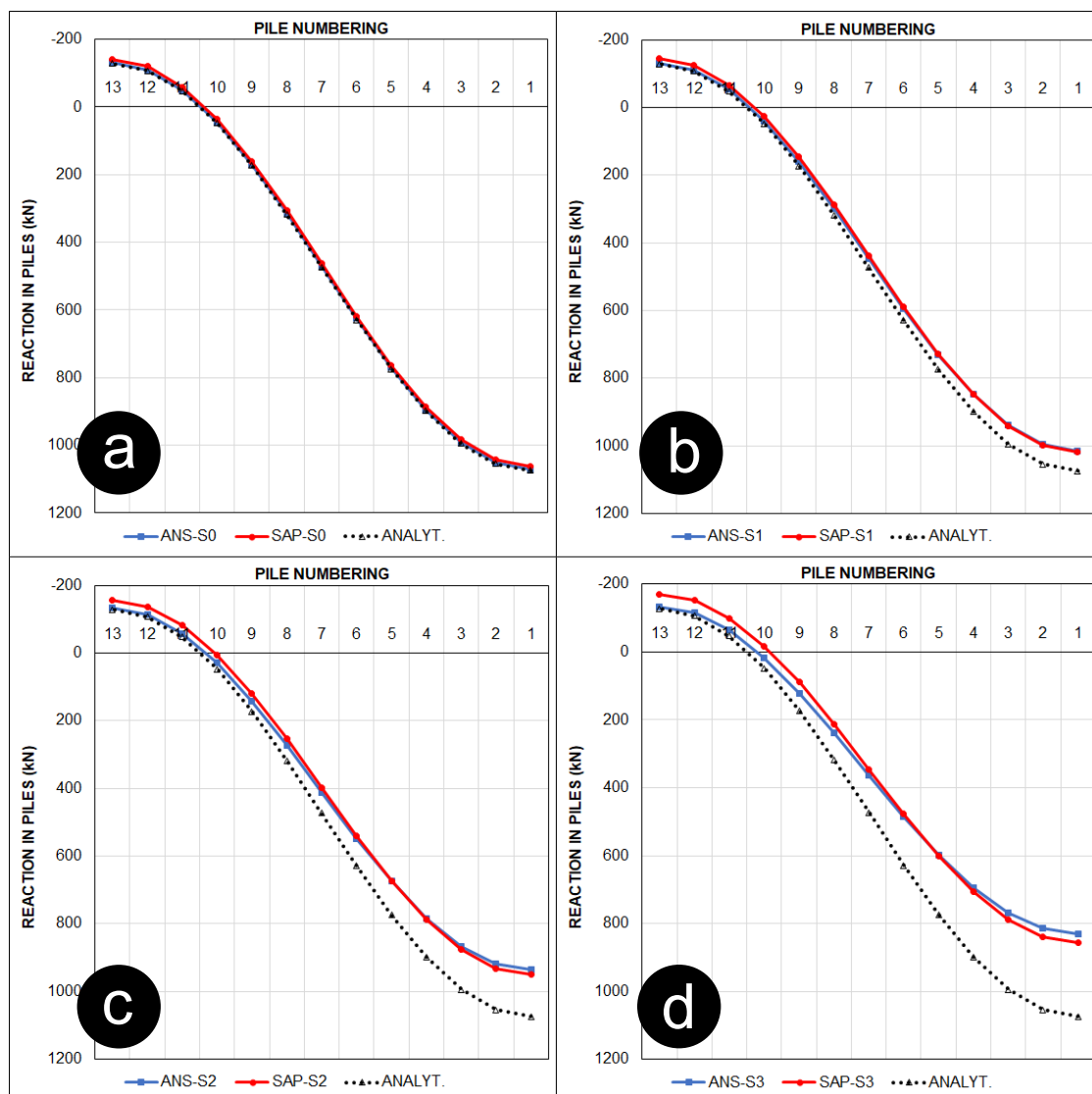
**Figure 8.** Reaction in piles for all the models, presented in equivalent pairs: ANS-S0 and SAP-S0 (a); ANS-S1 and SAP-S1 (b); ANS-S2 and SAP-S2 (c); ANS-S3 and SAP-S3 (d).

Based on Figure 8, it was found that the reaction in piles for the ANS-S0 and SAP-S0 models showed close values to each other, as well as with those calculated by the analytical approach. This was an expected result, considering the assumptions that were adopted in the models. In addition, it was observed that the reaction in piles for the ANS-S1 and SAP-S1 models was also nearly coincidental. In relation to the previous models, the pairs ANS-S2 and SAP-S2, as well as ANS-S3 and SAP-S3, indicated divergences between them, especially for the most tensile and compressed piles. Comparing the ANS-S2 and SAP-S2 models, the second one presented 18.61% higher maximum tensile reaction and 1.48% higher maximum compression reaction (in module). Comparing the ANS-S3 and SAP-S3 models, the second one presented 27.05% higher maximum tensile reaction and 3.22% higher maximum compression reaction (in module).

Based on Figure 8, the SAP models show a tendency to increase the tensile modulus of the reactions in piles 11, 12 and 13 with the increase in soil stiffness. From this perspective, the results presented may be contrary to the structural security of the foundation when the presence of soil under the pile cap base is not considered in the model. This is because the presence of soil under the pile cap causes a decrease in the portion of compressive load that goes directly to the piles, and tensioning at that moment.

Figure 9 shows the sum of reactions in piles for each of the models analyzed in this paper, as well as the sum of reactions in piles obtained by the analytical approach.
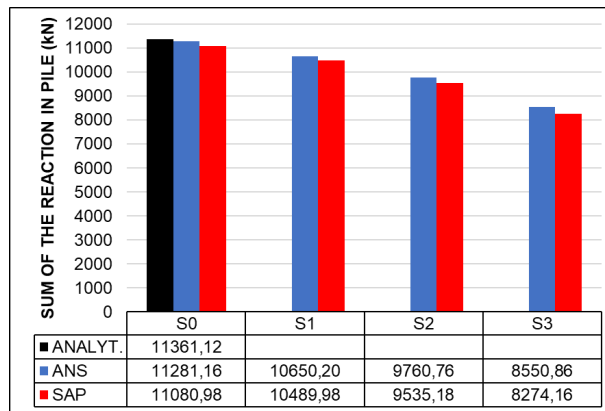
**Figure 9.** Total sum of reactions in piles for all models.

Considering the premises adopted in this paper, Figure 9 shows that the vertical load that goes to the piles is reduced with the increase in soil stiffness, decreasing from 11,281.16 kN in the ANS-S0 model (less soil stiffness) to 8,550.86 kN in the ANS-S3 model (most soil stiffness). Similarly, from 11,080.98 kN in the SAP-S0 model (less soil stiffness) to 8,274.16 kN in the SAP-S3 model (most soil stiffness). This reduction is because a larger portion of the vertical load applied to the pile cap goes directly to the soil with the increase in its stiffness, reducing the fraction destined for the piles. Thus, based on this figure it can be observed that the portion of the load destined to the soil represents a percentage value of (in relation to the models without soil): 5.59%, 13.48% and 24.20%, for the ANS-S1, ANS -S2 and ANS-S3 models, respectively; and 5.33%, 13.95% and 25.33%, for the SAP-S1, SAP-S2 and SAP-S3 models, respectively. These results corroborate the affirmation made earlier that the absence of soil in the model can lead to results that are contrary to safety in the presence of the moments in the system.
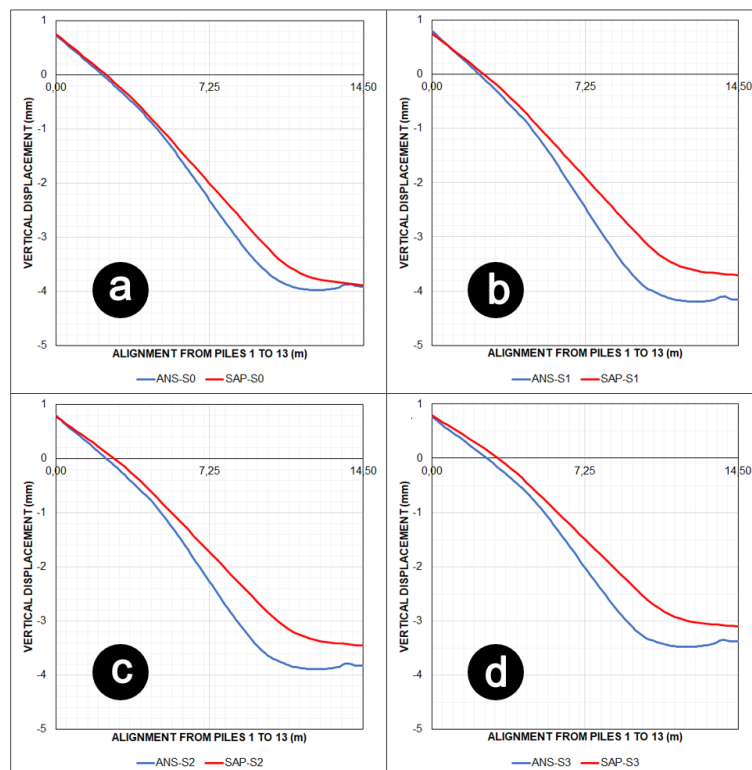


**Figure 10.** Comparisons between pairs of equivalent ANS-SAP models about the vertical displacement of the base of the pile cap long the alignment from piles 1 to 13: ANS-S0 and SAP-S0 (a); ANS-S1 and SAP-S1 (b); ANS-S2 and SAP-S2 (c); ANS-S3 and SAP-S3 (d).

In Figure 10, which shows comparisons between pairs of equivalent ANS-SAP models about the vertical displacement of the pile cap base along the alignment from piles 1 to 13, it is observed that this displacement decreases, in the module, with the increased soil stiffness. It can be verified that the displacements at the left end of the pile cap (0.00 m) presented compatible values for the equivalent ANS-SAP models. At the opposite end (14.50 m), the ANS-S0 and SAP-S0 models showed almost coincidental vertical displacements, while in the other cases, the ANS models indicated vertical displacement in the order of 10%, higher (in the module) than the equivalent SAP models.

Figure 11 shows the normal radial stresses ($S_{11}$) at the base of the pile cap for the ANS-S0 and SAP-S0 models. Figure 12 shows the principal stress vector for the ANS-S0 model in a section of the pile cap along the alignment from piles 1 to 13. This stress field can be used, for example, to support a strut-and-tie model, which cannot be observed in the SAP models.
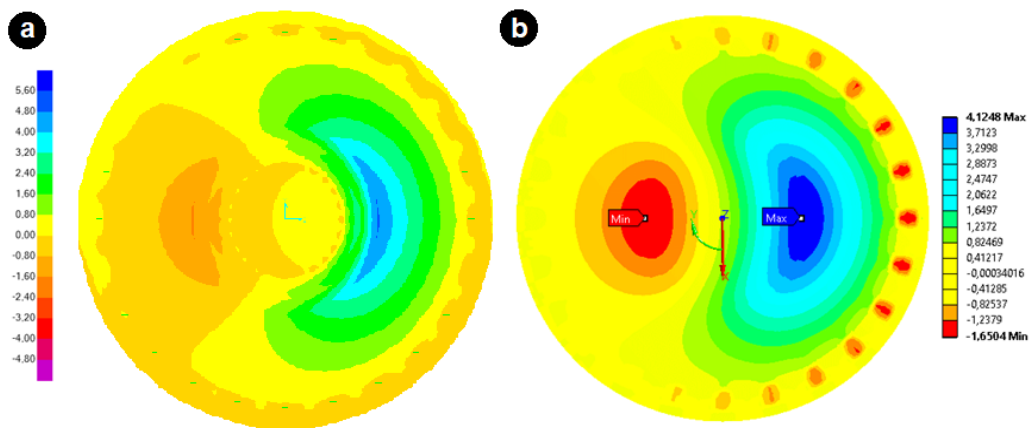


**Figure 11.** Normal radial stresses ($S_{11}$) - in MPa - at the base of the pile cap for the SAP-S0 (a) and ANS-S0 (b) models.

Table 5 summarizes the values of the normal radial stresses at the lower (elevation: 0 m) and upper (elevation: 1.80 m) ends of the pile cap, on the L and R lines, shown previously in Figure 12.

**Table 5.** Comparison between the normal radial stresses (MPa) of all the ANS and SAP models along the alignment from piles 1 to 13.

| Elev. (m) | Normal Radial Stress (MPa) | | | | | | | |
|---|---|---|---|---|---|---|---|---|
| | L | R | L | R | L | R | L | R |
| | ANS-S0 | | ANS-S1 | | ANS-S2 | | ANS-S3 | |
| 1.80 | 3.885 | -9.607 | 3.158 | -7.649 | 3.194 | -7.499 | 3.239 | -7.297 |
| 0.00 | -1.556 | 4.074 | -1.651 | 4.068 | -1.668 | 3.971 | -1.687 | 3.841 |
| | SAP-S0 | | SAP-S1 | | SAP-S2 | | SAP-S3 | |
| 1.80 | 2.037 | -5.596 | 2.075 | -5.491 | 2.162 | -5.310 | 2.262 | -5.067 |
| 0.00 | -2.037 | 5.596 | -2.075 | 5.491 | -2.162 | 5.310 | -2.262 | 5.067 |
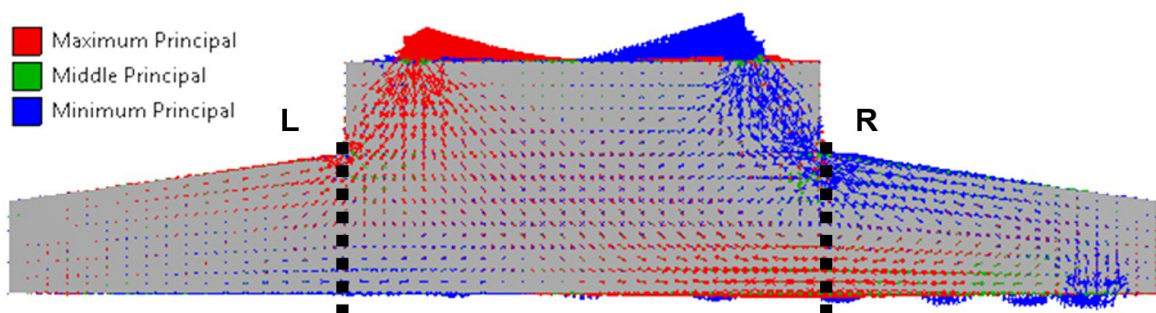


**Figure 12.** Principal stress vector for the ANS-S0 model in a section of the pile cap along the alignment from piles 1 to 13.

Rev. IBRACON Estrut. Mater., vol. 14, no. 5, e14504, 2021

11/14

The stress diagrams of the ANS models, shown in Figure 13, were used to calculate the resulting tensile and compression force, the length of the lever arm and the bending moment. Similarly, Figure 14 shows the equivalent diagrams for the SAP models. Analyzing Figures 13 and 14, it is observed that the normal stress diagrams of the ANS models show a different behavior from the equivalent SAP models in the region above the 1.20 m elevation, especially showing a non-linear stress field above the 1.60m height.
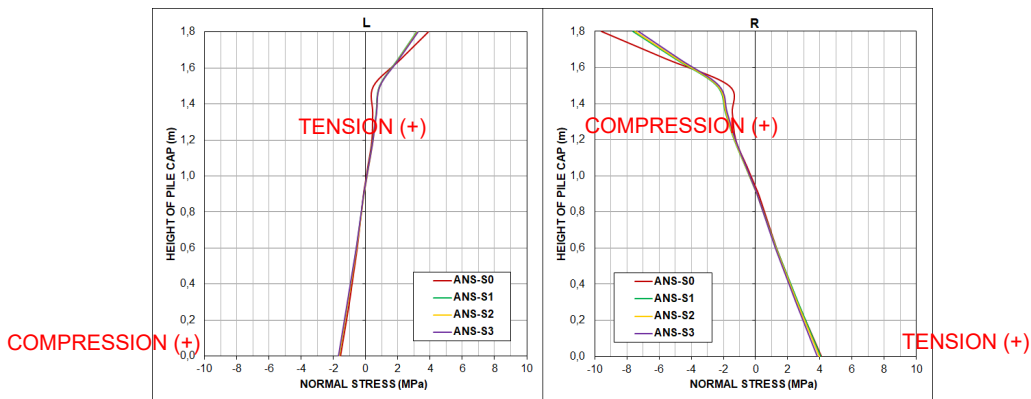


**Figure 13.** Stress diagrams of the ANS models in the L and R lines.
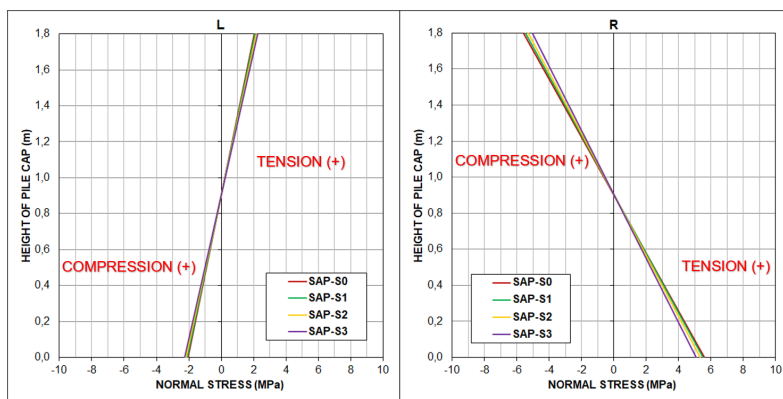


**Figure 14.** Stress diagrams of the SAP models in the L and R lines.

Table 6 shows the bending moments (around axis 2) for the ANS and SAP models, respectively, at the 4.25 and 10.25 m points (points equivalent to L and R lines) along the alignment from piles 1 to 13. The bending moments of the ANS models were obtained by integrating the stress diagrams on the L and R lines. Table 6 shows that the negative bending moments of the ANS models present, on average, values in the order of 92.63% of the equivalent SAP models, with a variation coefficient of 2.84%. For the positive bending moments, the average values of the ANS models are 85.21% of the equivalent SAP models, with a variation coefficient of 1.24%.

**Table 6.** Comparison between the bending moments (kN·m/m) of all the ANS and SAP models along the alignment from piles 1 to 13.

| x (m) | $M_2$ (kN·m/m) | | | | | | | |
|---|---|---|---|---|---|---|---|---|
| | SAP-S0 | ANS-S0 | SAP-S1 | ANS-S1 | SAP-S2 | ANS-S2 | SAP-S3 | ANS-S3 |
| 4.25 / L | -1078.78 | -994.45 | -1098.77 | -1054.27 | -1144.51 | -1062.70 | -1197.65 | -1072.53 |
| 10.25 / R | 2962.97 | 2500.09 | 2907.38 | 2455.51 | 2811.47 | 2399.57 | 2682.79 | 2324.46 |

From the results presented, it can be concluded that the differences observed between the pairs of equivalent models (e.g., ANS-S1 and SAP-S1) were due to the type of finite element used in each of the models, especially for modeling

the soil and the piles, in which the ANS models were modeled with solid elements, whereas in the SAP models they were represented by discrete springs.

The models produced of shell elements and springs instead of solid elements, considerably reducing the computational processing time. On the other hand, because they are more simplified, the SAP models showed more conservative results, indicating higher reaction values in the piles (in module) than those found in the equivalent ANS models, considering the most compressed pile (1) and the pile with the highest tensile strength (13).

## 3 CONCLUSIONS

It was observed that the reactions in the piles for the ANS-S0 and SAP-S0 models presented values close to each other, as well as those calculated by the analytical approach proposed by Schiel [16].

The equivalent ANS and SAP models, with soil, presented similar relative values for the portion of the load destined to the soil: 5.59%, 13.48% and 24.20%, for the ANS-S1, ANS-S2 and ANS-S3 models, respectively; and, 5.33%, 13.95% and 25.33%, for the SAP-S1, SAP-S2 and SAP-S3 models, respectively.

Analyzing the reactions in the piles soliciting more efforts, the SAP models showed more conservative results, indicating values higher than those of the equivalent ANS models. This was due to the more simplified modeling adopted for the soil and for the structural elements (pile cap and piles) for the SAP models. From this perspective, it is recommended that similar pile caps, with relevant discontinuities, and those with higher relative height that are classified as rigid, should be analyzed as a three-dimensional stress problem, as well as propose a strut-and-tie model for analysis and designing based on the stress field.

In some models, the numerical analyses showed results that are contrary to the structural safety of the foundation when the presence of the soil under the pile cap base was not considered, which allows to observe an increasing tensile modulus tendency for the reaction in piles with increasing soil stiffness. This finding was better observed in the SAP models.

It was observed that the discontinued region of the pile cap (between the base and the sloping part) presented a structural behavior which does not apply the classical hypothesis of the flat cross sections of Navier-Bernoulli, due to the great distortions experienced by the structure in this region. This observation was observed through the stress diagrams of the ANS models, which did not show a linear variation along the height of the L and R lines, especially in the pile cap section above the 1.20-m elevation. From this perspective, it is recommended that similar pile caps, with relevant discontinuities, and those with a higher relative height that are classified as rigid, should be analyzed as a three-dimensional stress problem, as well as it is recommended that strut-and-tie models should be used for the analysis and designing based on the stress field.

## ACKNOWLEDGMENTS

## REFERENCES

[1] F. M. Sinclair and B. R. Clayton, "Excitation and damping forces on offshore wind turbines," *Wind Eng.*, vol. 13, no. 6, pp. 276–292, 1989.

[2] J. van der Tempel and D. P. Molenaar, "Wind turbine structural dynamics – a review of the principles for modern power generation, onshore and offshore," *Wind Eng.*, vol. 26, no. 4, pp. 211–220, 2002.

[3] S. Adhikari and S. Bhattacharya, "Dynamic analysis of wind turbine towers on flexible foundations," *Shock Vib.*, vol. 19, pp. 37–56, 2012.

[4] M. A. Satari and S. S. E. Hussain, "Vibration based wind turbine tower foundation design utilizing soil-foundation-structure interaction," in *The 14th World Conf. Earthq. Eng.*, Pequim, China, 2008.

[5] A. S. Moura, S. Dantas, and M. F. P. Aguiar, "A comparative study of vibration frequency estimates of the surface foundations of wind turbines built on the sand dunes of the Ceará coast," *Dewi Magazin*, no. 33, 2008.

[6] A. R. Ribeiro, S. S. Lima, and S. H. C. Santos, "Análise de fadiga em estrutura de fundação de torre de turbina eólica," in *An. VII Cong. Bras. Pontes e Estrut.*, 2014.

[7] C. A. M. Araújo, A. Puel, and A. Candemil, "Análise numérica de fundações diretas de aerogeradores," in *An. VII Cong. Bras. Pontes e Estruturas*, Rio de Janeiro, 2014.

[8]  G. M. Maranhão, "Análise da rigidez rotacional de fundações estaqueadas de torres eólicas," in *An. IX Cong. Bras. Pontes e Estrut.*, Rio de Janeiro, 2016.

[9]  D. A. Velloso and F. R. Lopes, *Fundações - Critérios de Projeto, Investigação do Subsolo, Fundações Superficiais, Fundações Profundas*. São Paulo: Oficina de Textos, 2011.

[10] A. E. H. Love, *Mathematical Theory of Elasticity*. New York: Dover Publications, 1944.

[11] Associação Brasileira de Normas Técnicas, *Design of Concrete Structures – Procedure*, ABNT NBR 6118, 2014.

[12] H. G. Poulos, "Stresses and displacements in an elastic layer underlain by rough rigid base," *Geotechnique*, vol. 17, pp. 378–410, 1967.

[13] H. G. Poulos and E. H. Davis, *Elastic Solutions for Soil and Rock Mass*. New York: John Wiley & Sons, 1974.

[14] A. H. Teixeira and N. S. Godoy, "Análise, projeto e execução de fundações rasas," in *Fundações - Teoria e Prática*, W. Hachich, et al., Ed., 2ª. ed. São Paulo: Pini, 1998. cap. 7, p. 227–264.

[15] J. Boussinesq, *Application des POTENTIELS à L'étude de L'équilibre et du Mouvements des Solides Élastiques*. Paris: Gauthier-Villars, 1885.

[16] F. Schiel, *Estática das Construções* (Publicação 10). São Carlos: Esc. Eng. São Carlos, Univ. São Paulo, 1957.

[17] U. R. Alonso, *Exercício de Fundações*. São Paulo: Edgard Blücher, 1983. pp. 77–78.

Rev. IBRACON Estrut. Mater., vol. 14, no. 5, e14504, 2021

14/14

# IBRACON Structures and Materials Journal
## Revista IBRACON de Estruturas e Materiais

ORIGINAL ARTICLE

# Numerical analysis of the behavior of beam-column precast connections without continuity reinforcement

*Análise numérica do comportamento de ligações viga-pilar pré-moldadas sem armadura de continuidade*

João Victor Maciel de Andrade Silva[a]  iD
Leandro Vanalli[b]  iD
Luiz Antonio Farani de Souza[c]  iD
Caio Prestupa Malta Rolim[b]  iD

[a]Universidade Estadual de Mato Grosso do Sul – UEMS, Coordenação de Engenharia Ambiental e Sanitária, Dourados, MS, Brasil
[b]Universidade Estadual de Maringá – UEM, Departamento de Tecnologia, Umuarama, PR, Brasil
[c]Universidade Tecnológica Federal do Paraná – UTFPR, Coordenação de Engenharia Civil, Apucarana, PR, Brasil

**Abstract:** In this paper, the behavior of four beam-column connections in precast structures, without continuity reinforcement, subjected to negative bending moment was analyzed through numerical simulation using the ABAQUS®, which is based on the Finite Element Method. Nonlinear analysis was performed initially with calibration using an experimental model found in the literature. The analysis showed that the filling of the beam-pillar interfaces with rigid material allows for greater stiffness and bond strength, exhibiting a secant rotational flexural stiffness at the beginning of the yield of the anchor at least 5.5 times greater than in models without filling. There are benefits in considering the rotational stiffness of this type of connection in precast single-storey or small height structures in relation to their stress distribution that provide greater competitiveness to precast structures.

**Keywords:** finite element, ABAQUS, deformability, semi-stiffness.

**Resumo:** Nesta pesquisa foi analisado o comportamento de quatro modelos de ligações viga-pilar em estruturas pré-moldadas, sem armadura de continuidade, submetidas a momento fletor negativo por meio de simulação numérica com a utilização do programa ABAQUS®, o qual é baseado no Método dos Elementos Finitos. A análise mostrou que o preenchimento das interfaces viga-pilar com material rígido proporciona maior rigidez e resistência à ligação, exibindo rigidez rotacional secante ao início do escoamento do chumbador pelo menos 5,5 vezes maior que em modelos sem o preenchimento. Considerar a rigidez desse tipo de ligação em projetos de estruturas pré-moldadas de um pavimento ou de pequena altura permite benefícios na distribuição de esforços das mesmas tornando-as mais competitivas.

**Palavras-chave:** elementos finitos, ABAQUS, deformabilidade, semirrigidez.

# 1 INTRODUCTION

Precast structures are of great importance for the modernization process of civil construction, as their characteristics present great benefits, such as reduced input waste, technological innovation, increased yield, and reduced construction time, as reported by El Debs [1].

Recently, precast structures have had their use expanded with the social and technological development of Brazil. They have a wide range of applications, from buildings to large works of art and infrastructure. In buildings, precast structures can be used both in single-storey buildings (warehouses, halls, and event centers) and multi-storey buildings.

With the greater application of precast structures in civil constructions, there is an increasing need for research and development activities on the subject. In this sense, it is essential to understand how their connections work. Kataoka et al. [2] state that the main difference between precast structures and reinforced concrete structures cast on site is the presence of connections, and according to Lacerda et al. [3] connections are fundamental to the behavior of precast structures.

In recent years, much research has been carried out to conceive connections with high levels of stiffness at the bending moment, mainly for application in tall structures, which are under greater horizontal stresses and harder to stabilize, such as the research by Baldissera [4] and El Debs et al. [5]. Oliveira Júnior et al. [6], also looking for a connection with high stiffness, proposed the use of concrete with the incorporation of steel fibers for infrastructure works. More recently Lacerda et al. [3] evaluated the influence of grout filling of beam-column interfaces in connections with continuity reinforcement, and they observed an increase in the stiffness and resistance of the filled connections.

However, these stiffer connections, in general, are obtained through concrete cast at the site, in the region of the connection, prestressing, or welded metal sheets. The execution of connections with these characteristics reduces the speed of construction, which is one of the main advantages of precast concrete according to El Debs [1].

It should be noted that precast structures can also be applied in single-storey buildings and small buildings (up to 12 m high according to El Debs [1]). These types of buildings need less stiffness in their connections, given the lower intensity of horizontal stresses; in these cases, it is more interesting to use simple connections, which allow greater yield and speed in construction.

Sawasaki [7] conducted an experimental and numerical study of connections without continuity reinforcement, formed by anchor and bearing pad, for application in small buildings and warehouses. The connections showed low stiffness, however, the influence on the stress distribution in the structures was positive, with a reduction of up to 47.9% of the bending moment at the base of the columns.

In this context, this article presents a comparative analysis of the behavior of four different precast connections without continuity reinforcement. The analyzed connections are easy to implement and are basically formed by a corbel with anchor and bearing pad for beam connection with a half-joint.

The analysis was carried out by numerical simulation, with physical and geometric nonlinearity, using the computer program ABAQUS® based on the Finite Element Method (FEM). It considered the nonlinear behavior of concrete, reinforcement, and anchor. For concrete, the constitutive model 'Concrete Damaged Plasticity' (CDP) was used and for reinforcement, ideal elastoplastic behavior was used. The solution of the nonlinear problem was obtained using the Newton-Raphson method, in an incremental and iterative design.

## 2 ANALYSIS METHODOLOGY

For calibrating the numerical analysis, a simulation was carried out of the connection model analyzed experimentally by Miotto [8]. This connection is made by means of a corbel with an anchor and modified mortar pad (MMP). The connection has superior continuity reinforcement, next to the concrete topping of the precast slab and can be seen in Figure 1. This connection was chosen because it presents reliable results, in addition to having a vast description of all experimental steps. Another important factor for choosing this connection was its complexity, which displays several components and characteristics relevant to this research, which can be calibrated and later extrapolated for analysis in other models.
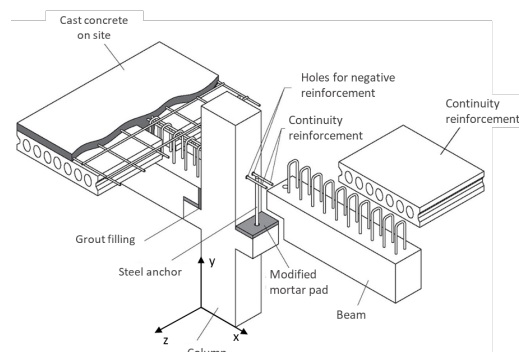


**Figure 1.** Calibration connection (Adapted from El Debs [1]).

*J. V. M. A. Silva, L. Vanalli, L. A. F. Souza, and C. P. M. Rolim*

In this context, the moment-rotation curve, the failure mode, the cracking and ultimate moments, and the cracking pattern were analyzed in the numerical model. From the calibration model, four connection models without continuity reinforcement and with different characteristics were proposed. All models are derived from a cross-shaped, central column connection with dimensions as shown in Figure 2.
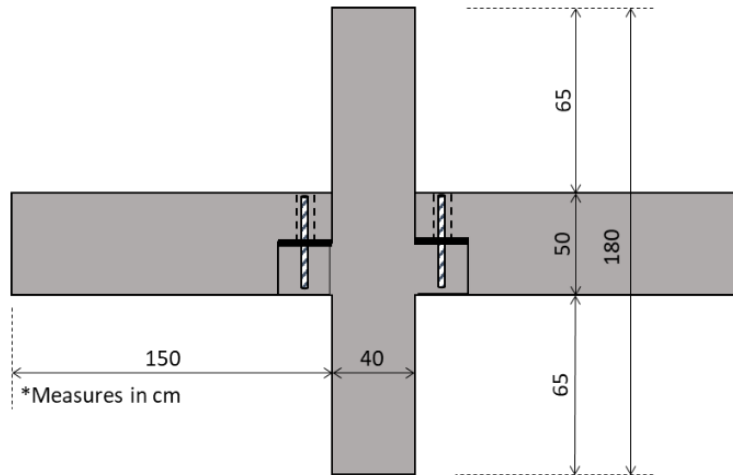


**Figure 2.** Basic model analyzed.

The characteristics of the connection were changed based on the basic model, assigning components that can increase the stiffness at the bending moment, such as anchoring the anchor, using a modified mortar pad (MMP), and filling the beam-column interfaces with grout. A summary of the models and their characteristics can be seen in Table 1 and Figure 3.

**Table 1.** Model characteristics.

| Characteristics | Connection model | | | |
|---|---|---|---|---|
| | **MP1** | **MP2** | **MP3** | **MP4** |
| **Bearing pad** | **Elastomer** | **MMP** | **MMP** | **MMP** |
| Anchoring the anchor to the top of the beam | ✕ | ✕ | ✔ | ✔ |
| Filling beam-column interfaces | ✕ | ✕ | ✕ | ✔ |
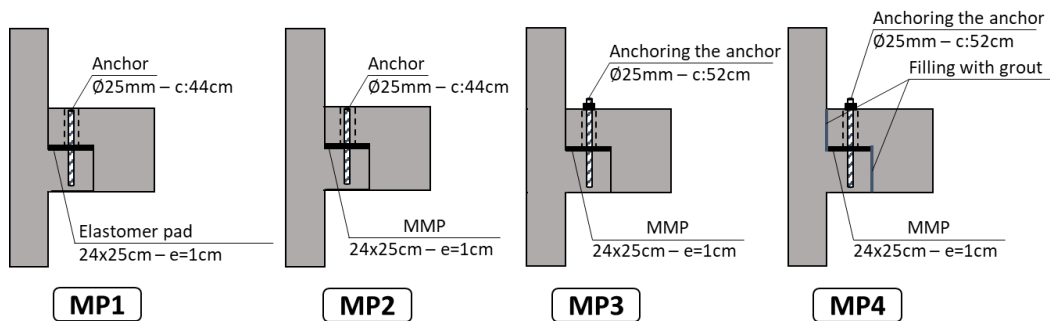


**Figure 3.** Connection models analyzed.

To analyze the behavior of the connections, the following variables were evaluated: moment-rotation curve, cracking and ultimate moments, and failure mode.

## 3 NUMERICAL ANALYSIS

The numerical analysis was performed using the computer program ABAQUS®, version 6.12, based on the Finite Element Method which allows the analysis of several engineering problems. All its theoretical foundation is described in the Abaqus Theory Manual prepared by Dassault Systèmes S.A [9].

In the analyses, physical and geometric nonlinearities were considered, as well as the contact between surfaces. The models were discretized into two types of finite elements available in the ABAQUS® library. In all solid parts, C3D8 tetrahedral continuous elements were used, which are three-dimensional elements with 8 nodes. The reinforcements were modeled as bars, using the T3D2 element with 2 nodes; however, the continuity reinforcements of the calibration model and the half-joint and corbel tie rods of all models were modeled as solid, using the C3D8 element.

Load increments were performed using steps with automatic size adjustment based on computational efficiency but limited to the maximum increment of 1.0 kN. The Newton-Raphson method was used to solve the nonlinear problem.

### 3.1 Materials

All mechanical parameters of material characteristics were based on the experimental characterization tests described in Miotto [8]. For concrete modeling, the constitutive model Concrete Damaged Plasticity (CDP) was used, based on the Theory of Plasticity and Continuum Damage Mechanics, initially proposed by Lubliner et al. [10]. This model assumes that concrete has two failure mechanisms - cracking in tension and crushing in compression. The evolution of the failure surfaces is controlled by two variables $\tilde{\varepsilon}_t^{pl}$ (equivalent plastic strain in tension) and $\tilde{\varepsilon}_c^{pl}$ (equivalent plastic strain in compression).

In Miotto's experimental model [8], two concretes with different characteristics were used: one used for beams and column, and the other for filling the topping. The mechanical characteristics used in the modeling were: mean compressive strength ( $f_c$ ), mean tensile strength ( $f_t$ ), tangent modulus of elasticity ( $E_c$ ), and Poisson's ratio ( $v_c$ ), which are shown in Table 2.

**Table 2.** Mechanical characteristics of concretes

|  | Beams and column | Topping |
|---|---|---|
| Compressive strength ( $f_c$ ) | 49.0 MPa | 33.2 MPa |
| Tensile strength ( $f_t$ ) | 3.2 MPa | 2.9 MPa |
| Modulus of elasticity ( $E_c$ ) | 32.8 MPa | 31.6 MPa |
| Poisson's ratio ( $v_c$ ) | 0.2 | 0.2 |

As Miotto [8] did not present the stress versus strain curves of the concretes used, data from Table 2 were extrapolated. To determine the stress versus strain curve of concrete under compression, the relationship proposed by Saenz [11] and modified by Hu and Schnobrich [12] was used, according to Equation 1 and which can be seen in Figure 4. For tension, the model used was the one proposed by Nayal & Rasheed [13] with the modifications from Wahalathantri et al. [14], as can be seen in Figure 5.

$$\sigma = \frac{E_c \varepsilon}{1 + \left(R + R_E - 2\right)\left(\dfrac{\varepsilon}{\varepsilon_0}\right) - \left(2R - 1\right)\left(\dfrac{\varepsilon}{\varepsilon_0}\right)^2 + R\left(\dfrac{\varepsilon}{\varepsilon_0}\right)^3} \tag{1}$$

Where: $\varepsilon_0$ : Strain corresponding to peak stress and adopted as 0.0025;

$\varepsilon_u$ : Ultimate strain adopted with 4 $\varepsilon_0$ according to Hu and Schnobrich [12];

$f_u$ : Ultimate stress adopted with $f_c$ /4 according to Hu and Schnobrich [12];

$E_0$ : Secant modulus of elasticity ( $f_c / \varepsilon_0$ );

$R_E$ : Relationship between tangent and secant modulus of elasticity ( $E_c / E_0$ );

$R_\varepsilon$ : Strain rate ( $\varepsilon_u / \varepsilon_0$ ), adopted as 4 according to Hu and Schnobrich [12];

$R_\sigma$ : Stress ratio ( $f_c / f_u$ ), adopted as 4 according to Hu and Schnobrich [12];

$$R = \left( R_E \left( R_\sigma - 1 \right) / \left( R_\varepsilon - 1 \right)^2 \right) - \left( 1 / R_E \right).$$
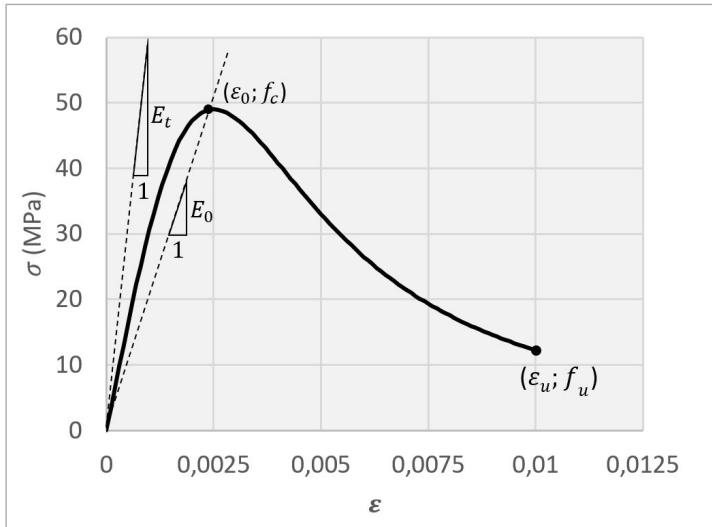


**Figure 4.** Stress versus strain curve to uniaxial compression adopted for the model. (From the author)
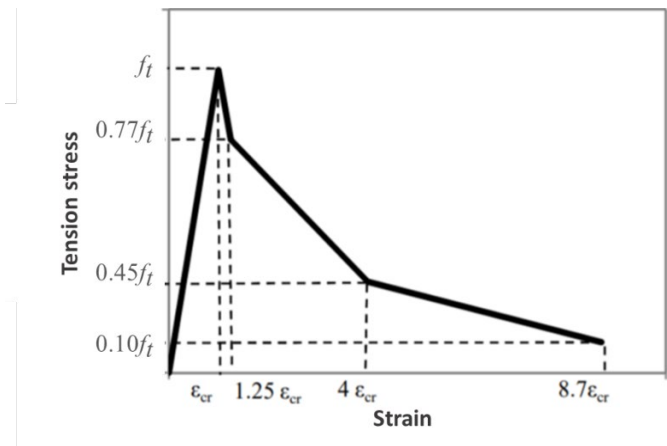


**Figure 5.** Constitutive relation for concrete (Adapted from Wahalathantri et al. [14]).

The reinforcement and anchor steels were modeled with perfect elastoplastic behavior. For reinforcement, CA 50 steel was used and for anchor bolts, SAE 1020 steel was used. The yield stresses of the steels were obtained experimentally in Miotto [8], as well as the modulus of elasticity of steel SAE 1020, whereas the modulus of elasticity of steel CA 50 was adopted with a value of 200 GPa. The mechanical characteristics of steels can be seen in Table 3.

**Table 3.** Mechanical characteristics of steels

| Type | Diameter (mm) | Yield stress ($f_y$) (MPa) | Modulus of elasticity ($E_s$) (GPa) |
|---|---|---|---|
| | 10.0 | 576 | 200* |
| CA 50 | 12.5 | 611 | 200* |
| | 16.0 | 589 | 200* |
| SAE 1020 | - | 576 | 201 |

*Values adopted due to the absence of experimental data

Rev. IBRACON Estrut. Mater., vol. 14, no. 5, e14505, 2021

5/17

In the calibration model, the bearing pad was made in modified mortar. This material has been researched in recent years (Ditz et al. [15], El Debs and Bellucio [16], Siqueira and El Debs [17]), in search of a composite that has a low modulus of elasticity, good mechanical resistance, and high tenacity. In this analysis, this material was modeled with elastic-linear behavior, using pad stiffness of 150 MPa.

In Model MP1, the material used in the pad was polychloroprene (Neoprene), a material widely used in elastomeric bearing pads by Brazilian manufacturers of precast structures. In this analysis, Neoprene was modeled with elastic-linear behavior and the relation proposed by Ferreira was used to determine the slab stiffness of this material [18], according to Equation 2.

$$E_n = K_1 GB + K_2 \sigma_m \tag{2}$$

Where: $E_n$ : Slab stiffness (MPa);

$K_1$ and $K_2$ : Adjustment coefficients, adopted as 7 and 6 for Concrete-Neoprene contact surfaces, respectively;

$G$ : Transverse modulus of elasticity (1.0 MPa);

$\sigma_m$ : Average compression stress (5 MPa);

$B$ : Form factor, given by Equation 3.

$$B = \frac{ab}{2h_n(a+b)} \tag{3}$$

Where: $a$ and $b$ : Plan dimensions of the pad;

$h_n$ : Pad thickness.

The stiffness obtained by Equation 2 for Neoprene is approximately 73 MPa, which is consistent with the experimental results obtained in Montedor [19]. The filling grout was modeled with elastic-linear behavior, with a modulus of elasticity $E_c$ of 4.94 GPa, according to experimental characterization tests performed by Miotto [8].

## 3.2 Contact

The models used in this analysis show several regions of interaction between surfaces, among them: the contact between the beam and column concrete and the bearing pad, the contact between the anchor and the surrounding concrete, and the contact between concrete surfaces of different ages.

Different tools available in ABAQUS® were used, which allowed the modeling of all regions of mechanical contact of the models. Basically, the embedded tool was used to simulate the relation between the reinforcement and the concrete, as well as the anchor and the concrete of the column. The tie constraint was used for the relation between concrete surfaces of different ages, as this constraint allows the nodes of a pair of surfaces to remain tied throughout the simulation; that is, all the translation and rotation movements of the nodes close to the two surfaces are equal.

For several interactions between surfaces, a possible relative sliding was considered, and the Coulomb Frictional Model was used. It is considered that two adjacent surfaces can transmit shear stresses up to a certain magnitude before relative sliding (adhesion) occurs. The stress which starts the relative sliding is given as a fraction of the contact pressure ($p$) and called critical stress ($\tau_{crit}$) determined according to Equation 4. From the critical shear stress, there is a relative sliding between the surfaces as shown in Figure 6.

$$\tau_{crit} = \mu\, p \tag{4}$$

Where: $\mu$ : Coefficient of friction;

$p$ : Contact pressure between surfaces.
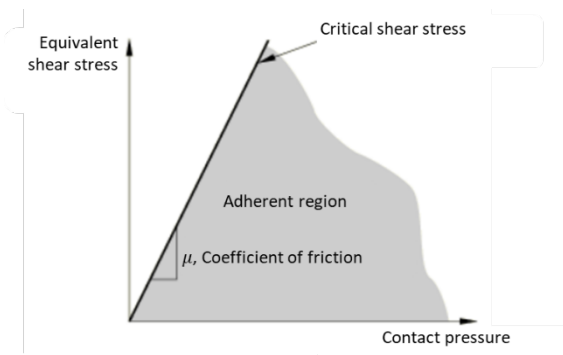
**Figure 6.** Sliding conditions between surfaces in contact (adapted from Dassault Systèmes S. A. [9]).

The friction coefficients considered between the different surfaces were determined according to Miotto [8], Ferreira [18], and Magliulo et al. [20]. For contact surfaces between precast concrete, a friction coefficient of 0.6 was considered. For the contact between the steel of the SAE 1020 anchor (smooth) and the surrounding concrete (grout), a coefficient of $\mu = 0.01$ was considered. For the contact between concrete and the modified mortar pad, the value adopted for the friction coefficient was 0.4.

For the contact between the elastomeric bearing pad and the column and beam concrete, the relation proposed by Magliulo et al. [20], represented in Equation 5, was used. In this case, the coefficient of friction between concrete and Neoprene depends on the contact pressure between surfaces.

$$\mu = 0.49 \, if \, \sigma_p \leq 0.14 \, MPa$$

$$\mu = 0.1 + \frac{0.055}{\sigma_p} if \, 0.14 < \sigma_p \leq 5 \, MPa \tag{5}$$

Where: $\mu$: Coefficient of friction;

$\sigma_p$: Average contact stress in the bearing pad.

For the consideration of the contact pressures between surfaces, this modeling used the hard relation of the program. Such relation considers that when surfaces are in contact, any stress is transmitted; however, when there is no contact between surfaces, there is no stress transmission, thus, surfaces that are initially separated are considered in contact when the separation distance between they are reduced to zero; from that moment, restrictions are imposed on the degrees of freedom of the nodes that form the surfaces and the stresses transmitted between them. This analysis is performed automatically by ABAQUS® between the surfaces previously defined and characterized by the user.

This modeling considered the contact formulation called surface pairs, in which the user can specify aspects of discretization, tracking approach, etc., specifically using the contact discretization called surface-to-surface that performs the analyses in average regions from the individual nodes of the surface.

## 4 CALIBRATION MODEL

Since the calibration model has symmetry in relation to two planes, the conditions of symmetry were used for the modeling, with the numerical model corresponding to 25% of the experimental structure, which allows the analysis to be performed at a lower computational cost. Symmetry was defined in the directions of the x and z axes, according to Figure 7. The boundary conditions were performed by setting the lower end of the column and applying stress to the beam end, as can be seen in Figure 7a. Figure 7b shows the reinforcement of the numerical model.

In this model, a total of 16136 C3D8 elements and 5580 T3D2 elements were used. The dimensions of the elements were varied and defined according to the degree of accuracy of the desired response.
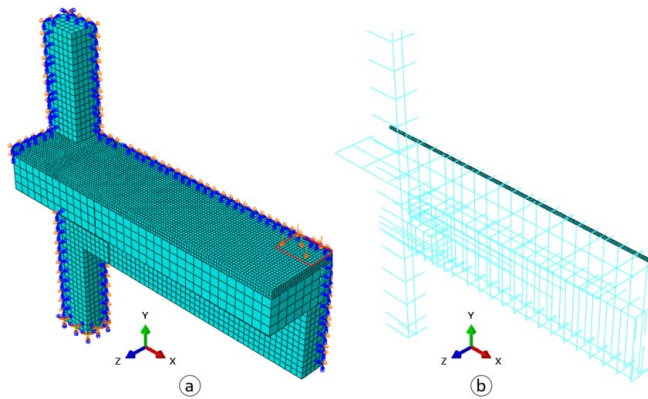
**Figure 7.** Boundary conditions of the calibration model.

## 4.1 Moment-rotation curve and cracking and ultimate moments

The numerical model exhibited a behavior like the experimental model both for rotational stiffness and the cracking and failure moments. The experimental model was also numerically analyzed by Miotto [8] using the computer program ANSYS®, version 5.5. Figure 8 shows the development of the moment-rotation curve for the negative bending moment of the experimental and numerical model by Miotto [8] that was carried out in this research using ABAQUS®, version 6.12.

Both the numerical model and the experimental model exhibit three well-defined stiffness stages. The numerical model showed high indexes of initial stiffness until -39.67 kNm, when the cracking of the connection occurs. From this stage on, the connection presents a sharp drop in stiffness, which remains constant until the bending moment of approximately -233.75 kNm, considered the ultimate moment of the connection. The comparison of the cracking and ultimate moments of the experimental and numerical models can be seen in Table 4.

The numerical model did not exhibit the same rhythm of loss of stiffness as the experimental model in the second stage, mainly from the bending moment of -125 kNm. This difference in behavior may be attributed to the modeling of the modified mortar bearing pad and grout with elastic-linear behavior.
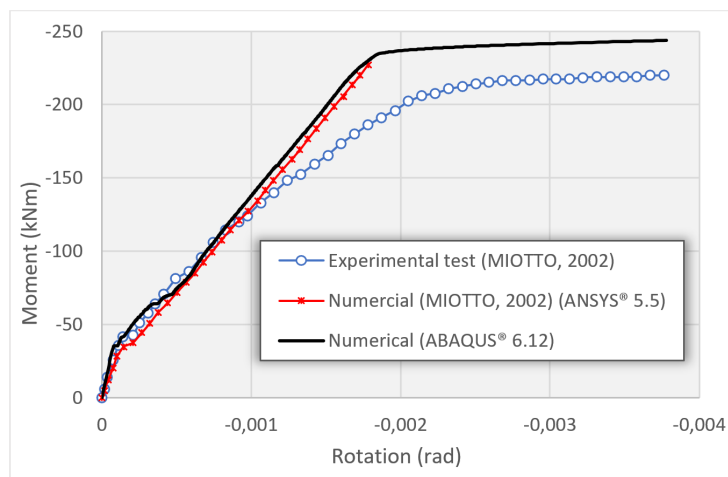


**Figure 8.** Moment-rotation curve of calibration model (Adapted from Miotto [8]).

**Table 4.** Comparisons of numerical and experimental bending moments

| Model | Cracking moment ($M_f$) (kNm) | $\dfrac{M_{f,exp}}{M_{f,num}}$ | Ultimate moment ($M_u$) (kNm) | $\dfrac{M_{u,exp}}{M_{u,num}}$ |
|---|---|---|---|---|
| Experimental (Miotto [8]) | -42.00 | | -220.75 | |
| Numerical (ABAQUS 6.12) | -39.67 | 1.059 | -233.75 | 0.944 |

## 4.2 Cracking pattern and failure mode

Both the numerical model and the experimental model showed failure from the yield of the continuity reinforcement present in the concrete topping. In both cases, the models showed intense cracking on the topping from the strain of the reinforcement. To analyze the cracking of the numerical model, the distribution of plastic deformations was verified, which indicates the occurrence of cracks in the concrete with certain accuracy.

Figure 9 shows the distribution of plastic deformations in the concrete of the numerical model and a diagram of the distribution of cracks in the experimental reference model for their respective ultimate moments. There is a good relation between the cracking patterns of the numerical model and the experimental model.

Miotto [8] mentions that cracks started near the column and were moving away to the external regions. This configuration was similar in the numerical model, in which the first crack occurred precisely in the protruding corner of the column. After the first crack, there were other cracks close to the region of symmetry, and with the increase of the acting moment, parallel cracks formed towards the load application region at the end of the beams.
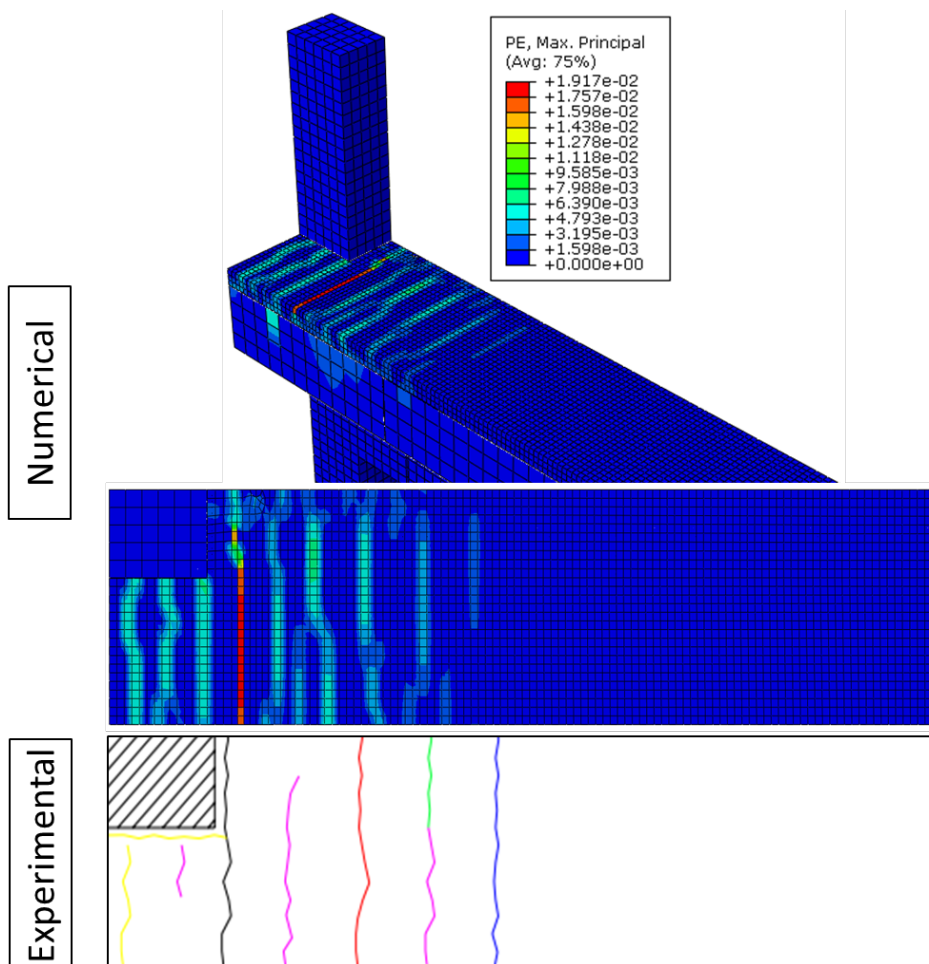


**Figure 9.** Comparison of the cracking pattern of the models. (Adapted from Miotto [8]).

## 5 NUMERICAL MODELS

With the good convergence of the behavior of the calibration model, the extrapolated models shown in Figure 3 could be analyzed. The results are presented in the following items.

The number of finite elements used in the models can be seen in Table 5. The boundary conditions were defined in a similar way to the calibration model and Figure 10 shows the numerical models.

Rev. IBRACON Estrut. Mater., vol. 14, no. 5, e14505, 2021

9/17

**Table 5.** Number of finite elements of the numerical models

| Model | Number of elements | |
|---|---|---|
| | C3D8 | T3D2 |
| MP1 | 8559 | 2403 |
| MP2 | 8559 | 2403 |
| MP3 | 8811 | 2403 |
| MP4 | 9474 | 2403 |
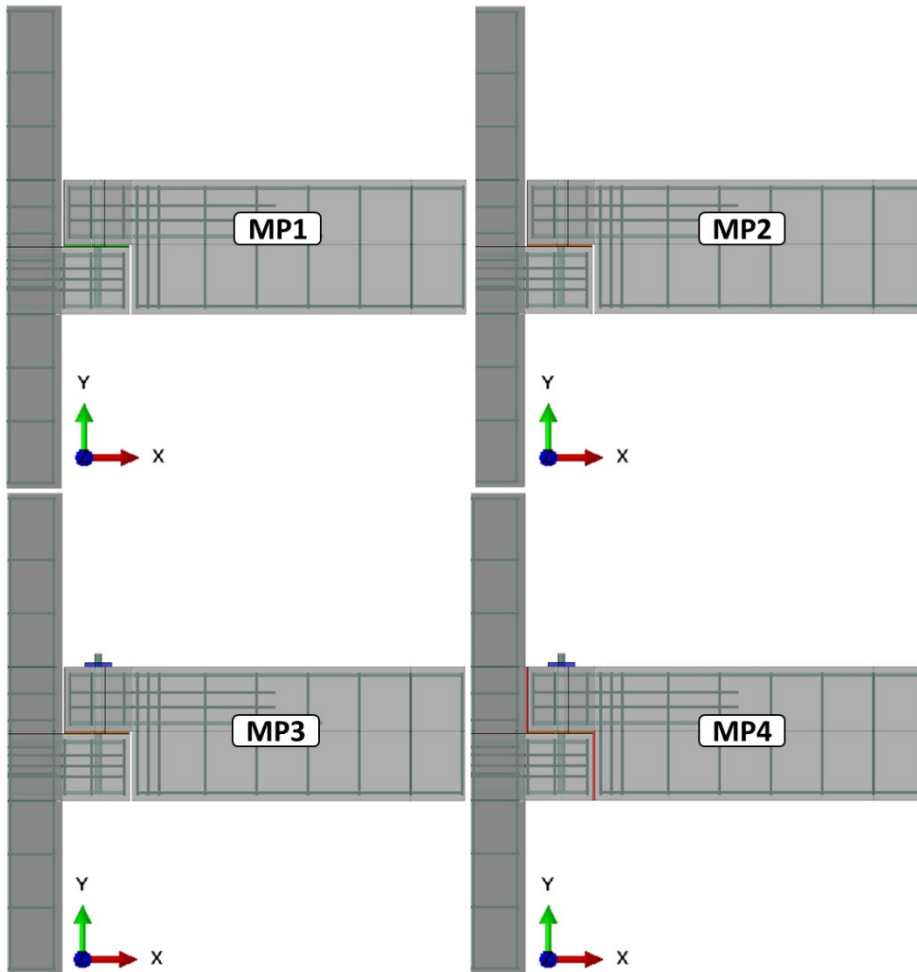


**Figure 10.** Numerical models.

The calculation of the reinforcements and the verification of the concrete in the corbels and half-joints of the models were made according to the calculation model indicated by the Brazilian technical standard NBR 9062 [21] for corbels and are composed of main reinforcement (tie rods) and secondary reinforcements that include horizontal and vertical stirrups and suspension reinforcement exclusively for the half-joint.

## 5.1 Moment-rotation curve

The moment-rotation curve of the models was determined similarly to the calibration model, by checking the relative horizontal displacement of the beam at the vertical joint near the column. The secant stiffness was determined when the yield of the anchor of the connections began, as well as its initial tangent stiffness. These curves were determined for all models and are shown below.

It is worth mentioning that the curves shown in Figures 12, 13, and 14 do not show the complete behavior of the models MP1, MP2 and MP3, since the part of the behavior that occurs after contact between the lower part of the corbel and the lower part of the half-joint was suppressed according to Figure 11.
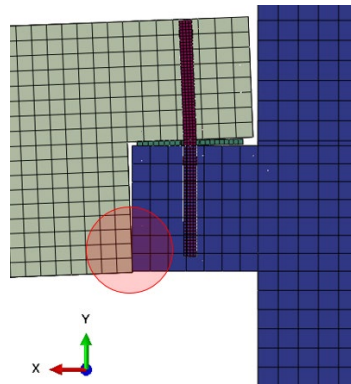


**Figure 11.** Contact between the half-joint and the corbel.

### 5.1.1 MP1

The only mechanism of resistance to rotation presented by the connection of model MP1 is the anchor subjected to bending by the pin effect; therefore, the model exhibits low initial tangent stiffness, with a value of 569.15 kNm/rad. This result can also be attributed to the low stiffness of the bearing pad, which in this model consists of polychloroprene (Neoprene). The moment-rotation curve of model MP1 can be seen in Figure 12. The moment that characterizes the beginning of the yield of the anchor was approximately -9.33 kNm and was obtained by monitoring the development of the main stresses in the anchor as the bending moment increments occurred.
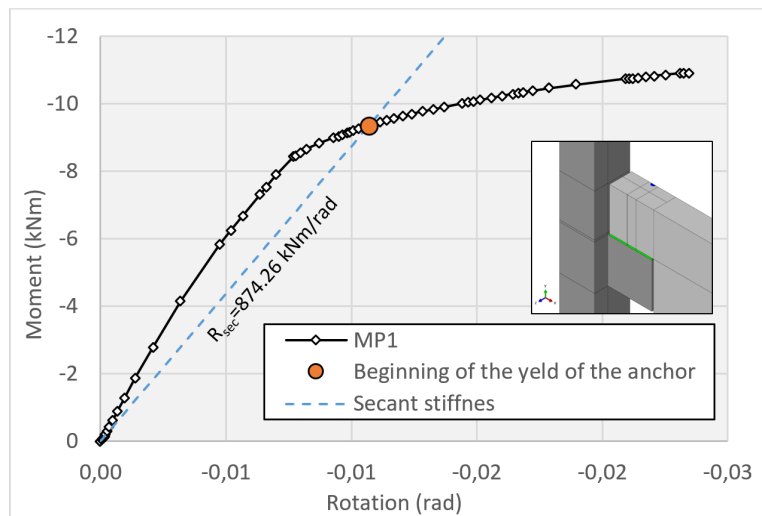


**Figure 12.** MP1 moment-rotation curve.

### 5.1.2 MP2

The only change in model MP2 is the use of a modified mortar pad in place of the elastomer. The model exhibits an initial tangent stiffness greater than MP1, with a value of 956.43 kNm/rad. The moment-rotation curve of model MP2 can be seen in Figure 13.
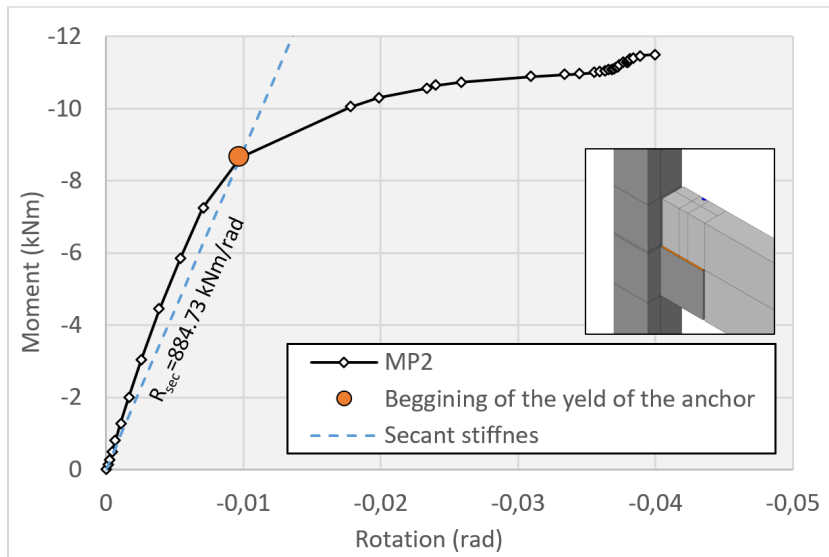
**Figure 13.** MP2 moment-rotation curve.

### 5.1.3 MP3

As shown in Figure 14, the anchoring of the anchor to the top of the beam changed the behavior of the connection, causing the moment-rotation curve not to show a marked drop in stiffness as in models MP1 and MP2. This is because with the anchoring the anchor is no longer mainly required by the bending, due to the pin effect, and it is also subjected to tension. This effect can be observed through the distribution and direction of the main stresses in the anchors of models MP2 and MP3 according to Figure 15, in the contact between the corbel and the half-joint.

It can be seen in Figure 15 that the anchor of model MP2 exhibits a concentration of stresses greater than 600 MPa both in tension and compression near the turning point of the connection (pin effect) forming a plastic hinge, while in model MP3 there is a distribution of more uniform tensile stresses along the anchor with values of approximately 500 MPa; it can also be observed that the stress directions in the anchor of model MP3 are almost entirely of axial tension, differently from the anchor of model MP2.

Another important factor for the more linear behavior of the moment-rotation curve of model MP3 is the fact that, in this case, virtually all the relative sliding that may occur between the anchor and the concrete surrounding the beam is practically eliminated from the anchoring of the anchor. The connection shows an initial tangent stiffness of 1081.27 kNm.
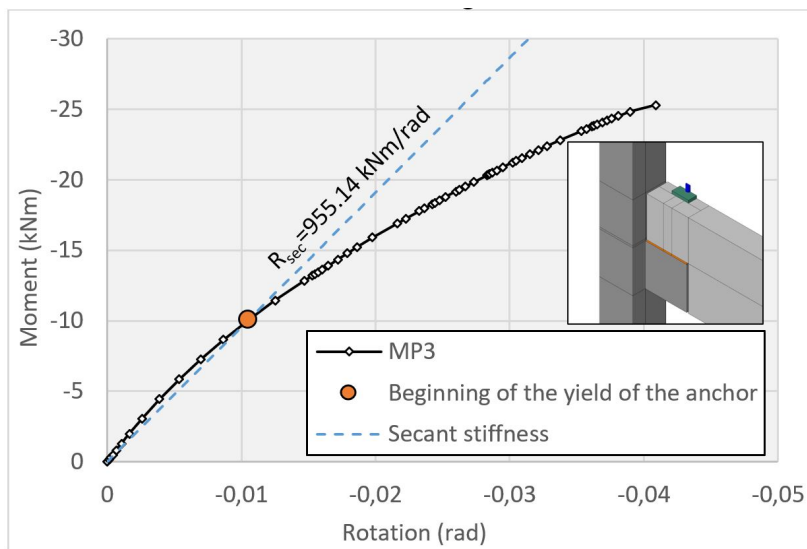


**Figure 14.** MP3 moment-rotation curve.

Rev. IBRACON Estrut. Mater., vol. 14, no. 5, e14505, 2021

12/17
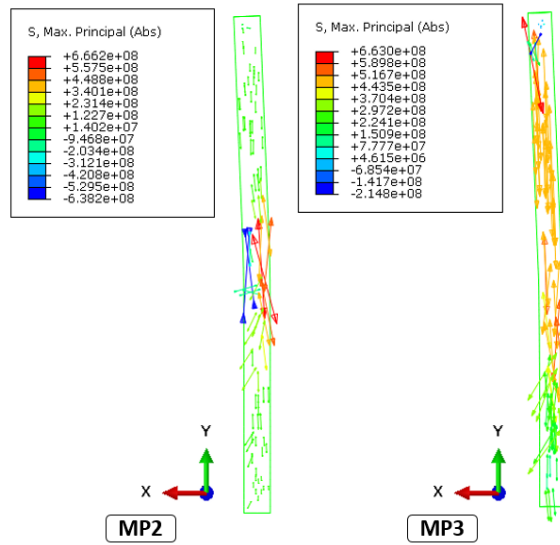
**Figure 15.** Distribution and direction of the main stresses in the anchors of models MP2 and MP3 (Stresses in Pa).

### 5.1.4 MP4

Grout filling in model MP4 considerably increased the stiffness of the connection. Model MP4 exhibited an initial tangent stiffness of 12156.08 kNm, noticeably greater than the other models. Figure 16 shows that the stiffness in the connection of Model MP4 is higher and more resistant than in models MP1, MP2, and MP3.
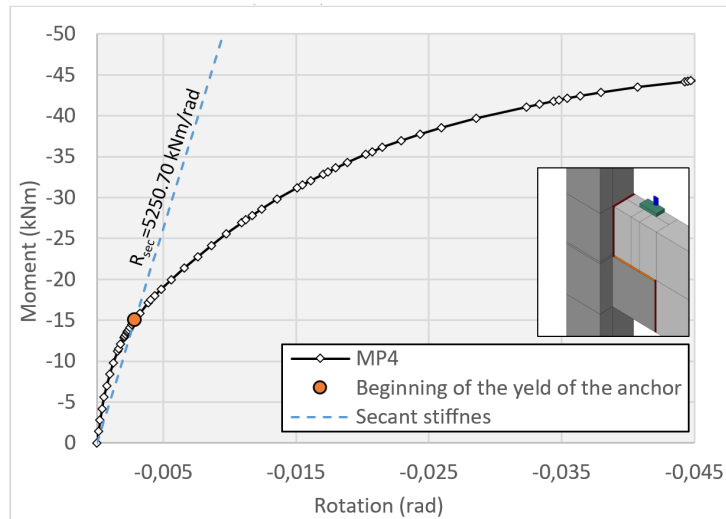


**Figure 16.** MP4 moment-rotation curve.

Figure 17 exhibits the complete moment-rotation curve of all models, showing an increase in the stiffness of models MP2 and MP3 after the beginning of the yield of the anchor, and this increase corresponds to the moment of contact between the corbel and half-joint.

### 5.2 Overview

Comparing the moment-rotation curves of all models in Figure 17, it appears that the initial behavior of models MP1, MP2, and MP3 is quite similar, and the only difference is that model MP3 does not show a sharp drop in stiffness as discussed in the previous paragraphs and shown in Figure 15.

The moments of the beginning of the yield of the anchors for models MP1, MP2, and MP3 are similar, as seen in Table 6, and this indicates that the changes proposed for these models were not effective to increase stiffness, not even the strength of the connections. On the other hand, the moment of the beginning of the yield of the anchor of model MP4 was 49.35% higher than for model MP3, which shows greater resistance ability.

Model MP4 also showed a considerably greater stiffness in relation to the other models, with its initial tangent stiffness 11.24 times greater than the stiffness of model MP3, and its secant stiffness at the beginning of the yield of the anchor was 5.5 times greater as shown in Table 7. This can be credited to the fact that the filling of the interfaces creates a resistance mechanism to the relative rotation between beam and column, limiting the strains in the compressed bottom because of the good resistance of the grout to compression and its high modulus of elasticity. However, in the upper region there is no type of tensile strength mechanism, since there is no considerable adherence between the filling grout and the concrete of the beam, thus making the anchor subjected to flexure-tension the fundamental element for resistance against the bending of the connection.
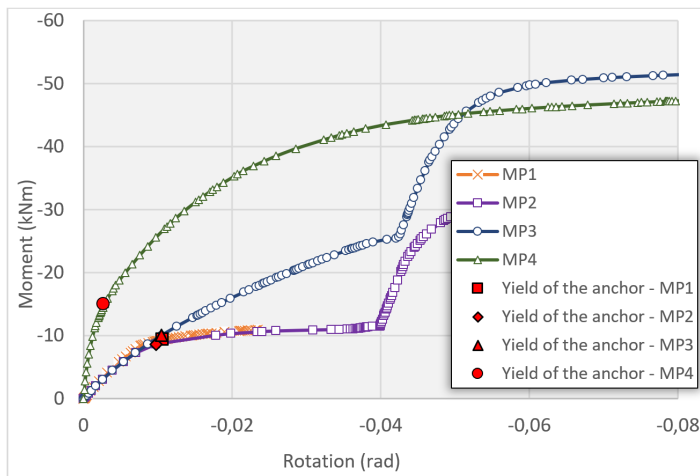


**Figure 17.** MP1, MP2, MP3, and MP4 moment-rotation curve.

**Table 6.** Model moments and rotations

| Model | $M_y$ (kNm) | Relative difference | $M_u$ (kNm) | Relative difference |
|---|---|---|---|---|
| MP1 | -9.33 | - | - | - |
| MP2 | -8.65 | -7.29% | -32.43 | - |
| MP3 | -10.05 | 16.18% | -50.88 | 56.89% |
| MP4 | -15.01 | 49.35% | -46.61 | -6.59% |
| Model | $\theta_y$ (rad) | Relative difference | $\theta_u$ (rad) | Relative difference |
| MP1 | 0.0107 | - | - | - |
| MP2 | 0.0098 | -8.63% | 0.0680 | - |
| MP3 | 0.0105 | 7.62% | 0.0610 | -10.26% |
| MP4 | 0.0029 | -72.83% | 0.0680 | 11.48% |

**Table 7.** Stiffness of models

| | MP1 | MP2 | | MP3 | | MP4 | |
|---|---|---|---|---|---|---|---|
| | Stiffness (kNm/rad) | Stiffness (kNm/rad) | $R_{MP2}/R_{MP1}$ | Stiffness (kNm/rad) | $R_{MP3}/R_{MP2}$ | Stiffness (kNm/rad) | $R_{MP4}/R_{MP3}$ |
| Initial (tangent) | 569.15 | 1083.35 | 1.903 | 1081.27 | 0.998 | 12156.08 | 11.242 |
| Yield of the anchor (secant) | 874.26 | 884.73 | 1.012 | 955.14 | 1.080 | 5250.70 | 5.497 |

Rev. IBRACON Estrut. Mater., vol. 14, no. 5, e14505, 2021

14/17

## 5.3 Failure mode

Model MP1 exhibited convergence problems, which can be attributed to the difficulty in modeling the contact relations between the concrete and the Neoprene pad. However, the connection already showed a well-established plastification of the anchor by the formation of a plastic hinge, which can be seen in Figure 18, and Figure 17 also shows that the MP1 and MP2 connection exhibit very similar behaviors except for initial tangent stiffness, which can be attributed to the difference in stiffness between the MMP and the polychloroprene pad, so that it can be said that the connections would exhibit similar behavior until failure. For the other models, the behavior could be observed at the ultimate moments.

All models presented plastification of the anchor from the bending caused by the pin effect in the region close to the bearing pad, forming a plastic hinge, as shown in Figure 18b. However, it is interesting to see that in models MP3 and MP4, the anchoring of the anchor to the upper part of the beam introduces tension effects to the anchor, as shown in Figure 15 and Figure 18.
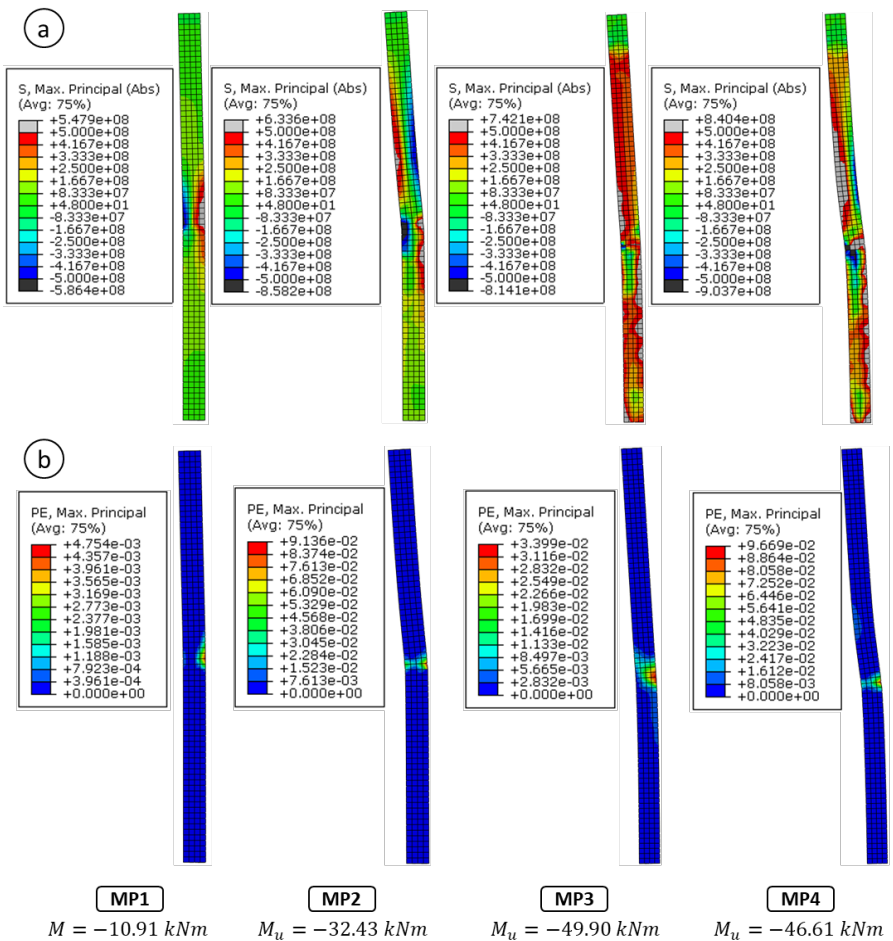


**Figure 18.** Anchors. a) Main maximum stresses; b) Main maximum strains. (Stresses in Pa).

The models had their ultimate moment reached mainly by the complete yield of the anchor; however, it is important to note that models MP3 and MP4 in their ultimate moment exhibit intense plastic strains in the corbel and in the half-joint. This is because in these models other mechanisms for transferring stresses are developed: (i) due to the anchoring of the anchor in the upper part of the beam, it compresses at the end of the upper side of the corbel in the region close to the half-joint thus causing plastic strains as shown in Figure 19; (ii) in model MP4, due to the filling of the interfaces, plasticization of the lower region of the corbel also occurs because of the compression caused by the negative bending moment.

We believe that the reason why model MP4 had lower ultimate resistance in relation to MP3, even though it exhibited greater $M_y$ and stiffness, is precisely the introduction of the new mechanisms for transferring stresses. It is

important to note that these new mechanisms for transferring stresses are not considered in the corbel calculation model presented by NBR 9062 [21]; therefore, in these cases, a systematic analysis of the structural behavior of the connection is essential to perform a correct design.



MP2
$M_u = -32,43\ kNm$

MP3
$M_u = -49,90\ kNm$

MP4
$M_u = -46,61\ kNm$
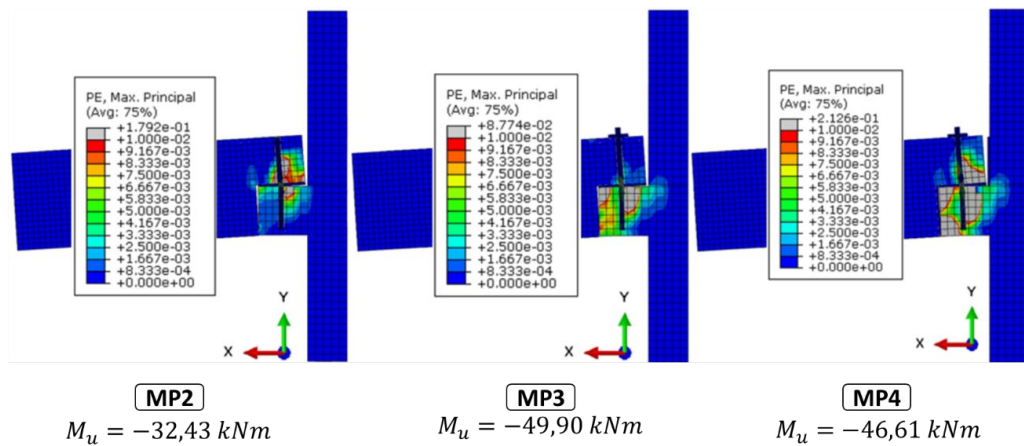
**Figure 19.** Distribution of plastic strains for $M_u$.

# 6 CONCLUSIONS

In this research, the behavior of precast beam-column connections, without continuity reinforcement, subjected to negative bending moment was analyzed through numerical simulation in a computer program based on the Finite Element Method. The connection experimentally analyzed in Miotto [8] was modeled to obtain the calibration of the numerical analysis and thus perform the extrapolation to the other proposed models. With the good relation between the behavior of the numerical model and the experimental reference model, analyses could be carried out.

With the main objective of analyzing the behavior of precast beam-column connections, subjected to negative bending moment, without continuity reinforcement, and easily executed, four connection models with different characteristics were proposed to evaluate the influence of connection components in their behavior.

Replacing the elastomeric bearing pad by MMP generated a significant difference in the initial tangent stiffness of the connection, which was 90.35% greater in the model with MMP, which is attributed to the difference in stiffness between the modified mortar and the polychloroprene rubber. However, the moment of the beginning of the yield of the anchor and the secant stiffness of the connections showed similar values.

The anchoring of the anchor to the upper region of the connection increased its ultimate resistance, as the anchoring introduces tension effects to the anchor and decreases its bending at the height of the interface with the upper surface of the corbel. The anchoring also introduces a compressed region on the upper side of the corbel and close to the half-joint of the beam; however, it did not influence the initial stiffness of the connection, nor did it influence the moment of the beginning of the yield of the anchor.

The filling of the beam-column interface regions with grout generated quite positive effects, increasing the moment of the beginning of the plasticization of the anchor by 49% and the secant stiffness by 5.5 times.

Therefore, it is possible to conclude, through the analyses of the numerical models, that the filling of the interfaces with rigid material allows for the increased strength and stiffness of the connection. However, it is important to note that the use of this resource introduces new mechanisms for transferring stresses in the connection, which must be considered in its structural design.

There are benefits in considering the stiffness of this type of connection in precast single-storey or small height structures in the distribution of their stresses, which allows greater competitiveness of precast structures in relation to other structural systems.

In this context, future work should evaluate the behavior of connections without continuity reinforcement with filling the connection of the beam-column interface, to understand the stress distribution in the connection to propose structural calculation models, as well as the influence of its behavior in precast structures.

# 7 ACKNOWLEDGMENTS

To the Department of Civil Engineering (DEC) of the State University of Maringá (UEM) and all its professors for supporting this research and for providing the computer program and other tools necessary for its development.

## REFERENCES

[1]   M. K. El Debs, *Concreto Pré-moldado: Fundamentos e Aplicações*, 2. ed. São Paulo: Oficina dos Textos, 2017.

[2]   Kataoka, M. N., Ferreira, M. A., and El Debs, A. L. H. C., "A study on the behavior of beam-column connections in precast concrete structures: experimental analysis," *Rev. IBRACON Estrut. Mater.*, vol. 5, no. 5, pp. 848–873, 2012.

[3]   Lacerda, M. M. S. et al. "Influence of the vertical grouting in the interface between corbel and beam in beam-to-column connections of precast concrete structures – An experimental analysis," *Eng. Struct.*, vol. 172, pp. 201–213, Maio 2018. https://doi.org/10.1016/j.engstruct.2018.05.113

[4]   A. Baldissera Estudo experimental de uma ligação viga-pilar de concreto pré-moldado parcialmente resistente a momento fletor. Universidade de São Paulo, 2006.

[5]   M. K. El Debs, A. M. Miotto, and A. L. H. C. El Debs, "Analysis of a semi-rigid connection for precast concrete," *Proc. Inst. Civ. Eng., Struct. Build.*, vol. 163, no. 1, pp. 41–51, 2010. Accessed: Oct. 12, 2018. [Online]. Available: http://www.icevirtuallibrary.com/doi/10.1680/stbu.2009.163.1.41

[6]   L. A. Oliveira Júnior et al., "Precast beam–column connection subjected to cyclic and dynamic loadings," *Struct. Eng. Int.*, vol. 27, no. 1, pp. 114–126, 2017. Accessed: Oct. 12, 2018. [Online]. Available: http://www.ingentaconnect.com/content/10.2749/101686617X14676303589075

[7]   F. Y. Sawasaki, "Estudo teórico-experimental de ligação viga-pilar com almofada de argamassa e chumbador para estruturas de concreto pré-moldado," Master thesis, Univ. S. Paulo, São Carlos, SP, 2010.

[8]   A. M. Miotto, "Ligações viga-pilar de estruturas de concreto pré-moldado análise com ênfase na deformabilidade ao momento fletor," Doctoral dissertation, Univ. S. Paulo, São Carlos, SP, 2002.

[9]   Dassault Systèmes, *ABAQUS 6.12*. Documentation. French: Dassault Systèmes, 2012.

[10] J. Lubliner et al., "A plastic-damage model for concrete," *Int. J. Solids Struct.*, vol. 25, no. 3, pp. 299–326, 1989.

[11] L. P. Saenz, "Discussion of 'Equation for the stress–strain curve of concrete' by Desayi, P. and Krishnan, S.," *ACI Journal*, vol. 61, pp. 1229–1235, 1964.

[12] H.-T. Hu and W. C. Schnobrich, "Constitutive modeling of concrete by using nonassociated plasticity," *J. Mater. Civ. Eng.*, vol. 1, no. 4, pp. 199–216, 1990.

[13] R. Nayal and H. A. Rasheed, "Tension stiffening model for concrete beams reinforced with steel and FRP bars," *J. Mater. Civ. Eng.*, vol. 18, no. 6, pp. 831–841, 2006.

[14] B. L. Wahalathantri et al. "A material model for flexural crack simulation in reinforced concrete elements using ABAQUS," *Inf. Transp. Urban Develop.*, pp. 260–264, 2011.

[15] J. D. Ditz, M. K. E. L. Debs, and G. H. Siqueira, "Modified mortar pad behavior in the transfer of compressive stresses," *Rev. IBRACON Estrut. Mater.*, vol. 9, no. 3, 2016.

[16] M. K. El Debs and E. K. Bellucio, "Almofadas de apoio feitas de argamassa para ligações de concreto pré-moldado: estudo da rugosidade superficial," *Rev. IBRACON Estrut. Mater.*, vol. 5, no. 1, pp. 38–67, 2012.

[17] G. H. Siqueira, and M. K. El Debs, "Cement-based bearing pads for precast concrete connections," *Proc. Inst. Civ. Eng. – Const. Mater.*, vol. 166, no. 5, pp. 286–294, 2013. Accessed: Oct. 12, 2018. [Online]. Available: http://www.icevirtuallibrary.com/doi/10.1680/coma.11.00055

[18] M. A. Ferreira, "Deformabilidade de ligações viga-pilar de concreto pré-moldado," Doctoral dissertation, Univ. S. Paulo, São Carlos, SP, 1999.

[19] L. C. Montedor, "Desenvolvimento de compósito a ser utilizado como almofada de apoio nas ligações entre elementos pré-moldados," Master thesis, Univ. S. Paulo, São Carlos, SP, 2004.

[20]    G. Magliulo et al., "Neoprene-concrete friction relationships for seismic assessment of existing precast buildings," *Engineering Structures*, vol. 33, no. 2, pp. 535–538, 2011. http://dx.doi.org/10.1016/j.engstruct.2010.11.011

[21] Associação Brasileira de Normas Técnicas. *Projeto e Execução de Estruturas de Concreto Pré-moldado*, NBR 9062, 2017.

# IBRACON Structures and Materials Journal
## Revista IBRACON de Estruturas e Materiais

ORIGINAL ARTICLE

# Punching shear in flat slabs by strut and tie model

## Punção em lajes lisas via modelo de bielas e tirantes

Ricardo José Carvalho Silva[a]  (iD)
Dênio Ramam Carvalho de Oliveira[b]  (iD)
Nívea Gabriela Benevides de Albuquerque[b]  (iD)
Thiago Andrade Gomes[a]  (iD)
Aaron Kadima Lukanu Lwa Nzambi[b]  (iD)

[a]Universidade Estadual Vale do Acaraú – UVA, Faculdade de Engenharia Civil, Sobral, CE, Brasil
[b]Universidade Federal do Pará – UFPA, Faculdade de Engenharia Civil, Belém, PA, Brasil

**Abstract:** Research on behavior of flat slabs under punching shear, performed by Kinnunen, Regan and Muttoni influenced the main design recommendations. Meanwhile, studies about strut and tie model developed by Schlaich for beams, deep beams and corbels also influenced these design codes. This work aimed to adapt the strut and tie model for the punching shear resistance analysis in flat slabs. The punching shear resistance of 30 flat slabs verified through strut and tie model was compared to the one designed following Brazilian, American and European codes recommendation. Subsequently, this same model was validated by comparing the test results of 32 flat slabs. The strut and tie model results, when compared with the test results, showed a better average than those from codes, and the modified strut and tie model can become an alternative for punching shear strength prediction.

**Keywords:** flat slab, punching shear, strut and tie model.

**Resumo:** Pesquisas sobre punção em lajes lisas, realizadas por Kinnunen, Regan e Muttoni influenciaram sobremaneira as principais recomendações normativas. Enquanto isso, os estudos sobre o modelo de bielas e tirantes desenvolvido por Schlaich para vigas, vigas paredes e consolos também influenciaram essas normas. Este trabalho teve o objetivo de adaptar o modelo de bielas e tirantes para a análise da resistência à punção em lajes lisas. Comparou-se a resistência à punção de 30 lajes lisas calculadas via modelo de bielas e tirantes com a resistência calculadas pelas normas brasileira, americana e européia. Posteriormente, este mesmo modelo foi validado comparando com os resultados experimentais de 32 lajes lisas. Os resultados do modelo de bielas e tirantes, quando comparados aos experimentais, apresentaram melhor média que as estimativas normativas, podendo o modelo modificado se tornar uma alternativa para estimar a resistência ao puncionamento.

**Palavras-chave:** laje lisa, punção, modelo de bielas e tirantes.

## 1 INTRODUCTION

Punching shear is a type of fragile failure that occurs in flat slabs. The reaction of the column on the slab leads to the appearance of principal stresses that create a punching shear cone. This cone can cause the slab to completely disconnect with the column, providing a redistribution of efforts and a possible progressive collapse in the structure. The strut and tie model (STM) was developed by Schlaich et al. [1] through an idealization of an imaginary truss within the structure, in the ultimate limit state, where the compression fields are called struts and are the truss bars represented by concrete, while the tensile fields are called ties and are the bars of the truss represented by the reinforcements.

Subsequently, Schäfer & Schlaich [2], [3] defined criteria for choosing the most appropriate truss model for each structural part. Currently, this model is extremely well accepted in the analysis of beams, wall beams, corbels, etc.

The recent inclusion of STM for the most diverse analyzes in the concrete standards, together with the simplicity of the method, justify its adaptation for analysis of punching in flat slabs. Furthermore, it is a subject of great scientific utility due to the high potential for application in flat slabs with the most diverse contour conditions and physical and mechanical properties, including shear reinforcement. Thus, to present an alternative to satisfactorily estimate the punching shear resistance of reinforced concrete flat slabs, the modified STM was applied to tested slabs from works in the literature and the results found were better than those estimated by the codes analyzed here.

## 2 PUNCHING SHEAR IN FLAT SLABS

The first relevant mechanical model for punching shear analysis in flat slabs came with the studies by Kinnunen & Nylander [4]. They tested 61 circular slabs without shear reinforcement on circular columns. Experimental observations on cracks and deformations were the basis for the classic model. As the load increased, radial cracks appeared on the top face of the slab and, subsequently, a circumferential crack outlined "slices" of a slab. These "slices" of the slab were deformed by rotating around a center, causing the crushing of the compressed area on the bottom face of the slab. The model by Kinnunen & Nylander [4] correlates the punching shear resistance of the flat slab with the balance of forces that cause this crushing of the compressed area of the slab (Figure 1).
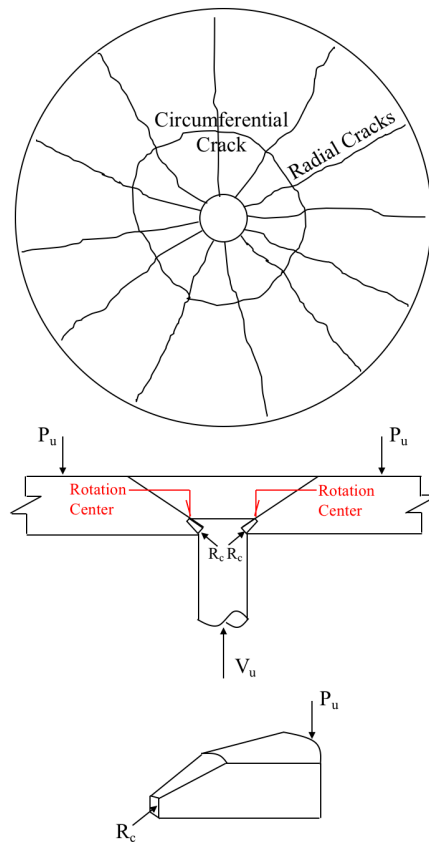


**Figure 1.** Mechanical model by Kinnunen & Nylander [4].

It is also worth highlighting the important contribution of Regan's and Regan & Bræstrup's experimental works [5], [6], [7]. In these works, the author has always tried to calibrate the equations adopted by the codes with the experimental findings of the various analyzed slabs. One of the most important findings in these publications was that the increase in the bending reinforcement rate increases the punching shear resistance to slab.

Muttoni [8] developed the theory of critical shear cracking observing that the punching shear resistance curve in flat slabs was inversely proportional to the slab rotation curve. Thus, the increase in the opening of the critical crack causes the punching shear failure in the slab (Figure 2). Based on this observation, the author considered the load-rotation relationship, thus being able to find a value for the slab punching shear resistance.
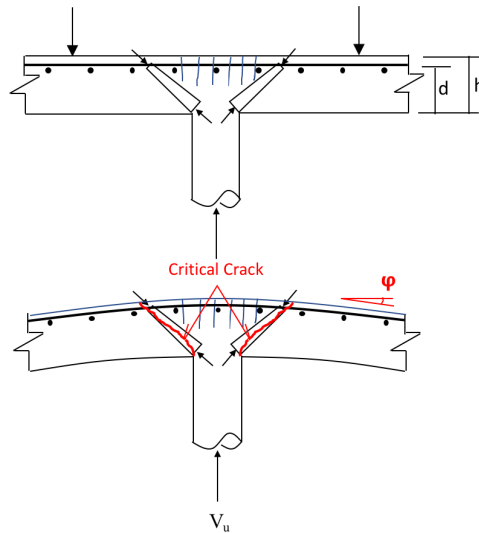


**Figure 2.** Muttoni's Critical Shear Crack Theory [8].

The most interesting thing is to note that the three different theories validate themselves. For example: Regan [5], [6], [7] states that increasing the reinforcement rate increases the punching shear resistance. With the increase in the reinforcement rate, there is a reduction in the rotation observed by Muttoni [8], which confirms the increase of the punching shear resistance. With the reduction of the slab rotation, there is a reduction of the compression in the compressed zone of Kinnunen & Nylander [4] which confirms the increase of the punching shear resistance.

## 2.1 STM applied to flat slabs

Muttoni [8] showed that the critical crack appears in the compression strut, with the slab rotation. Kinnunen & Nylander [4] found experimentally that after the slab rotation, the compressed zone, in the STM represented by the CCC node, is crushed in the instant of the punching shear failure. Putting this two information together, in this article, a STM was conceived where the punching shear failure was characterized when the model's CCC node was crushed.

In this work, to estimate the punching shear resistance in flat slabs, without shear reinforcement, a STM was proposed for each axis. One STM on the X axis, with the bending reinforcement of the X axis, and another on the Y axis, with the reinforcement of the Y axis. It was assumed as a model hypothesis that the ties would be the longitudinal reinforcement within the central band "c+1.5·d". The struts would be the compression fields that would connect the CCC node to the tie (Figure 3). The limit compression stress of $0.85 \cdot f_c$ was adopted for the CCC node, as recommended by NBR 6118 [9]. The value of the punching shear load estimated by this method is the sum of the vertical reactions of the X-axis and Y-axis models, through the balance of forces at the CCC node (Equation 1).

$$V_{MBT} = 2 \cdot \left( T_x \cdot tg\left(\theta\right)_x + T_y \cdot tg\left(\theta\right)_y \right) \tag{1}$$

The values of $T_x$, $T_y$, $tg(\theta)_x$ and $tg(\theta)_y$ can be found using equations 2, 3, 4 and 5.

$$T_x = A_{s,x} \cdot f_{s,x} \quad T_y = A_{s,y} \cdot f_{s,y} \tag{2}$$

Rev. IBRACON Estrut. Mater., vol. 14, no. 5, e14506, 2021

3/13

$$h_{node,x} = \frac{T_x}{(0.85 \cdot f_c) \cdot c_y} \quad h_{node,y} = \frac{T_y}{(0.85 \cdot f_c) \cdot c_x} \tag{3}$$

$$z_x = d - \frac{1}{2} \cdot h_{Nó,x} \quad z_y = d - \frac{1}{2} \cdot h_{Nó,y} \tag{4}$$

$$tg(\theta)_x = \frac{z_x}{2 \cdot d} \quad tg(\theta)_y = \frac{z_y}{2 \cdot d} \tag{5}$$

Where:

$V_{STM}$ = punching shear resistance for flat slab without shear reinforcement via STM;

$f_c$ = compressive resistance of concrete;

$A_{s,x}$ e $A_{s,y}$ = steel area on the x and y axes, respectively;

$f_{s,x}$ e $f_{s,y}$ = stress in the longitudinal reinforcements of the x and y axes, respectively ($f_{s,x} = E_{s,x} \cdot \varepsilon_{s,x} \le f_{y,x}$ and $f_{s,y} = E_{s,y} \cdot \varepsilon_{s,y} \le f_{y,y}$);

$d = (d_x + d_y)/2$ = average effective depth;

$T_x$ e $T_y$ = normal forces in the ties of the x and y axis models, respectively;

$h_{Node,x}$ e $h_{Node,y}$ = height of the CCC node for the x and y axes, respectively;

$z_x$ e $z_y$ = distance between the axis of the longitudinal reinforcement and half the height of the node for the x and y axes, respectively;

$c_x$ e $c_y$ = dimensions of the support on the x and y axes, respectively;

$(\theta)_x$ e $(\theta)_y$ = inclination angle of the compressed strut for models on the x and y axes, respectively.
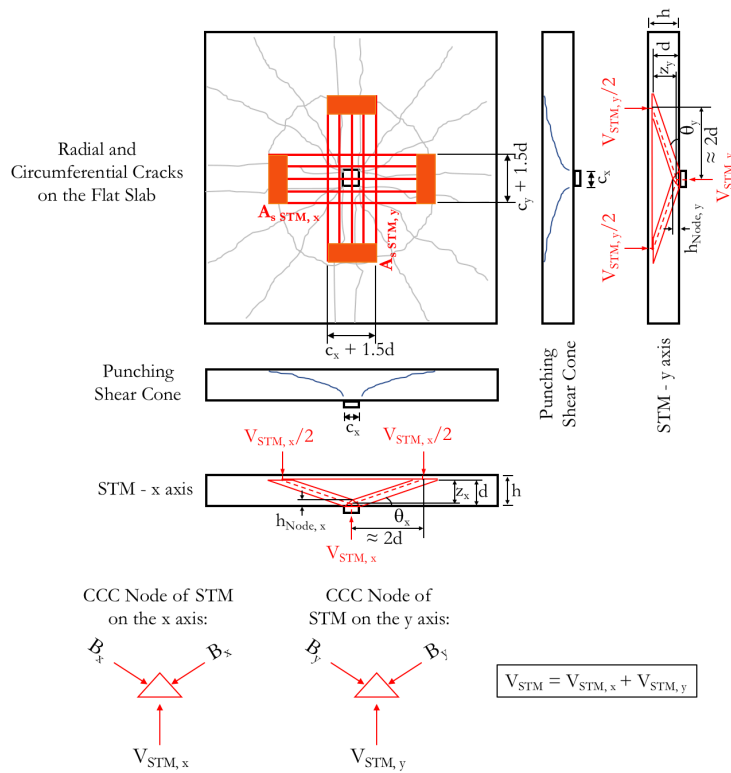


**Figure 3.** Strut and tie model proposed.

Rev. IBRACON Estrut. Mater., vol. 14, no. 5, e14506, 2021

4/13

Figure 4 shows the STM on the X axis with the efforts made compatible with the strains of the slab. In the study, the efforts of the $B_x$ strut crush the CCC node, and how the STM is inside of a slab in flexure, in the face between the node and the strut the stress and the strain were considered $0.85 \cdot f_c$ and 3.5‰, respectively. Tension in the longitudinal reinforcement ($f_{sx}$) can be estimated by comparing the factors $k_{h\,node,\,x}$ with $k_{Lim,\,x}$. The relation $k_{h\,node,\,x}$ if less than or equal to $k_{Lim,\,x}$ indicates that the reinforcements have yielded ($f_{s,\,x} = f_{y,\,x}$), otherwise, the reinforcements would be in the elastic regime ($f_{s,\,x} = E_{s,\,x} \cdot \varepsilon_{s,\,x}$). The same procedure applies to STM on the Y axis.
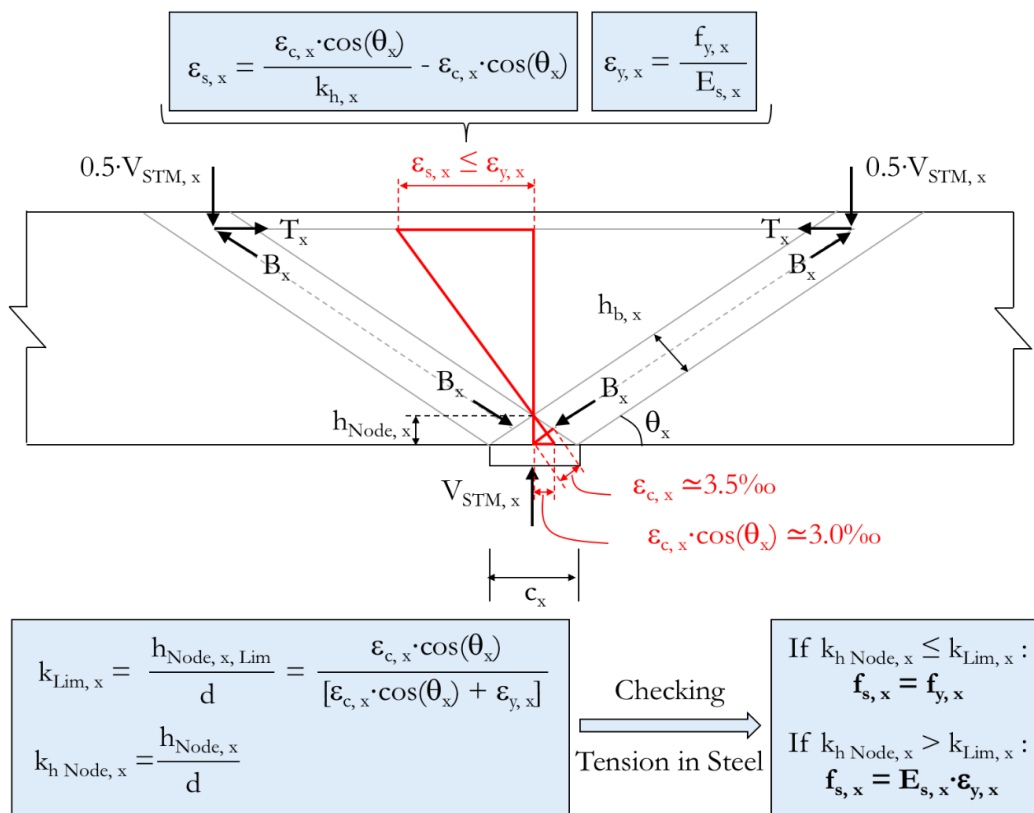


**Figure 4.** Compatibility of efforts with strains in the STM on X-axis.

Other researchers had similar ideas for estimating punching shear resistance in slabs. In 2012, Rizk, Marzouk and Tiller [10] devised a STM for calculating the punching shear resistance for thick flat slabs. The peculiarity of this model was the conical shape, simulating the punching shear failure cone. In 2016, Bompa & Onet [11] also suggested an alternative equation based on STM for punching shear. The model proposed in this work was a function directly of the Mohr-Coulomb theory for plane stress state. Unlike these studies, the STM proposed in this work originated from the classic Schlaich truss and through the balance of the efforts of the CCC node in the punching shear failure.

## 2.2 Code recommendations

### 2.2.1 ACI 318 [12]

The American code [12] estimates the punching shear failure load ($V_{ACI}$), for flat slabs without shear reinforcement, through the lowest result among Equations 6, 7 and 8. Being $f_c$ the compressive strength of concrete (limited to 70 MPa), $\beta_c$ the ratio between the largest and smallest column dimensions, $\alpha_s$ the constant that assumes a value equal to 40 for internal columns or 30 for edge columns or 20 for corner columns, d the effective depth and $u_1$ the control perimeter according to ACI 318 (Figure 5).

$$V_{ACI} = 0.33 \cdot \sqrt{f_c} \cdot u_1 \cdot d \tag{6}$$

$$V_{ACI} = 0.17 \cdot \left(1 + \frac{2}{\beta_c}\right) \cdot \sqrt{f_c} \cdot u_1 \cdot d \tag{7}$$

$$V_{ACI} = 0.083 \cdot \left(2 + \frac{\alpha_s\, d}{u_1}\right) \cdot \sqrt{f_c} \cdot u_1 \cdot d \tag{8}$$

### 2.2.2 Eurocode 2 (EC2)

The European code EC2 [13] estimates the punching shear failure load ($V_{EC}$), for flat slabs without shear reinforcement, according to Equation 9. In this equation, $\rho_l$ is the longitudinal reinforcement rate and not greater than 0.02, $\xi = \left(1 + \sqrt{200/d}\right) \leq 2.0$ and $u_1$ is the control perimeter according to EC2 (Figure 5).

EC2 recommends that the 0.18 coefficient is divided by a safe factor $\gamma_c$. However, in this research, it was decided to remove any safe factor ($\gamma_c = 1.0$), to compare code estimates with experimental results.

$$V_{EC} = 0.18 \cdot \xi \cdot \left(100 \cdot \rho_l \cdot f_c\right)^{\frac{1}{3}} \cdot u_1 \cdot d \tag{9}$$

### 2.2.3 NBR 6118

The Brazilian code estimates the punching shear failure load ($V_{NBR}$), for flat slabs without shear reinforcement, according to Equation 10. Being: $\xi = \left(1 + \sqrt{200/d}\right)$ and $u_1$ equal to the control perimeter according to NBR 6118 (Figure 5). It is worth mentioning that NBR 6118 does not limit the size effect ($\xi$) nor the longitudinal reinforcement rate ($\rho_l$), different of the EC2.

Unlike EC2, NBR 6118 has a formula with the coefficient 0.13 with a safe factor already built in. Using the same reasoning as EC2, it was decided to remove this safe factor, for this reason, the NBR 6118 coefficient was 0.18 ($1.4 \cdot 0.13 = 0.18$).

$$V_{NBR} = 0.18 \cdot \xi \cdot \left(100 \cdot \rho_l \cdot f_c\right)^{\frac{1}{3}} \cdot u_1 \cdot d \tag{10}$$



(a) ACI 318      (b) EC2 and NBR 6118
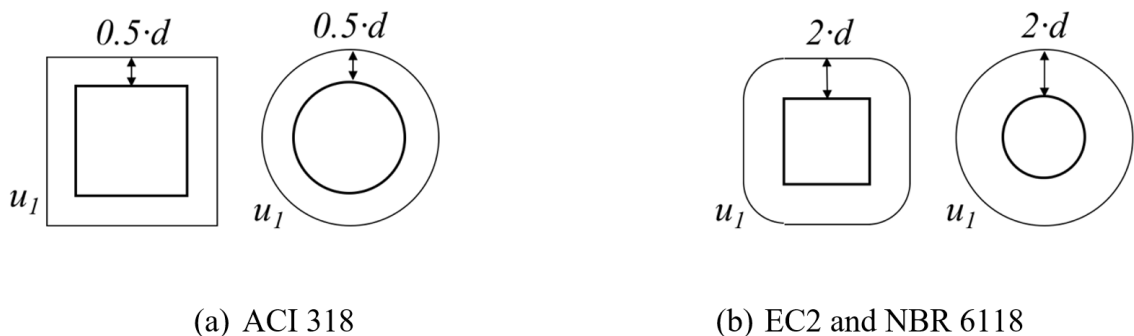
**Figure 5.** Control perimeters according to ACI 318, EC2 and NBR 6118.

### 2.3 Analyzed slabs

In this research, 30 idealized flat slabs of reinforced concrete without shear reinforcement were initially analyzed, divided into 3 groups of 10 slabs each. In group A, slabs A1 to A10 varied only the reinforcement rates ($\rho$) between 0.59% to 1.10%. In group B, slabs B1 to B10 varied only the compressive strength of the concrete ($f_c$) between 30 MPa and 48 MPa. In group C,

slabs C1 to C10 varied only the width (c) of the square supports between 120 mm to 165 mm (Table 1) (Figure 6). All 30 slabs had a height (h) equal to 180 mm, an effective depth (d) equal to 160 mm, reinforcement yield stress ($f_y$) equal to 500 MPa and a size of 2220 mm × 2220 mm. These slabs should be tested experimentally, in another stage of the research, therefore, the choice of this reduced size. It is also worth mentioning that this research is purely qualitative, where it was intended to compare the slabs of reduced size between them. At no time was the intention to do a quantitative research, where the models are correlated with full-scale prototypes. In addition, in this same article, in order to validate the strut and tie model proposed, the model results were compared with the experimental results of 32 flat slabs (18 by Regan [5], [6], [7], 1 by Marzouk & Hussein [14], 6 by Moe [15] and 7 by Elstner & Hognestad [16]).

**Table 1.** Data from the analyzed slabs.

| Slabs | $f_c$ | c | Codes c+6d | STM c+1.5d | $A_{s, Total}$ | Codes $A_{s, Prop}$ | STM $A_{s, Prop}$ | $\rho_l$ |
|---|---|---|---|---|---|---|---|---|
| | (MPa) | (mm) | (mm) | (mm) | (mm²) | (mm²) | (mm²) | (%) |
| A1 | | | | | 2107.20 | 1053.60 | 370.18 | 0.59 |
| A2 | | | | | 2307.20 | 1153.60 | 405.32 | 0.65 |
| A3 | | | | | 2507.20 | 1253.60 | 440.45 | 0.71 |
| A4 | | | | | 2707.20 | 1353.60 | 475.59 | 0.76 |
| A5 | 30 | 150 | 1110 | 390 | 2907.20 | 1453.60 | 510.72 | 0.82 |
| A6 | | | | | 3107.20 | 1553.60 | 545.86 | 0.87 |
| A7 | | | | | 3307.20 | 1653.60 | 580.99 | 0.93 |
| A8 | | | | | 3507.20 | 1753.60 | 616.13 | 0.99 |
| A9 | | | | | 3707.20 | 1853.60 | 651.26 | 1.04 |
| A10 | | | | | 3907.20 | 1953.60 | 686.40 | 1.10 |
| B1 | 30 | | | | | | | |
| B2 | 32 | | | | | | | |
| B3 | 34 | | | | | | | |
| B4 | 36 | | | | | | | |
| B5 | 38 | 150 | 1080 | 390 | 3907.20 | 1953.60 | 686.40 | 1.10 |
| B6 | 40 | | | | | | | |
| B7 | 42 | | | | | | | |
| B8 | 44 | | | | | | | |
| B9 | 46 | | | | | | | |
| B10 | 48 | | | | | | | |
| C1 | | 120 | 1080 | 360 | | 1900.80 | 633.60 | |
| C2 | | 125 | 1085 | 365 | | 1909.60 | 642.40 | |
| C3 | | 130 | 1090 | 370 | | 1918.40 | 651.20 | |
| C4 | | 135 | 1095 | 375 | | 1927.20 | 660.00 | |
| C5 | 30 | 140 | 1100 | 380 | 3907.20 | 1936.00 | 668.80 | 1.10 |
| C6 | | 145 | 1105 | 385 | | 1944.80 | 677.60 | |
| C7 | | 150 | 1110 | 390 | | 1953.60 | 686.40 | |
| C8 | | 155 | 1115 | 395 | | 1962.40 | 695.20 | |
| C9 | | 160 | 1120 | 400 | | 1971.20 | 704.00 | |
| C10 | | 165 | 1125 | 405 | | 1980.00 | 712.80 | |

To calculate the reinforcement rate of the codes, only the reinforcements within the central band "c+6d" were considered, as recommended by EC2 and NBR6118, and for the adopted STM, only the reinforcements within the central band "c+1.5d" were considered. The hypothesis that the width "c+1.5d" was the most adequate was proven when the results of the STM ($V_{STM}$) were compared, using bands of "c+d", "c+1.5d" and "c+2d", with the experimental results ($V_u$) presented in the course of that paper. The ratio ($V_{STM}/V_u$), when using the "c+d" band, presented an average equal to 0.87, standard deviation equal to 0.11 and coefficient of variation equal to 12.26%, when using the "c+1.5d", presented an average of 0.97, standard deviation equal to 0.11 and a variation coefficient of 11.51% and when using the "c+2d", presented an average equal to 1.04, standard deviation equal to 0.14 and a variation coefficient equal to 13.06%.
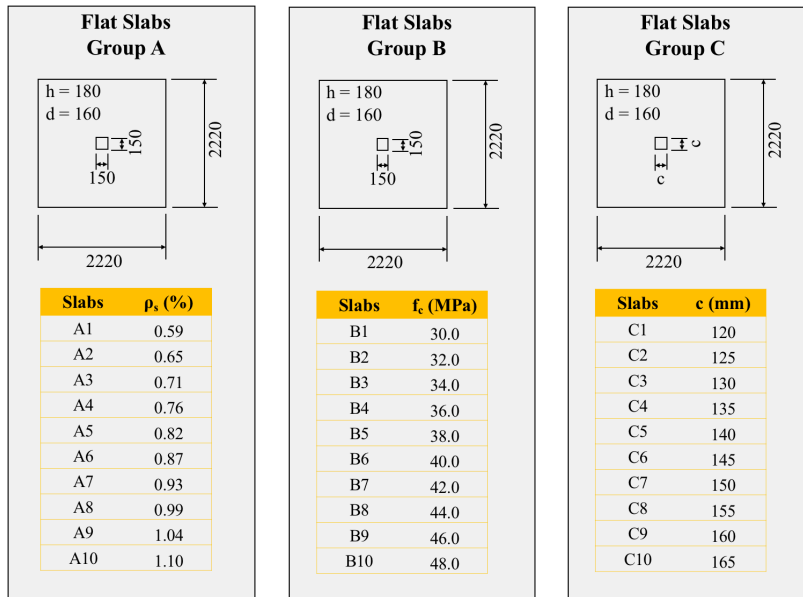
**Figure 6.** Slabs from groups A, B and C.

## 3 RESULTS AND DISCUSSIONS

It was observed that the STM results for group A slabs were closer to the EC2 estimates, with the average of $(V_{STM}/V_{EC})$ equal to 0.93, while they were farther from the ACI 318 estimates, with the average $(V_{STM}/V_{ACI})$ equal to 1.14 (Table 2). Figure 7 shows that STM, NBR 6118 and EC2 increase the punching shear resistance with the increase in the bending reinforcement rate, while the ACI 318 remains constant.
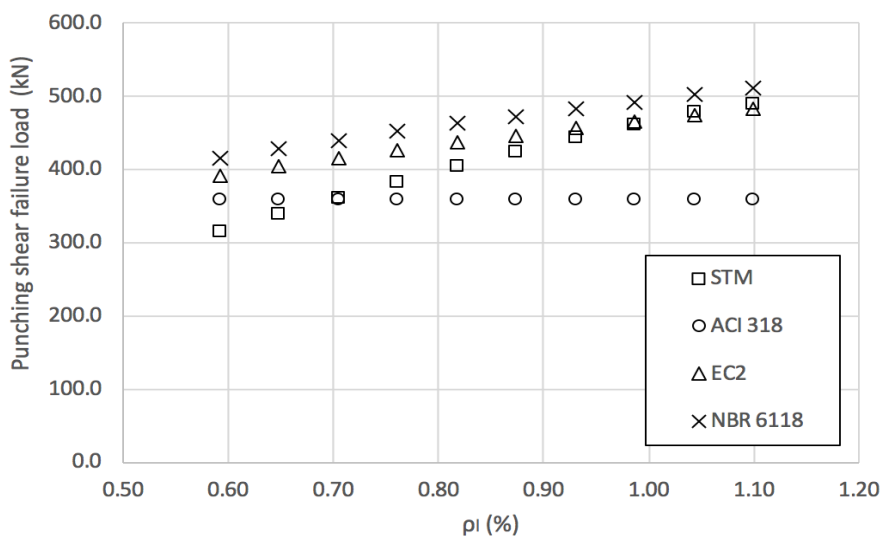


**Figure 7.** Longitudinal reinforcement rate versus punching shear resistance - Group A slabs.

Rev. IBRACON Estrut. Mater., vol. 14, no. 5, e14506, 2021

8/13

It was noted that the STM results for group B slabs were closer to the EC2 estimates, with the average of $(V_{STM}/V_{EC})$ equal to 1.02, followed by NBR 6118, with the average of $(V_{STM}/V_{NBR})$ equal to 0.96, while ACI 318 again presented the most distant results, with the average of $(V_{STM}/V_{ACI})$ equal to 1.31 (Table 2). Figure 8 shows that STM, NBR 6118, EC2 and ACI 318 increase the resistance with the increasing of the compressive resistance of the concrete.
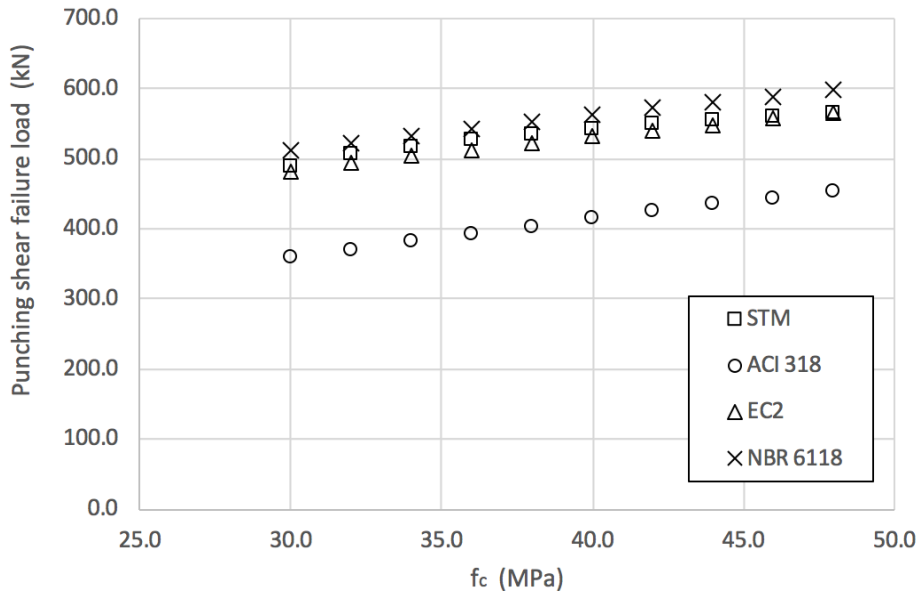


**Figure 8.** Resistance to concrete compression versus punching shear resistance - Group B slabs.

It was observed that the STM results for group C slabs were closer to the EC2 estimates, with the average of $(V_{STM}/V_{EC})$ equal to 0.93, followed by NBR 6118, with the average of $(V_{STM}/V_{NBR})$ equal to 0.88, while ACI 318 again presented the most distant results, with the average of $(V_{STM}/V_{ACI})$ equal to 1.27 (Table 2). Figure 9 shows that the STM, NBR 6118, EC2 and ACI 318 increase the resistance with the increasing of the size of the support, and for supports with $c \leq 140$ mm, the results of the STM move away from the results of the EC2.
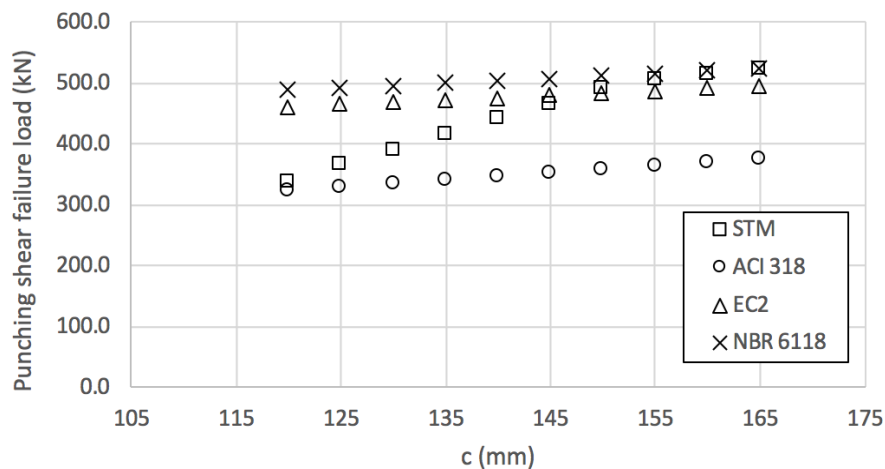


**Figure 9.** Support dimension versus punching shear resistance - Group C slabs.

Table 2 shows that as the size of the support decreases, the result of the STM decreases to a greater proportion than the codes estimates. Particularly in EC2, the slabs C5 (c = 140mm), C4 (c = 135mm), C3 (c = 130mm), C2 (c = 125mm) and C1 (c = 120mm) presented the $V_{STM}/V_{EC}$ ratios of 0.93, 0.88, 0.84, 0.79 and 0.74, respectively. This is because Equation 3 overestimates the height of the node and consequently underestimates punching shear resistance ($V_{STM}$), for columns with width less than or equal to 140 mm.

**Table 2.** Results of the analyzed slabs.

| Slabs | $V_{STM}$ (kN) | $V_{STM}/V_{ACI}$ | $V_{STM}/V_{EC}$ | $V_{STM}/V_{NBR}$ |
|---|---|---|---|---|
| Varying $\rho_l$ between 0.59% and 1.10% | | | | |
| A1 | 314.2 | 0.88 | 0.80 | 0.76 |
| A2 | 338.2 | 0.94 | 0.84 | 0.79 |
| A3 | 361.2 | 1.01 | 0.87 | 0.82 |
| A4 | 383.2 | 1.07 | 0.90 | 0.85 |
| A5 | 404.2 | 1.13 | 0.92 | 0.87 |
| A6 | 424.1 | 1.18 | 0.95 | 0.90 |
| A7 | 443.1 | 1.24 | 0.97 | 0.92 |
| A8 | 461.1 | 1.29 | 0.99 | 0.94 |
| A9 | 478.0 | 1.33 | 1.01 | 0.95 |
| A10 | 489.9 | 1.37 | 1.02 | 0.96 |
| Average | | 1.14 | 0.93 | 0.87 |
| Standard Deviation | | 0.14 | 0.06 | 0.06 |
| Coefficient of variation (%) | | 12.09 | 6.57 | 6.57 |
| Varying $f_c$ between 30 MPa and 48 MPa | | | | |
| B1 | 489.9 | 1.37 | 1.02 | 0.96 |
| B2 | 506.0 | 1.37 | 1.03 | 0.97 |
| B3 | 516.6 | 1.35 | 1.03 | 0.97 |
| B4 | 526.0 | 1.34 | 1.03 | 0.97 |
| B5 | 534.5 | 1.32 | 1.02 | 0.97 |
| B6 | 542.1 | 1.31 | 1.02 | 0.96 |
| B7 | 548.9 | 1.29 | 1.02 | 0.96 |
| B8 | 555.2 | 1.28 | 1.01 | 0.96 |
| B9 | 560.9 | 1.26 | 1.01 | 0.95 |
| B10 | 566.1 | 1.25 | 1.00 | 0.95 |
| Average | | 1.31 | 1.02 | 0.96 |
| Standard Deviation | | 0.04 | 0.01 | 0.01 |
| Coefficient of variation (%) | | 2.71 | 0.66 | 0.66 |
| Varying $c$ between 120 mm and 165 mm | | | | |
| C1 | 338.6 | 1.05 | 0.74 | 0.69 |
| C2 | 364.8 | 1.11 | 0.79 | 0.74 |
| C3 | 390.6 | 1.16 | 0.84 | 0.79 |
| C4 | 415.9 | 1.22 | 0.88 | 0.83 |
| C5 | 440.9 | 1.27 | 0.93 | 0.88 |
| C6 | 465.6 | 1.32 | 0.97 | 0.92 |
| C7 | 489.9 | 1.37 | 1.02 | 0.96 |
| C8 | 504.1 | 1.38 | 1.04 | 0.98 |
| C9 | 514.2 | 1.39 | 1.05 | 0.99 |
| C10 | 524.1 | 1.39 | 1.06 | 1.00 |
| Average | | 1.27 | 0.93 | 0.88 |
| Standard Deviation | | 0.11 | 0.10 | 0.09 |
| Coefficient of variation (%) | | 8.35 | 10.42 | 10.42 |

To approximate the results of STM and EC2, for slabs with supports of c ≤ 140 mm, a hypothetical value of $c_{new,\,x}$ and $c_{new,\,y}$ can be used in the calculation of STM, according to Equations 11 and 12.

Rev. IBRACON Estrut. Mater., vol. 14, no. 5, e14506, 2021

10/13

$$c_{new,\ x} = k_x \cdot c_x \quad c_{new,\ y} = k_y \cdot c_y \tag{11}$$

$$k_x = 2.11 - 1.36 \cdot \left(\frac{c_x}{h}\right) \quad k_y = 2.11 - 1.36 \cdot \left(\frac{c_y}{h}\right) \tag{12}$$

These equations arose from the observation that the correction factor that brings the results from STM to EC2 ($k_x$ e $k_y$) is linearly proportional to the relation of the support width ($c_x$ e $c_y$) divided by the slab height (h). With this simple correction, for slabs with c ≤ 140 mm, the ratios ($V_{STM}/V_{EC}$) of slabs C5 to C1 that were from 0.93 to 0.74, as shown in Table 2, became 1.01 to 1.00.

To validate the model experimentally, the punching shear resistance of 32 flat slabs was calculated (18 by Regan [5], [6], [7], 1 by Marzouk & Hussein [14], 6 by Moe [15] and 7 by Elstner & Hognestad [16]), using the STM, and compared with the experimental results (Table 3). The results in general were satisfactory. When compared with the experimental results, STM was the one with the best average, with ($V_{STM}/V_u$) equal to 0.97, followed by NBR 6118 with ($V_{NBR}/V_u$) equal to 1.04 and EC2 with ($V_{EC}/V_u$) equal to 0.87, while ACI was the one with the worst average with ($V_{ACI}/V_u$) equal to 0.76.

**Table 3.** Data and experimental results from slabs of Regan [5], [6], [7], Marzouk & Hussein [14], Moe [15] and Elster & Hognestad [16].

| Slabs | $f_c$ MPa | $f_y$ MPa | $E_s$ GPa | c mm | d mm | h mm | $\rho_l$ % | $V_u$ (kN) | $V_{STM}/V_u$ | $V_{ACI}/V_u$ | $V_{EC}/V_u$ | $V_{NBR}/V_u$ |
|---|---|---|---|---|---|---|---|---|---|---|---|---|
| | | | | | | Regan | | | | | | |
| I/2 | 23.4 | 500 | 200 | 200 | 77 | 100 | 1.20 | 176.0 | 1.26 | 0.77 | 0.85 | 1.10 |
| I/4 | 32.3 | 500 | 200 | 200 | 77 | 100 | 0.90 | 194.0 | 0.98 | 0.82 | 0.78 | 1.01 |
| I/6 | 21.9 | 480 | 200 | 200 | 79 | 100 | 0.80 | 165.0 | 0.98 | 0.83 | 0.80 | 1.04 |
| I/7 | 30.4 | 480 | 200 | 200 | 79 | 100 | 0.80 | 186.0 | 0.92 | 0.86 | 0.79 | 1.03 |
| II/1 | 34.9 | 530 | 200 | 250 | 200 | 250 | 1.00 | 825.0 | 1.14 | 0.85 | 1.00 | 1.00 |
| II/2 | 33.3 | 485 | 200 | 160 | 128 | 160 | 1.00 | 390.0 | 0.91 | 0.72 | 0.85 | 0.96 |
| II/3 | 34.3 | 485 | 200 | 160 | 128 | 160 | 1.00 | 365.0 | 0.98 | 0.78 | 0.92 | 1.04 |
| II/4 | 33.3 | 480 | 200 | 80 | 64 | 80 | 1.00 | 117.0 | 0.75 | 0.60 | 0.71 | 0.99 |
| II/5 | 34.3 | 480 | 200 | 80 | 64 | 80 | 1.00 | 105.0 | 0.84 | 0.68 | 0.80 | 1.11 |
| II/6 | 36.2 | 480 | 200 | 80 | 64 | 80 | 1.00 | 105.0 | 0.85 | 0.70 | 0.82 | 1.13 |
| III/1 | 23.2 | 494 | 200 | 150 | 95 | 120 | 0.80 | 197.0 | 0.90 | 0.75 | 0.82 | 1.01 |
| III/3 | 37.8 | 494 | 200 | 150 | 95 | 120 | 0.80 | 214.0 | 0.90 | 0.88 | 0.89 | 1.09 |
| III/5 | 26.8 | 464 | 200 | 150 | 93 | 120 | 1.50 | 214.0 | 1.19 | 0.72 | 0.95 | 1.17 |
| III/6 | 42.6 | 464 | 200 | 150 | 93 | 120 | 1.50 | 248.0 | 1.23 | 0.79 | 0.95 | 1.18 |
| V/1 | 34.3 | 628 | 200 | 54 | 118 | 150 | 0.80 | 170.0 | 0.50 | 0.92 | 1.28 | 1.47 |
| V/2 | 32.2 | 628 | 200 | 170 | 118 | 150 | 0.80 | 280.0 | 1.19 | 0.91 | 0.97 | 1.12 |
| V/3 | 32.4 | 628 | 200 | 110 | 118 | 150 | 0.80 | 265.0 | 0.98 | 0.76 | 0.91 | 1.05 |
| V/4 | 36.2 | 628 | 200 | 102 | 118 | 150 | 0.80 | 285.0 | 0.90 | 0.72 | 0.87 | 1.00 |
| | | | | | | Marzouk & Hussein | | | | | | |
| NS1 | 42.0 | 490 | 200 | 150 | 95 | 120 | 1.50 | 320.0 | 1.02 | 0.62 | 0.76 | 0.93 |
| | | | | | | Moe | | | | | | |
| S1-60 | 23.3 | 399 | 179 | 254 | 114 | 152 | 1.10 | 389.0 | 0.89 | 0.69 | 0.76 | 0.89 |
| S1-70 | 24.5 | 483 | 171 | 254 | 114 | 152 | 1.10 | 393.0 | 1.03 | 0.70 | 0.77 | 0.89 |
| S5-60 | 22.2 | 399 | 179 | 203 | 114 | 152 | 1.10 | 343.0 | 0.86 | 0.66 | 0.78 | 0.91 |
| S5-70 | 23.0 | 483 | 171 | 203 | 114 | 152 | 1.10 | 378.0 | 0.90 | 0.61 | 0.72 | 0.83 |
| H1 | 26.1 | 328 | 195 | 254 | 114 | 152 | 1.10 | 372.0 | 0.81 | 0.76 | 0.83 | 0.96 |
| M1A | 20.8 | 481 | 195 | 305 | 114 | 152 | 1.50 | 433.0 | 1.03 | 0.66 | 0.79 | 0.92 |
| | | | | | | Elster & Hognestad | | | | | | |
| A-1b | 25.2 | 332 | 200 | 254 | 118 | 152 | 1.20 | 365.0 | 0.94 | 0.80 | 0.91 | 1.04 |
| A-1c | 29.0 | 332 | 200 | 254 | 118 | 152 | 1.20 | 356.0 | 0.98 | 0.88 | 0.97 | 1.12 |
| A-1d | 36.6 | 332 | 200 | 254 | 118 | 152 | 1.20 | 351.0 | 1.03 | 1.00 | 1.07 | 1.23 |
| A-1e | 20.3 | 332 | 200 | 254 | 118 | 152 | 1.20 | 356.0 | 0.92 | 0.73 | 0.86 | 0.99 |
| A-7b | 27.9 | 321 | 200 | 254 | 114 | 152 | 2.50 | 512.0 | 1.09 | 0.57 | 0.81 | 0.94 |

Rev. IBRACON Estrut. Mater., vol. 14, no. 5, e14506, 2021

11/13

**Table 3.** Continued…

| Slabs | $f_c$ MPa | $f_y$ MPa | $E_s$ GPa | c mm | d mm | h mm | $\rho_l$ % | $V_u$ (kN) | $V_{STM} / V_u$ | $V_{ACI} / V_u$ | $V_{EC} / V_u$ | $V_{NBR} / V_u$ |
|---|---|---|---|---|---|---|---|---|---|---|---|---|
| A-4 | 26.1 | 332 | 200 | 356 | 118 | 152 | 1.20 | 400.0 | 1.08 | 0.94 | 0.97 | 1.12 |
| B-9 | 43.9 | 341 | 200 | 254 | 114 | 152 | 2.00 | 505.0 | 1.11 | 0.73 | 0.88 | 1.03 |
| Average | | | | | | | | | 0.97 | 0.76 | 0.87 | 1.04 |
| Standard Deviation | | | | | | | | | 0.11 | 0.08 | 0.09 | 0.09 |
| Coefficient of variation (%) | | | | | | | | | 11.51 | 11.09 | 9.83 | 8.44 |

However, the result of the slab V/1 via STM stood out negatively, presenting the ratio ($V_{STM}/V_u$) equal to 0.50. This slab had the support with c = 54 mm. When recalculated using Equations 11 and 12, the ratio ($V_{STM}/V_u$) went from 0.50 to 1.27. However, it is worth mentioning that for this slab, the result that came closest to the experimental one was ACI ($V_{ACI}/V_u$) with 0.92, followed by STM ($V_{STM}/V_u$) with 1.27, EC2 ($V_{EC}/V_u$) with 1.28 and NBR 6118 ($V_{NBR}/V_u$) with 1.47.

## 4 CONCLUSIONS

In this work, a STM adapted for the calculation of punching shear resistance in flat slabs was presented. The results of this model were compared with codes for the analysis of 30 slabs, divided into 3 groups of 10 slabs: with different: average compressive strength $f_c$ (group A), bending reinforcement rate $\rho$ (group B) and dimension of the support c (group C). In addition, the results of this model were also compared with the experimental results of 32 flat slabs, 18 by Regan [5], [6], [7], 1 by Marzouk & Hussein [14], 6 by Moe [15] and 7 by Elstner & Hognestad [16]. When compared with the experimental results, it was observed that the STM results were the ones that came closest, followed by the NBR6118 estimates. When analyzing the 30 slabs of groups A, B and C, it was noted that the STM results were closer to the results of EC2 and NBR 6118. For columns with width less than or equal to 140 mm, the results of the proposed model decrease more than the norms, however, when the correction using the $c_{new}$ ($c_{new, x} = k_x \cdot c$ e $c_{new, y} = k_y \cdot c$) was used, the results of the modified strut and tie model returned to the EC2 estimates again. Finally, it was noted that the ACI 318 underestimated the resistance of the slabs more than the other codes and the STM. However, more theoretical, computational, and experimental analyzes are needed for more comprehensive conclusions.

## ACKNOWLEDGEMENTS

## REFERENCES

[1] J. Schlaich, K. Schafer, and M. Jennewein, "Toward a consistent design of structural concrete," *PCI-Journal Chic.*, vol. 32, no. 3, pp. 74–150, May./Jun. 1987.

[2] K. Schafer and J. Schlaich, Consistent design of structural concrete using strut and tie models, in *Colóquio sobre Comportam. Projeto de Estrut*, Rio de Janeiro, RJ, Brasil, 1988.

[3] K. Schafer and J. Schlaich, "Design and detailing of structural concrete using strut-and-tie models," *Struct. Eng. (Lond.)*, vol. 69, no. 06, pp. 113–125, 1991.

[4] S. Kinnunen and H. Nylander, *Punching of Concrete Slabs Without Shear Reinforcement*, no. 158, Stockholm, Sweden: Transactions of the Royal Institute of Technology, 1960, 112 pp.

[5] P. E. Regan, "Symmetric punching of reinforced concrete slabs," *Mag. Concr. Res. Lond.*, vol. 38, no. 136, pp. 115–128, Sep 1986.

[6] P. E. Regan, *Behavior of Reinforced Concrete Flat Slabs*, Report 89. London: Construction Industry Research and Information Association (CIRIA), Feb. 1981, 89 pp.

[7] P. E. Regan and M. W. Bræstrup, *Punching Shear in Reinforced Concrete* (Bulletin d›Information, No. 168). London: Comité Euro-International du Béton, Jan. 1985, 232 pp.

[8] A. Muttoni, "Punching shear strength of reinforced concrete slabs without transverse reinforcement," *ACI Struct. J. Farmington Hills*, vol. 105, no. 4, pp. 440–450, Jul./Aug. 2008.

[9] Associação Brasileira de Normas Técnicas, *Design of Concrete Structures – Procedure,* NBR 6118, 2014.

[10] E. Rizk, H. Marzouk, and R. Tiller, "Design of thick concrete plates using strut-and-tie model," *ACI Struct. J. Farmington Hills*, vol. 109, no. 5, pp. 677–686, 2012.

Rev. IBRACON Estrut. Mater., vol. 14, no. 5, e14506, 2021

12/13

[11] D. V. Bompa and T. Onet, "Punching shear strength of rc flat slabs at interior connections to columns," *Mag. Concr. Res. Lond.*, vol. 68, no. 1, pp. 24–42, 2016.

[12] American Concrete Institute, *Building Code Requirements for Structural Concrete and Commentary,* ACI 318M-14, 2014.

[13] British Codes Institution, *Design of Concrete Structures, Part 1, General codes and codes for buildings, DD ENV,* EUROCODE 2, 2010.

[14] H. Marzouk and A. Hussein, "Experimental investigation on the behavior of high-strength concrete slabs," *ACI Struct. J. Farmington Hills*, vol. 88, no. 6, pp. 701–713, Nov./Dec. 1991.

[15] J. Moe, *Shearing Strength of Reinforced Concrete Slabs and Footings Under Concentrated Loads. Development Department Bulletin D47*, Skokie, Illinois: Portland Cement Association, Apr. 1961, 129 pp.

[16] R. C. Elstner and E. Hognestad, "Shearing strength of reinforced concrete slabs," *ACI Struct. J. Farmington Hills*, vol. 53, no. 1, pp. 29–58, Jul 1956.

---

# IBRACON Structures and Materials Journal
## Revista IBRACON de Estruturas e Materiais

ORIGINAL ARTICLE

# Flexure shear capacity of prestressed hollow core slabs

## Resistência à flexo-cortante de lajes alveolares protendidas

Bruna Catoia[a] iD
Arthur Lima Rocha[a] iD
Marcelo de Araújo Ferreira[a] iD

[a]Universidade Federal de São Carlos – UFSCar, Departamento de Engenharia Civil, São Carlos, SP, Brasil

**Abstract:** Provided that the anchorage capacity is guaranteed at the supports, the bearing capacity of hollow core slabs depends on the shear capacity of the pretensioned concrete webs, wherein the critical section is in a region between h and 2h from the support. For line loads acting within 2h to 6h from the supports, especially for shallow slabs 150 to 200 mm deep, it is likely to have flexure-shear cracks within the transfer region, wherein the bearing capacity is highly affected by the actual prestressing forces at the critical section. Therefore, one of the major questions pondered by structural engineers is to determine the effective amount of prestressing force that affects the shear resistance mechanism near to the support. According to ABNT NBR 14861:2011, the shear capacity is based on the flexure-shear mechanism, wherein the shear strength is a sum of the tensile concrete strength in the slab webs plus the contribution of the prestressing forces at the critical section, wherein a coefficient of 0.15 is considered. However, in both codes NBR 14861 and NBR 6118 it is required that this coefficient 0.15 should be further multiplied by an additional reduction factor in order to take into account the effect of the transmission length near to the support. Considering the current revision of the NBR 14861, this paper presents a theoretical-experimental comparison from standard shear tests of hollow core slabs with nominal depths from 150 to 200 mm carried out in different research at NETPre-UFSCar. Based on the analytical study of each term of the equation for the flexure-shear capacity, it has been observed that the coefficient 0.15 provides a conservative limit for the contribution of the actual prestressing force. Therefore, there is no need to apply any additional reduction factor in order to guarantee a safe design limit for the shear capacity.

**Keywords:** hollow core slabs, precast concrete, flexure-shear, shear capacity.

**Resumo:** A resistência ao cisalhamento das lajes alveolares protendidas sem armadura transversal é influenciada por diferentes fatores, como a altura útil da laje, a largura total das nervuras dos alvéolos, a resistência à tração do concreto e a tensão da protensão efetiva na seção crítica. A equação recomendada na NBR 14861:2011 está associada ao mecanismo flexo-cortante que ocorre na situação da presença de fissuração por flexão na laje alveolar fora da região do comprimento de transferência próxima aos apoios, sendo obtida pela soma da contribuição da seção transversal de concreto e da contribuição da força de protensão efetiva na região crítica próxima ao apoio. No caso da expressão normativa em questão, a parcela decorrente da contribuição da protensão é considerada multiplicando-se a tensão de protensão por um fator redutor (0.15) com a intenção de considerar a tensão atuante efetiva na seção crítica para a resistência à flexo-cortante. No entanto, nos textos normativos em vigência da NBR 14861:2011 e NBR 6118:2014, além desse fator de redução presente no equacionamento, é prescrita redução adicional na tensão de protensão com o intuito de considerar o efeito da protensão efetiva no comprimento de transferência. Assim, este artigo apresenta um estudo do fator redutor de multiplicação (0.15) da tensão de protensão na equação da resistência à flexo-cortante, baseado na comparação de resultados de ensaios padronizados de cisalhamento em lajes alveolares protendidas realizados em pesquisas no NETPre-UFSCar. A partir do confronto dos resultados experimentais com as previsões teóricas, estudando os termos analíticos da equação em questão, foi possível demonstrar que o fator de redução 0.15 já representa um limite inferior para a contribuição da força atuante de protensão na seção crítica da região próxima ao apoio e, portanto, já considera o efeito da variação da protensão efetiva no comprimento de transferência, não necessitando de fatores adicionais.

**Palavras-chave:** lajes alveolares, concreto pré-moldado, flexo-cortante, capacidade ao cisalhamento.

# 1 INTRODUCTION

The use of precast systems provides an effective improvement for the site construction, with a higher rationalization of the production processes and better quality control of the final building systems. Worldwide, hollow core slabs are the main product within the precast concrete industry. This trend is due mainly to a combination of high structural performances with standardized production methods, with choice of depth and capacity, speed of construction, environmental friendliness without the need for molding and propping on site. Hollow core slabs are produced in casting beds with lengths from 100 to 150 meters, wherein strands positioned in one or two rows within the bottom flange area, aligned with the webs, are pretensioned from 1000 to 1500 MPa, without the presence of transverse reinforcement. The first prestressed hollow core slabs produced in Brazil were 150, 200 or 265 mm in thickness.

According to Lindström [1], the effective prestressing stress that contributes to the shear capacity depends on the transmission length at the slab ends, which also depends on the bond stresses and level of prestressing and type of strand or wire. For the flexure-shear mechanism, wherein there is a possibility of occurrence of bending cracks within 2h from 6h from the slab support, it is essential that the anchorage capacity is secured in order to avoid any failure by bond-slip at the supports. For detailed analysis, the design value for shear force needs to be checked against the design shear capacity at all critical points in the region of cracked in bending for the given value of design load, wherein the bending moment at a specific position needs to be increased due to the inclined shear flexure crack. In the presence of imposed concentrated loads, also according to Lindström [1], there is a real possibility of occurrence of interaction between flexure-shear and bending mechanisms, wherein they cannot be utilized at their respective maximum capacities.

According to the Brazilian code of practice for hollow core slabs NBR 14861 [2], the shear capacity is based on the flexure-shear mechanism of prestressed concrete slabs with and without structural toppings according to the FIB Bulletin 6 [3] for hollow core slabs, which coincides with the Brazilian code of practice for structural concrete NBR 6118 [4], both inspired in the CEB-FIP Model Code 1978 [5]. As explained by Marquesi [6], this expression was modified from early expressions presented by Walraven and Mercx [7], based on experimental studies on rectangular beams and solid slabs elements, considering the main parameters that affect the shear capacity. Within the normative documents NBR 14861 [2] and NBR 6118 [4], the coefficient 0.15 that affects the actual prestressing force (after losses) needs to be multiplied by an additional reduction factor in order to take into account the effect of the transmission length for the shear capacity mechanism at the support region of the slab.

Considering the current revision of the NBR 14861, this paper presents an experimental-theoretical comparison from results of standard shear tests of hollow core slabs with depths varying from 150 to 200 mm, which were carried out at NETPre-UFSCar, analyzing the contribution of each parcel of the expression for the flexure-shear capacity in order to verify if the coefficient 0.15 is enough to consider the contribution of the actual prestressing force or if there is still the need to apply any additional reduction factor in order to take in account the effect of the transmission length for the flexure-shear capacity.

# 2 LITERATURE REVIEW

## 2.1 Failure mechanisms

In general, hollow core slabs can present different failure mechanisms: loss of anchorage due to bond-slip of the tendons; tension failure due to shear at the critical point in the web; shear in a cracked region (with combined effects of shear, flexure, and bond-slip); combined effects of shear and torsion (in elements that are not perfect planes); flexure (ULS), with great possibility, close to failure, strand slip near to the support; interaction of bending and shear mechanisms.

From several tests, Kong et al. [8] concluded that the failure mode is strongly affected by the relationship between the span subjected to shear ($a_v$) and the effective height (d). Depending on the type of applied loading, a given failure mechanism will prevail over the other one, or there might be a combination of these two mechanisms.

In Figure 1 the main failure modes can be observed, which are described as follows.
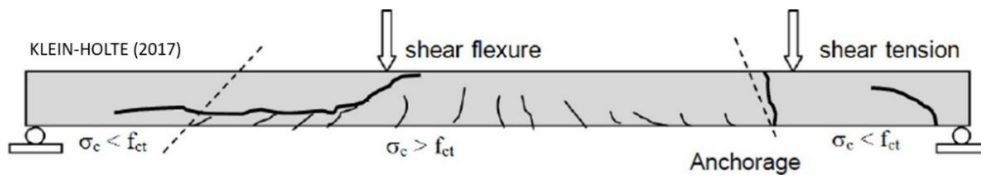
**Figure 1.** Main failure modes in hollow core slabs [9].

### 2.1.1 Shear failure

The tension shear failure corresponds to an important design criterion for prestressed hollow core slabs. Although the failure mechanism is quite clear, it is difficult to accurately determine the tensile strength according to the theoretical consideration. Thus, it was developed a standard test method to determine the tension shear capacity as well as to gain greater knowledge concerning to different parameters related to the performance of the slabs.

In that cases where the concrete tensile strength is higher than the normal stresses at the bottom surface of prestressed hollow core slabs, without flexural cracks, it is possible to occur an inclined shear crack in the web (Figure 2). The diagonal crack spreads in both directions, ascending and descending, and results in a brittle failure.
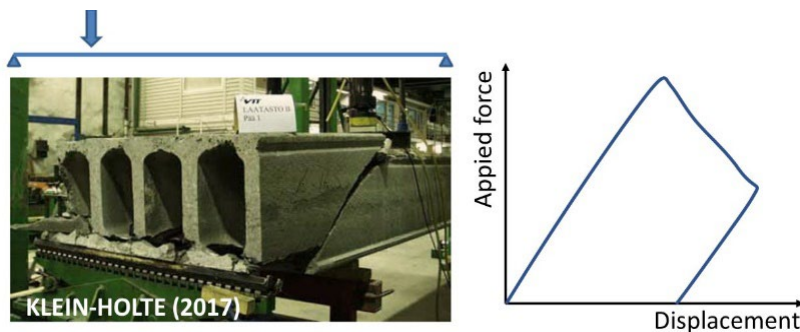


**Figure 2.** Shear Main failure.

The crack is usually formed in the region where the favorable influence of the vertical normal stress caused by the support reaction [10], and the prestressing force has not yet fully developed. This mechanism characterizes a type of brittle failure. Thus, a crack in the web close to the support can usually lead to tension shear failure due to the fact that the webs of the prestressed hollow core slab are generally very narrow, and there is no shear reinforcement.

### 2.1.2 Flexure failure

When the slab is subjected to positive bending moments generating normal stresses in the lower fibers that are higher than the concrete tensile strength, then bending cracks will occur on the bottom surface of the slab. Provided that no compression failure occurs in the concrete at the top fibers of the slab section, there will be a ductile failure.

### 2.1.3 Flexure-shear failure

Considering a slab subjected to shear with the presence of bending cracks, the distribution of tangential stresses along the section leads to an increase of tension in the bottom fibers of the slab, in the region of the strand, resulting in an interaction between flexural cracks and diagonal shear cracks. Thus, in regions where shear and bending mechanisms interact, bending cracks can propagate to the inclined shear cracks, and the failure mechanism is not always well defined because it can result from the interaction or combination of mechanisms (Figure 3).
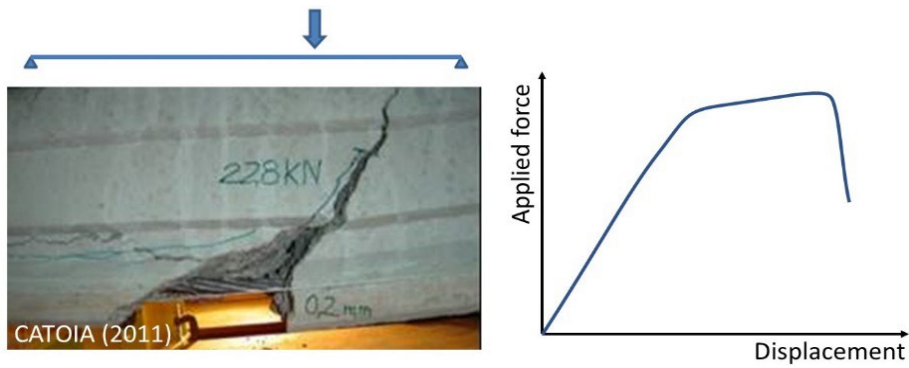
**Figure 3.** Failure due to interaction between bending moment and shear.

### 2.1.4 Anchorage failure

The required length for transferring the entire prestressing force to the concrete is called transmission length ($l_{bpt}$). Along this length, the prestressing force develops approximately according to a parabolic function, as can be seen in Figure 4.
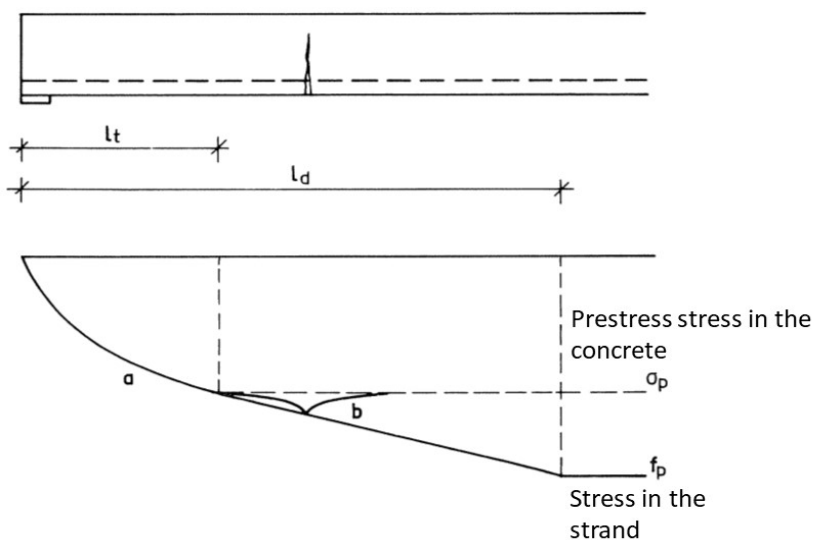


**Figure 4.** Critical situation of cracking in the anchorage failure [7].

The transfer of prestress along the transmission length is essential for the structural behavior of hollow core slabs. The bond-slip of the tendons must be measured to control whether the required bond strength has been exceeded. The maximum allowed slip depends on the allowed transmission length.

According to Walraven and Mercx [7], if somewhere along the transmission length (region a, Figure 4), a flexural crack appears, it will be difficult to increase the tension in the steel, due to the limit state of equilibrium that exists in that area. If the crack occurs outside the transmission length, an increase in the steel tension is possible. On both sides of the crack (region b), the steel tension is increased over a certain length as long as it is sufficient to transmit the additional strength in the tendons by the bond stress. However, if the steel stress due to cracking is very large and invades the region where the prestressing stress is not fully transferred to the concrete (region a, in Figure 4), the equilibrium along the transfer region is disturbed, causing the slip of the tendons. If the distance from the end of the element is large enough, the ultimate tension in the tendons can be achieved. This distance is called the development or regularization length ($l_d$). A typical force versus displacement curve for an anchorage failure mechanism is illustrated in Figure 5.
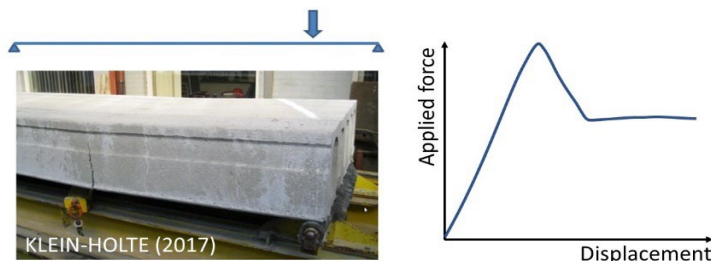
**Figure 5.** Critical situation of cracking in the anchorage failure [9].

## 2.2 Parameters that affect flexure-shear mechanisms

The interaction of shear and flexure mechanisms is difficult to be analyzed due to the complex redistribution of stresses along the section after the start of concrete cracking. Thus, for the calculation of shear strength in cracked regions, empirical equations were developed and calibrated through experimental tests in order to consider the most significant variables such as: the concrete tensile strength and the actual axial stress (due to prestressing).

The main parameters that affect the shear strength in cracked regions are: concrete tensile strength; longitudinal reinforcement rate; scale factor; influence of axial forces (due to prestressing), type, and the aggregate size.

The influence of the concrete tensile strength, reinforcement, scale factor, and prestress are considered in the equation recommended by NBR 14861: 2011 [2], according to Figure 6.



$$V_{Rd1} = [0.25 \cdot f_{ctd} \cdot k \cdot (1.2 + 40\rho_1) + 0.15 \cdot \sigma_{cp}] \cdot b_w \cdot d$$

**Figure 6.** Identification of the parameters considered in the equation recommended by NBR 14861 [2].

## 2.2.1 Contribution of the shear transfer actions

According to Cavagnis et al. [11], the contribution of the basic shear transfer actions along the critical crack in elements without transverse reinforcement can be divided into four parts:
1. Part related to the concrete residual tensile strength contribution ($V_{Res}$);
2. Part related to the dowelling action of longitudinal reinforcement ($V_{dowel}$);
3. Part related to the aggregate interlock contribution ($V_{agg}$);
4. Part related to the contribution of the compression zone ($V_{comp}$).

The combination of these actions can be seen in Figure 7, and are described as follows:

$$V_c = V_{Res} + V_{agg} + V_{dowel} + V_{comp} \tag{1}$$
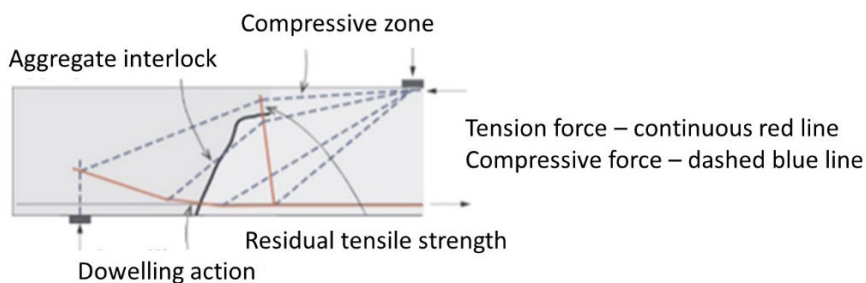


**Figure 7.** Basic shear transfer actions described with strut and tie models [11].

These four mechanisms are responsible for the transmission of a part of the total shear force along the element, as follows:

- $V_{comp}$ corresponds to the shear force transferred through the compressive chord originated by the flexure.
- $V_{Res}$ corresponds to the residual tensile stresses due to "concrete bridges" along the crack. According to Marquesi [6], cracks with widths of up to 0.15 mm are capable of transmitting shear force through residual stresses.
- $V_{agr}$ corresponds to the part of the shear force transmitted through the aggregate interlock. $V_{agr}$ is transferred after the appearance of a flexural crack and retransmitted by the tensile stress in the element web. The existence of significant roughness between the aggregates contributes to prevent the sliding of the crack surfaces. This interlock allows the transmission of oblique forces across the cracks. In the case of concrete with compressive strength up to 70 MPa, cracks occur in the cementitious matrix. On the other hand, for concrete with a compressive strength greater than 70 MPa, the cracks pass through the aggregates, and, thus, the interlock action is lost.
- $V_{dowel}$ corresponds to the part of the shear force transferred by means of dowel action. $V_{dowel}$ is transmitted through the flexural crack by the longitudinal reinforcement, which behaves like a connecting pin between the crack surfaces, being retransmitted by tension in the web section between two adjacent cracks. In addition, the longitudinal reinforcement also helps to prevent further crack widths and contributes to the other transfer mechanisms previously mentioned.

According to Cavagnis et al. [11], shear strength and the strain capacity are related to a criterion of failure, and wherein lower strengths are associated with greater strain capacities (and thus, greater crack widths). Also, the contribution of each shear-transfer action depends on the location of the shear critical crack, its widths and spreading, and its roughness properties. In their studies, Cavagnis et al. [11] concluded that for slender slab members, the failure load is eventually governed by shear transfer actions so that:

✓ For low crack widths, both aggregate interlock and residual tensile strength of concrete play an important role. For large crack widths, aggregate interlock becomes more dominant.

✓ The dowel action of the longitudinal reinforcement exhibits a more limited contribution than the other shear-carrying actions. Yet, its contribution is not necessarily negligible.

✓ The contribution of the inclined compression chord for slender members depends significantly on the location of the tip of the critical shear crack. For critical shear cracks located at a certain distance from the load introduction, its contribution is relatively low.

### 2.2.2 Concrete tensile strength

The concrete tensile strength contribution in the shear strength is taken into account by the Brazilian codes of practice [2], [4] by means of the term $0.25 \cdot f_{ctd}$, as shown in Figure 6. The equation of $V_{Rd1}$ (Figure 6) prescribed by Brazilian codes corresponds to a similar equation employed by the previous version of EC2 [12]. According to the EC2 Commentary [13], there was a change in the formula recommended by EC2 due to high values of standard deviations obtained in elements composed of high-strength concrete, above 50 MPa. However, this reality does not apply to slabs commonly used in Brazil, whose concrete usually has a strength around 50 MPa.

### 2.2.3 Influence of the axial prestressing force in the shear strength

Tension forces present in a structural element favor the appearance of cracks and contribute to the increasing of the existing cracks widths, reducing the shear strength. On the other hand, the compression forces are able to delay the appearance of cracks and to contribute to the "closing" of existing cracks, ensuring the transfer of efforts.

In the equations recommended by EC2 [12] and Brazilian codes, the influence of axial stress in shear strength is considered through the term $(0.15 \cdot \sigma_{cp} \cdot b_w \cdot d)$, positive for compression and negative for tension. This $(0.15 \cdot \sigma_{cp} \cdot b_w \cdot d)$ originally comes from the prestressing contribution and is later extrapolated for the contribution of any axial effort in the shear strength.

### 2.2.4 Transfer length

The transfer length is defined as the bonded length between concrete and the tendon that is required to develop an effective prestressing force in both within the anchorage zone [14]. The transfer length is essential to the shear resistance

Rev. IBRACON Estrut. Mater., vol. 14, no. 5, e14507, 2021

6/17

design, even more in precast hollow core slabs that do not have shear reinforcement. However, it is exceedingly difficult to determinate this parameter due to its variability.

In the anchorage zone of pre-tensioned concrete elements (such as hollow core slabs), some extremely important parameters must be considered, as such:

- Transfer length of prestressing strands/wire ($l_{bpt}$): necessary length to transfer the prestress tension from the strand/wire to the concrete.
- Regularization length ($l_p$): necessary length to distribute the prestress tension through the concrete cross-section.
- Anchorage length ($l_{bpd}$): necessary length to anchorage in the concrete all the tension in the strand/wire, in Ultimate Limit State.

The bond between concrete and reinforcement exists because of three different mechanisms: bond by adhesion, bond by friction, and mechanical bond

Bond by adhesion originates from the physicochemical bond between the concrete slurry and the reinforcement. This bond has a small resistance and is lost when small slips happen.

Bond by friction happens due to the surface roughness of all the components and the transverse compression of the reinforcement. This transverse compression happens because the reinforcement attempts to return to its initial diameter after the release of the prestress, being gradually prevented by the concrete surrounding it (without prevention in external cross-section and totally prevented after a certain length). Such a situation is called the Hoyer effect, but it is necessary to identify the hollow core slab's design situation.

The mechanical bond exists due to the reinforcement protrusions (strands or wires), causing the interlock between the rebars and the surrounding compressed concrete.

Through these three mechanisms, it is possible to understand that the bond stress between concrete and reinforcement. Assuming that this bond tension is constant, Eurocode 2 [12] presents a formulation to verify it, considering the type of reinforcement, the bond condition, and the tensile strength at the moment of the release of prestress. The name of this bond stress is $f_{bpt}$ and can be determined by Equation 2.

$$f_{bpt} = \eta_{p1} \cdot \eta_1 \cdot f_{ctd} \tag{2}$$

Where:

$\eta_{p1}$: Coefficient that takes into account the type of tendon;

$\eta_1$: Coefficient that takes into account the bond situation at release. It is 1 for good bond condition and 0.7 otherwise.

$f_{ctd}$: is the design tensile value of strength at the time of release.

Considering this bond stress as constant, it can be assumed that the prestress will be transferred to the concrete through a determined transfer length $l_{bpt}$. This length, assuming the Eurocode 2 [12] method, is calculated by Equation 3:

$$l_{bpt} = \alpha_1 \cdot \alpha_2 \cdot \phi \cdot \frac{\sigma_{mp0}}{f_{bpt}} \tag{3}$$

Where:

$\alpha_1$: Coefficient that takes into account the type of prestress release, using 1 for gradual release and 1.25 for sudden release.

$\alpha_2$: Coefficient that takes into account the cross-section of the reinforcement, using 0.25 for circular cross-section and 0.19 for 3 and 7-wire strands.

$\phi$: is the nominal diameter of the tendon.

$\sigma_{mp0}$: is the tendon stress just after the release.

As described, the transfer length must be modified accordingly to the verification made (tendon slippage, shear strength, spalling, among others). It occurs due to the change in the diameter of the tendon according to the existent stress, modifying the transverse compression stress (bond by friction). The Eurocode 2 [12] presents the possibilities of the transfer length using $l_{pt1}$ and $l_{pt}$, (modifications of the $l_{bpt}$). These lengths are used accordingly to the necessary verification. Their values are:

$$l_{pt1} = 0.8 \cdot l_{bpt} \tag{4}$$

$$l_{pt2} = 1.2 \cdot l_{bpt} \tag{5}$$

Thereby, the increase of stress in a tendon generates a bigger transfer length, so the study of a hollow core slab in the Ultimate Limit State considers the higher value $l_{pt2}$.

## 2.3 Determination of flexure-shear strength

At the beginning of the research on prestressed hollow core slabs in Brazil, related to the study of their shear capacity, the aim was to observe if the equation recommended by the NBR 6118 [4] would need adjustments to represent the behavior of hollow core slabs with shallow slabs, between 150 to 200 mm deep, which were the main heights produced in Brazil at that time.

The research carried out by Fernandes [15] helped to define the standard test to determine the flexure-shear capacity of prestressed hollow core slabs, which was not included in any Brazilian code until then, after a significant number of tests were performed inside of precast factories in Brazil. It helped to detail a test procedure based on the quality control manual of FIP [16].

In the research carried out by Catoia [17], 65 tests were assembled, varying the typology of the slabs (different depths, with or without a cast in place topping and filled core), to verify if the recommended equation in the code NBR 6118 [4] would be capable to represent the usual behavior of the slabs. Typical slabs produced in four different industries in Brazil were used. Moreover, the recommended equations of ACI [18] and EC2 [12] were verified too. From an extensive study, it was possible to observe that if considered a force applied in a distance equal to 2.5 h from the support axis, the results obtained at tests were more approximated to the results obtained using the equation of the code NBR 6118 [4] than for the values reached using the equations of ACI [18] and EC2 [12], accordingly to the Figure 8. It was found that the equation recommended by the EC2 [12] gives results more conservative than the values obtained in experiments, and the equation recommended by ACI [18] presents a better approximation when the force is applied more distant from the support axis of the slab (near to 5.75h). In her research, Catoia [17] contributed to a better knowledge of the structural behavior of most used hollow core slabs produced in Brazil, in particular, slabs with 150 and 200 mm in height, providing a safe indication that the equation for shear capacity prescribed by the Brazilian code of practice for structural concrete NBR 6118 [4] could be adopted to design of the shear strength of hollow core slabs by the new code NBR 14861 [2], which was still being developed at that time. After that, new researches in Brazil started to focus on the structural performance of slabs with higher depths, wherein it is possible to develop the tension shear mechanism of the slab web, in a region without bending cracks, achieving higher shear capacities but with a brittle manner of failure.
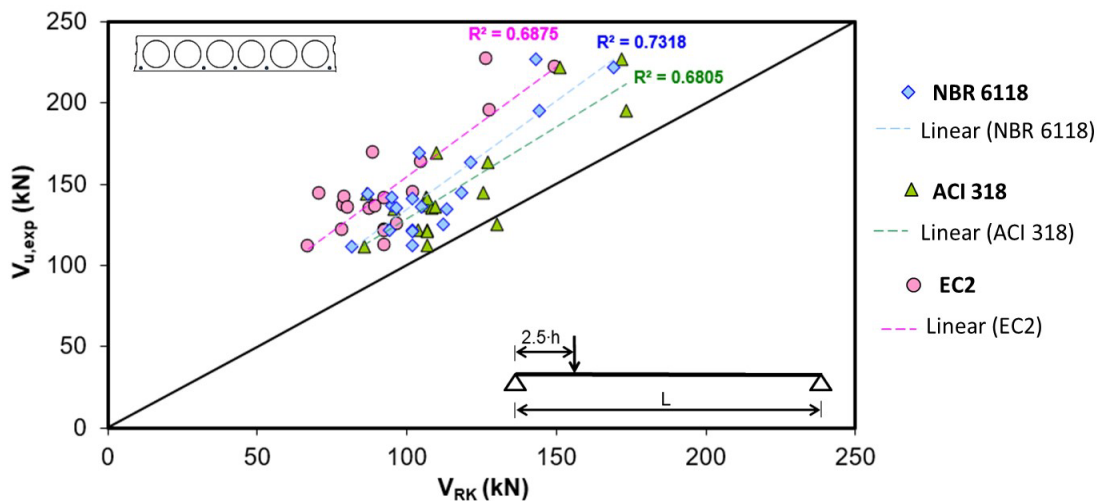


**Figure 8.** Relationship between $V_{u,exp}$ e $V_{Rk}$ considering the use of equations recommended by NBR 6118, EC2 e ACI 318 [17].

## 2.3.1 Origin of the coefficient 0.15

The design models used to determine the shear strength of prestressed hollow core slabs come from experiments considering a rectangular beam section. The contribution parcel of the prestress ($V_p$) can be obtained by an analytical deduction, as shown by Marquesi [6]. Basically, the influence of prestress can be considered based on the principle proposed by Hedman and Losberg [19] that considered the rectangular beam cross-section and propose that in relation to the shear strength, a prestressed beam can be considered as just reinforced beam when the decompression flexure moment is reached. In this context, the shear strength of a prestressed concrete element is the sum of the shear strength of the reinforced concrete and the parcel of the shear force generated by the load responsible for provoking the decompression in cross-section studied, being formulated as:

$$V_{Rd} = V_c + V_p \tag{6}$$

Thus:

$V_c$: shear strength of a reinforced concrete beam;

$V_p$: contribution of the prestress force in the shear strength, being formulated as:

$$V_p = \frac{M_0}{a} \tag{7}$$

Where:

$M_o$: decompression flexure moment;

a: distance of the force to the support axis (Figure 9).
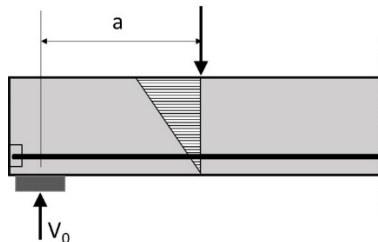


**Figure 9.** Calculation of the prestress contribution in the shear strength. [adapted from 19].

Thus, the calculus of $V_p$ considers $M_0/a$, and the moment $M_o$ is determined by assuming the equilibrium of stresses in the bottom fiber of a prestressed beam, using the equation:

$$\frac{N_p \cdot e_p}{W} + \frac{N_p}{A} - \frac{M_0}{W} = 0$$

Being:

$$W = \frac{I}{y} = \frac{\frac{b \cdot h^3}{12}}{\frac{h}{2}} = \frac{b \cdot h^2}{6}$$

And isolating $M_0$:

Rev. IBRACON Estrut. Mater., vol. 14, no. 5, e14507, 2021

9/17

$$M_0 = N_p \cdot e_p + \frac{N_p}{A} \cdot \frac{b \cdot h^2}{6}$$

Considering

$$V_p = \frac{M_0}{a}$$

Replacing Mo, then:

$$V_p = \left( N_p \cdot e_p + \frac{N_p}{b \cdot h} \cdot \frac{b \cdot h^2}{6} \right) \cdot \frac{1}{a} \quad \rightarrow \quad V_p = \left( N_p \cdot e_p + \frac{N_p \cdot h}{6} \right) \cdot \frac{1}{a}$$

Putting $N_p$ and h in evidence:

$$V_p = N_p \cdot \left( \frac{h}{a} \right) \cdot \left( \frac{e_p}{h} + \frac{1}{6} \right) \tag{10}$$

Considering the effective depth of a cross section as d = 0.85·h [13], h = 1.176·d and then:

$$V_p = 1.18 \cdot N_p \cdot \frac{d}{a} \cdot \left( \frac{e_p}{h} + \frac{1}{6} \right) \tag{11}$$

Assuming $e_p/h = 0.35$ (according to [13], in most shears experiments made by Hedman and Losberg [19] in beams, the relation $e_p/h$ correspond to 0.35), then:

$$V_p = 1.18 \cdot N_p \cdot \frac{d}{a} \cdot (0.35 + 0.166) \quad \rightarrow \quad V_p = 0.608 \cdot \frac{N_p}{\frac{a}{d}} \tag{12}$$

With the distance of the force to the support axis (a) varying from 2.5·d to 4.0·d, it has:
Superior limit (minimum distance a = 2.5·d):

$$V_p = 0.608 \cdot \frac{N_p}{\frac{2.5 \cdot d}{d}} = 0.24 \cdot N_p \quad \rightarrow \quad V_p = 0.24 \cdot \sigma_p \cdot b \cdot d$$

Inferior limit (maximum distance a = 4.0·d):

$$V_p = 0.608 \cdot \frac{N_p}{\frac{4 \cdot d}{d}} = 0.15 \cdot N_p \quad \rightarrow \quad V_p = 0.15 \cdot \sigma_p \cdot b \cdot d$$

Therefore, varying the relation a/d between 2.5·d and 4·d, as it happens in most of shear tests, the parcel of the contribution of the acting prestressing forcers $V_p$ in the shear strength $V_{Rd1}$ will vary from $0.15 \cdot \sigma_p \cdot b \cdot d$ to $0.24 \cdot \sigma_p \cdot b \cdot d$. In such way, the factor 0.15 corresponds to the lower limit.

## 2.3.2 Recommendations based on NBR 14861:2011 and NBR6118:2114

According to item 19.4.1 of the code NBR 6118 [4], solid or ribbed slabs can be executed without transversal reinforcement to resist the tensile force from the shear mechanism when they meet the requirement:

$$V_{Sd} \leq V_{Rd1}$$

Where:

$$V_{Rd1} = \left[ \tau_{Rd} \cdot k \cdot (1.2 + 40 \cdot \rho_1) + 0.15 \cdot \sigma_{cp} \right] \cdot b_w \cdot d \tag{13}$$

$$\tau_{Rd} = 0.25 \cdot f_{ctd} \tag{14}$$

$$f_{ctd} = \frac{f_{ctk,inf}}{\gamma_c} \tag{15}$$

$$\rho_1 = \frac{A_{s1}}{(b_w \cdot d)} \tag{16}$$

$$\sigma_{cp,1} = \left( \frac{N_{sd}}{A_c} \right) \cdot \alpha \tag{17}$$

$k = 1.6 - d \geq 1$ , with d in meters (m)

Where:
$\tau_{Rd}$: design concrete shear strength
$f_{ctd}$ is the design concrete tensile strength at the web the hollow core slab
$b_w$: minimum width of the cross-section in the effective depth d;
$A_{s1}$: tensile reinforcement cross-section area;
$\rho_1$: reinforcement ratio for longitudinal reinforcement only in the hollow core slabs cross-section area;
$\sigma_{cp}$: compression stress due to design prestress force for slabs without filled cores (or with cores filled after the release);
$N_{sd}$: longitudinal force in the section due to prestress or load (consider positive signal to compression)
$A_c$: hollow core slab cross-section area.

Furthermore, in the same item of the referred code, it is also stated that for pre-tensioning it must have an additional reduction in the term $V_p$ in order to consider the effect of the transfer length on the effective prestressing force in order to determine the slab bearing capacity. Thus, the coefficient 0.15 that multiplies the compression stress $\sigma_{cp}$ due to design prestress force needs to be also multiplied by an additional reduction factor. During the process of the preparation of the final text of NBR 14861 [2] a reduction factor called α was incorporated within the calculation of the compression stress $\sigma_{cp}$ with the purpose to take into account the effect of the reduction the prestressing in the prestressing transfer length and thus harmonizing both texts of NBR 14861 and NBR 6118. According to NBR 14861 [2]:

$$\alpha = \frac{l_x}{l_{pt2}} \leq 1 \tag{18}$$

Where: $l_x$: distance of the section x to the end of the slab; $l_{pt2}$: upper design value for the transfer length (fixed in 85·f according to the FIB Bulletin 6 [3]).

However, there was an additional reduction factor α required in order to guarantee the safety of the flexure-shear mechanism of a prestressed concrete slab with or without structural toppings according to the FIB Bulletin 6 [3], also inspired in the CEB-FIP MC1978 [5].

# 3 TESTS TO DETERMINE THE SHEAR CAPACITY OF PRESTRESSED HOLLOW CORE SLABS

As aforesaid, the shear strength of hollow core slabs depends on several factors, such as: concrete tensile strength, geometric shapes of the cores, concrete dosage, and the fabrication process. The concrete tensile strength is difficult to be determined considering the standard methods and the influence of the cross-section shape and of the fabrication method can not be directly determined.

Thus, it was developed a pattern test to determine the shear capacity of hollow core slabs, with the purpose to verify the operation of the extrusion as well as to determine some parameters related to bearing capacity. This pattern test initially was indicated by FIP [16] and by European Code EN 1168 [20], being posteriorly added in NBR 14861 [2].

## 3.1 Characterization of the hollow core slabs

It is important to emphasize that the present study is restricted to the prestressed hollow core slabs with a cross-section composed by circular voids and a maximum height of 210 mm.

In addition, all slabs presented flexure shear failure. The description of the tested slabs can be observed in Table 1.

**Table 1** Characterization of the tested slabs.

| Identification | n° bars | $P_i$ (kN) | $N_{p,00}$ (kN) | $A_c$ (mm²) | $f_{ck}$ (MPa) | $f_{ctk,inf}$ (MPa) | $\Sigma b_w$ (mm) | $d$ (mm) |
|---|---|---|---|---|---|---|---|---|
| L1-15-6D9.5-X | 6 | 79 | 379.2 | 131236 | 55.9 | 3.072 | 463.5 | 115.2 |
| L2-20-8D12.7-X | 8 | 144.5 | 924.8 | 170503 | 48.4 | 2.789 | 411.5 | 167.1 |
| L3-20-6D12.7-Y | 6 | 145 | 696.0 | 135685 | 53.3 | 2.973 | 250.2 | 169.5 |
| L4-20-6D12.7-Y | 6 | 145 | 696.0 | 132400 | 53.5 | 2.980 | 269.3 | 174.8 |
| L5-20-6D12.7-Y | 6 | 145 | 696.0 | 132610 | 53.5 | 2.980 | 269.0 | 168.4 |
| L6-20-7D9.5-Y | 7 | 75 | 420.0 | 130553 | 53.5 | 2.983 | 262.4 | 165.6 |
| L7-20-7D9.5-Y | 7 | 75 | 420.0 | 136572 | 53.5 | 2.983 | 268.7 | 164.7 |
| L8-20-7D9.5-Y | 7 | 75 | 420.0 | 134024 | 53.5 | 2.983 | 263.9 | 167.5 |
| L9-20-7D9.5-Y | 7 | 75 | 420.0 | 135666 | 53.5 | 2.983 | 267.9 | 169.2 |
| L12-20-5D12.7-Z | 5 | 114 | 456.0 | 137795 | 40.0 | 2.456 | 320.0 | 165.0 |
| L13-20-5D12.7-Z | 5 | 114 | 456.0 | 137795 | 40.0 | 2.456 | 320.0 | 165.0 |
| L14-20-5D12.7-Z | 5 | 114 | 456.0 | 137795 | 40.0 | 2.456 | 320.0 | 165.0 |
| L15-20-5D12.7-Z | 5 | 114 | 456.0 | 137795 | 40.0 | 2.456 | 320.0 | 165.0 |
| L17-21-7D9.5-W | 7 | 81.03 | 453.8 | 146064 | 47.0 | 2.735 | 312.5 | 171.4 |
| L18-21-7D9.5-W | 7 | 81.03 | 453.8 | 145948 | 47.0 | 2.735 | 307.0 | 172.9 |
| L25-16-5D9.5-W | 5 | 81.03 | 324.1 | 126449 | 47.0 | 2.735 | 323.5 | 134.6 |
| L26-16-5D9.5-W | 5 | 81.03 | 324.1 | 129085 | 47.0 | 2.735 | 346.5 | 135.7 |

Considered: Total losses of 20%; $A_{s,9.5mm}$=55.5 mm², $A_{s,12.7mm}$=101 mm².

## 3.2 Methodology

To analyze the prestress contribution in the flexure-shear capacity, it was considered an effective reduction factor (called $\alpha_{ef}$) which value was experimentally determined for each tested slab.

### 3.2.1 Shear tests

From several experimental studies and tests carried out by the Research Group for Studies and Technology in Precast Concrete (NETPre) that have been carried out at UFSCar since 2007, it was later systematized a standard procedure for quality control tests of hollow core slabs, which were adapted from the test recommendations from FIP [16] and EN 1168 [20]. The test setup is illustrated in Figure 10 and described as follows.
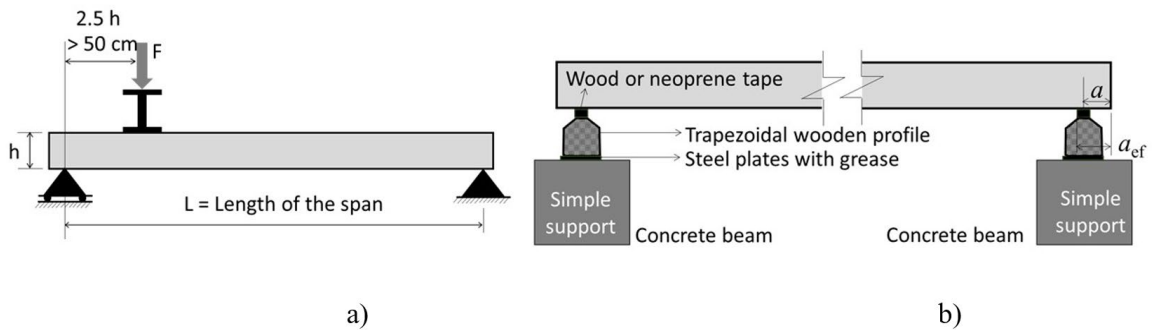
**Figure 10.** a) Layout of the pattern test to determine the shear capacity of hollow core slabs; b) Detail of the support.

Elements with a length of 6 m and actual width were tested under temperatures between 0°C and 40°C. With the purpose of obtaining reference values of concrete strength, cylindrical specimens were tested. These specimens were fabricated with the same conditions employed in the slabs tested, including the same concrete.

In order to obtain an unfavorable effect of flexure on the shear strength mechanism, the load was applied at a distance of 2.5 h (where h is the slab height) from the support, being this distance always greater than 50 cm. The transfer of force to the slab was performed by a rigid steel beam (Figure 10a), with a height of 250 mm. A uniform distribution of forces was ensured over the entire width. Below the steel transfer beam, sand was used to compensate possible irregularities present on the slab surface that prevent its proper leveling.

The supports were composed of a trapezoidal wooden profile positioned on a concrete beam, according to Figure 10b). To guarantee proper transfer of shear force over the support, it was used a wood with a thickness of 10 mm (instead of wood, a neoprene tape could be used). At the end of the slab, next to the force application was created a roller support with the purpose to avoid the appearance of horizontal efforts. The roller support was obtained with the use of grease between two thin steel plates placed between the trapezoidal wooden profile and concrete beam, as shown in Figure 10b).

Hydraulic actuators with a loading capacity of 500 kN were used for continuous application of load (monotonic test) with a speed of around 50 kN/min. The load was applied on the unidirectional roller support located over the transfer steel beam. Load cell (CC) with a capacity of 1000 kN were used to measure the applied force, and linear displacement transducers (TD) were used to measure vertical displacements next to the point of the force application. The experimental tests used in this paper were carried out in the [15] and [17].

It is noteworthy that these correspond to control tests because they simulate a critical design situation, where a concentrated load is applied in a region with the risk of cracking in thin slabs (up to 21 cm).

Figure 11 illustrates the cracking configuration of the slabs L2 and L4 close to the failure. In both slabs, it is possible to observe the interaction of shear and flexure mechanisms.



**Figure 11.** Hollow core slabs submitted to the shear test [17].

### 3.2.2 Determination of $\alpha_{ef}$

According to NBR 14861 [2], it is possible to divide the equation to determine the shear strength of prestressed hollow core slabs into two parcels, one that considers the concrete contribution ($V_{c,1}$) and the other that consider the tendons contribution ($V_{p,1}$), as follows.

$$V_{Rd1} = V_{c,1} + V_{p,1}$$

From the experimental tests, it is possible to determine the shear strength $V_{Ru,exp}$, which can be described by the following equation.

$$V_{Ru,exp} = V_{c,k} + V_{p,k}$$

In this case, $V_{c,k}$, and $V_{p,k}$ corresponds to the characteristic values (without considering any safety factor) of the tendons and concrete contribution, respectively.

Isolating the part related to the tendon's contribution $V_{p,k}$:

$$V_{p,k} = V_{Ru,exp} - V_{c,k}$$

Replacing the equation of $V_{p,k}$ as a function of the reduction factor $\alpha_{ef}$, it is possible to obtain the following equation:

$$V_{p,k} = \alpha_{ef} \cdot \sigma_{cp} \cdot b_w \cdot d = V_{Ru,exp} - V_{c,k}$$

Thus, isolating the reduction factor $\alpha_{ef}$, it is possible to determine its value from the results of shear strength obtained in the tests, as follows:

$$\alpha_{ef} = \frac{V_{Ru,exp} - V_{c,k}}{\sigma_{cp} \cdot b_w \cdot d}$$

Where:

$$V_{c,k} = 0.25 \cdot f_{ctk,inf} \cdot k \cdot (1.2 + 40 \cdot \rho_1) \cdot \Sigma b_w \cdot d \quad ; \quad f_{ctk,inf} = 0.7 \cdot 0.3 \cdot (f_{ck})^{\frac{2}{3}}$$

$$\sigma_{cp} = \frac{N_p}{A_c}$$

## 4 RESULTS AND DISCUSSIONS

From the experimental results of the shear strength ($V_{Ru,exp}$), the values for the contribution of the concrete strength ($V_{c,k}$) and the values of $\alpha_{ef}$ were calculated, which are shown in Table 2. Considering the slabs tested, it has been found an average value of $\alpha_{ef,average} = 0.37$, with values of $\alpha_{ef}$ ranging from 0.21 to 0.65. In addition, it is possible to observe that the slabs with the presence of tendons with 12.7 mm diameter presented lower values of $\alpha_{ef}$ than the slabs with tendons of 9.5 mm diameter (as can be seen in Figure 12). This can be explained due to the fact that slabs with tendons of smaller diameters need shorter lengths for the transfer of prestressing to concrete, which results in lower values of $l_{bpt}$. This means that the smaller area of concrete will not have the prestressing fully distributed, and, consequently, the contribution of prestressing in the slab shear strength will be greater. Thus, the factor $\alpha_{ef}$ that decreases the contribution of prestressing in the shear strength will present higher values. It is noteworthy that the importance of the transfer length

is related to the fact that in cases where the failure of slab occurs due to flexure-shear model, the maximum tensile stress will occur in a place with the greatest interaction between the bending moment and shear stress, that is between 2.5·d and 4·d. It is important to highlight that the strength parcel related to the prestressing also depends on the slab bearing length over the support. The support region provides compression stresses that contribute to the anchorage of the prestress bars, and consequently, with the transfer of the compression stress to the precast concrete element.

**Table 2 D**etermination of the total reduction factor $\alpha_{ef}$

| Identification | k (1.6-d) | $\rho$ | $\sigma_{ci}$ (MPa) | $\sigma_{cp}$ (MPa) | $V_{c,k}$ (kN) | $V_{Ru,exp}$ (kN) | $\alpha_{ef}$ |
|---|---|---|---|---|---|---|---|
| L1-S-15-6D9.5-X_C | 1.485 | 0.0062 | 1.4 | 2.9 | 88.2 | 134.5 | 0.30 |
| L2-S-20-8D12.7-X_C | 1.433 | 0.0118 | 1.4 | 5.4 | 114.7 | 222.4 | 0.29 |
| L3-S-20-6D12.7-Y_C | 1.431 | 0.0143 | 1.4 | 5.1 | 79.9 | 125.1 | 0.21 |
| L4-S-20-6D12.7-Y_C | 1.425 | 0.0129 | 1.4 | 5.3 | 85.7 | 163.5 | 0.31 |
| L5-S-20-6D12.7-Y_C | 1.432 | 0.0134 | 1.4 | 5.2 | 83.8 | 144.5 | 0.26 |
| L6-S-20-7D9.5-Y_C | 1.434 | 0.0089 | 1.4 | 3.2 | 72.4 | 121.7 | 0.35 |
| L7-S-20-7D9.5-Y_C | 1.435 | 0.0088 | 1.4 | 3.1 | 73.5 | 137.0 | 0.47 |
| L8-S-20-7D9.5-Y_C | 1.433 | 0.0088 | 1.4 | 3.1 | 73.3 | 142.2 | 0.50 |
| L9-S-20-7D9.5-Y_C | 1.431 | 0.0086 | 1.4 | 3.1 | 74.6 | 135.4 | 0.43 |
| L12-S-20-5D12.7-Z_C | 1.435 | 0.0096 | 1.1 | 3.3 | 73.6 | 121.4 | 0.27 |
| L13-S-20-5D12.7-Z_C | 1.435 | 0.0096 | 1.1 | 3.3 | 73.6 | 120.8 | 0.27 |
| L14-S-20-5D12.7-Z_C | 1.435 | 0.0096 | 1.1 | 3.3 | 73.6 | 141.2 | 0.39 |
| L15-S-20-5D12.7-Z_C | 1.435 | 0.0096 | 1.1 | 3.3 | 73.6 | 111.9 | 0.22 |
| L17-S-21-7D9.5-W_C | 1.429 | 0.0073 | 1.5 | 3.1 | 78.0 | 136.2 | 0.35 |
| L18-S-21-7D9.5-W_C | 1.427 | 0.0073 | 1.5 | 3.1 | 77.3 | 168.8 | 0.55 |
| L25-S-16-5D9.5-W_C | 1.465 | 0.0064 | 1.5 | 2.6 | 63.5 | 111.1 | 0.43 |
| L26-S-16-5D9.5-W_C | 1.464 | 0.0059 | 1.5 | 2.5 | 67.6 | 144.1 | 0.65 |
| Average | | | | | | | 0.37 |
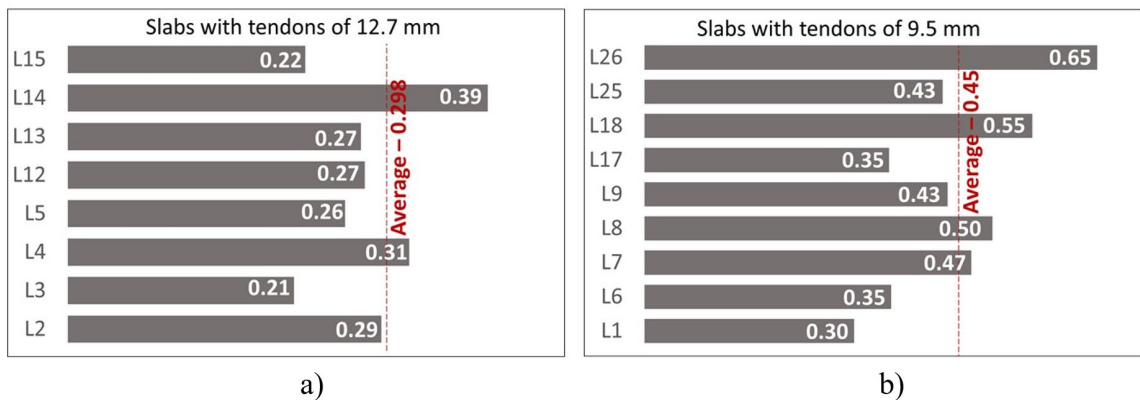


**Figure 12.** a) Values of $\alpha_{ef}$ considering slabs with tendons of 12.7 mm; b) Values of $\alpha_{ef}$ considering slabs with tendons of 9.5 mm.

The study was carried out to calibrate the equation considering the strength value $V_{Rk}$ using $\alpha_{ef}$ of 0.24 (named $V_{Rk (0.24)}$) and of 0.15 (named $V_{Rk (0.15)}$). The relationships between the experimental shear strengths and the characteristic shear strengths can be seen in Figure 13a).

It is possible to observe that most of the experimental results were higher than the characteristic values calculated considering the reduction factors of 0.24 and 0.15. Therefore, the use of the coefficient 0.15 is shown to be a lower limit for the flexure-shear mechanism.

Moreover, the value of the design shear strength ($V_{Rd}$), considering $\gamma_c$ of 1.3 for the calculation of $V_{cd}$ and considering 0.15 for the calculation of $V_p$, was determined and compared with the ultimate experimental strength, as presented in Table 3 and Figure 13b).

**Table 3** Relationship between ultimate experimental shear strength ($V_{Ru,exp}$) and design shear strength considering $\alpha_{ef}$ of 0.15 ($V_{Rd\,(0.15)}$)

| Identification | $V_{Ru,exp}$ (kN) | $V_{Rk\,(0.15)}$ (kN) | $V_{Rd\,(0.15)}$ (kN) | $V_{Ru,exp} / V_{Rd\,(0.15)}$ | $V_{Ru,exp} / V_{Sd}$ |
|---|---|---|---|---|---|
| L1-S-15-6D9.5-X_C | 134.5 | 111.4 | 91.0 | 1.48 | 2.07 |
| L2-S-20-8D12.7-X_C | 222.4 | 170.7 | 144.2 | 1.54 | 2.16 |
| L3-S-20-6D12.7-Y_C | 125.1 | 112.5 | 94.1 | 1.33 | 1.86 |
| L4-S-20-6D12.7-Y_C | 163.5 | 122.8 | 103.0 | 1.59 | 2.23 |
| L5-S-20-6D12.7-Y_C | 144.5 | 119.5 | 100.1 | 1.44 | 2.02 |
| L6-S-20-7D9.5-Y_C | 121.7 | 93.4 | 76.6 | 1.59 | 2.23 |
| L7-S-20-7D9.5-Y_C | 137.0 | 93.9 | 76.9 | 1.78 | 2.49 |
| L8-S-20-7D9.5-Y_C | 142.2 | 94.0 | 77.1 | 1.84 | 2.57 |
| L9-S-20-7D9.5-Y_C | 135.4 | 95.7 | 78.5 | 1.73 | 2.42 |
| L12-S-20-5D12.7-Z_C | 121.4 | 99.8 | 82.8 | 1.47 | 2.06 |
| L13-S-20-5D12.7-Z_C | 120.8 | 99.8 | 82.8 | 1.46 | 2.04 |
| L14-S-20-5D12.7-Z_C | 141.2 | 99.8 | 82.8 | 1.70 | 2.38 |
| L15-S-20-5D12.7-Z_C | 111.9 | 99.8 | 82.8 | 1.35 | 1.89 |
| L17-S-21-7D9.5-W_C | 136.2 | 102.9 | 84.9 | 1.60 | 2.24 |
| L18-S-21-7D9.5-W_C | 168.8 | 102.1 | 84.2 | 2.00 | 2.80 |
| L25-S-16-5D9.5-W_C | 111.1 | 80.2 | 65.6 | 1.69 | 2.37 |
| L26-S-16-5D9.5-W_C | 144.1 | 85.3 | 69.7 | 2.07 | 2.90 |
| Average | | | | 1.63 | 2.28 |

Thus, it was possible to determine an average value of the relationships between experimental values and design values equal to 1.63. In other words, in the average, the experimental values were 63% higher than the theoretically calculated values. In addition, from Table 3, considering the relation $V_{Ru,exp}/V_{Sd}$, for the coefficient $\gamma_f$ of 1.4, an average value for the safety factor was found higher than 2.28.



a)                                                  b)
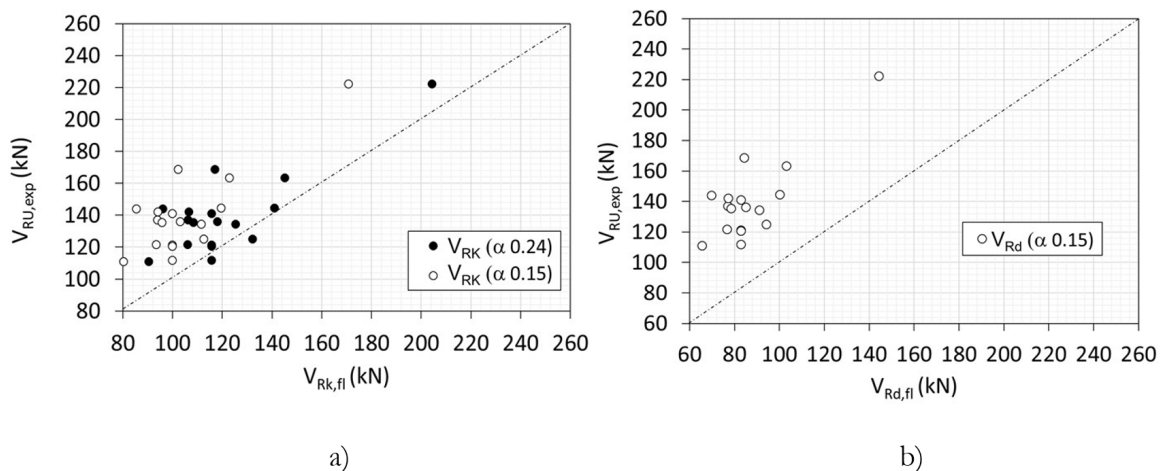
**Figure 13.** a) Graphs $V_{R,exp}$ versus $V_{Rk\,(0.24)}$ and $V_{R,exp}$ versus $V_{Rk\,(0.15)}$, b) Graphs $V_{Ru,exp}$ versus $V_{Rd\,(0.15)}$.

## 5 CONCLUSIONS

Hollow core slabs are prestressed precast elements without transverse reinforcement in which the bearing capacity is related to the shear mechanism of failure that is dependent on both the concrete section of the webs and the actual prestressing forces acting on the tendons at the critical section within the transfer length between a distance from h to 2h from the support. For the slabs from 150 to 200 mm deep underline loads from 2h to 4h from the support, the shear capacity is mostly related to the flexure-shear mechanism, wherein there is a combination of bending and shear cracks.

This paper has presented a literature review on the development of the main assumptions for the flexure-shear mechanism, which is the basis for the theoretical expression for the bearing capacity of hollow core slabs with and without structural topping according to NBR 14861 [2], which also was inspired by FIB Bulletin 6 [3].

Considering the characteristic tensile strength of concrete $f_{ctk,inf} = 0.7 f_{ctm}$ for the calculation of the term $V_{c,k} = 0.25 \cdot f_{ctk,inf} \cdot k \cdot (1.2 + 40\rho_1) \cdot \Sigma b_w \cdot d$ and comparing the theoretically predicted values with the experimental results from shear tests of slabs with 150 and 200 mm, it has been found an average value of $\alpha_{ef,med} = 0.37$ (being $\alpha_{ef,med} = 0,298$ considering slabs with tendons of $\phi 12.7$ mm and $\alpha_{ef,med} = 0,45$ considering slabs with tendons $\phi 9.5$ mm), with $\alpha_{ef}$ ranging from 0.21 to 0.65. Therefore, the $V_{p,1} = 0.15 \cdot \sigma_{cp} \cdot b_w \cdot d$ proved to be a lower limit to take into account the effective contribution of the prestressing tendons at the critical section in the transfer region, within a distance between h and 2h from the support. Therefore, it has been verified that there is no further need for the reduction factor $\alpha = L_x / L_{pt2}$ to be multiplied by the portion $0.15 \cdot \sigma_{cp}$.

## ACKNOWLEDGEMENTS

## REFERENCES

[1] G. Lindström, *Cross Section Design.* Lausanne: CEB-FIB, 2007. Draft.

[2] Associação Brasileira de Normas Técnicas, *Laje Pré-Fabricada – Painel Alveolar de Concreto Protendido – Requisitos*, NBR 14861, 2011.

[3] Federation Internationale du Beton, *Guide to Good Practice: Special Design Considerations for Precast Prestressed Hollow Core Floors.* Lausanne: CEB-FIB, 2000.

[4] Associação Brasileira de Normas Técnicas, *Projeto de Estruturas de Concreto – Procedimento*, NBR 6118, 2014.

[5] Federation Internationale du Beton, *Model Code for Concrete Structures*. Lausanne: CEB-FIB, 1978.

[6] M. L. G. Marquesi, "Contribuição ao estudo dos mecanismos resistentes à força cortante em lajes alveolares protendidas," M.S. thesis, Univ. Fed. São Carlos, São Carlos, 2014.

[7] J. C. Walraven and W. P. M. Mercx, "The bearing capacity of prestressed hollow core slabs," *Heron.*, vol. 28, no. 3, 1983.

[8] F. K. Kong, R. H. Evans, and V. M. Ohn, *Reinforced and Prestressed Concrete.* UK: Spon Press, 2001.

[9] R. Klein-Holte, "Shear and anchorage resistance," in *IPHA Tech. Sem.*, Tallin, Estonia, 2017.

[10] T. Telford, *Precast Prestressed Hollow Core Floors.* London: Telford, 1988.

[11] F. Cavagnis, M. F. Ruiz, and A. Muttoni, "A mechanical model for failures in shear of members without transverse reinforcement based on development of a critical shear crack," *Eng. Struct.*, vol. 157, pp. 300–315, 2018.

[12] Comité Européen de Normalisation, *Eurocode 2 – Projeto de Estruturas de Betão – Parte 1-1: Regras Gerais e Regras para Edifícios*, EN 1992-1-1, 2004.

[13] European Concrete Platform ASBL, *Eurocode 2 Comentary*, 2008.

[14] K. S. Elliott, "Transmission length and shear capacity in prestressed concrete hollow core slabs," *Mag. Concr. Res.*, vol. 66, no. 12, pp. 585–602, 2014.

[15] N. S. Fernandes, "Cisalhamento em lajes alveolares pré-fabricadas em concreto protendido: ensaio padrão de apoio para controle de qualidade," M.S. thesis, Univ. Fed. São Carlos, São Carlos, 2007.

[16] Federation Internationale de la Précontrainte, *Guide to Good Practice: Quality Assurance of Hollow Core* Slab. London: FIP, 1992.

[17] B. Catoia, "Lajes alveolares protendidas: cisalhamento em região fissurada por flexão," Ph.D. dissertation, Univ. São Paulo, São Carlos, 2011.

[18] American Concrete Institute, *Building Code Requirements for Structural Concrete (ACI 318-08) and Commentary*, ACI Committee 318, 2008.

[19] O. Hedman, and A. Losberg, *Design of concrete structures with regard to shear forces, in shear and torsion* (CEB Bulletin D'Information 126). Paris, 1978.

[20] Comité Européen de Normalisation, *Precast Concrete Products – Hollow Core Slabs*, EN 1168, 2005.

ORIGINAL ARTICLE

# Theoretical analysis of the behavior of steel frame infilled with masonry walls by the diagonal strut method

*Análise teórica do comportamento de pórtico de aço preenchido com alvenaria participante pelo método da barra diagonal equivalente*

Alba Bruna Cintra De Grandi[a] 
Roberto Márcio da Silva[a] 
Rita de Cássia Silva Sant'Ana Alvarenga[b] 
José Carlos Lopes Ribeiro[b] 
Guilherme Aris Parsekian[c] 
Wallison Angelim Medeiros[c] 

[a]Universidade Federal de Minas Gerais – UFMG, Departamento de Engenharia de Estruturas, Belo Horizonte, MG, Brasil
[b]Universidade Federal de Viçosa – UFV, Departamento de Engenharia Civil, Viçosa, MG, Brasil
[c]Universidade Federal de São Carlos – UFSCar, Departamento de Engenharia Civil, São Carlos, SP, Brasil

**Abstract:** In the last decades, several studies have been developed regarding structures composed by frames infilled with masonry walls, proving the increase of lateral stiffness by the infill. In this work, an analysis was carried out, based on design codes which adopt the equivalent diagonal strut method, to compare theoretical results with experimental ones of tests performed on steel frames infilled with concrete block masonry. Two of the three assessed codes specify lateral stiffness smaller than that measured from experimental testing, as safety measures for design. Regarding the masonry ultimate loads, the two specifications analyzed yielded similar values of critical force, although they pointed out different failure modes. The equivalent diagonal strut method has been proved to be a simple and useful tool for considering masonry walls and it should be used in case of reduced horizontal loads, prior to initial cracks of the infill wall.

**Keywords:** structural masonry, infilled frame, equivalent diagonal strut method, theoretical evaluation.

**Resumo:** Nas últimas décadas, inúmeros estudos têm sido desenvolvidos a respeito de estruturas de pórticos preenchidos com alvenaria participante, comprovando o aumento de rigidez lateral proporcionado por esta. Neste trabalho, análise foi realizada, baseada em prescrições normativas que adotam o método da barra diagonal equivalente, com o objetivo de comparação aos resultados experimentais de ensaios de pórtico de aço preenchido com alvenaria de blocos de concreto. Duas das três normas técnicas estudadas sugeriram valores de rigidez lateral inferiores aos resultados experimentais, como condição de segurança ao dimensionamento. Sobre as forças de ruptura da alvenaria, os dois procedimentos analisados apresentaram valores próximos de força crítica, embora tenham apontado modos críticos de colapso distintos. O método da barra diagonal equivalente se mostrou uma ferramenta útil e simples para a consideração da alvenaria participante, devendo ser empregado em caso de ações horizontais reduzidas, prévias ao estágio inicial de fissuração do painel.

**Palavras-chave:** alvenaria estrutural, pórtico preenchido, método da barra diagonal equivalente, avaliação teórica.

A. B. C. De Grandi, R. M. Silva, R. C. S. S. Alvarenga, J. C. L. Ribeiro, G. A. Parsekian, and W. A. Medeiros

# 1 INTRODUCTION

Over the past few decades, several researchers have confirmed that masonry infills have a significant influence on the behavior of framed structures. The infill increases frame stiffness and, consequently, helps limit the displacements of the structure when subject to lateral forces [1], [2]. However, in most cases, infill walls are treated only as partition member and their influence on the behavior of the structure is not considered [2], [3]. Nevertheless, the practice of disregarding the structural interaction between the masonry wall and the surrounding frame can lead to less economical projects and does not necessarily result in a safer design. Unexpected and undesirable behavior of the structure may occur when disregarding the infill, especially regarding its dynamic behavior, which can have its natural vibration period reduced and the ductile failure mode changed to a brittle failure mode [4]–[6].

Several models have been proposed for the design of masonry infill panels [3], the equivalent diagonal strut method being the most widespread. In this model, the infill panel is replaced by a diagonal strut, with defined geometric and mechanical properties (Figure 1), which is activated under compression to resist the loading.
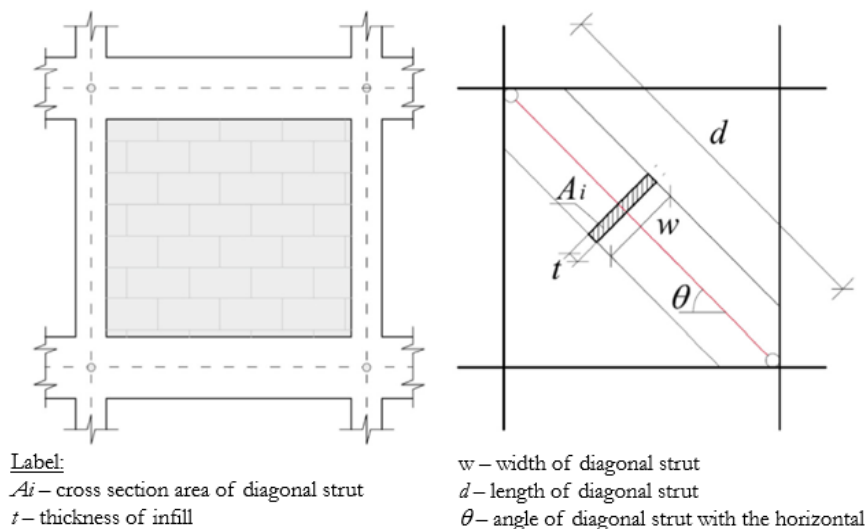


Label:
$Ai$ – cross section area of diagonal strut
$t$ – thickness of infill

w – width of diagonal strut
d – length of diagonal strut
$\theta$ – angle of diagonal strut with the horizontal

**Figure 1.** Definition of the diagonal strut and its geometric characteristics. Source: Adapted from Asteris et al. [7]

Based on this model, some design codes specifications were developed or reformulated in order to quantify the stiffness and strength provided by the masonry walls, so that their consideration as infill panels in a structural design is possible. Analytical models based on the equivalent diagonal strut method comprise the most effective way to include the contribution of stiffness and strength of the infill panels in framed structures, overcoming the enormous computational effort required by refined models using the Finite Element Method [7], [8].

However, despite numerous research and evidence regarding the efficiency of infilled frames, the most widespread analytical methods and calculation procedures have not achieved practical application in Brazil yet. Thus, designers still tend to disregard masonry as a bracing element, mainly due to the lack of a normative guideline comprising projects that consider the contribution of infill panels [9], [10].

In fact, due to the complexity and non-regularity of the infill's behavior, uncertainties still persist on this subject. Many factors such as material properties, type of loading, openings in walls and construction details lead to complex behavior of the system [6], [11]–[13].

Therefore, this work was carried out to contribute to a better understanding of the behavior of infilled framed structures, investigating the stiffness gain provided by the presence of masonry wall. The main objective was to evaluate methods proposed by standard codes that consider masonry walls as bracing elements, comparing the theoretical results with experimental results obtained by De Grandi [14]. The analysis assessed the lateral displacements of the structure considering the determination of the effective width of equivalent diagonal strut, as well as ultimate lateral forces of the infilled panel. It is noteworthy, however, that this work was exclusively restricted to the theoretical analysis of analytical methods that provide the consideration of masonry infill. Reader should refer to De Grandi [14] for details on the experimental tests.

## 2 THE EQUIVALENT DIAGONAL STRUT METHOD

Polyakov [15] was one of the pioneers in presenting approximate methods that allow the consideration of masonry on infilled frame structures. He introduced the concept of the equivalent diagonal strut, which was later developed by Holmes [16].

It was observed [15] that the application of a lateral load on the structure causes separation between infill and frame in a significant length on each side, leaving only a limited contact area at the compressed corners. In contrast, Holmes [16] suggested that the geometry of the diagonal strut is a function of the dimensions and physical properties of the infill wall. He indicates that the diagonal strut has the same thickness and modulus of elasticity as the masonry infill and its width can be taken as one third of its length. In addition, it was concluded that, at failure, the lateral displacement of an infilled frame is significantly lower than the displacement of the bare frame.

Stafford-Smith and Carter [17] were the first to propose an analytical equation to estimate the width of the equivalent diagonal strut. It was indicated that the diagonal stiffness of infill panel is not only a function of its dimensions and physical properties, but also depends on the contact length between frame and infill (Figure 2).
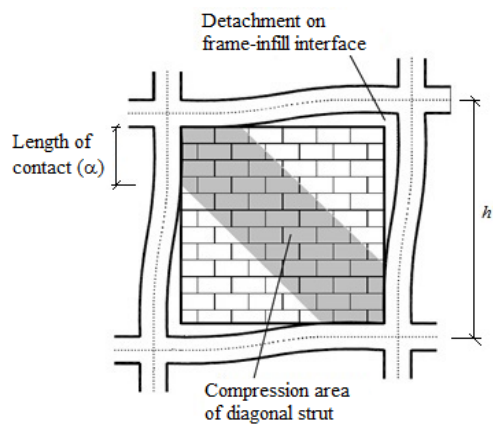


**Figure 2.** Length of contact between frame and infill. Source: Adapted from Asteris et al. [5]

This length of contact ($\alpha$) is governed by the relative stiffness between panel and frame and can be estimated by Equation 1:

$$\frac{\alpha}{h'} = \frac{\pi}{2\lambda h'} \tag{1}$$

where $\lambda h'$ is a dimensionless parameter which expresses the relative stiffness between the frame and the infill panel, and $h'$ is the height of the column between the beam axes. The parameter $\lambda$ can be determined by Equation 2:

$$\lambda = \sqrt[4]{\frac{E_m t \sin(2\theta)}{4 E_f I_c h}} \tag{2}$$

where $E_m$, $t$ and $h$ are the elastic modulus, the thickness, and the height of the infill panel, respectively; $E_f$ and $I_c$ are the modulus of elasticity and the moment of inertia of the column, and $\theta$ is the angle between the diagonal and horizontal axis.

From experimental investigations, the authors were able to affirm that, in case of multi-story structures, the column stiffness has an important influence on stiffness and on the final load capacity of the system. On the other hand, variations in the beam stiffness showed little effect on the behavior of the structure. The small influence of the beam member on the stiffness of the structure may be associated with the fact that, regardless of beam stiffness, the length of contact between beam and panel is approximately half of its span.

Knowing the contact length between panel and frame, and carrying out a series of stress analysis, Stafford-Smith and Carter [17] concluded that the effective width of the diagonal strut is influenced by the following factors:
- relative stiffness between frame and panel;
- length-height ratio of the panel;
- stress-strain ratio of the infill material;
- intensity of the internal force acting on the diagonal.

Thus, Equation 3 was determined to calculate the width of the diagonal strut:

$$w = \sqrt{\alpha^2 + \left(\frac{l}{2}\right)^2} \tag{3}$$

where $l$ is the span of upper beam of the frame.

Mainstone [18] adopted the equivalent strut model for steel frames and conducted a series of reduced-scale tests, with infill panels of microconcrete and ceramic block. He proposed equations to calculate the width of the diagonal strut for the two types of infill material, using the parameter $\lambda h'$ by Stafford-Smith and Carter [17] Equation 4 refers to ceramic block infills, while Equation 5 refers to microconcrete ones.

$$\frac{w}{L_d} = 0.175(\lambda h')^{-0.4} \tag{4}$$

$$\frac{w}{L_d} = 0.115(\lambda h')^{-0.4} \tag{5}$$

where $w$ is the width of diagonal strut and $L_d$ is its length.

Wood [19], observing tests previously carried out by other researchers, in addition to categorizing four different failure modes for infilled frames, introduced a reduction factor of masonry compression strength ($f'_m$) in the model to achieve a reasonable approach to experimental results.

Liauw and Kwan [20] proposed a plastic theory observing three main modes of failure of the system, including the panel corners crushing and compressing of the diagonal. Using some of the previously defined parameters, Liauw and Kwan [20] presented Equation 6 for calculating the width of diagonal strut.

$$w = \frac{0.86 h \cos\theta}{\sqrt{\lambda h}} \le 0.45 h \cos\theta \tag{6}$$

Comparing analytical methods to experimental data, Tucker [21] proposed Equation 7 for calculating the width of diagonal strut ($w$):

$$w = 0.25 L_d (\lambda h)^{-1.15} \tag{7}$$

where $L_d$ is the length of diagonal, $h$ is the height of the panel and $\lambda$ is the same as defined in Equation 2. Tucker [21] also presented two groups of equations that predict the cracking strength of the panel ($P_{fc}$) and the ultimate load capacity of the infilled frame ($P_{ult}$) for different types of masonry, depending on the compressive strength of the masonry infill ($f'_m$), of the width of diagonal ($w$), of the slope between diagonal and horizontal ($\theta$), and of the thickness of infill ($t$). Equations 8 and 9 allow estimating $P_{fc}$ and $P_{ult}$ for infills of masonry concrete blocks.

$$P_{fc} = 0.6 f'_m wt \cos\theta \tag{8}$$

$$P_{ult} = 1.05 f'_m wt \cos\theta \tag{9}$$

It is important to mention that the compressed diagonal strut model is a simplified method and limited to linear analysis and is not effective after the cracking limit of the infill wall. This is because the system stiffness gradually decreases with the increase in lateral strength and the appearance of cracks in the panel, which makes the compressed diagonal model less consistent with the actual behavior of the structure. Then, the model can be used to check the service limit state of the structure and is not suitable for verifications of the ultimate limit state [22]. After defining the geometric properties of the diagonal strut, it is possible to determine internal forces in each structural member and the frame lateral displacements with a 2D frame model stiffened by the inclusion of the pinned diagonal strut.

The diagonal strut formulations for the consideration of masonry infill were developed to evaluate the masonry behavior when considered in the lateral stiffening of general framed structures taking into account the physical and mechanical properties of the masonry and of the frame materials. There are no limitations on the use of these expressions for different materials and different connection conditions of structural elements.

## 2.1 Codes which consider masonry infill contribution

### 2.1.1 Determination of the width of diagonal strut

#### 2.1.1.1 According to ABNT NBR 16868:2020 [23]

For designing purposes, the Brazilian code admits that geometric properties of compressed diagonal strut depend on the length of contact between panel and column ($\alpha_H$) and between panel and beam ($\alpha_L$), expressed by Equations 10 and 11:

$$\alpha_H = \frac{\pi}{2} \cdot \sqrt[4]{\frac{4 E_p I_p H}{E_a t_{ap} \sin(2\theta)}}$$

(10)

$$\alpha_L = \pi \cdot \sqrt[4]{\frac{4 E_p I_v L}{E_a t_{ap} \sin(2\theta)}}$$

(11)

where:
$E_a$ and $E_p$ are the modulus of elasticity of masonry and frame material, respectively;
$I_p$ and $I_v$ are the moments of inertia of the cross section of columns and beam of the frame, respectively;
$H$ and $L$ are the height and length of infill panel, respectively;
$t_{ap}$ is equal to twice the sum of the thickness of longitudinal walls of the block for the case of hollow block not fully grouted; or it is the wall thickness for a solid brick or hollow block fully grouted;
$\theta$ is the angle of inclination of the diagonal strut, that is, equal to $\tan^{-1}$ (h / l).

It is observed that this procedure is based on the apparent thickness of infill panel instead of the total thickness $(t_{ap})$, in the case of hollow blocks. Such consideration comes from the fact that, in practice, masonry walls are neither commonly built with solid blocks nor do have hollow blocks grouted in their entirety. In the Brazilian design, masonry properties (including $E_a$, prism strength, wall geometry) refers to the masonry gross area. The use of the total thickness of the block in this situation would not be consistent with the formulations assessed in the former section. Considering the $t_{ap}$, which basically multiply by two the effective masonry thickness, makes the formulation consistent to the gross area properties, since regular hollow blocks have the gross area approximately equal to twice the net area.

From this, the width of equivalent diagonal ($w$) can be determined by Equation 12.

$$w = \sqrt{{\alpha_H}^2 + {\alpha_L}^2}$$

(12)

However, to consider an idealized and safe stress distribution, the effective width of compressed diagonal ($w_{eff}$) is taken as $w/2$ and must not exceed a quarter of the diagonal length.

An important recommendation is that the effective stiffness of compressed diagonal, used for displacement calculations, must be reduced by 50% of its nominal value, in order to consider the panel in cracked conditions.

### 2.1.1.2 According to TMS 402-16 [24]

The American code TMS 402-16 [24] uses Equation 13 to calculate the width of diagonal strut:

$$w_{inf} = \frac{0.3}{\lambda_{strut} \cos \theta_{strut}} \tag{13}$$

where:

$$\lambda_{strut} = \sqrt[4]{\frac{E_m t_{netinf} \sin 2\theta_{strut}}{4 E_{bc} I_{bc} h_{inf}}} \tag{14}$$

$E_m$ and $E_{bc}$ are the modulus of elasticity of masonry and frame material respectively;
$I_{bc}$ is the moment of inertia of the cross section of columns and beam of the frame;
$h_{inf}$ is the height of infill panel;
$t_{net,inf}$ is the effective thickness of panel;
$\theta_{strut}$ is the angle between diagonal and horizontal axis.

In addition, the American code also recommends that a 50% reduction shall be applied to the load capacity and stiffness of the diagonal strut.

### 2.1.1.3 According to NZS 4230:2004 [25]

The New Zealand code NZS 4230:2004 [25] recommends that the diagonal strut width shall be taken as a quarter of the diagonal length.

The thickness of the diagonal strut is taken as the effective thickness of masonry panel, the same way it was considered in the analysis of the American codes.

### 2.1.2 Determination of masonry ultimate load capacity

Three modes of failure are foreseen for the masonry infill, namely: bed-joint sliding, diagonal tension failure, and diagonal compression failure. In this section, equation to predict the ultimate load capacity for these three failure modes are presented, following the recommendations of the Brazilian code ABNT NBR 16868:2020 [23] and the American guidelines from FEMA 306 [26]

The horizontal force applied to the structure at the height of upper beam axis is considered as $F_H$. The compression axial force acting on the diagonal strut is $N$ and its horizontal ($V$) and vertical ($P$) components are given by Equations 15 and 16, respectively.

$$V = N \cos \theta \tag{15}$$

$$P = N \sin \theta \tag{16}$$

### 2.1.2.1 According to ABNT NBR 16868:2020 [23]

The compressive strength of the diagonal strut is calculated in the same way as structural masonry walls, except that it must be multiplied by a factor which adjust the compressive strength normal to the bed joint to the resistance in the diagonal direction. In the absence of this information, the code states that this factor should be taken equal to 0.5. Thus, the compressive strength can be calculated by Equation 17, where $R$ is a factor that considers the effects of slenderness; and $f_m$ is the average compressive strength of masonry walls, taken as 70% of the average compressive strength of the prisms ($f_{pm}$) obtained experimentally, as reported in De Grandi [14] It should be note that the code specifies characteristics values, but average values are considered here for assessing the test results.

$$f_{k,strut} = 0.5 f_m R \tag{17}$$

where:

$$f_m = 0{,}7\,f_{pm} \tag{18}$$

$$R = 1 - \left(\frac{\lambda}{40}\right)^3 \tag{19}$$

$$\lambda = \frac{h_{ef}}{t_{ef}} \tag{20}$$

The effective height ($h_{ef}$) of the compressed diagonal must be considered equal to the length of the diagonal minus $w/2$.

For design purposes, the diagonal strut cross section area is taken as the product between the effective width ($w_{eff}$) and the infill thickness ($t$). In this case, the maximum load that can be applied on the panel is given by limiting the compressive stress ($\sigma_d$) to less than or equal to the masonry compressive strength ($f_d$).

For the verification of the bed-joint sliding, the masonry shear strength was adopted equal to the average value determined experimentally from wall shear tests ($f_{vm} = 0.2$ MPa $= 0.02$ kN/cm$^2$), see De Grandi [14] Thus, shear stress must be less than or equal to this resistance value, that is, $\tau \le f_{vm}$. In the case of bed-joint sliding, shear force occurs through the horizontal component of the diagonal compression V. Then, Equation 21 is used for this verification.

$$\tau = \frac{V}{A_{cis}} \le f_{vm} \tag{21}$$

The area resisting to the shear load on the panel ($A_{cis}$) is given by the length of the panel ($l$) multiplied by its total thickness ($t$).

In the case of the shear strength by diagonal tension, even that it is not provided by the Brazilian code for masonry infills, this check is implicit in item 11.4.3 of ABNT NBR 16868: 2020 [23], which deals with the verification of shear in elements of masonry. The shear strength is limited by Equation 22:

$$f_{vk} = 0.4\,\gamma_g\sqrt{f_{pk}} \tag{22}$$

where:

$f_{pk}$ is the characteristic compressive strength of the prism. In this case, the average compressive strength obtained experimentally ($f_{pm}$) was used; $\gamma_g$ is the coefficient which considers the possibility of the wall being totally grouted or made of solid blocks. It must be equal to 1.0 for these cases, or equal to the ratio between the effective area of mortar and the gross area of the block, not exceeding 0.5.

In the same way as other verifications, the critical force of failure by diagonal tension is obtained from the premise that stresses ($\tau$) must be smaller than the strength ($f_v$).

### 2.1.2.2 According to FEMA 306 [26]

For evaluation of initial shear strength due to bed-joint slipping, the American code uses the Mohr-Coulomb criterion. Hence, the critical horizontal force for this failure mode is given by Equation 23.

$$V_{slide} = \left(\tau_0 + \sigma_y \tan\varnothing\right) L_{inf}\, t_{inf} \tag{23}$$

where:
$L_{inf}$ and $t_{inf}$ are the length and thickness of the infill panel, respectively;
$\phi$ is the angle of friction of the masonry along the bed joint;

$\sigma_y$ is the pre-existing vertical compression stress on the panel; and
$\tau_0$ is the mortar cohesion, which can be estimated by Equation 24 in the absence of data:

$$\tau_0 = \frac{f'_{me90}}{20} \tag{24}$$

being $f'_{me90}$ = compressive strength of masonry in the horizontal direction, taken as 50% of the average compressive strength of prisms ($f_{pm}$).

According to Federal Emergency Management Agency [26], the tangent of masonry friction angle ($tan\phi$) is taken as the friction coefficient $\mu$, which value was considered as 0.5, following recommendations from ABNT NBR 15961-1:2011 [27].

Regarding the diagonal compression failure mode, FEMA 306 [26] establishes the Equation 25 for determining the shear force resisted by the panel:

$$V_c = a\,t_{inf}\,f'_{me90}\cos\theta \tag{25}$$

where $t_{inf}$, $f'_{me90}$ and $\theta$ are the same as previously defined; and $a$ is the width of the diagonal strut, calculated according to Equation 26:

$$a = 0.175(\lambda h_{col})^{-0.4}\,r_{inf} \tag{26}$$

in which:
$\lambda$ is the same as defined in Equation 2;
$h_{col}$ is the column height taken from axis to axis of beams; and
$r_{inf}$ is the diagonal length.

In case of failure by diagonal tension, the resistant force of the panel is given [26] by Equation 27:

$$V_{cr} = \frac{2\sqrt{2}\,t_{inf}\,L_{inf}\,\sigma_{cr}}{\left(\dfrac{L_{inf}}{h_{inf}} + \dfrac{h_{inf}}{L_{inf}}\right)} \tag{27}$$

where
$h_{inf}$ is the height of infill;
$L_{inf}$ and $t_{inf}$ are the same as already defined; and
$\sigma_{cr}$ is the masonry cracking capacity, estimated by Equation 28:

$$\sigma_{cr} = \frac{f'_{me90}}{20} \tag{28}$$

being $f'_{me90}$ the same as previously defined.


## 3 MATERIALS AND METHODOLOGY

The study consisted of a numerical analysis of a steel frame infilled with a concrete masonry wall, subjected to horizontal loads, by using the equivalent diagonal strut method. The experimental data is taken from De Grandi [14]. Masonry infill wall was considered as a compressed strut connected to the frame by hinges. Furthermore, failure force of the masonry wall was estimated by prescriptions from technical codes.

To determine the width of diagonal strut, the procedures of American (TMS 402-16 [24]) and New Zealand (NZS 4230:2004 [25]) codes were compared, besides the Brazilian code ABNT NBR 16868:2020 [23]. Once the geometric

Rev. IBRACON Estrut. Mater., vol. 14, no. 5, e14508, 2021

8/15

properties of the diagonal were defined, a linear analysis of the steel frame was performed using the Ftool software to obtain the maximum lateral displacements at the top of the infilled frame. The diagonal strut was added to the structure with the geometric properties defined by the theoretical models and elastic properties of masonry. Figure 3 shows the structure modeling scheme, in which bottoms of the columns were simulated as perfectly rigid supports and beam-column connections were considered pinned. The displacements were analyzed until the lowest cracking load obtained in the experimental tests is reached, equals to 72 kN.
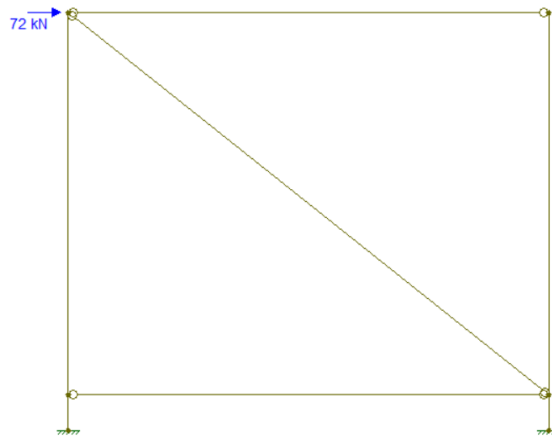


**Figure 3.** Structural model for linear analysis considering the equivalent diagonal strut. Source: The author

Regarding the verification of forces that leads the infill panel to failure, the following codes were evaluated: ABNT NBR 16868:2020 [23] and FEMA 306 [26].

For analysis purposes, the same materials tested by De Grandi [14] were used as parameters. De Grandi [14] dealt with the experimental evaluation of a steel frame infilled with concrete masonry, which properties are presented in section 3.1, under cyclic loads. The theoretical results obtained from the guidelines mentioned above were compared with the experimental results of De Grandi [14], discussing relevance and limitations of these methods.

## 3.1 Material properties and description of experimental tests

The frame structure from De Grandi [14] was constituted of ASTM A36 steel welded members, with a height/length ratio equal to 0.83, being a full-scale specimen. Beams and columns were made by the same steel profile, with cross section indicated in Figure 4. Columns had a total length of 268 cm, while beams had a length of 300 cm (from axis to axis of column). Column bottoms were fixed in the laboratory reaction slab and beam-column connections were made with bolted angles.



I-section members:

web height ($h_w$) = 204 mm
web thickness ($t_w$) = 6,3 mm
flange width ($b_f$) = 200 mm
flange thickness ($t_f$) = 8 mm

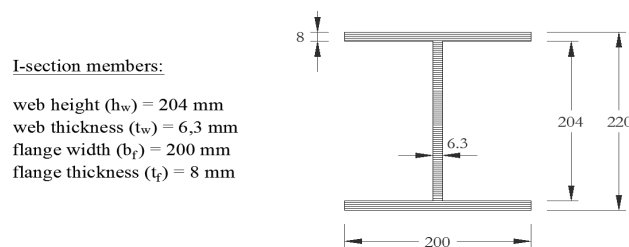**Figure 4.** Steel cross section of columns and beams used by De Grandi [14]. Source: De Grandi [14]

The infill walls were built with hollow concrete blocks with compressive strength of 6 MPa and dimensions of 14 x 19 x 39 cm. Industrialized mortar with 6 MPa compressive strength was used to completely fill vertical and horizontal joints. The frame-panel interfaces were filled by industrialized mortar with an expansive admixture.

Frame tests were performed by the application of horizontal cyclic loading applied at the level of upper beam axis, through a hydraulic actuator model MTS DuraGlide 244.31 from MTS company. Figure 5 illustrates the experimental setup, showing the structural arrangement and force application system.
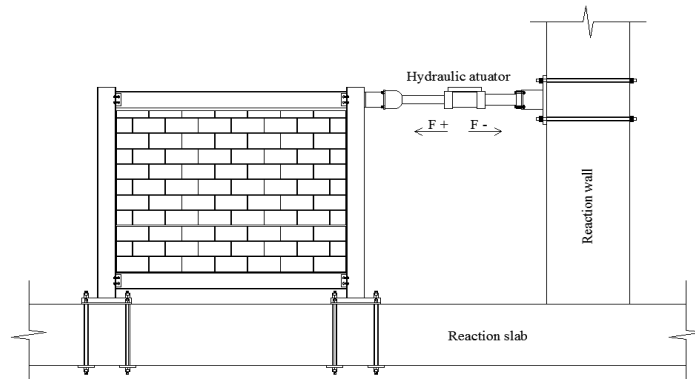


**Figure 5.** Experimental setup by De Grandi [14]. Source: De Grandi [14]

The summary of material properties used in the experimental program is shown in Table 1. Three infilled frames tests were carried out, namely PP-1-0.5/2.0, PP-2-CE-0.5/2.0 and PP-3-CE-0.5/2.0, under the same test conditions, and the experimental results were compared with theoretical analysis in this work.

**Table 1.** Material properties of experimental tests from De Grandi [14]

| Frame | Symbol | Value |
|---|---|---|
| Steel modulus of elasticity | *Ef* | 200 GPa |
| Moment of inertia (columns and beams) | *Ic* and *Ib* | 4043 cm$^4$ |
| **Masonry** | **Symbol** | **Value** |
| Height of panel | *h* | 213 cm |
| Length of panel | *l* | 278 cm |
| Nominal thickness of panel | *t* | 14 cm |
| Effective thickness of panel | *te* | 5.6 cm |
| Masonry modulus of elasticity | *Em* | 4 GPa |
| Compressive strength of blocks | *fbk* | 6.13 MPa |
| Average compressive strength of prisms | *fpm* | 5.55 MPa |
| Average shear strength of masonry | *fvm* | 0.2 MPa |

## 4 RESULTS AND DISCUSSIONS

## 4.1 Lateral displacements of the infilled frame

### 4.1.1 Calculation of the equivalent diagonal strut width (*w*)

The specifications of three normative codes were taken as reference for determining the width of equivalent diagonal strut of the masonry infilled frame studied in this work. There are the Brazilian code ABNT NBR 16868:2020 [23], the American code TMS 402-16 [24] and the New Zealand code NZS 4230:2004 [25].

As described in section 2, ABNT NBR 16868:2020 [23] establishes a procedure for calculating the diagonal width of the equivalent strut according to Equations 10, 11 and 12. Therefore,

$$\alpha_H = \frac{\pi}{2} \sqrt[4]{\frac{4E_p I_p H}{E_a t_{ap} \sin(2\theta)}} = \frac{\pi}{2} \sqrt[4]{\frac{4 \times 200 \times 4043 \times 213}{4.00 \times 11.2 \times \sin(2 \times 37.46°)}} = 99.23\,cm$$

$$\alpha_L = \pi \sqrt[4]{\frac{4E_p I_v L}{E_a t_{ap} \sin(2\theta)}} = \pi \sqrt[4]{\frac{4 \times 200 \times 4043 \times 278}{4.00 \times 11.2 \times \sin(2 \times 37.46°)}} = 212.13\,cm$$

$$w = \sqrt{\alpha_H{}^2 + \alpha_L{}^2} = \sqrt{99.23^2 + 212.13^2} = 234.19\,cm$$

However, the effective width of compressed diagonal ($w_{eff}$) is taken as $w/2$ and must not exceed a quarter of the diagonal length. So,

$$w_{eff} = \frac{w}{2} = \frac{234.19}{2} = 117.09\,cm$$

$$\frac{L_d}{4} = \frac{350}{4} = 87.5\,cm$$

Therefore, in this case, the effective width of compressed diagonal must be taken as a quarter of its length $L_d$. That is, $w_{eff} = 87.5$ cm.

According to TMS 402-16 [24], the width of the diagonal strut is determined following Equations 13 and 14, presented in section 3.2.2. Using the known properties of the frame and of the masonry yields to:

$$\lambda_{strut} = \sqrt[4]{\frac{E_m t_{netinf} \sin(2\theta_{strut})}{4E_{bc} I_{bc} h_{inf}}} = \sqrt[4]{\frac{4.00 \times 5.6 \times \sin(2 \times 37.46°)}{4 \times 200 \times 4043 \times 213}} = 0.0133\,/\,cm$$

$$w = \frac{0.3}{\lambda_{strut} \cos\theta_{strut}} = \frac{0.3}{0.0133 \times \cos 37.46°} = 28.4\ cm$$

The New Zealand code NZS 4230:2004 [25] recommends that the width of diagonal strut be taken as a quarter of the length of the diagonal. Therefore,

$$w = \frac{L_d}{4} = \frac{350}{4} = 87.5cm$$

## 4.1.2 Obtention of lateral displacements

Figure 6 shows a comparison among displacements obtained experimentally and analytically from the studied models.
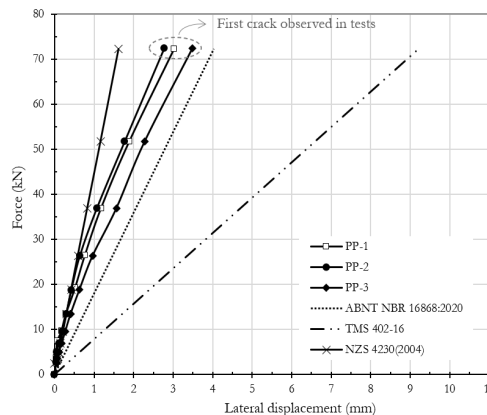


**Figure 6.** Load-displacement diagrams obtained from technical codes in comparison to experimental results. Source: The author

It is possible to conclude that the American code TMS 402-16 [24] presents a more conservative method for considering masonry infill walls as bracing element, since lateral stiffness provided by the diagonal strut is much smaller than the values found experimentally and by other codes. Comprising the same levels of applied horizontal forces, the lateral displacements obtained by the method of TMS 402-16 [24] are much greater.

Specifications from the Brazilian code ABNT NBR 16868:2020 [23] showed stiffness values close to the experimental results. The observed difference can be attributed to uncertainties related to the behavior of the structure when masonry panel works as part of the bracing system, leading to a reduction in stiffness for design purposes.

On the other hand, the New Zealand code NZS 4230:2004 [25] presented a load-displacement curve with displacement values lower than experimental results, indicating a greater stiffness provided by the diagonal strut estimated by this guideline. However, it is possible to observe that, for lower loads (up to 25 kN), the New Zealand code demonstrated a good correlation with experimental results, with a greater discrepancy for higher load levels. This can be explained by the fact that, unlikely the other two codes, NZS 4230:2004 [25] does not consider a factor for reducing the stiffness of diagonal strut due to masonry wall cracking, which can develop internal microcracking, even if not showing visible cracks to unaided eye.

Table 2 shows the values of lateral stiffness for the three test specimens and for the theoretical models of equivalent diagonal strut. The proportion obtained for the stiffness of the theoretical models in relation to the average of experimental tests is also presented. It is observed that the stiffness of 17.9 kN/mm obtained by the ABNT NBR 16868:2020 [23] indicated a 76% relationship with the experimental values. In contrast, the NZS 4230:2004 [25] code exhibited a stiffness of 32.0 kN/mm, a value 36% higher than the experimental average. Finally, as previously mentioned, the method recommended by TMS 402-16 [24] proved to be the most conservative, presenting a stiffness of only 7.9 kN/mm, equivalent to over 30% of the average value obtained in experimental tests.

**Table 2.** Relative lateral stiffnesses for experimental tests and theoretical methods.

| Specimen / Theoretical model | Stiffness (kN/mm) | $K_{theor}/K_{exp}$ |
|---|---|---|
| PP-1-0.5/2.0 | 23.9 | - |
| PP-2-CE-0.5/2.0 | 26.1 | - |
| PP-3-CE-0.5/2.0 | 20.7 | - |
| ABNT NBR 16868:2020 | 17.9 | 0.76 |
| TMS 402-16 | 7.9 | 0.33 |
| NZS 4230:2004 | 32.0 | 1.36 |

## 4.2 Estimation of the infill failure load

Table 3 presents a summary of the theoretical results for failure loads of the studied infill panel. The values presented herein refer to the critical horizontal force applied to the frame ($F_H$) for each analyzed failure mode. For comparison purposes, it is indicated that masonry critical forces observed experimentally were 72 kN, 101 kN and 75 kN for the three test specimens. Figure 7 shows the final cracking pattern at the masonry infill wall after the end of the test, for the PP-2-CE-0.5/2.0 specimen, being that this typical behavior mode was also observed on the other tests, indicating failure by diagonal tension.

**Table 3.** Masonry failure loads by technical codes.

| Technical code | Behavior mode | Failure load (kN) |
|---|---|---|
| ABNT NBR 16868:2020 | Diagonal compression | 209 |
| | Bed-joint sliding | 91 |
| | Diagonal tension | 214 |
| FEMA 306 (1998) | Diagonal compression | 131 |
| | Bed-joint sliding | 106 |
| | Diagonal tension | 89 |

**Figure 7.** Typical masonry cracking after failure – PP-2-CE-0.5/2.0 (Highlighted in red: first crack register). Source: De Grandi [14]

Regarding the results of theoretical analysis, it is observed that the values of failure load obtained by ABNT NBR 16868: 2020 [23] indicate that the critical failure mode is the bed-joint slipping, which presented an estimated critical force of 91 kN. The calculated diagonal tension failure load was equal to 214 kN, considerably higher than the experimental values.

On the other hand, FEMA 306 [26] presents diagonal tension as a critical failure mode, which was observed during the experimental tests. The failure load was 89 kN, like the critical force value obtained by the Brazilian code, although the failure modes indicated by these two guidelines were different. The infill diagonal compression was not a critical failure mode, presenting a failure force of 131 kN.

## 5 CONCLUSIONS

The contribution of masonry walls to the stiffening of framed structures is undeniable. However, despite numerous studies already carried out and findings regarding the effectiveness of infill panels, the consideration of these elements as part of the structural bracing system is still unusual.

After the analyses of a steel frame infilled with concrete masonry, the following conclusions can be stated:

- In terms of stiffness, the American code TMS 402-16 [24] proved to be the most conservative method, presenting the lowest lateral stiffness among all the assessed diagonal strut models. The Brazilian code (ABNT NBR 16868:2020 [23]) proved to be less conservative even though the calculated contribution of the masonry wall to the stiffening of the structure was smaller than the measured experimental tests average. The New Zealand code (NZS 4230:2004 [25]) reached stiffness values higher than the results of experimental tests for accentuated loads. This may be associated with the fact that this guideline does not predict a reduction factor in the stiffness of the diagonal strut to consider a stiffening decrease due to cracking of masonry;

- Concerning the ultimate load, those determined by the Brazilian code equations [23] indicated a joint sliding shear failure, while the results obtained by equations from FEMA 306 [26] indicate the critical diagonal tension failure, equivalent to the observations during experimental tests. Nevertheless, the value of critical force determined by FEMA 306 [26] was close to that obtained by ABNT NBR 16868:2020 [23].

It is important to highlight that the experimental results presented here were obtained by cyclic tests, in which the stiffness degradation may be greater than that observed in monotonic tests, due to the frequent variation on the direction of loading application. Even though, experimental results for stiffness proved to be higher than those calculated using code specifications.

In conclusion, the equivalent diagonal strut method, adopted by several authors and technical codes, proved to be a simple and useful tool for predicting the contribution of infill panels to structure stiffening. However, the model predicts the structure behavior in the initial cracking stages.

Finally, although the contribution of masonry panels in the lateral stiffness of the structure is demonstrated, the lack of a universally accepted theory for the analysis of such structural systems and the divergence observed between the methods available in the literature lead the consideration of infill panels as bracing elements to be treated with some

caution in the new Brazil code specifications. It is recommended that studies about infilled frames be encouraged, to refine the simplified design methods.

## ACKNOWLEDGEMENTS

## REFERENCES

[1] A. B. Mehrabi, P. B. Shing, M. P. Schuller, and J. L. Noland, "Experimental evaluation of masonry-infilled RC frames," *J. Struct. Eng.*, vol. 122, no. 3, pp. 228–237, 1996.

[2] A. Kauffman and A. M. Memari, "Performance evaluation of different masonry infill walls with structural fuse elements based on in-plane cyclic load testing," *Buildings*, vol. 4, pp. 605–634, 2014.

[3] S. M. M. Emami, M. Mohammadi, and P. B. Lourenço, "Equivalent diagonal strut method for masonry walls in pinned connection and multi-bay steel frames," *J. Seismol. Earthq. Eng.*, vol. 19, no. 4, pp. 199–311, 2017.

[4] A. Mohebkhah, A. A. Tasnimi, and H. A. Moghadam, "Nonlinear analysis of masonry-infilled steel frames with openings using discrete element method," *J. Construct. Steel Res.*, vol. 64, no. 12, pp. 1463–1472, Dec 2008.

[5] P. G. Asteris, D. J. Kakaletsis, C. Z. Chrysostomou, and E. E. Smyrou, "Failure Modes of In-filled Frames," *Electron. J. Struct. Eng.*, vol. 11, no. 1, pp. 11–20, 2011.

[6] P. G. Asteris, C. Z. Chrysostomou, I. P. Giannopoulos, and E. Smyrou, "Masonry infilled reinforced concrete frames with openings," in *III ECCOMAS Thematic Conf. Comput. Meth. Struct. Dyn. Earthq. Eng.*, Corfu, Grece, 2011, 15 p.

[7] P. G. Asteris, L. Cavaleri, F. Di Trapani, and A. K. Tsaris, "Numerical modelling of out-of-plane response of infilled frames: State of the art and future challenges for the equivalent strut macromodels," *Eng. Struct.*, vol. 132, no. 1, pp. 110–122, 2017.

[8] L. Cavaleri and F. Di Trapani, "Cyclic response of masonry infilled RC frames: experimental results and simplified modeling," *Soil. Dyn. Earthquake Eng.*, vol. 65, no. 1, pp. 224–242, 2014.

[9] P. B. Shing and A. B. Mehrabi, "Behaviour and analysis of masonry-infilled frames," *Prog. Struct. Eng. Mater.*, vol. 4, pp. 320–331, 2002.

[10] N. M. Noh, L. Liberatore, F. Mollaioli, and S. Tesfamariam, "Modelling of masonry infilled RC frames subjected to cyclic loads: state of the art review and modelling with OpenSees," *Eng. Struct.*, vol. 150, no. 1, pp. 599–621, 2017.

[11] D. Markulak, I. Radic, and V. Sigmund, "Cyclic testing of single bay steel frames with various types of masonry infill," *Eng. Struct.*, vol. 51, no. 1, pp. 267–277, Jun 2013.

[12] R. C. S. S. Alvarenga "Análise teórico-experimental de estruturas compostas de pórticos de aço preenchidos com alvenaria de concreto celular autoclavado," Ph.D. dissertation, Esc. Eng. São Carlos, Univ. São Paulo, São Carlos, 2002.

[13] A. Fiore, A. Netti, and P. Monaco, "The influence of masonry infill on the seismic behavior of RC frame buildings," *Eng. Struct.*, vol. 44, no. 1, pp. 133–145, 2012.

[14] A. B. C. De Grandi, "Avaliação experimental por meio de ensaios cíclicos de pórtico de aço preenchido com alvenaria participante," M.S. thesis, Univ. Fed. Viçosa, Viçosa, 2018.

[15] S. V. Polyakov, *On the Interaction Between Masonry Filler Walls and Enclosing Frame When Loaded in the Plane of the Wall.* San Francisco, EUA: Earthq. Eng. Res. Inst., 1960, pp. 36-42.

[16] M. Holmes, "Steel frames with brickwork and concrete infilling," *Proc.- Inst. Civ. Eng.*, vol. 19, no. 4, pp. 473–478, 1961.

[17] B. Stafford-Smith and C. Carter, "A method of analysis for infilled frames," *Proc.- Inst. Civ. Eng.*, vol. 44, no. 1, pp. 31–48, 1969.

[18] R. J. Mainstone, "On the stiffnesses and strengths of infilled frames," *Proc.- Inst. Civ. Eng.*, vol. 49, no. 4, pp. 57–90, 1971.

[19] R. H. Wood, "Plasticity, composite action and collapse design of unreinforced shear wall panels in frames," *Proc.- Inst. Civ. Eng.*, vol. 65, no. 2, pp. 381–411, 1978.

[20] T. C. Liauw and K. H. Kwan, "Plastic theory of non-integral infilled frames," *Proc.- Inst. Civ. Eng.*, vol. 75, no. 2, pp. 379–396, 1983.

[21] C. J. Tucker, "Predicting the in-plane capacity of masonry infilled frames," Ph.D. dissertation, Tennessee Technol. Univ., Cookeville, TN, EUA, 2007.

[22] G. A. Parsekian, A. A. Hamid, and R. G. Drysdale, *Comportamento e Dimensionamento de Alvenaria Estrutural*, 2. ed. São Carlos: EdUFSCar, 2014.

[23] Associação Brasileira de Normas Técnicas, *Alvenaria Estrutural – Parte 1: Projeto*, NBR 16868:2020, 2020.

[24] The Masonry Society, *Building Code Requirements for Masonry Structures, Masonry Standards Joint Committee*, TMS 402-16, 2016.

[25] New Zealand Standard, *Design of Reinforced Concrete Masonry Structures*, NZS 4230:2004, 2004.

[26] Federal Emergency Management Agency, *Evaluation of Earthquake Damaged Concrete and Masonry Wall Buildings – Basic Procedures Manual*, FEMA 306, 1998.

[27] Associação Brasileira de Normas Técnicas, *Alvenaria Estrutural – Blocos de Concreto – Parte 1: Projeto*, NBR 15961-1:2011, 2011.

[28] J. L. Dawe and C. K. Seah, "Behaviour of masonry infilled steel frames," *Can. J. Civ. Eng.*, vol. 16, pp. 865–876, 1989.

[29] G. M. S. Alva, J. Kaminski Jr, G. Mohamad, and L. R. Silva, "Serviceability limit state related to excessive lateral deformations to account for infill walls in the structural model," *Rev. IBRACON Estrut. Mater.*, vol. 8, no. 3, pp. 390–426, Jun 2015.

Rev. IBRACON Estrut. Mater., vol. 14, no. 5, e14508, 2021

15/15

# IBRACON Structures and Materials Journal
## Revista IBRACON de Estruturas e Materiais

ORIGINAL ARTICLE

# Thermal analysis of steel and concrete composite beams cross sections in fire situations

*Análise térmica de seções transversais de vigas mistas de aço e concreto submetidas a situação de incêndio*

Mateus de Souza Furriel Dias[a]  
Vânia José Karam[a]

[a] Universidade Estadual do Norte Fluminense Darcy Ribeiro, Civil Engineering Laboratory, Campos dos Goytacazes, Rio de Janeiro, Brazil

**Abstract:** The fire poses a considerable risk to human safety and, therefore, fire protection is a solution that should be incorporated into the construction system of a building. Composite beams, when subjected to fire, lose strength and stiffness due to the degradation of the mechanical properties of their materials. This paper aims to perform the thermal analysis of steel and concrete composite beams in fire situation. The software ABAQUS Version 6.14 [1] was used to develop numerical methods, whose results were analyzed and compared with the values obtained by the simplified calculation method prescribed in ABNT NBR 14323:2013 [2]. Thereby, the thermal behavior of the composite cross-section and the influence of the material and the type of fire protection were analyzed. The results showed that, for a certain type of protection and size of the metallic profile, the temperatures given by the Brazilian Standard may differ substantially from those obtained by numerical simulation.

**Keywords:** steel and concrete composite beams; numerical models; fire; fire protection.

Resumo: O incêndio constitui um risco considerável à segurança humana e, dessa forma, o revestimento contra fogo é uma solução que pode ser incorporada ao sistema construtivo de uma edificação. As vigas mistas, quando submetidas ao fogo, perdem resistência e rigidez devido à degradação das propriedades mecânicas de seus materiais. Este artigo tem como objetivo realizar a análise térmica de vigas mistas de aço e concreto em situação de incêndio. Foram elaborados modelos numéricos no software ABAQUS Versão 6.14 [1], cujos resultados foram analisados e comparados com valores obtidos pelo método simplificado de cálculo prescrito na ABNT NBR 14323:2013 [2]. Com isso, analisou-se o comportamento térmico da seção transversal mista e a influência do material e do tipo de revestimento contrafogo. Os resultados mostraram que, para certo tipo de revestimento e tamanho do perfil metálico, as temperaturas previstas pela Norma Brasileira podem diferir substancialmente daquelas obtidas pela simulação numérica.

**Palavras-chave:** vigas mistas aço e concreto; modelagem numérica; incêndio; revestimento contrafogo.

## 1 INTRODUCTION

The structural systems composed of composite elements of steel and concrete aim to make the most of the advantages of each of these materials and bring some advantages, such as material savings and ease of execution. Composite steel and concrete beams emerged because of the use of steel beams underneath concrete slabs. The interaction between these two elements is guaranteed by metallic elements known as shear connectors.

Composite beams, when exposed to high temperatures, during typical fire conditions, have reduced mechanical strength and stiffness, which can cause all or part of the construction to collapse. In view of this, active or passive protections were developed, making it possible, to safely vacate the places that are part of a building of interest. Under

this assumption, the verification of composite steel and concrete structures in fire situation becomes an important step in the execution of projects. It is important to highlight that an analysis in a fire situation must be done thinking about the overall behavior of the structure and not only in terms of isolated elements.

The first research on composite steel and concrete beams were carried out using experimental models. Furnace tests, despite being an essential part of understanding structural fire behavior, are still expensive and time-consuming [3], which is why, on many occasions, numerical models are built that, once validated, allow obtaining various types of information, such as thermal fields, displacements, and stresses. Therefore, many research have been developed and published to analyze the behavior of composite structures in fire situations based on a numerical response. Among the existing tools for numerical analysis, stand out specific computer packages for structures in fire situations and commercial packages developed based on the Finite Element Method (FEM), which make it possible to reproduce the behavior of a structure.

Concern about the safety of structures in fire situation has been around for a long time in many European countries and in the United States. However, although fire is an extremely important issue, the concern in designing fire-resistant structures is recent in the Brazilian context.

One of the first finite element programs for the analysis of steel plane frames at high temperatures was designed by Jain and Rao [4], considering the change in material properties due to temperature increase, creep effect and large deformations. In the early 1990s, Burgess et al. [5] developed a numerical procedure that analyzed cross-sections of metallic beams, considering that the thermal and mechanical properties of steel changed with the non-linearity of the temperature along the cross-section. On passive protections, Wang [6] presented experimental and numerical results, proposing a new model that aimed to reduce the cost of fire protection coating material in composite beams.

The SAFIR software, a specific computer program for modeling structures in fire situation, was used in Cazeli et al. [7], in which numerical analyzes were carried out on steel beams in a fire situation, subject to the phenomenon of lateral buckling. Wong and Ghojel [8] analyzed heat transfer formulations in relation to fire-coated steel elements and noticed that, for certain types of fire protection coating materials, the temperatures calculated using EN 1993-1-2:2005 [9] differed substantially from those calculated using analytical solutions. Ribeiro [10] developed a computational algorithm for performing transient and nonlinear thermal analysis of two-dimensional and three-dimensional models of composite structural elements, based on the Finite Element Method. The results obtained were compared with the results found using the procedures of the main text of the revision of the standard ABNT NBR 14323:1999 [11], elaborated in 2003. In Rodrigues [12], a numerical and analytical study was carried out on the behavior of composite beams in fire situation, analyzing the fire phenomenon, its types of models, the degradation of steel properties with the temperature increase, thermal insulation of structures and the mechanisms of heat transmission.

Numerical models of composite steel and concrete partially coated beams were developed, in Rocha and Munaiar Neto [13], using the computational package DIANA, to evaluate the thermal and structural performance of this construction system. Fischer and Varma [14] developed 3D finite element models to predict the behavior and failure of composite beams in fire situations, which include both heating and cooling phases. A computational tool was developed, in Melão [15], able to calculate the resistant stress and temperatures of steel beams at room temperature and in fire situation, according to Brazilian Standards, including ABNT NBR 14323:2013 [2].

In this paper, two-dimensional numerical models of composite steel and concrete beams in fire situation are elaborated in the commercial software ABAQUS Version 6.14 [1], developed based on the Finite Element Method (FEM). The objective, based on the development of these models, is to perform thermal analysis of composite beams without and with fire protection coating of the contour and box types. The results obtained from the numerical models are compared with the results obtained through the simplified calculation method proposed in ABNT NBR 14323:2013 [2], to analyze the possible differences between these methods in the temperatures of the steel profile, shear connector and concrete slab. In this comparison, steel profiles with different dimensions are analyzed to verify the influence of the profile size on the evolution of the steel "temperature vs time" curve. This analysis is justified by the lack of papers that use this most recent standard and compare the results with variations in the profiles sizes.

Also, in this context, a new equation is proposed to determine the mass factor of the profile web in situations without fire protection and with contour-type fire protection coating, as a normative contribution. An analysis of the thermal behavior of the cross-section of the composite beam without fire protection is made from the results of the modeling, to verify the evolution of the temperature field and the heat flow during the time of exposure to fire. The maximum temperature points in each part of the composite section, the effect of the profile mass factor on the temperature rise and the efficiency of the type of fire protection coating on the steel profile and concrete slab are identified. In addition, the profile dimensions and the properties of the fire protection coating material that most influence the heat rise rate of the composite beam are evaluated.

Rev. IBRACON Estrut. Mater., vol. 14, no. 5, e14509, 2021

2/20

## 2 ASPECTS ADOPTED IN STEEL AND CONCRETE COMPOSITE BEAM MODELS

The thermal analysis of a structural element in fire situation corresponds to the verification of the development and distribution of the temperature field due to the heat transfer between the hot gases of the fire and the structure.

Each composite beam cross-section used in this project consists of a concrete slab with a flat bottom face, supported on the upper flange of the steel I-beam, containing or not the shear stud bolt connector. This is because, for the composite beam, a cross-section that passes through the shear connector and a section that does not pass through the connector were considered. Therefore, the disregard of the connector in the studied model occurs only in the thermal analysis of the composite section and this does not mean that composite beam does not have connectors between the steel profile and the concrete slab.

At this step of the thermal analysis, it is assumed that the part of the structural element that is totally immersed in the flames of the compartment, that is, where are located the steel beam and the bottom face of the concrete slab, is called "side exposed to fire", and the upper face of the slab is called "side not exposed to fire", where there is no fire, and the air is at room temperature. Figure 1 illustrates the composite beam parts and the regions exposed to fire and room temperature.

To determine the temperature of the structural element in a fire situation, the "temperature x time" curve of the hot gases, called standard fire, can be used together with the required time of fire resistance (RTFR), as determined in ABNT NBR 14323:2013 [2]. The ABNT NBR 5628:2001 [16] recommends the use of the following equation to determine the "temperature x time" curve of the standard fire:

$$\theta_g = \theta_{g0} + 345 \log\left(8t + 1\right) \tag{1}$$

where $t$ is the time, in minutes; $\theta_g$ is the gas temperature in the fire environment, in °C; and $\theta_{g0}$ is the gas temperature at the instant $t = 0$, in °C. The RTFR, according to ABNT NBR 14432:2001 [17], is the minimum time that a constructive element must resist fire when subjected to standard fire and can vary from 30 to 120 minutes.

The steel beam profiles (VS Series) used are welded and have dimensions specified by ABNT NBR 5884:2013 [18]. The steel beam profiles are: composite beam 1 - VS 350 x 42; composite beam 2 - VS 650 x 155; composite beam 3 - VS 250 x 32; composite beam 4 - VS 450 x 60. The choice for this type of profile is related to the greater flexibility of specifications and variety of sizes, making it possible to obtain profiles with different dimensions. Figure 2 shows the nomenclatures of the dimensions of the composite beam. It is important to point out that the profiles of the composite beams 2, 3 and 4 were chosen in order that they had different thicknesses and lengths of the flanges and web and that the dimensional variations were not disproportionate. Thus, it was considered that the steel profile of the composite beam 4 was intermediate to the steel profiles of the composite beams 2 and 3. All the slabs used in the composite beams have an effective width, W, equal to 1 m and a height, H, equal to 0.1 m. The connector used, illustrated in Figure 3, is the stud bolt and its dimensions are based on the Inox-Par M19 connector.
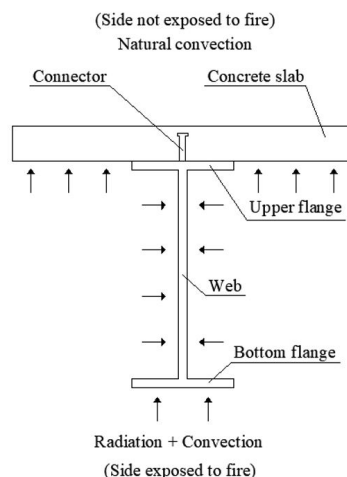


**Figure 1.** Proposed model of composite steel and concrete beam in a fire situation.
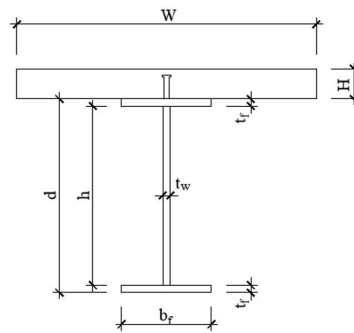
**Figure 2.** Nomenclatures of the dimensions of composite beam cross-section.
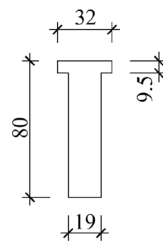


**Figure 3.** Dimensions of stud bolt connector, in mm.

For this project, contour and box types of fire protection coating were used for the steel profiles (without gaps), with thickness $t_m$, as shown in Figure 4.

Each cross-section of composite steel and concrete beam is indicated by its number followed by acronyms according to its boundary conditions, as follows:

- NP-C: has no fire protection coating and contains the stud bolt connector;
- NP-NC: has no fire protection coating and does not contain the stud bolt connector;
- CP-NC: has a contour-type fire protection coating and does not contain the stud bolt connector;
- BP-NC: has a box-type fire protection coating and does not contain the stud bolt connector.
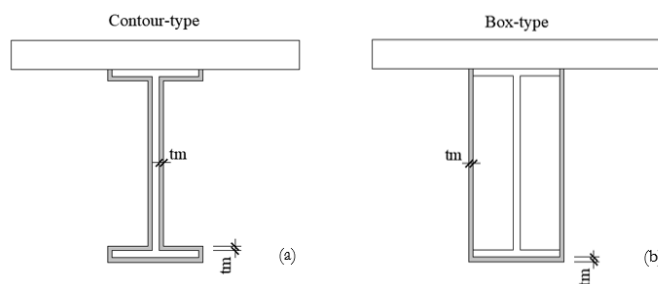


**Figure 4.** Fire protection coating: (a) contour-type and (b) box-type.

In all models, a resulting emissivity, $\varepsilon_{res}$, equal to 0.7, was adopted for steel and fire protection coating material. This value is standardized by the ABNT NBR 14323:2013 [2], although it mentions this value only for the emissivity resulting from steel. In accordance with recommendations prescribed in EN 1992-1-2:2004 [19], for the concrete, a resulting emissivity, $\varepsilon_{res}$, equal to 0.7 was adopted. The convective heat transfer coefficient, $\alpha_c$, on the side exposed to standard fire, was adopted equal to 25 W/m²·°C, as prescribed in ABNT NBR 14323:2013 [2]. Regarding the concrete slab, the heat exchange between the surface not exposed to fire and the environment was considered through an $\alpha_c$ coefficient equal to 9 W/m²·°C, according to recommendations prescribed in EN 1991-1-2:2002 [20]. For all composite beams, the initial temperature adopted in the cross-section was 20 °C, as standardized by the ABNT NBR 14323:2013 [2].

The thermal properties, such as specific heat and thermal conductivity, and the specific mass of the materials vary with temperature, however, simplified values of the properties of steel and concrete were used, as prescribed by ABNT NBR 14323:2013 [2] and ABNT NBR 15200:2012 [21], respectively, which are independent of temperature. The properties of the fire protection coating material used have similar values to the properties of ceramic fiber coatings, which are currently commercialized. The suppliers of these materials specify constant values for thermal properties, that is, they do not vary depending on the temperature. The same fire coating material was used to modeling composite beams with both contour and box fire protection types. The values of the properties and thickness of the steel, concrete and fire protection coating materials are shown in Table 1.

**Table 1.** Properties of the steel, concrete, and fire protection coating materials.

| Properties | Material | | |
|---|---|---|---|
| | Steel | Concrete | Coating |
| Specific mass (kg/m³) | 7850 | 2400 | 320 |
| Specific heat (J/kg·°C) | 600 | 1000 | 1100 |
| Thermal conductivity (W/m·°C) | 45 | 1.30 | 0.135 |
| Thickness (mm) | - | - | 13 |

In the numerical model of the composite beam with box-type fire protection coating, it was considered that the mechanism of heat transmission that predominates inside the cavity is only the heat conduction through the air, differently from what is considered in ABNT NBR 14323:2013 [2], where the existence of air is neglected. The values of the thermal properties of the air are shown in Table 2.

## 3 CALCULATION METHODOLOGY AND NUMERICAL MODELING

The models used in this paper to obtain the temperature evolution in the cross-section of the composite beam are the simplified and advanced calculation models. The simplified calculation model refers to the simplified equations of ABNT NBR 14323:2013 [2], which allow to obtain the temperature rise in a homogeneous way for each part of the cross-section. The advanced calculation model refers to the resolution of the problem through numerical simulation performed using the ABAQUS version 6.14 calculation code [1], which provides the researcher with the necessary resources for the modeling in question.

In the next items, conceptual aspects and procedures related to obtaining the temperature rise in the composite beams will be presented.

**Table 2.** Air properties inside the cavity of the box-type fire protection coating, Ribeiro [10].

| Temperature (ºC) | Specific mass (kg/m³) | Specific heat (J/kg·°C) | Thermal conductivity (W/m·°C) |
|---|---|---|---|
| 20 | 1.17 | 1000 | 0.025 |
| 100 | 0.94 | 1012 | 0.032 |
| 180 | 0.78 | 1025 | 0.038 |
| 260 | 0.65 | 1040 | 0.043 |
| 340 | 0.56 | 1056 | 0.048 |
| 420 | 0.50 | 1073 | 0.052 |
| 500 | 0.45 | 1090 | 0.056 |
| 580 | 0.41 | 1107 | 0.060 |
| 660 | 0.38 | 1125 | 0.063 |
| 740 | 0.35 | 1141 | 0.067 |
| 820 | 0.32 | 1158 | 0.071 |
| 900 | 0.30 | 1173 | 0.075 |
| 980 | 0.27 | 1188 | 0.080 |
| 1060 | 0.25 | 1201 | 0.086 |

## 3.1 Simplified calculation method of thermal analysis

ABNT NBR 14323:2013 [2] standardized a simplified method of calculation that aims to determine the thermal action and design of steel structures and composite structures of steel and concrete in fire situation. The simplified method of thermal analysis is applicable to structural steel elements with and without fire protection coating material, located inside the building, fully immersed in the fire environment.

For a uniform temperature distribution in the cross-section, the increase of temperature $\Delta\theta_{a,t}$, in °C, of the steel without fire protection coating over the time interval $\Delta t$, in seconds, can be determined by:

$$\Delta\theta_{a,t} = 0.9 \frac{(u/A_g)_b}{(u/A_g)} \times \frac{(u/A_g)}{c_a \rho_a} \varphi \Delta t \tag{2}$$

where $u$ is the perimeter of the steel structural element exposed to fire, in m; $A_g$ is the cross-sectional area of the steel structural element, in m²; $(u/A_g)$ is the mass factor for steel structural elements without fire protection coating, in m⁻¹; $(u/A_g)_b$ is the value of the mass factor defined as the ratio between the perimeter exposed to the fire of a hypothetical box that surrounds the profile and the cross-sectional area of the profile, in m⁻¹; $\rho_a$ is the specific mass of the steel, in kg/m³; and $c_a$ is the specific heat of the steel, in J/kg·°C.

The heat flow value $\varphi$, in W/m², is given by:

$$\varphi = \varphi_c + \varphi_r \tag{3}$$

with

$$\varphi_c = \alpha_c \left( \theta_g - \theta_a \right) \tag{4}$$

and

$$\varphi_r = 5.67 \times 10^{-8} \varepsilon_{res} \left[ \left( \theta_g + 273 \right)^4 - \left( \theta_a + 273 \right)^4 \right] \tag{5}$$

where $\varphi_c$ is the component of the heat flow due to convection, in W/m²; $\varphi_r$ is the component of the heat flow due to radiation, in W/m²; $\theta_a$ is the temperature on the steel surface exposed to fire, in °C; $\theta_g$ is the temperature of the gases, in °C; $\varepsilon_{res}$ is the resulting emissivity; and $\alpha_c$ is the convection heat coefficient, in W/m²·°C.

In steel profiles with fire protection coating, the heat reaching the steel depends on the conduction through the protection coating material, unlike what occurs in the elements without fire protection coating, in which the heat is transmitted by convection and radiation. Consequently, for a uniform temperature distribution in the cross-section, the temperature rise $\Delta\theta_{a,t}$, in °C, of the steel surrounded by a fire protection coating material during a time interval $\Delta t$, in seconds, can be determined by:

$$\Delta\theta_{a,t} = \frac{\lambda_m \left( \dfrac{u_m}{A_g} \right) \left( \theta_{g,t} - \theta_{a,t} \right)}{t_m \rho_a c_a \left( 1 + \dfrac{\xi}{4} \right)} \Delta t - \frac{\Delta\theta_{g,t}}{\dfrac{4}{\xi} + 1} \tag{6}$$

where $\Delta\theta_{a,t} \geq 0$ if $\Delta\theta_{g,t} > 0$

Rev. IBRACON Estrut. Mater., vol. 14, no. 5, e14509, 2021

6/20

with

$$\xi = \frac{c_m \rho_m}{c_a \rho_a} t_m \left( \frac{u_m}{A_g} \right) \tag{7}$$

where $u_m$ is is the effective perimeter of the fire protection coating material, in m; $\left( u_m / A_g \right)$ is the mass factor for structural steel elements with fire protection coating material, in m$^{-1}$; $c_m$ is the specific heat of the fire protection coating material, in J/kg·°C; $\lambda_m$ is the thermal conductivity of the fire protection coating material, in W/m·°C; $\rho_m$ is the specific mass of the fire protection coating material, in kg/m$^3$; and $t_m$ is the thickness of the fire protection coating material, in m.

The time interval $\Delta t$ was adopted as 5 seconds for all analyzed cases. When the steel profile is not surrounded by fire protection coating material or has a contour-type fire protection coating, the temperature distribution in the steel profile must be taken as non-uniform. In this way, the cross-section is divided into three parts: bottom flange, web and upper flange. In this case, it is considered that there is no heat transfer between these parts or between the upper flange and the concrete slab. Therefore, the mass factor $u / A_g$ or $u_m / A_g$, in m$^{-1}$, must be equal to:

- For the bottom flange: $2 \left( b_f + t_f \right) / b_f t_f$ (8)
- For the upper flange overlaid with solid slab: $\left( b_f + 2 t_f \right) / b_f t_f$ (9)
- For the web: $2h / t_w$ (10)

with $b_f$, $t_f$, $h$ and $t_w$ in meters.

For steel components with box-type fire protection coating, a uniform temperature can be considered in the profile.

Regarding the concrete slab, it is considered that the temperature distribution is constant along the effective width and the temperature variation in the slab height can be obtained from Table A.1 of ABNT NBR 14323:2013 [2], dividing the slab height into a maximum of 14 slices. In a simplified form, it can be considered the uniform temperature along the height of the concrete slab, and equal to:

$$\theta_c = \frac{1}{H} \sum_{j=1}^{n} \theta_{c,j} e_j \tag{11}$$

where $n$ is the number of slices into which the slab was divided; $H$ is the thickness of the concrete slab, in mm; $\theta_{c,j}$ is the temperature, in °C; and $e_j$ is the thickness of a slice $j$, in mm.

## 3.2 Numerical modeling in the software ABAQUS

The study of the thermal behavior of composite beams in fire situation through numerical simulations allows more detailed analysis of some aspects of interest to the composite system, such as, for example, the field and temperature evolution, thermal gradients, and thermal flows in a certain region. Thus, two-dimensional models of composite beams are proposed to satisfactorily simulate their thermal behavior in fire situation.
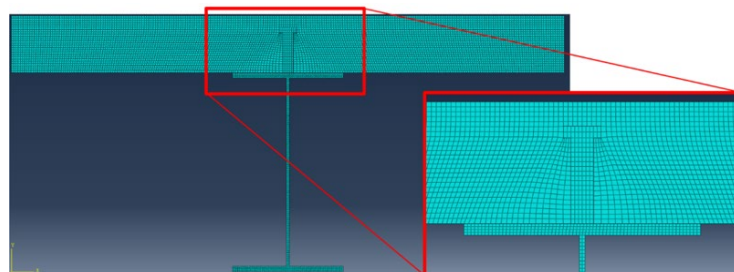


**Figure 5.** Finite element mesh of the composite beam 1 (NP-C).

Rev. IBRACON Estrut. Mater., vol. 14, no. 5, e14509, 2021

7/20

In this paper, all parts of the structural element were defined as solid, homogeneous, and two-dimensional elements. The finite element used in the discretization of the entire composite beam is DC2D4, a 4-node quadrilateral element belonging to the heat transfer family. It is important to highlight that the finite element meshes were designed so that there was node located exactly at each point where it is desired to determine the temperature. Several meshes, less and more refined, were considered, observing that, after a certain degree of mesh refinement, the results converged to the presented results. For each model of composite beam simulated in ABAQUS, a different mesh was used, due to the variations of the sizes of the steel profile. The Figure 5 illustrates the mesh of the composite beam 1 (NP-C).

An analysis step of 7200 seconds was created for a transient response, with an increment of 60 seconds, which makes it possible to determine the distribution and values of temperatures as a function of time.

In the amplitude of the temperature reached in the composite beam contour, the "temperature x time" curve of the "Standard Fire" was respected, establishing a maximum gas temperature equal to 1049 °C. Thus, were introduced the thermal interactions of the composite beam with hot gases and gases at room temperature, and of the steel profile with the concrete slab, with the fire protection coating material and with the air present in the box-type fire protection coating. The temperatures are expressed from the scale of temperature in Celsius degrees, considering, in this case, the absolute temperature equal to -273.15 °C, and the Stefan-Boltzmann constant equal to 5.67 x $10^{-8}$ kW/m$^2$·K$^4$.

In the numerical modeling of these composite beams in ABAQUS, it was considered that there is heat exchange between the parts of the metallic profile (bottom flange, upper flange and web) and also between the upper flange and the concrete slab.

## 4 RESULTS AND DISCUSSIONS

As a result of the thermal analysis, the evolution and distribution of the temperature field is observed in the cross-section of the entire composite beam. The results of the analysis were divided into four stages: analysis of the thermal behavior of the composite beam cross-section, comparative thermal analysis (ABAQUS vs ABNT NBR 14323:2013), analysis of composite beams without fire protection coating material and analysis of composite beams with fire protection coating material.

### 4.1 Analysis of the thermal behavior of the composite beam cross-section

This analysis, carried out using ABAQUS program, aims to describe the thermal behavior of the cross-section of the composite beam 1 in fire situation, without fire protection coating and with the stud bolt connector at the interface between the profile and the concrete slab. The analysis was made only in this composite beam because the evolution of the temperature field and the heat flow are maintained with the same pattern in other cross-sections of the same model.

### 4.1.1 Temperature field of the cross-section

With the temperature field, it is possible to analyze the temperature distribution along the cross-section, observing the regions that have higher temperatures. Figure 6 shows the temperature field of the composite beam 1 (NP-C) in 120 minutes of fire duration.
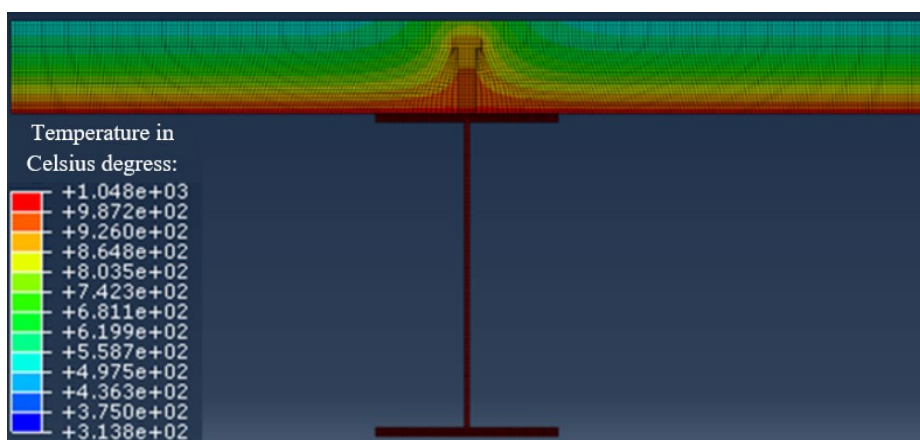


**Figure 6.** Temperature field (°C), in 120 minutes of fire duration, of the composite beam 1 (NP-C).

The temperature field in the concrete slab is uniform along the effective width, except in the region that contains the connector, due to the difference in thermal conductivity between steel and concrete. The concrete slab temperature is higher on the surface exposed to the fire and decreases as it approaches the surface in contact with room temperature. It is observed that the steel profile presented the highest temperatures in the composite section and that the connector does not have a uniform temperature along its height.

### 4.1.2 Temperature distribution at specific points

It is possible to analyze the temperature field in more detail using the temperature values calculated at certain specific points and observe the difference in the temperature gradient in each specific part of the composite beam. Figure 7 shows temperature values at fifteen specific points in the composite section during the fire duration times of 30 and 60 minutes for the composite beam 1 (NP-C).
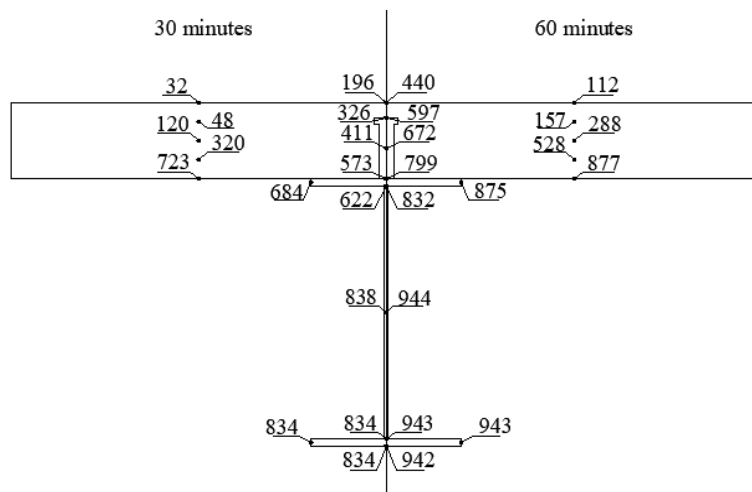


**Figure 7.** Distribution of temperatures (°C) in the composite beam 1 (NP-C) for the fire duration times of 30 and 60 minutes.

The upper flange, as it was not fully exposed to fire due to the presence of the concrete slab, reached the lowest temperatures of the steel profile. All regions of the bottom flange had the same temperature for a certain time of fire. The web, in addition to having the highest temperature in the cross-section, had a non-uniform temperature distribution along its length. The temperature of the connector was higher in the region closest to the upper flange due to the conduction of heat between these two parts. The maximum temperature regions $\theta_{max}$ of each part of the composite beam and the concrete slab sections for thermal analysis are shown in Figure 8.
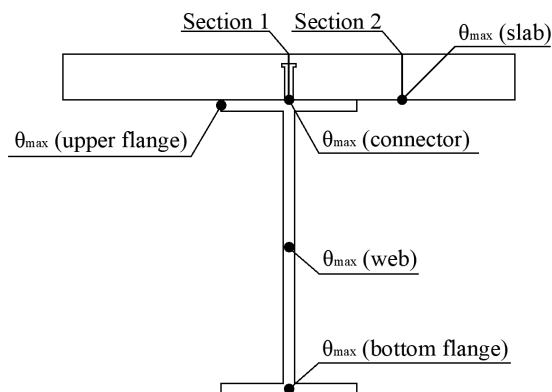


**Figure 8.** Maximum temperature regions of the composite cross-section parts.

Rev. IBRACON Estrut. Mater., vol. 14, no. 5, e14509, 2021

9/20

### 4.1.3 "Temperature x time" curves

The "temperature x time" curves make it possible to observe the temperature evolution of a certain point in the cross-section over time. The points chosen for analysis are those with the maximum temperature of the flanges, web, concrete slab and connector. The "temperature x time" curves of these regions of the composite beam 1 (NP-C), the upper flange of the composite beam 1 (NP-NC) and the standard fire are shown in Figure 9.

The temperature of the entire composite beam increases with time, as does the temperature of the gases in fire situation. The "temperature x time" curves of the web and the bottom flange had a more pronounced elevation in comparison to the other parts of the section in the first 20 minutes, until reaching the temperature equal to that of atmospheric air. The maximum temperature of the concrete slab develops faster than the temperature of the upper flange in the first 50 minutes, and then the curves of these parts become similar. The connector was the element that had the lowest maximum temperature during the entire fire duration.
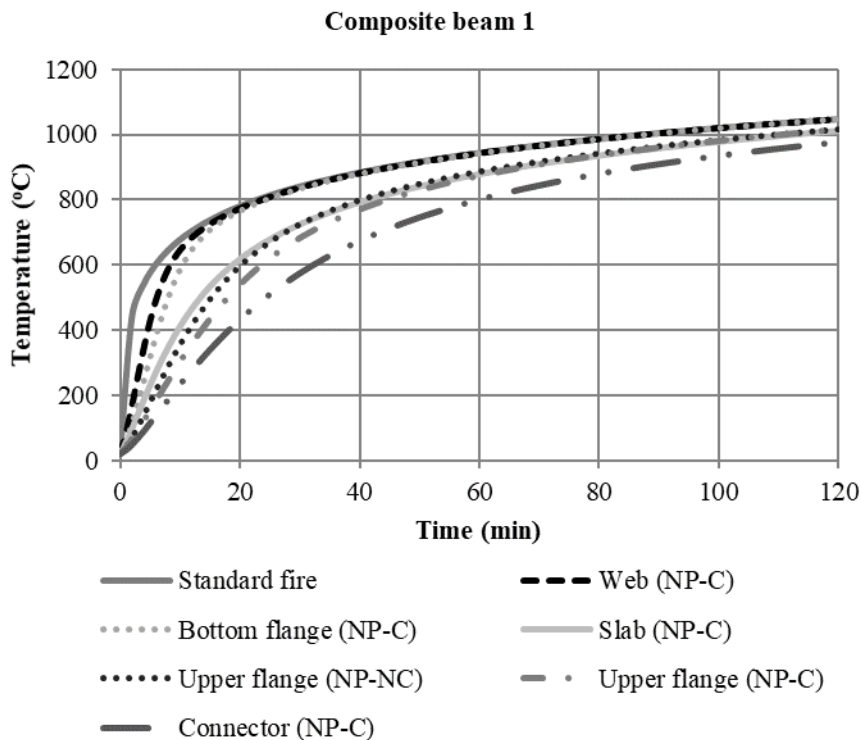


**Figure 9.** "Temperature x time" curves of the parts of the composite beam 1 and standard fire.

In the "temperature x time" curve of the center of the upper flange of the composite beam 1 (NP-NC), in the section without the presence of the shear connector, it can be observed that the maximum temperature reached was higher than the maximum temperature of the upper flange in the section where there is a connector. This shows that the presence of the shear connector increased the heat flow from the upper flange, causing a decrease in the temperature on the flange. Therefore, since the flange temperature of the steel profile of the composite beam 1 was analyzed in two cross-sections (with and without the shear connector), the thermal analyzes can be done without the presence of the connector and considering the maximum temperature of the upper flange at its center.

### 4.2 Comparative thermal analysis: ABAQUS x ABNT NBR 14323:2013

The purpose of this analysis is to compare the results obtained by the numerical modeling performed at ABAQUS with those obtained by the simplified method proposed in ABNT NBR 14323:2013 [2]. In this analysis, it is possible to compare the temperature of the cross-section of the composite beams 1, 2 and 3 at various times of the fire duration

in three situations: profile without fire protection coating, profile with contour-type fire protection coating and profile with box-type fire protection coating.

### 4.2.1 "Temperature x time" curves

For this step, the composite beam 2, with larger dimensions, and the composite beam 3, with smaller dimensions, were chosen to verify if the difference in the size and linear mass of the profile generates any influence in the comparison of its curves. The Equation (10) determined in ABNT NBR 14323:2013 [2] to calculate the mass factor of the web of the steel profile is dimensionless, that is, it does not have the correct unit representing the mass factor that is m$^{-1}$. It is also possible to verify that, when the mass factor of the web, $(u/A_g)$, is determined, considering the ratio of its perimeter by the area of its cross-section, the following equation is found:

$$Mass\ Factor = \frac{2 \times (h + t_w)}{h \times t_w} \tag{12}$$

where $h$ and $t_w$ are in meters and the final unit of the mass factor is in m$^{-1}$.

Therefore, it is believed that the Equation (10), obtained from the standard, is incorrect. Thus, the "temperature x time" curve of the web was calculated using the ABNT NBR 14323:2013 [2] method, using the Equation (10), and the method proposed in this paper, applying the Equation (12), for the profile without fire protection coating and with contour-type fire protection coating. With respect to the upper and bottom flanges of the steel profile, Equations (8) and (9), obtained from the standard, provide the correct unit of mass factor, respecting the $(u/A_g)$ ratio, and it is not necessary to propose a new equation for these parts of the steel profile.

Figures 10, 11, and 12 show the "temperature x time" curves from the two calculation methods to the parts of the steel beam, in the case of the profile without a fire protection coating, with a contour-type fire protection coating and with a box-type fire protection coating, respectively.

#### 4.2.1.1 Profile without fire protection coating

The "temperature x time" curve for composite beams without fire protection coating can be seen in the Figure 10.

Concerning to the bottom flange, the temperature obtained by ABAQUS was higher than the temperature obtained using the method proposed by the standard around the first 40 minutes. The difference in the curves obtained through these two methods was more significant in the profile of the composite beam 2 (NP-NC), and, after that, the two "temperature x time" curves were equal. Given these results, there was a greater similarity of the curves as the dimensions of the bottom flange became smaller.

With respect to the web, the curve obtained by ABAQUS was higher than the curve obtained using the standard method and this difference was smaller in the composite beam 2 (NP-NC). However, the ABAQUS curve was closer to the curve obtained with a change in the equation of the mass factor of the web, for all profiles analyzed. This shows that the use of the Equation (12) provides profile temperatures closer to the temperatures obtained by numerical modeling.

Regarding the upper flange, the "temperature x time" curve obtained by ABAQUS was higher than the curve obtained by the standard equation in the first 40 minutes and 20 minutes for the profile of the composite beams 2 (NP-NC) and 3 (NP-NC), respectively. After that time, the curve obtained by the standard method remains slightly higher.

#### 4.2.1.2 Profile with contour-type fire protection coating

In Figure 11, the "temperature x time" curves can be observed for the composite beams with contour-type fire protection coating.

The "temperature x time" curves of the bottom flange are very close to each other, mainly for the lighter profile, used in the composite beam 3 (CP-NC).

In the web, there was a more prominent difference between the curves obtained by ABAQUS and standard equation, which is more evident in the composite beam 3 (CP-NC), and the curves tended to be closer as the profile became larger, as the case of composite beam 2 (CP-NC). The results obtained by the simplified method with alteration in the

equation of the web mass factor overestimate the results obtained by ABAQUS, and were closer to the composite beam 2 (CP-NC).

In relation to the upper flange, the curves are similar in the profile of the composite beam 2 (CP-NC), while in the profile of the composite beam 3 (CP-NC), whose upper flange has smaller dimensions, the difference between the curves becomes greater with time.

### 4.2.1.3 Profile with box-type fire protection coating

In Figure 12, the "temperature x time" curves can be observed for composite beams with box-type fire protection coating.

The "temperature x time" curves obtained by the standard method are the same in the parts of a same steel profile because a uniform temperature is considered along the profile. However, each part of the steel profile with box-type fire protection coating has different "temperature x time" curves obtained by modeling in ABAQUS. It is possible to note that the curve obtained by the standard method was higher than the curve obtained by ABAQUS in the entire profile, for any profile analyzed and for the entire fire duration. The difference between these curves was greater over the fire duration. Comparing the results of steel profiles with different sizes, an increase in the size of the profile did not significantly influence the difference between the curves of the flanges and the web.
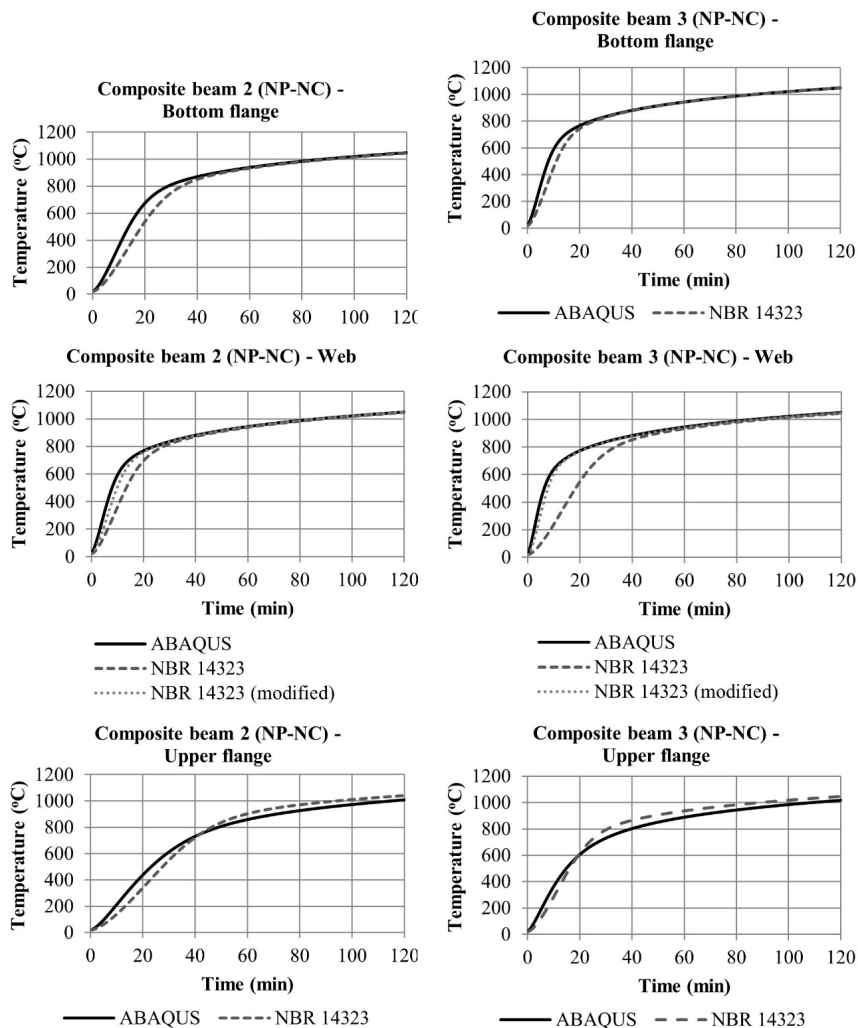


**Figure 10.** "Temperature x time" curves obtained by the simplified method and by the advanced calculation method for the profiles of composite beams 2 (NP-NC) and 3 (NP-NC).

Rev. IBRACON Estrut. Mater., vol. 14, no. 5, e14509, 2021

12/20

**Figure 11.** "Temperature x time" curves obtained by the simplified method and by the advanced calculation method for the profiles of composite beams 2 (CP-NC) and 3 (CP-NC).

### 4.2.2 Uniform temperature in the concrete slab sections

This step allows to analyze, in ABAQUS, the temperature of the slab in two sections: one in the connector region (section 1) and the other located between the connector and the end of the effective width (section 2). For comparison with the results obtained using the method prescribed by ABNT NBR 14323:2013 [2], composite beam 2 with and without fire protection coating was used. Table 3 shows these temperatures over four fire times.

**Figure 12.** "Temperature x time" curves obtained by the simplified method and by the advanced calculation method for the profiles of composite beams 2 (BP-NC) and 3 (BP-NC).
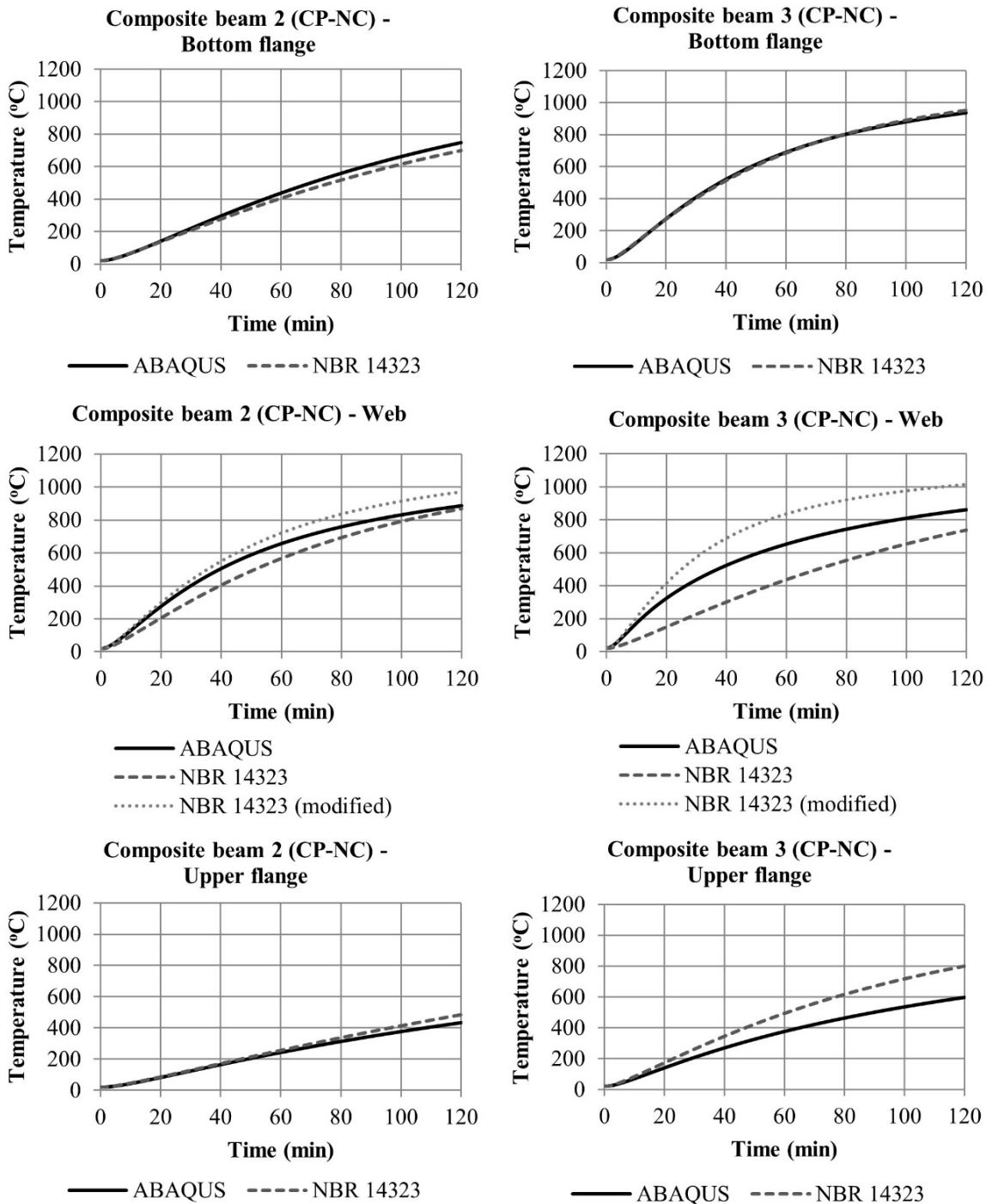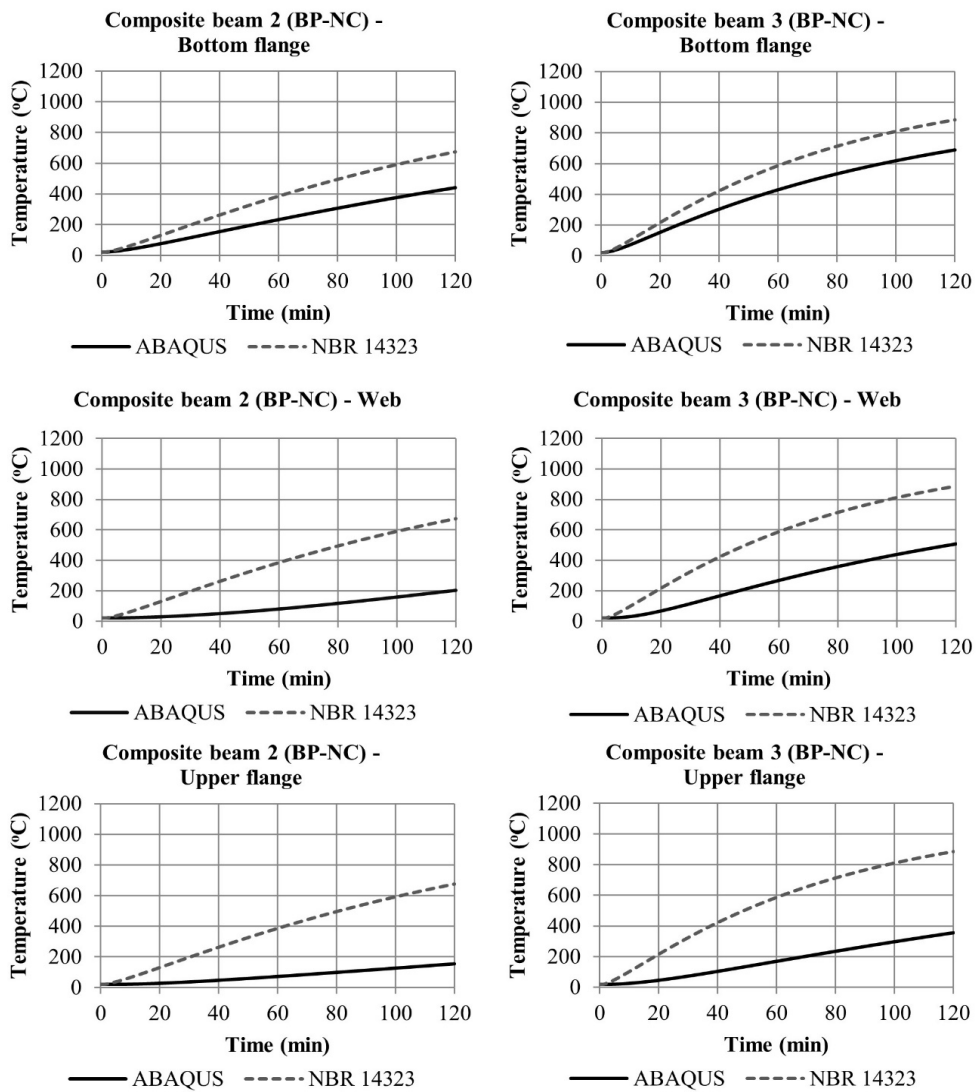
**Table 3.** Uniform temperature in the concrete slab sections.

| Time (min) | Temperature of concrete slab sections (ºC) | | | | | | |
|---|---|---|---|---|---|---|---|
| | NBR 14323 | ABAQUS - Section 1 | | | ABAQUS - Section 2 | | |
| | | 2 (NP-NC) | 2 (CP-NC) | 2 (BP-NC) | 2 (NP-NC) | 2 (CP-NC) | 2 (BP-NC) |
| 30 | 190 | 155 | 41 | 23 | 214 | 213 | 213 |
| 60 | 296 | 327 | 88 | 35 | 369 | 365 | 366 |
| 90 | 343 | 459 | 146 | 55 | 488 | 479 | 480 |
| 120 | 361 | 561 | 209 | 81 | 582 | 568 | 568 |

ABNT NBR 14323:2013 [2] presents an equation to calculate a uniform temperature in the concrete slab that does not change neither with the properties of the concrete, nor with the type of profile and nor with the presence of a fire protection coating. For comparison, temperatures were determined in fourteen slices of the slab in ABAQUS and uniform temperatures were calculated using the Equation (11) from the standard.

Rev. IBRACON Estrut. Mater., vol. 14, no. 5, e14509, 2021

14/20

The temperatures in the concrete slab, both in section 1 and section 2, are different from the values calculated according to the standard. The section 1 of the slab, along its height, presented a different temperature at certain time for each situation in which the steel profile is (with and without fire protection coating). Among the fire protection coatings used, the box-type fire protection coating resulted in lower temperature values and the slab showed higher temperatures when it had no fire protection coating. Section 2 presented the same temperature in any situation where the composite beam is subjected, depending only on the thermal properties of the concrete of the slab. This section, due to the highest temperatures, was considered the critical section of the concrete slab; therefore, it is the ideal section to compare with the values obtained using the standard method. In this section of the slab, the temperature found by ABAQUS was higher than the temperature found by the use of the standard equation, and this difference was greater with a longer fire duration.

The same composite beam 2 (NP-NC) was analyzed considering the thickness of the concrete slab equal to 7 cm through the two calculation methods. It was possible to note that the decrease in thickness increased the uniform temperature of the slab in the two sections, but still with the temperature obtained by ABAQUS higher than the temperature obtained by the standard equation. The minimum temperature reached by the concrete slab (section 2 surface not exposed to fire) is higher when the slab thickness is reduced, while the maximum concrete slab temperature (section 2 surface exposed to fire) has not changed significantly. The decrease in the slab height did not result in a modification in the "temperature x time" curve of the metallic beam upper flange.

### 4.2.3 Connector temperature

According to ABNT NBR 14323:2013 [2], the connector temperature can be considered, conservatively, equal to the highest temperature among those of the connected structural elements. However, this standard specifies that the design resistant force of a shear connector in fire situation must be determined at a temperature equivalent to 80% of the temperature of the upper flange of the steel profile. As can be seen in the graph of Figure 9, referring to the composite beam connector 1 (NP-C) used in item 4.1.3, the "temperature x time" curve of the connector is closer to the curve of the upper flange, and shows that this element reached the lowest maximum temperature of the composite section. It is possible to note that the temperature of the connector was, on average, equal to 80% of the temperature of the upper flange during the first 30 minutes of fire, and higher than 80% after that time.

### 4.3 Analysis of composite beams without fire protection coating material

This item aims to analyze, using ABAQUS, the temperature rising in the steel section as function of the mass factor and the dimensions (h, bf, tw and tf) of each part of the steel section and, also, evaluate the development of the concrete slab temperature during the time of exposure to fire. For this analysis, composite beam 2 (NP-NC), with a larger dimension profile, composite beam 3 (NP-NC), with a smaller dimension profile, and the beam 4 (NP-NC), with intermediate dimension profile, were used.

### 4.3.1 Influence of the mass factor

Table 4 shows the values of the mass factors of the steel profiles and of each profiles parts. It is possible to note that the profile of the composite beam 3 (NP-NC), with lower linear mass, has the largest mass factor, as well as its parts. Comparing the results of each part of a profile, the web had a higher value of the mass factor, the bottom flange presented an intermediate value and the upper flange, being protected from fire in one side, presented the lowest factor.

**Table 4.** Mass factor of each part and of the metallic profiles of the composite beams 2 (NP-NC), 3 (NP-NC) e 4 (NP-NC).

| Composite beam | Mass factor ($m^{-1}$) | | | |
|---|---|---|---|---|
| | Upper flange | Bottom flange | Web | Metallic profile |
| 2 (NP-NC) | 46 | 86 | 250 | 110 |
| 3 (NP-NC) | 115 | 220 | 421 | 235 |
| 4 (NP-NC) | 87 | 167 | 317 | 194 |

Figure 13 shows the "temperature x time" curves of the parts of each profile used in this analysis, up to 40 minutes, to analyze the heating speed of the steel as a function of the mass factor.

The first minutes of fire are the most important, once are when the profile temperature increases most rapidly. Comparing the "temperature x time" curves of each part of the profile, among the analyzed profiles, it is observed that the curves tended to be equivalent at some point.

The parts of the profile of the composite beam 3 (NP-NC), with smaller dimensions and greater mass factor, had a higher temperature increase. In contrast, the profile of the composite beam 2 (NP-NC), with less mass factor, took longer to heat up when subjected to high temperature, while the profile of the composite beam 4 (NP-NC) showed an intermediate temperature increase. It is observed that profile 3 (NP-NC) has a mass factor closer to profile 4 (NP-NC), and the "temperature x time" curves of these profiles are also closer. This behavior shows that a profile with a greater mass factor will present the slope of the "temperature x time" curve steeper, indicating that it has a faster temperature rise.
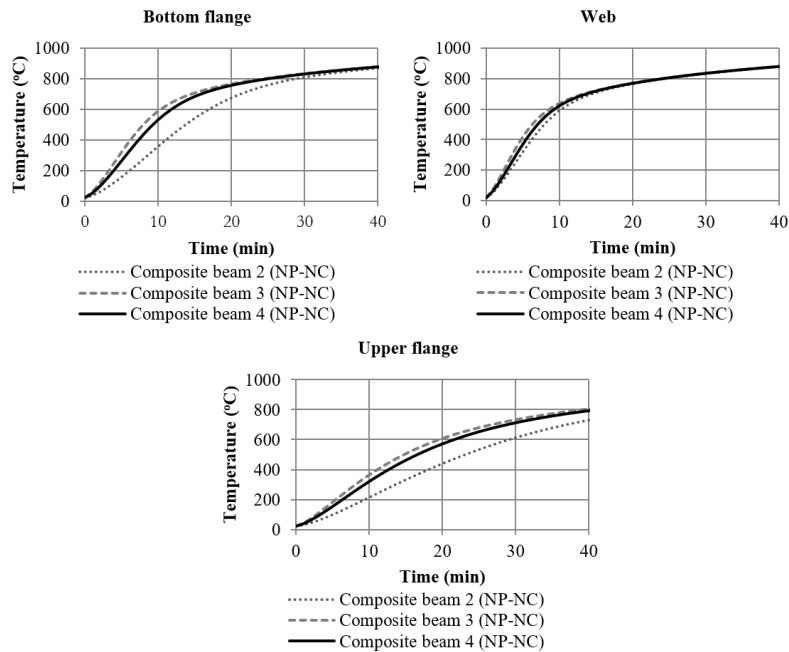


**Figure 13.** Temperature development in each part of the steel profiles up to 40 minutes.

### 4.3.2 Uniform temperature in the concrete slab sections

The uniform temperatures of the slabs of the composite beams 2 (NP-NC) and 3 (NP-NC) were analyzed, with the objective of verifying the influence of the profile mass factor in the analyzed sections. The temperature values for the two analyzed sections of each concrete slab are shown in Table 5. In section 1, the highest temperatures corresponded to the profile of the composite beam 3 (NP-NC), with the highest mass factor and the lowest linear mass. Therefore, the size of the metallic profile, mainly the length (bf) of the upper flange, influenced the temperature of the region where the shear connector is located. Hence, higher the mass factor of the profile, higher the temperature in the connector. The temperatures of section 2 of the concrete slab were practically the same for both profiles, showing that the size and mass factor of the profile did not influence the maximum temperature of the slab.

**Table 5.** Uniform temperature in the concrete slab sections of the composite beams 2 (NP-NC) and 3 (NP-NC).

| | Temperature of the concrete slab sections (ºC) | | | |
|---|---|---|---|---|
| Time (min) | ABAQUS - Section 1 | | ABAQUS - Section 2 | |
| | 2 (NP-NC) | 3 (NP-NC) | 2 (NP-NC) | 3 (NP-NC) |
| 30 | 155 | 203 | 214 | 214 |
| 60 | 327 | 365 | 369 | 370 |
| 90 | 459 | 488 | 488 | 489 |
| 120 | 561 | 584 | 582 | 584 |

## 4.4 Analysis of composite beams with fire protection coating material

This analysis aims to evaluate the thermal performance of the composite beam with fire protection coating material and to verify which of the two types of fire protection coating types, contour or box, is the most efficient to delay the temperature rise in the composite beam. In addition, the influence of the variation in the properties of the fire protection coating material was analyzed. For this analysis, the ABAQUS was used for the numerical modeling of the composite beam 2.

### 4.4.1 "Temperature vs time" curve of the profile parts

In Figure 14, the "temperature x time" curves of the parts of the steel profile without fire protection coating, with contour-type fire protection coating and with box-type fire protection coating are found. With these curves, it is possible to verify the effect that the type of fire protection coating has on the heat retardation in steel.

The temperature of the steel profile can increase rapidly or not, depending on the degree of fire protection coating applied (or its absence). The use of fire protection coating prevented a very rapid temperature rise in the initial minutes, which can be observed when comparing the slope of the "temperature x time" curves of the profile with and without fire protection coating, and caused a decrease in temperature in all parts of the profile over the time.

With a contour-type fire protection coating, the upper flange showed a greater temperature drop in relation to the web and the bottom flange. The box-type fire protection coating showed the highest thermal efficiency, once it ensures that the surface affected by the fire is largely away from the steel profile. With this type of coating, the highest temperature is found on the bottom flange, while in the web, which is away from the surface affected by the fire due to the coating, the temperature is slightly higher than the temperature of the upper flange.
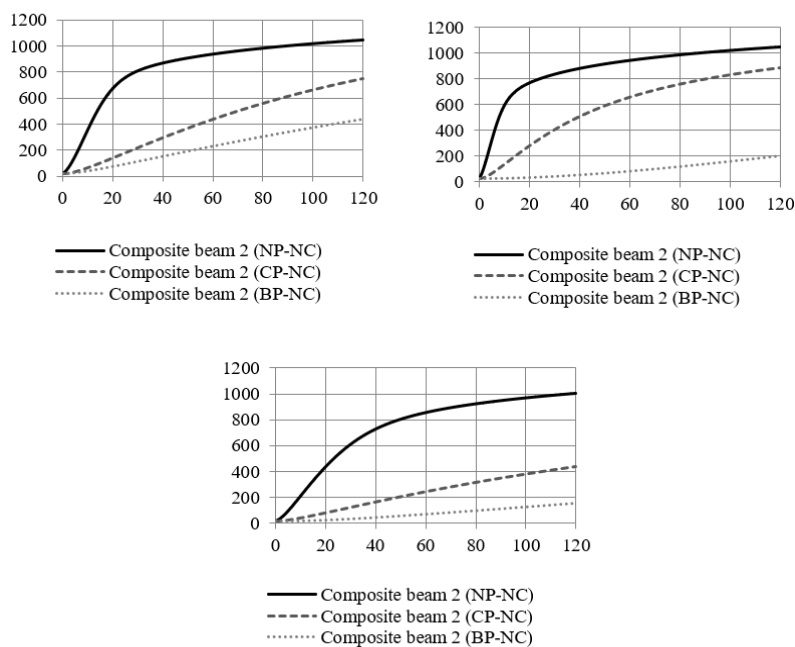


**Figure 14.** Temperature development in composite beam 2 with and without fire protection coating during the time of exposure to fire.

### 4.4.2 Variation in the properties of the fire protection coating material

This step makes it possible to analyze the influence of each thermal property and the thickness of the fire protection coating material. For this, the composite beam 2 was used as a reference for cases without fire protection coating, with contour-type fire protection coating and with box-type fire protection coating. The analyzed situations had only a thermal property or the thickness changed, with an increase of 20% of its value. Table 6 shows the reference values and the four cases analyzed, called cases (a), (b), (c) and (d).

**Table 6.** Values of the properties of the fire protection coating material for the cases analyzed.

| Fire protection coating material properties | Reference values | Case (a) | Case (b) | Case (c) | Case (d) |
|---|---|---|---|---|---|
| Thermal conductivity (W/m·ºC) | 0.135 | 0.162 | 0.135 | 0.135 | 0.135 |
| Specific mass (kg/m³) | 320 | 320 | 384 | 320 | 320 |
| Specific heat (J/kg·ºC) | 1100 | 1100 | 1100 | 1320 | 1100 |
| Thickness (mm) | 13 | 13 | 13 | 13 | 15.6 |

The graphs in Figure 15 show the "temperature x time" curves of the reference situation and the cases analyzed for the three parts of the steel profile, with a contour and box-type fire protection coating.

For the profile with contour-type fire protection coating, in case (a), when the thermal conductivity value increased, the "temperature x time" curve for all parts of the profile was higher, unlike other situations, when the temperature of the profile tended to decrease with the increase of the properties. The most significant decrease in temperature occurred in case (d) when there was a variation in the thickness of the fire protection coating. In cases (b) and (c), the curves are close to the reference curve for all parts of the profile, that is, the increase in specific mass and heat generated an insignificant decrease in temperature for all profile parts.
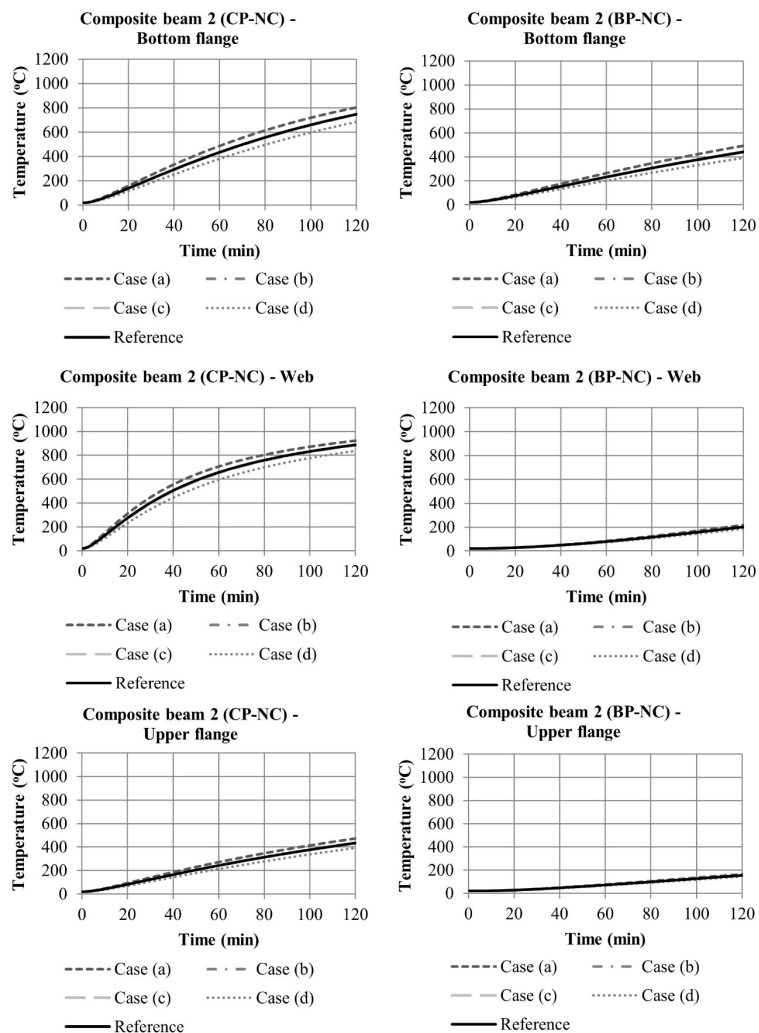


**Figure 15.** "Temperature x time" curves of reference metallic profile and of the situations analyzed with contour and box-type fire protection coating.

Rev. IBRACON Estrut. Mater., vol. 14, no. 5, e14509, 2021

18/20

Regarding the box-type fire protection coating, the variation in properties had a similar influence to the use of the contour-type fire protection coating. It is possible to note a greater influence of the variations in the properties of the fire protection coating material on the bottom flange, where the difference between the "temperature x time" curves of the different cases and the reference was more accentuated. In relation to the upper flange and the web, changes made to any property of the fire protection coating material did not result in a significant variation in temperature.

## 5 CONCLUSIONS

In this paper, thermal analyzes of composite steel and concrete beams were carried out using numerical modeling and the simplified calculation proposed by ABNT NBR 14323:2013 [2], with the main result being conclusions about the thermal behavior of the composite cross-section, in addition to the importance of considering fire protection coating. Considering these results, it can be concluded for the analysis of thermal behavior that:

- The temperature of the entire composite system without fire protection coating has increased over the time, as expected;
- The profile, connector and concrete slab presented a non-uniform temperature field over the duration of the fire, as expected;
- The presence of the shear connector decreased the maximum temperature reached on the upper flange.

By comparing the two methods of thermal analysis (ABAQUS and Brazilian Standard), the following conclusions are reached:

- For all parts of the profile with and without fire protection coating, the "temperature x time" curve obtained by modeling in ABAQUS had the same trend as the curve obtained by the use of the ABNT NBR 14323:2013 [2] method, as expected;
- There was a better agreement between the "temperature x time" curves of the web of a profile without fire protection coating, obtained by the standard equation and by numerical modeling, when the mass factor was changed for the profile without fire protection coating, which it is justified by the fact that the equation proposed in the present paper was determined from the definition of the mass factor and provides the correct unit for this factor, which does not occur with the unit of the standard equation;
- It can be seen from the graphs that the results obtained with the use of the web mass factor equation proposed by the standard are lower than the results obtained by numerical modeling in the first 40 minutes of fire of the composite beam without fire protection coating and in all fire duration in the composite beam with contour-type fire protection coating, which indicates that, in these cases, the values obtained by the standard equation are against safety;
- It is evident that the greatest discrepancy, comparing the profiles without and with fire protection coating, occurred for the case with the box-type fire protection coating. This is due to the fact that the standard presents equations that were developed assuming a uniform temperature distribution in the steel profile;
- The slab had the highest temperatures in section 2. This section, considered the critical section, has the same temperatures, regardless of the profile conditions;
- In a simplified form, the temperature of the connector can be considered equal to the temperature of the upper flange.
In the analysis of composite beams without fire protection coating material, the following conclusions can be drawn:
- The temperature increase rate of the steel profile in fire situation is proportional to its mass factor. Hence, a greater mass factor caused a "temperature x time" curve of the parts of the profile that were more steep, as expected;
- The size of the steel profile did not influence the temperature of section 2 of the slab.
In the analysis of composite beams with fire protection coating material, the following conclusions can be drawn:
- The use of both types of fire protection coating was efficient to delay the access of heat to steel, mainly for box-type fire protection coating;
- The modification in the properties of the fire protection coating material and in the geometry caused a greater difference when the profile has a contour-type fire protection coating. To have the lowest temperatures in steel, the correct is to use fire-retardant coating materials with higher values of specific mass, specific heat and thickness. However, a higher specific mass causes an increase in the weight of the structure and an increase in thickness can generate a higher material cost.

# REFERENCES

[1] SIMULIA. *ABAQUS Software. Version 6.14*. Dassault Systèmes, 2014.

[2] Associação Brasileira de Normas Técnicas, *Projeto de estruturas de aço e de estruturas mistas de aço e concreto de edifícios em situação de incêndio – Procedimento*, ABNT NBR 14323, 2013. Accessed: Jul. 16, 2017. [Online]. Available: https://www.abntcatalogo.com.br/norma.aspx?ID=260570

[3] Y. C. Wang, *Steel and Composite Structures - Behaviour and Design for Fire Safety*, 1st ed. London and New York: Spon Press, 2002.

[4] P. C. Jain and M. N. G. Rao, "Analysis of steel frames under fire environment," *Int. J. Numer. Methods Eng.*, vol. 19, pp. 1467–1478, 1983., http://dx.doi.org/10.1002/nme.1620191005.

[5] I. W. Burgess, J. A. El-Rimawi, and R. J. Plank, "Analysis of beams with non-uniform temperature profile due to fire exposure," *J. Construct. Steel Res.*, vol. 16, pp. 169-192, 1990., http://dx.doi.org/10.1016/0143-974X(90)90008-5.

[6] Y. C. Wang, "Composite beams with partial fire protection," *Fire Saf. J.*, vol. 30, pp. 315-332, 1998. http://dx.doi.org/10.1016/S0379-7112(97)00000-3.

[7] R. Cazeli, P. M. M. Vila Real, V. P. Siva, and P. A. G. Piloto "Análise numérica de vigas I de aço em situação de incêndio, sujeitas à flambagem lateral. Contribuição para a validação de uma proposta de revisão do Eurocode 3 - Parte 1.2", In *IV Seminário Internacional "O uso de Estruturas Metálicas na Construção Civil" e I Congresso Internacional de Construção Metálica – I CICOM*, São Paulo, Brazil, 2001. Accessed: March 30, 2017. [Online]. Available: http://hdl.handle.net/10198/2092

[8] M. B. Wong and J. I. Ghojel, "Sensitivity analysis of heat transfer formulations for insulated structural steel components," *Fire Saf. J.*, vol. 38, pp. 187-201, 2003. http://dx.doi.org/10.1016/S0379-7112(02)00057-7.

[9] European Committee for Standardization, *Design of steel structures. General rules - Structural fire design. Eurocode 3*, EN 1993-1-2, 2005. Accessed: July 20, 2017. [Online]. Available: https://eurocodes.jrc.ec.europa.eu/showpage.php?id=133

[10] J. C. L. Ribeiro "Simulação via método dos elementos finitos da distribuição tridimensional de temperatura em estruturas em situação de incêndio", M.S. thesis, Departamento de Eng. Estruturas - DEES, Universidade Federal de Minas Gerais - UFMG, Belo Horizonte, MG, Brazil, 2004. [Online]. Available: http://hdl.handle.net/1843/FACO-6AYG27

[11] Associação Brasileira de Normas Técnicas, *Dimensionamento de estruturas de aço de edifícios em situação de incêndio – Procedimento*, ABNT NBR 14323, 1999.

[12] L. D. T. Rodrigues "Determinação numérica e analítica da carga crítica uniformemente distribuída de vigas de aço em situação de incêndio natural", M.S. thesis, ENC, UnB/FT, Brasília, Brazil, 2013. [Online]. Available: https://repositorio.unb.br/handle/10482/14068

[13] F. M. Rocha and J. Munaiar No, "Análise de vigas mistas de aço e concreto pertencentes a pisos de baixa altura em situação de incêndio: ênfase à influência dos modelos constitutivos do concreto," *Rev. IBRACON Estrut. Mater.*, vol. 7, pp. 158–177, 2014., http://dx.doi.org/10.1590/S1983-41952014000100008.

[14] E. C. Fischer and A. H. Varma, "Fire behavior of composite beams with simple connections: Benchmarking of numerical models," *J. Construct. Steel Res.*, vol. 111, pp. 112–125, 2015. http://dx.doi.org/10.1016/j.jcsr.2015.03.013.

[15] A. R. Melão "Sobre perfis I de aço em situação de incêndio paramétrico", M.S. thesis, PEF, EPUSP, São Paulo, Brazil, 2016. [Online]. Available: https://www.teses.usp.br/teses/disponiveis/3/3144/tde-02122016-090138/pt-br.php

[16] Associação Brasileira de Normas Técnicas, *Componentes construtivos estruturais - determinação da resistência ao fogo*, ABNT NBR 5628, Rio de Janeiro, 2001. [Online]. Available: https://www.abntcatalogo.com.br/norma.aspx?ID=2529

[17] Associação Brasileira de Normas Técnicas, *Exigências de resistência ao fogo de elementos construtivos de edificações – Procedimento*, ABNT NBR 14432, 2001. [Online]. Available: https://www.abntcatalogo.com.br/norma.aspx?ID=2541

[18] Associação Brasileira de Normas Técnicas, *Perfil I estrutural de aço soldado por arco elétrico - Requisitos gerais*, ABNT NBR 5884, 2013. [Online]. Available: https://www.abntcatalogo.com.br/norma.aspx?ID=255454

[19] European Committee for Standardization, *Design of concrete structures. General rules - Structural fire design*, Eurocode 2 – EN 1992-1-2, Bruxelas, 2004. [Online]. Available: https://eurocodes.jrc.ec.europa.eu/showpage.php?id=132

[20] European Committee for Standardization, *Actions on structures. General actions - Actions on structures exposed to fire*, Eurocode 1 – EN 1991-1-2, Bruxelas, 2002. [Online]. Available: https://eurocodes.jrc.ec.europa.eu/showpage.php?id=131

[21] Associação Brasileira de Normas Técnicas, *Projeto de estruturas de concreto em situação de incêndio*, ABNT NBR 15200, 2012. [Online]. Available: https://www.abntcatalogo.com.br/norma.aspx?ID=90682

# IBRACON Structures and Materials Journal
## Revista IBRACON de Estruturas e Materiais

ORIGINAL ARTICLE

# Effect of Carbon Nanotubes (CNTs) aspect ratio on the rheology, thermal conductivity and mechanical performance of Portland cement paste

*Efeito da relação de aspecto dos nanotubos de carbono (NTCs) na reologia, condutividade térmica e desempenho mecânico de pastas de cimento Portland*

Eduardo Batiston[a,b] iD
Philippe Jean Paul Gleize[a] iD
Paula Mezzomo[a] iD
Fernando Pelisser[a] iD
Paulo Ricardo de Matos[a,c] iD

[a]Universidade Federal de Santa Catarina – UFSC, Departamento de Engenharia Civil, Programa de Pós-graduação em Engenharia de Civil – PPGEC, Florianópolis, SC, Brasil
[b]Universidade Comunitária da Região de Chapecó – UNOCHAPECÓ, Departamento de Engenharia Civil, Chapecó, SC, Brasil
[c]Universidade Federal de Santa Maria – UFSM, Santa Maria, RS, Brasil

Abstract: Carbon nanotubes (CNTs) are potential candidates to enhance the heat balance of concrete, reducing internal stresses caused by differential heating in massive concrete elements. The higher the aspect ratio (AR) and content of CNTs, the greater the expected thermal conductivity (TC). However, high AR may impair the proper dispersion of CNTs in cementitious matrix, potentially harming the workability and mechanical strength of the composite. This work evaluated the effect of the AR (35, 250, 900, and 3500) and content (0.05% and 0.10%) of CNTs on the TC, rheology (squeeze flow), and mechanical strength of cement paste. Results showed that 0.05% CNT increased the TC of paste by up to 15% for AR of 250, but further increasing AR progressively reduced the TC of the composite. In turn, 0.10% CNT incorporation did not result in significant TC gains. The yield stress and viscosity of the mixes progressively increased as CNTs content and AR increased, by up to 119% compared with plain cement paste. No significant differences were observed in 28-day compressive strength with 0.05% CNT incorporation, while 0.10% CNT led to slight strength reductions for some mixes. Regarding flexural strength, 0.05% incorporation of either CNT decreased the strength of the mixes while 0.10% incorporation generally compensated this reduction, except for the lowest aspect ratio. Overall, CNTs with intermediate AR (around 250) was effective in improving the thermal conductivity of cement paste, increasing it by 15% with relatively low content (0.05%) while did not significantly impair the fresh and mechanical performance of the composite.

Keywords: carbon nanotube, aspect ratio, Portland cement, rheology, thermal conductivity.

Resumo: Nanotubos de carbono (NTCs) são potenciais candidatos a melhorar o balanço térmico do concreto, reduzindo as tensões internas causadas pelo aquecimento diferencial em elementos maciços de concreto. Quanto maior a relação de aspecto (RA) e o teor de NTCs, maior será a condutividade térmica (CT) esperada. Porém, uma RA elevada pode prejudicar a dispersão adequada do NTCs na matriz cimentícia, potencialmente prejudicando a trabalhabilidade e resistência mecânica do compósito. Este estudo avaliou o efeito do RA (35, 250, 900 e 3500) e teor (0,05% e 0,10%) de NTCs na CT, reologia (*squeeze flow*) e resistência mecânica das pastas de cimento. Os resultados mostraram que a incorporação de 0,05% NTC aumentou a CT da pasta em até 15% para uma RA de 250, mas o aumento da RA reduziu progressivamente a CT do compósito. Por sua vez, a incorporação de 0,10% NTC não resultou em ganhos significativos de CT. A tensão de escoamento e a viscosidade das misturas aumentaram progressivamente com o aumento do teor de NTC e da RA, em até

*E. Batiston, P. J. P. Gleize, P. Mezzomo, F. Pelisser, and P. R. de Matos*

119% em comparação com a pasta de cimento sem NTCs. Nenhuma diferença significativa foi observada na resistência à compressão de 28 dias com incorporação de 0,05% NTCs, enquanto 0,10% NTCs levou a pequenas reduções de resistência para algumas misturas. Em relação à resistência à flexão, a incorporação de 0,05% de qualquer um dos NTCs diminuiu a resistência das misturas, enquanto a incorporação de 0,10% geralmente compensou essa redução, exceto pela RA mais baixa. No geral, os NTCs com RA intermediária (~250) foram eficazes em melhorar a condutividade térmica da pasta de cimento, aumentando-a em 15% com teor relativamente baixo (0,05%), enquanto não prejudicou significativamente o desempenho fresco e mecânico do compósito.

**Palavras-chave:** nanotubos de carbono, relação de aspecto, cimento Portland, reologia, condutividade térmica.

# 1 INTRODUCTION

Recently, nanotechnology has gained much attention for research in the development of materials with unique properties. Nanoengineering (or nanomodification) of Portland cement-based materials is a rapid emerging field. Synthesis and assembly of materials with dimensions in the range 0.1–100 nm offer possibilities for the development of materials with new functions and smart properties not currently available [1]. Concrete can be nanoengineered by incorporating nanosized additions to control material behavior and add novel properties, or by grafting molecules onto cement particles, cement phases, aggregates, and admixtures that can provide surface functionality to promote specific interfacial interactions [2], [3]. Furthermore, recent studies reported the synthesis of nanoparticles directly on Portland clinker [4].

Carbon nanotubes (CNTs) are potential candidates for use as nano reinforcements in Portland cement-based materials [5]. It exhibits extraordinary strength (tensile strength in the range of GPa) and modulus of elasticity in the order of TPa, in addition to having unique electronic and chemical properties [1]. As a result, several works showed that CNTs improved the compressive strength [6]–[10], tensile/flexural strength [7], [11]–[14], and modulus of elasticity [8], [15] of cementitious composite. In addition, CNTs may improve the durability of composite mainly by reducing the porosity of the cementitious matrix [10], [16]–[18].

Most research efforts have focused on the influence of CNTs on the mechanical performance and durability of cementitious composites, but very few studies investigated its effect on thermal properties. In fact, to the authors' best knowledge, there are no studies investigating the effect of CNTs aspect ratio on the thermal conductivity of cementitious composite. Due to the high thermal conductivity of CNTs (about 750 W/m·K [19]), they have been used to enhance the thermal conductivity of heating or cooling fluids [20]. In addition, its aspect ratio ranges from 20 up to 10000, making CNTs an interesting choice for electrical/thermal conductive or percolating networks at lower loadings. Although low thermal conductivity values are often desired for building materials (e.g. to improve thermal insulation), high thermal conductivity can be used as a tool to improve the heat balance of large volumes of concrete [21], facilitating the cooling of the interior of massive concrete elements (e.g. dams and foundation elements) and avoiding the appearance of internal stresses caused by differential heating [22]. There are reports of substantial increases in the thermal conductivity with CNTs incorporation in epoxy [23]–[25] and polyurethane composites [26]. Thus, the incorporation of CNTs in Portland cement matrix may increase the thermal conductivity of the composite.

Regarding the fresh state performance of CNT-reinforced cementitious composites, the incorporation of nanotubes tends to negatively affect the flowability of the materials. Overall, the very high specific surface area of CNTs and their trend for clustering tend to reduce the flowability of cement paste when CNTs are added [27]. However, such flowability loss may be overcome with the incorporation of superplasticizer as confirmed by Skripkiunas et al. [28]. In this context, most of the studies investigated the effect of CNTs dispersion mechanism and content on the fresh state performance of cement paste, while the effect of the CNTs aspect ratio was few investigated. Collins et al. [29] investigated such effect through the mini slump test, but this is an empirical test and can lead to errors in estimating the rheological properties of the material.

Thus, this work investigated the effect of CNTs aspect ratio on the thermal conductivity and rheological properties of cement paste (through the squeeze flow test), in addition to mechanical performance characterization.

*E. Batiston, P. J. P. Gleize, P. Mezzomo, F. Pelisser, and P. R. de Matos*

## 2 EXPERIMENTAL PROGRAM

### 2.1 Materials and mixes

Multiwalled CNTs with four different aspect ratios (i.e. length/diameter ratios) were used: 35, 250, 900, and 3500. The CNTs were purchased from Nanostructured & Amorphous Materials and Cheap Tubes Inc. The characteristics of the CNTs used were provided by the manufacturers and are shown in Table 1. One can note that CNT's specific surface area (SSA) generally increased as its aspect ratio increased, in agreement with previous literature reports [30], [31].

**Table 1.** Carbon nanotubes characteristics.

| Type | Density (g/cm³) | External Ø (nm) | Length (µm) | Aspect ratio | Purity (%) | SSA (m²/g) |
|------|-----------------|-----------------|-------------|--------------|------------|------------|
| CNT-35 | 1.7 – 1.9 | 40-60 | 0.5-2 | 17-50 | 95 | > 40 |
| CNT-250 | 2.1 | 40-70 | 5-15 | 125-375 | 94 | > 40 |
| CNT-900 | 1.5 – 1.9 | 20-30 | 10-30 | 333-1500 | 95 | 110 |
| CNT-3500 | 1.5 -1.9 | 8-15 | 10-50 | 666-6250 | 95 | 233 |

An ordinary Portland cement (CP I-S 32 [32]), a polycarboxylate-based superplasticizer (with density of 1.09 g/cm³ and solid content of 30.5%) and distilled water were used for paste production. The water/cement (w/c) ratio and the superplasticizer content were fixed for all the mixes, respectively at 0.30 and 0.1% by weight of cement. The use of such w/c ratio was previously reported in the literature [27], [28], [30], while this superplasticizer content allowed to produce flowable pastes. Each CNT was added in the amount of 0.05% (CNT 0.05) and 0.10% (CNT 0.10) by weight of cement. Cement paste without CNT (Ref) was also prepared for comparison purpose.

### 2.2 Sample preparation

Firstly, CNTs, water and superplasticizer were mixed and sonicated for 20 min at 55 kHz in a low energy water bath sonicator (to prevent damaging the CNTs). Then, this suspension was added to the mixer container together with cement, and the paste was mixed for 3 min. After mixing, a portion of the sample was immediately used for the rheological measurements, while the remainder was used for casting the specimens as seen next.

For each mix, the following specimens were cast: 3 cylindrical specimens of 20 mm x 50 mm (diameter x height) for thermal conductivity measurements; 5 cylindrical specimens of 20 mm x 40 mm (diameter x height) for compressive strength tests; and 4 prismatic specimens of 5 mm x 20 mm x 60 mm (thickness x height x length) for flexural strength tests. One day after casting, the specimens were demolded and stored in lime-saturated water until testing. All the tests were conducted at 28 days of age.

### 2.3 Testing methods

The rheological behavior of the pastes was evaluated through the squeeze flow test. It consists of applying a load on a fresh disc sample placed between two parallel plates at a constant normal strain [33], [34]. This test was successfully used to evaluate the fresh state behavior of cement pastes [35], [36] and mortars [37]–[39]. Tests were conducted in paste samples of 93 mm in diameter and 10 mm in thickness, using a universal testing machine Instron 5569. The displacement rate was 0.1 mm/s and the total displacement was 5 mm. A 25 mm-diameter steel punch was used, meeting the minimum Øsample/Øpunch ratio of 3 prescribed by Min et al. [35] to minimize compressive stresses generated by sample confinement. Tests were conducted on three fresh samples for each mix.

The rheological parameters viscosity ($\eta$, in Pa.s) and yield stress ($\tau 0$, in Pa) were estimated using respectively Equations 1 and 2, proposed by Meeten [34]. Although the actual yield stress is measured by rotational rheometry [40], similar approaches have been successfully used to estimate the yield stress of cement-based materials [37], [38], [41].

$$\eta = \frac{64Ft}{3\pi\left(h^{-2} - h_0^{-2}\right)D^4} \tag{1}$$

$$\tau_0 = \frac{12hF}{\pi D^3} \qquad (2)$$

where $F$ = force (N); $t$ = testing time elapsed (s); $h_0$ = initial sample height (mm); $h$ = final sample height (mm); and $D$ = sample diameter (mm).

At 28 days, compressive and flexural strength (three-point bending) tests were conducted using the same universal testing machine mentioned above, with testing rates of 2.5 and 0.01 mm/min, respectively. Prior to flexural strength test, the density of the specimens was determined using a hydrostatic balance. Thermal conductivity tests were conducted using a C-Therm TCi analyzer, based on the transient plane source (TPS) method [42]. A Wakefield thermal grease was used as a contact agent between the probe and the sample.

## 3 RESULTS AND DISCUSSIONS

### 3.1 Rheological behavior

Figure 1 shows the squeeze flow curves of the pastes and Figure 2 shows the rheological parameters of the mixes. The increase in CNT content progressively increased the yield stress and viscosity of paste for a given aspect ratio. These increases were of up to 119% both for yield stress and viscosity (CNT 3500 – 0.10%), in comparison with the Ref mix. This may be associated with the very high specific surface area of CNTs (40-223 m$^3$/g, shown in Table 1) and their tendency to agglomerate. According to Roussel et al. [43], in cementitious suspension, the colloidal surface interactions form a particle network within the first few seconds. In addition, the first hydration products form C-S-H bridges between the particles already in the first 100 seconds. Both phenomena increase the hardness of the particle network – and therefore of the cement paste – in a very early age. In this regard, the increase in flocculation strength and floc size with the incorporation of nanomaterials was already reported for cementitious systems [3], [44], which can increase the stiffness of paste, consequently increasing its yield stress and viscosity. In addition, CNTs tend to self-associate into micro-scale agglomerates [45]. Such clustering traps part of the water and superplasticizer, reducing their availability for lubricating and dispersing the cement grains and the nanotubes itself [10]. These results are in line with those reported in the literature. Skripkiunas et al. [27] found yield stress increases of up to 270% when incorporated 0.12% CNT in cement pastes with superplasticizer. Ma et al. [46] observed viscosity and yield stress increases of about 30% when incorporated 0.01% CNT in Portland cement paste. Mohamadian et al. [47] observed viscosity and yield stress increases of up to 16% and 61%, respectively, when incorporated up to 5% of a Methyl Methacrylate-CNT composite in oil/gas wellbore cement paste. Despite yield stress increases, Skripkiunas et al. [27] reported reductions in the shear thickening behavior with CNTs incorporation. This phenomenon corresponds to the progressive increase in viscosity as the shear rate increases. In cementitious systems, it is mainly caused by the formation of clusters of un-adsorbed superplasticizer molecules, which hinders the flow during shear [48], [49]. Considering that superplasticizer is commonly used to disperse CNTs in cementitious matrix [10], [29], [50], the incorporation of CNTs may adsorb such "leftover" polymer molecules, reducing the shear thickening occurrence. This may be of practical interest, such as for pumping applications where the material is subjected to high shear rates.

Furthermore, for a given CNT content, the increase in its aspect ratio generally increased the yield stress and viscosity of paste, and these increases were higher for the highest CNT content. For example, CNT-3500 had yield stress and viscosity 56% higher than CNT-35 for 0.05% CNT, and 85% higher for 0.10% CNT. This can be explained by the higher difficulty to disperse longer CNTs, together with the increase in the SSA of CNT as its aspect ratio increased (Table 1). In agreement with that, Abu Al-Rub et al. [51] investigated the effect of CNTs aspect ratio on the mechanical properties of cement paste, finding that shorter CNTs resulted in higher dispersion in cement paste and improved homogeneity (i.e. reduced CNT-free volume of cement paste). Also, electron microscopy images indicated that longer CNTs further bridge the neighboring hydration products, which can increase the stiffness of the paste as discussed above. Similarly, Konsta-Gdoutos et al. [15] concluded that longer CNTs are more difficult to disperse. Regarding the impact of CNT aspect ratio on the fresh performance of cement paste, Collins et al. [29] incorporated CNTs with average aspect ratios of 200, 1000 and 1125 in cement pastes with 0.05% CNT, finding no significant differences in the mini slump flow (from 67.6 to 69.4 mm) for the mixes. However, two aspects must be stressed in their study: (i) the authors did not incorporate superplasticizer in these pastes, which may prevent proper dispersion of CNTs; and (ii) previous studies [52] showed that the mini slump test may be inaccurate to predict the yield stress of paste especially at such low mini slump spread, i.e., around 60 mm where the sample is not completely self-leveling.

E. Batiston, P. J. P. Gleize, P. Mezzomo, F. Pelisser, and P. R. de Matos

In turn, the squeeze flow test has been shown to be a precise tool to evaluate the rheological properties of cement-based composites [37], [41] and is more sensitive to small property variations.
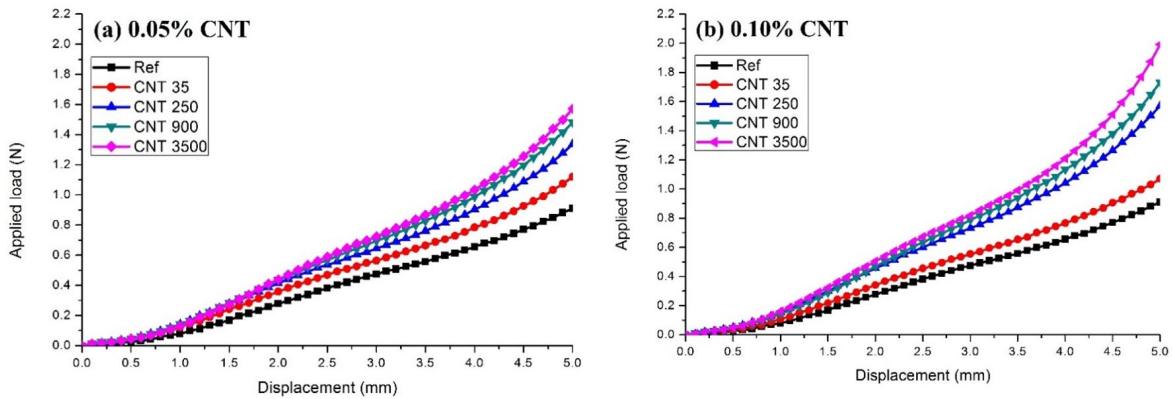


**Figure 1.** Squeeze flow test curves (applied load vs. displacement) of the pastes. (a) 0.05% CNT; (b) 0.10% CNT.
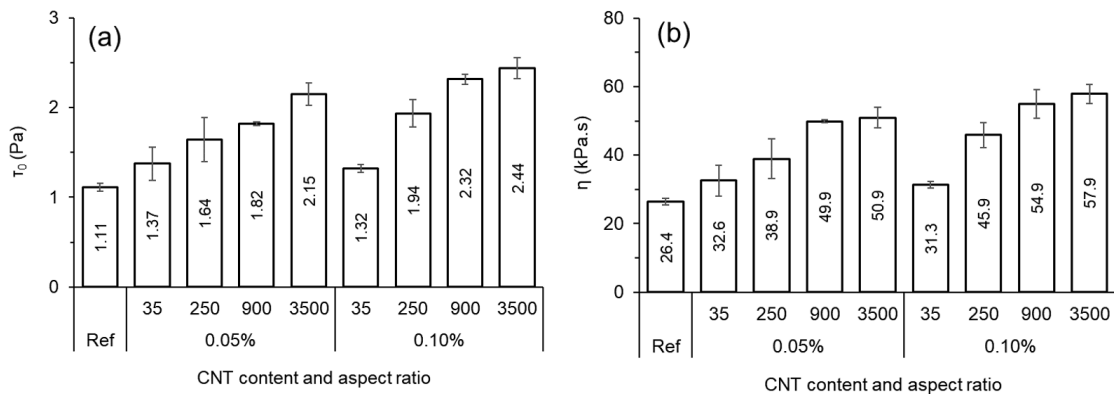


**Figure 2.** Rheological parameters of the pastes. (a) yield stress; (b) viscosity.

## 3.2 Mechanical tests

Figure 3 and Figure 4 respectively show the compressive and flexural strength of the pastes at 28 days. No significant differences were observed between the compressive strength of the reference mix and the paste with 0.05% CNT, regardless of the CNTs aspect ratios. However, a slight compressive strength decrease was observed in mixtures with 0.10% CNT. The lack of significant strength gain (or even strength reduction) with CNTs incorporation was already addressed in the literature. MacLeod et al. [53] conducted an extensive survey on the effect of CNTs incorporation on the 28-day compressive strength of cement-based composites. From 13 mixes with water/binder ratio below 0.35 (as used in the current work), only two mixes had a significant compressive strength increase with nanotube incorporation. Ma et al. [46] found equivalent 7- and 28-day compressive strength for plain and CNT-reinforced fly ash-blast furnace slag-cement mortars with 0.01% CNT. Collins et al. [29] also found 28-day compressive strength reductions of 8% and 11% when incorporated 0.05% CNT with mean aspect ratios of 200 and 1125, respectively, compared with plain cement paste. Finally, Hu et al. [6] and Mohsen et al. [54] reported negligible differences in compressive strength with CNTs addition in up to 0.10%. By contrast, in the survey of MacLeod et al. [53], the highest 28-day strength improvements were reported for mixes with water/binder ratios above 0.45, reaching improvements of the order of 60%. This trend can be associated with the harder dispersion of CNTs in paste with low water/binder ratio, also reported by Mendoza-Reales et al. [55] and Zhou et al. [9].

Regarding the flexural strength, incorporating 0.05% CNT decreased the strength of composite regardless of the CNTs aspect ratio. This was confirmed by one-way ANOVA, dividing the samples in groups according to the CNT type used;

p-values were 0.096, 0.456, 0.245 and 0.084 respectively for CNT 35, 250, 900 and 3500, indicating significant difference for 95% reliability. Similarly, Tyson et al. [56] reported flexural strength reduction of about 70% with CNTs incorporation at the latter age tested (i.e. 21 days). Flexural strength is generally more sensitive to heterogeneities and defects in the matrix than compressive strength [57]. In turn, increasing the CNT content up to 0.10% generally compensated the strength loss observed for 0.05% CNT incorporation, except for CNT-35. This behavior was similar to the one reported by Mohsen et al. [54], which obtained equivalent strengths for 0% and 0.08% CNT incorporation. According to Sobolkina et al. [58], during load, cracks are originated in the weaker zones of the composite which generally correspond to the contacts between the C-S-H regions. CNTs bridge C-S-H regions (in the scale of around 1 μm) and promotes an interlock of needle-like C-S-H crystals, therefore reinforcing such week zones and promoting strength increase. In the case of CNT-35, its low length (around 1 μm compared with 5-50 μm for the others) prevented the flexural strength gain promoted by increased nanotube content. These results agree with the findings of Abu Al-Rub et al. [51], which evaluated cement pastes with "long CNTs" (length of 10-30 μm, comparable with CNT-3500) and "short CNTs" (length of 1.5 μm, comparable with CNT-35) in 0.04% and 0.1%. The authors observed that long CNTs led to 28-day flexural strengths from 20% to 30% higher than short CNTs did, for the same incorporation level.

Concerning the effect of CNTs aspect ratio, the main conclusion of Konsta-Gdoutos et al. [15], [30] and Abu Al-Rub et al. [51] was that, to achieve the same mechanical performance level, lower CNTs content are needed as the aspect ratio increases. In our work, the optimum CNT content and aspect ratio were 0.10% and 900, respectively; higher aspect ratio decreased the compressive strength while shorter aspect ratio prevented proper flexural strength improvement.
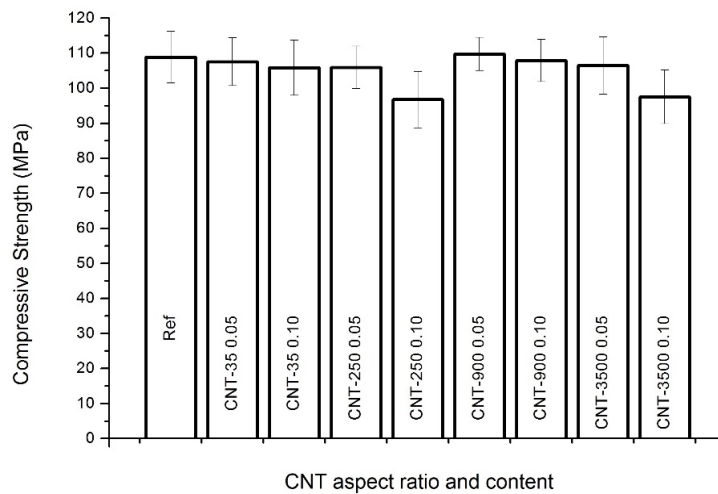


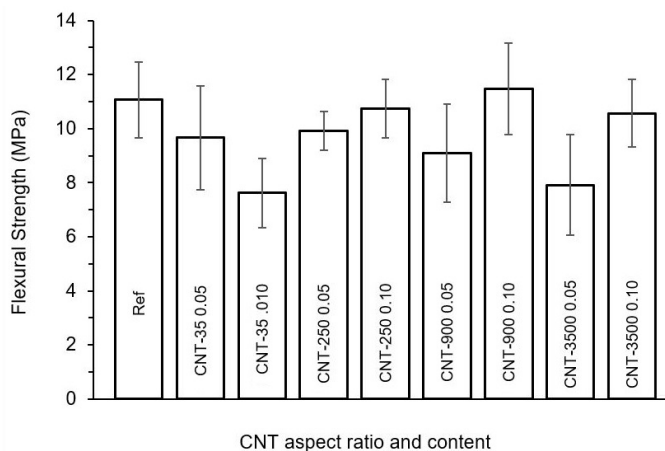**Figure 3.** Compressive strength of the pastes at 28 days.



**Figure 4.** Flexural strength of the pastes at 28 days.

*E. Batiston, P. J. P. Gleize, P. Mezzomo, F. Pelisser, and P. R. de Matos*

## 3.3 Thermal conductivity

Figure 5 shows the density of the pastes and Figure 6 shows the effect of the CNTs on their thermal conductivity. No significant differences were observed between the density of the composites; therefore, the differences in thermal conductivity may be attributed to the presence of CNTs. The addition of 0.05% CNT improved the thermal conductivity of the composite by up to 15% when the CNTs aspect ratio increased up to 250, regardless of the CNT content. This finding was expected, since CNTs thermal conductivity is about 1000 times higher the one of plain cement paste (discussed next), and increasing the CNTs aspect ratio tends to increase the conductivity of the composite since it enables the formation of a more extensive network of nanotubes at the same weight content [23]. Furthermore, incorporating 0.05% of both CNT-900 and CNT-3500 slightly decreased the thermal conductivity of composite compare with the 0.05% CNT-250 mix, but they were still higher those of the 0.05% CNT-35 and Ref mixes. A similar overall trend was observed for 0.10% CNT incorporation when its aspect ratio increased (except for CNT-3500), but the thermal conductivity values found for the highest CNT content were lower than those found for the lowest CNT content when comparing respective aspect ratios. From the viewpoint of thermal conductivity, this behavior seems to be contradictory. However, increasing the CNT content and aspect ratio tend to increase the difficulty to homogeneously disperse it on the cementitious matrix, and this was evidenced by the fact that the highest CNTs aspect ratio and content led to the lowest thermal conductivity among the pastes, even lower than that of plain cement paste. Nonetheless, thermal conductivity tests showed a substantial improvement on such property (by up to 15%) with the incorporation of relatively low content of CNTs (0.05%), confirming the potential of this nanomaterial to improve the thermal conductivity of cement-based materials.
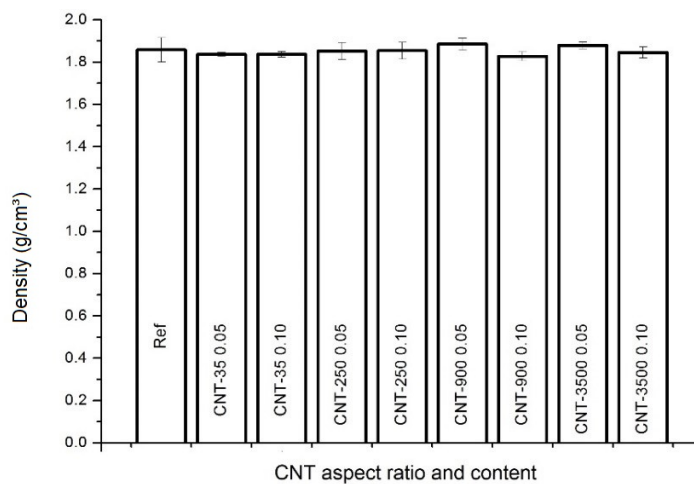
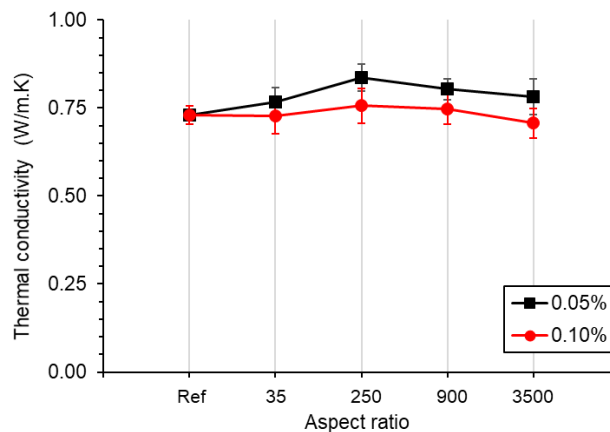

**Figure 5.** Density of the cement pastes.



**Figure 6.** Thermal conductivity of the pastes as a function of CNT aspect ratio and content.

Furthermore, the experimental values of thermal conductivity were compared with theoretical values calculated using the Lewis-Nielsen model. The advantages of this model are its simplicity and coverage of a broad range of particle shapes and patterns, particularly the fiber aspect ratio [59], [60]. The thermal conductivity ($K$) of a two-phase system composed of a non-conductive matrix (here, cementitious matrix) and a conductive filler (here, CNT) was determined by Equations 3–5, according to works reported in the literature [59], [61].

$$K = k_1 \left( \left( 1 + AB\Psi\varnothing_2 \right) \right) \tag{3}$$

$$B = \left( \frac{k_2}{k_1} - 1 \right) / \left( \frac{k_2}{k_1} + A \right) \tag{4}$$

$$\Psi = 1 + \left( \frac{1 - \phi_m}{\phi_{m^2}} \right) \phi_2 \tag{5}$$

Where $k_1$ = thermal conductivities of the cement paste matrix (W/m·K); $k_2$ = thermal conductivities of CNT (equal to 750, estimated from [19]) (W/m·K); $A$ = CNT aspect ratio; $\varnothing_2$ = filler volume fraction; and $\phi_m$ = maximum filler volume fraction.

Figure 7 compares the measured thermal conductivity values with those predicted by the Lewis-Nielsen model and Table 2 details the values. Good agreement between the theoretical and measured values was observed for the incorporation of CNT-35 and CNT-250 in 0.05% (differences of up to 2.7%). However, as the CNTs aspect ratio and content increased, the experimental results deviated from those predicted by the Lewis-Nielsen model. This is because the theoretical model assumes that the "filler" phase (i.e. CNTs) is perfectly distributed throughout the matrix, while such homogeneity worsens as the CNT content and aspect ratio increases. Finally, Figure 7 shows the great potential of CNTs to improve the thermal conductivity of cement composite, more than doubling the conductivity of the paste with the incorporation of 0.10% CNT in theory.
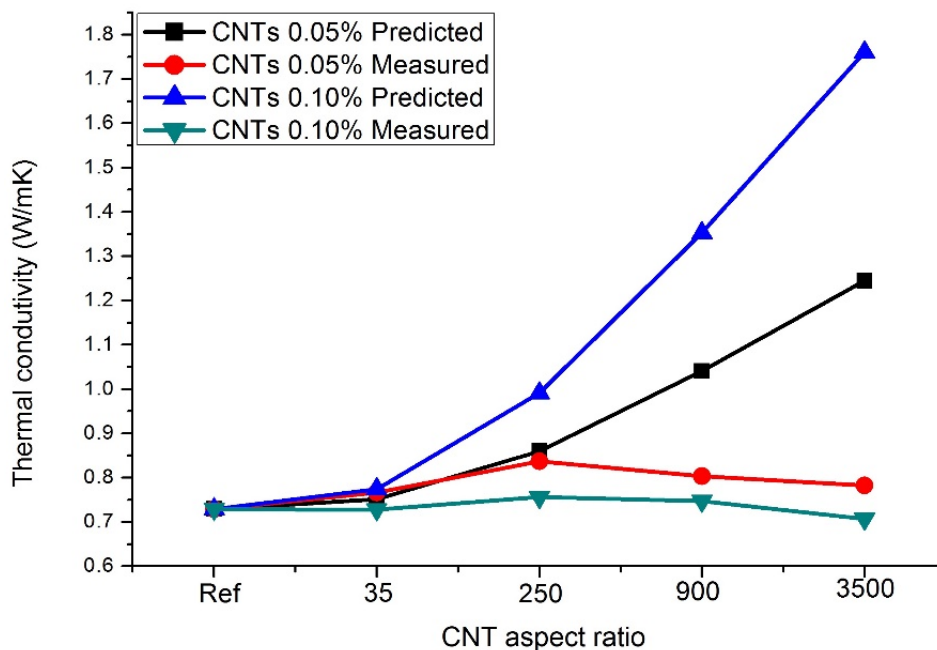


**Figure 7.** Predicted (Lewis-Nielsen model) and measured thermal conductivity of the CNT-reinforced cement pastes, for the different CNT aspect ratio and content.

Rev. IBRACON Estrut. Mater., vol. 14, no. 5, e14510, 2021

8/12

**Table 2.** Detailed data from the Lewis-Nielsen prediction model.

| | CNT volume fraction | A | B | Ψ | PTC (W/m·K) | MTC (W/m·K)* |
|---|---|---|---|---|---|---|
| Reference paste | 0 | - | - | - | 0.729 | 0.729 (0.026) |
| CNT-35-0.05% | 0.00089 | 35 | 0.9661 | ~1 | 0.752 | 0.766 (0.042) |
| CNT-35-0.1% | 0.00178 | 35 | 0.9661 | ~1 | 0.774 | 0.728 (0.051) |
| CNT-250-0.05% | 0.00089 | 250 | 0.8037 | ~1 | 0.860 | 0.837 (0.038) |
| CNT-250-0.1% | 0.00178 | 250 | 0.8037 | ~1 | 0.991 | 0.756 (0.049) |
| CNT-900-0.05% | 0.00089 | 900 | 0.5328 | ~1 | 1.041 | 0.803 (0.029) |
| CNT-900-0.1% | 0.00178 | 900 | 0.5328 | ~1 | 1.352 | 0.747 (0.042) |
| CNT-3500-0.05% | 0.00089 | 3500 | 0.2269 | ~1 | 1.245 | 0.782 (0.051) |
| CNT-3500-0.1% | 0.00178 | 3500 | 0.2269 | ~1 | 1.760 | 0.707 (0.042) |

PTC: Predicted thermal conductivity; MDC: Measured thermal conductivity; *average (standard deviation).

## 4 CONCLUSIONS

This work investigated the effect of the CNTs aspect ratio on the rheology, thermal conductivity and mechanical properties of Portland cement paste. Specifically, CNTs with aspect ratios of 35, 250, 900, and 3500 were added in 0.05% and 0.10% over the cement weight. Based on the results presented, the following conclusions were drawn:

(i) Squeeze flow test showed that the increase in CNT content progressively increased the yield stress and viscosity of the paste, by up to 119% in comparison with plain cement paste. The increase in CNTs aspect ratio also increased these properties for a given incorporation level, reaching values 86% higher when 0.10% CNT-3500 was incorporated compared with the same level of CNT-35.

(ii) No significant differences were observed in the compressive strength of paste when 0.05% CNT was incorporated regardless of its aspect ratio. In turn, 0.10% incorporation led to slight strength reductions in some mixes (i.e. for CNT-250 and -3500). Regarding flexural strength, 0.05% incorporation of either CNTs decreased the strength of the mixes, while 0.10% incorporation generally compensated this reduction except for the lowest aspect ratio.

(iii) Thermal conductivity tests showed that incorporating 0.05% CNT improved the thermal conductivity of the composite regardless of the CNTs aspect ratio. These improvements were of up to 15% for CNT-250. In turn, further incorporating CNTs did not result in major improvements in this property, eventually decreasing the thermal conductivity of the composite (e.g. for 0.10% of CNT-3500). Furthermore, thermal conductivity experimental values were compared with theoretical values obtained by the Lewis-Nielsen model. Good agreement between the theoretical and measured values was observed for the incorporation of CNT-35 and CNT-250 in 0.05% (differences of up to 2.7%); however, as the CNTs aspect ratio and content increased, the experimental results deviated from those predicted.

These findings indicate the good potential of CNTs to improve the thermal conductivity of cement-based materials while keeping their fresh and mechanical performance. The incorporation of CNTs with an intermediate aspect ratio (i.e. 250) led to a 15% increase in the thermal conductivity of the composite for a relatively low CNTs content (0.05% over the cement weight). Finally, the good dispersion of the CNTs would be a key factor to reach better performance.

## ACKNOWLEDGEMENTS

## REFERENCES

[1] F. Sanchez and K. Sobolev, "Nanotechnology in concrete: a review," *Constr. Build. Mater.*, vol. 24, no. 11, pp. 2060–2071, 2010, http://dx.doi.org/10.1016/j.conbuildmat.2010.03.014.

[2] A. P. Svintsov, E. L. Shchesnyak, V. V. Galishnikova, R. S. Fediuk, and N. A. Stashevskaya, "Effect of nano-modified additives on properties of concrete mixtures during winter season," *Constr. Build. Mater.*, vol. 237, pp. 117527, 2020, http://dx.doi.org/10.1016/j.conbuildmat.2019.117527.

[3] S. Kawashima, P. Hou, D. J. Corr, and S. P. Shah, "Modification of cement-based materials with nanoparticles," *Cement Concr. Compos.*, vol. 36, no. 1, pp. 8–15, 2013, http://dx.doi.org/10.1016/j.cemconcomp.2012.06.012.

[4]  T. C. de Souza, G. Pinto, V. S. Cruz, M. Moura, L. O. Ladeira, and J. M. Calixto, "Evaluation of the rheological behavior, hydration process, and mechanical strength of Portland cement pastes produced with carbon nanotubes synthesized directly on clinker," *Constr. Build. Mater.*, vol. 248, pp. 118686, 2020, http://dx.doi.org/10.1016/j.conbuildmat.2020.118686.

[5]  L. Silvestro and P. Jean Paul Gleize, "Effect of carbon nanotubes on compressive, flexural and tensile strengths of Portland cement-based materials: a systematic literature review," *Constr. Build. Mater.*, vol. 264, pp. 120237, Dec 2020, http://dx.doi.org/10.1016/j.conbuildmat.2020.120237.

[6]  Y. Hu, D. Luo, P. Li, Q. Li, and G. Sun, "Fracture toughness enhancement of cement paste with multi-walled carbon nanotubes," *Constr. Build. Mater.*, vol. 70, pp. 332–338, 2014, http://dx.doi.org/10.1016/j.conbuildmat.2014.07.077.

[7]  R. Hamzaoui, S. Guessasma, B. Mecheri, A. M. Eshtiaghi, and A. Bennabi, "Microstructure and mechanical performance of modified mortar using hemp fibres and carbon nanotubes," *Mater. Des.*, vol. 56, pp. 60–68, 2014, http://dx.doi.org/10.1016/j.matdes.2013.10.084.

[8]  S. Parveen, S. Rana, R. Fangueiro, and M. C. Paiva, "Microstructure and mechanical properties of carbon nanotube reinforced cementitious composites developed using a novel dispersion technique," *Cement Concr. Res.*, vol. 73, pp. 215–227, 2015, http://dx.doi.org/10.1016/j.cemconres.2015.03.006.

[9]  C. Zhou, F. Li, J. Hu, M. Ren, J. Wei, and Q. Yu, "Enhanced mechanical properties of cement paste by hybrid graphene oxide/carbon nanotubes," *Constr. Build. Mater.*, vol. 134, pp. 336–345, 2017, http://dx.doi.org/10.1016/j.conbuildmat.2016.12.147.

[10] M. Jung, Y. Lee, S.-G. Hong, and J. Moon, "Carbon nanotubes (CNTs) in ultra-high performance concrete (UHPC): Dispersion, mechanical properties, and electromagnetic interference (EMI) shielding effectiveness (SE)," *Cement Concr. Res.*, vol. 131, pp. 106017, 2020, http://dx.doi.org/10.1016/j.cemconres.2020.106017.

[11] X. Song, S. Shang, D. Chen, and X. Gu, "Multi-walled carbon nanotube reinforced mortar-aggregate interfacial properties," *Constr. Build. Mater.*, vol. 133, pp. 57–64, 2017, http://dx.doi.org/10.1016/j.conbuildmat.2016.12.034.

[12] B. S. Sindu and S. Sasmal, "Properties of carbon nanotube reinforced cement composite synthesized using different types of surfactants," *Constr. Build. Mater.*, vol. 155, pp. 389–399, 2017, http://dx.doi.org/10.1016/j.conbuildmat.2017.08.059.

[13] B. Zou, S. J. Chen, A. H. Korayem, F. Collins, C. M. Wang, and W. H. Duan, "Effect of ultrasonication energy on engineering properties of carbon nanotube reinforced cement pastes," *Carbon N. Y.*, vol. 85, pp. 212–220, 2015, http://dx.doi.org/10.1016/j.carbon.2014.12.094.

[14] S. Xu, J. Liu, and Q. Li, "Mechanical properties and microstructure of multi-walled carbon nanotube-reinforced cement paste," *Constr. Build. Mater.*, vol. 76, pp. 16–23, 2015, http://dx.doi.org/10.1016/j.conbuildmat.2014.11.049.

[15] M. S. Konsta-Gdoutos, Z. S. Metaxa, and S. P. Shah, "Highly dispersed carbon nanotube reinforced cement based materials," *Cement Concr. Res.*, vol. 40, no. 7, pp. 1052–1059, 2010, http://dx.doi.org/10.1016/j.cemconres.2010.02.015.

[16] B. Rodriguez, E. Correa, Y. P. Arias, J. H. Quintero, J. A. Calderón, and O. A. Mendoza, "Carbonation study in a cement matrix with carbon nanotubes," *J. Phys. Conf. Ser.*, vol. 1247, no. 1, pp. 012024, 2019, http://dx.doi.org/10.1088/1742-6596/1247/1/012024.

[17] V. Potapov, R. Fediuk, and D. Gorev, "Obtaining sols, gels and mesoporous nanopowders of hydrothermal nanosilica," *J. Sol-Gel Sci. Technol.*, vol. 94, no. 3, pp. 681–694, 2020., http://dx.doi.org/10.1007/s10971-020-05216-z.

[18] A. Cwirzen, K. Habermehl-Cwirzen, and V. Penttala, "Surface decoration of carbon nanotubes and mechanical properties of cement/carbon nanotube composites," *Adv. Cement Res.*, vol. 20, no. 2, pp. 65–73, 2008, http://dx.doi.org/10.1680/adcr.2008.20.2.65.

[19] H. Xie, A. Cai, and X. Wang, ""Thermal diffusivity and conductivity of multiwalled carbon nanotube arrays," *Phys. Lett. Sect. A Gen*," *Solid State Phys.*, vol. 369, no. 1–2, pp. 120–123, 2007, http://dx.doi.org/10.1016/j.physleta.2007.02.079.

[20] J. Makar, J. Margeson and J. Luh, *Carbon Nanotube/Cement Composites: Early Results and Potential Applications.* Ottawa: NRC, 2005.

[21] D. D. L. Chung, "Cement-matrix structural nanocomposites," *Met. Mater. Int.*, vol. 10, no. 1, pp. 55–67, 2004., http://dx.doi.org/10.1007/BF03027364.

[22] P. R. de Matos, R. Junckes, E. Graeff, and L. R. Prudêncio Jr, "Effectiveness of fly ash in reducing the hydration heat release of mass concrete," *J. Build. Eng.*, vol. 28, pp. 101063, 2019. http://dx.doi.org/10.1016/j.jobe.2019.101063.

[23] M. J. Biercuk, M. C. Llaguno, M. Radosavljevic, J. K. Hyun, A. T. Johnson, and J. E. Fischer, "Carbon nanotube composites for thermal management," *Appl. Phys. Lett.*, vol. 80, no. 15, pp. 2767–2769, 2002, http://dx.doi.org/10.1063/1.1469696.

[24] L. E. Evseeva and S. A. Tanaeva, "Thermal conductivity of micro-and nanostructural epoxy composites at low temperatures," *Mech. Compos. Mater.*, vol. 44, no. 1, pp. 87–92, 2008, http://dx.doi.org/10.1007/s11029-008-0010-1.

[25] P. C. Ma, B. Z. Tang, and J. K. Kim, "Effect of CNT decoration with silver nanoparticles on electrical conductivity of CNT-polymer composites," *Carbon N. Y.*, vol. 46, no. 11, pp. 1497–1505, 2008, http://dx.doi.org/10.1016/j.carbon.2008.06.048.

[26] D. Cai and M. Song, "Latex technology as a simple route to improve the thermal conductivity of a carbon nanotube/polymer composite," *Carbon N. Y.*, vol. 46, no. 15, pp. 2107–2112, 2008, http://dx.doi.org/10.1016/j.carbon.2008.09.001.

[27] G. Skripkiunas, E. Karpova, J. Bendoraitiene, and I. Barauskas, "Effect of MWCNT and PCE plasticizer on the properties of cement pastes," *IOP Conf. Ser. Mater. Sci. Eng*., vol. 660, no. 1, 012032, 2019, http://dx.doi.org/10.1088/1757-899X/660/1/012032.

[28] G. Skripkiunas, E. Karpova, I. Barauskas, J. Bendoraitiene, and G. Yakovlev, "Rheological properties of cement pastes with multiwalled carbon nanotubes," *Adv. Mater. Sci. Eng.*, vol. 2018, pp. 1–13, 2018, http://dx.doi.org/10.1155/2018/8963542.

[29] F. Collins, J. Lambert, and W. H. Duan, "The influences of admixtures on the dispersion, workability, and strength of carbon nanotube-OPC paste mixtures," *Cement Concr. Compos.*, vol. 34, no. 2, pp. 201–207, 2012, http://dx.doi.org/10.1016/j.cemconcomp.2011.09.013.

[30] M. S. Konsta-Gdoutos, Z. S. Metaxa, and S. P. Shah, "Multi-scale mechanical and fracture characteristics and early-age strain capacity of high performance carbon nanotube/cement nanocomposites," *Cement Concr. Compos.*, vol. 32, no. 2, pp. 110–115, 2010, http://dx.doi.org/10.1016/j.cemconcomp.2009.10.007.

[31] R. K. Abu Al-Rub, A. I. Ashour, and B. M. Tyson, "On the aspect ratio effect of multi-walled carbon nanotube reinforcements on the mechanical properties of cementitious nanocomposites," *Constr. Build. Mater.*, vol. 35, pp. 647–655, 2012, http://dx.doi.org/10.1016/j.conbuildmat.2012.04.086.

[32] Associação Brasileira de Normas Técnicas, *Cimento Portland – Requisitos,* NBR 16697, 2018.

[33] J. Engmann, C. Servais, and A. S. Burbidge, "Squeeze flow theory and applications to rheometry: a review," *J. Nonnewton. Fluid Mech.*, vol. 132, no. 1–3, pp. 1–27, 2005, http://dx.doi.org/10.1016/j.jnnfm.2005.08.007.

[34] G. H. Meeten, "Yield stress of structured fluids measured by squeeze flow," *Rheol. Acta*, vol. 39, no. 4, pp. 399–408, 2000, http://dx.doi.org/10.1007/s003970000071.

[35] B. H. Min, L. Erwin, and H. M. Jennings, "Rheological behaviour of fresh cement paste as measured by squeeze flow," *J. Mater. Sci.*, vol. 29, no. 5, pp. 1374–1381, 1994, http://dx.doi.org/10.1007/BF00975091.

[36] T. H. Phan and M. Chaouche, "Rheology and stability of self-compacting concrete cement pastes," *Appl. Rheol.*, vol. 15, no. 5, pp. 336–343, Oct 2005, http://dx.doi.org/10.1515/arh-2005-0017.

[37] F. A. Cardoso, V. M. John, R. G. Pileggi, and P. F. G. Banfill, "Characterisation of rendering mortars by squeeze-flow and rotational rheometry," *Cement Concr. Res.*, vol. 57, pp. 79–87, 2014, http://dx.doi.org/10.1016/j.cemconres.2013.12.009.

[38] F. A. Cardoso, V. M. John, and R. G. Pileggi, "Rheological behavior of mortars under different squeezing rates," *Cement Concr. Res.*, vol. 39, no. 9, pp. 748–753, 2009, http://dx.doi.org/10.1016/j.cemconres.2009.05.014.

[39] A. R. G. Azevedo, J. Alexandre, E. B. Zanelato, and M. T. Marvila, "Influence of incorporation of glass waste on the rheological properties of adhesive mortar," *Constr. Build. Mater.*, vol. 148, pp. 359–368, 2017, http://dx.doi.org/10.1016/j.conbuildmat.2017.04.208.

[40] P. R. Matos, R. Pilar, C. A. Casagrande, P. J. P. Gleize, and F. Pelisser, "Comparison between methods for determining the yield stress of cement pastes," *J. Braz. Soc. Mech. Sci. Eng.*, vol. 42, no. 1, pp. 24, 2020, http://dx.doi.org/10.1007/s40430-019-2111-2.

[41] F. A. Cardoso et al., "Experimental developments of the squeeze flow test for mortars," in *Proc. Int. Conf. Rheol. Process. Constr. Mater.*, 2020, pp. 182–190.

[42] T. Log and S. E. Gustafsson, "Transient plane source (TPS) technique for measuring thermal transport properties of building materials," *Fire Mater.*, vol. 19, no. 1, pp. 43–49, 1995, http://dx.doi.org/10.1002/fam.810190107.

[43] N. Roussel, G. Ovarlez, S. Garrault, and C. Brumaud, "The origins of thixotropy of fresh cement pastes," *Cement Concr. Res.*, vol. 42, no. 1, pp. 148–157, 2012, http://dx.doi.org/10.1016/j.cemconres.2011.09.004.

[44] S. C. Paul, A. S. van Rooyen, G. P. A. G. van Zijl, and L. F. Petrik, "Properties of cement-based composites using nanoparticles: A comprehensive review," *Constr. Build. Mater.*, vol. 189, pp. 1019–1034, 2018., http://dx.doi.org/10.1016/j.conbuildmat.2018.09.062.

[45] L. Vaisman, H. D. Wagner, and G. Marom, "The role of surfactants in dispersion of carbon nanotubes," *Adv. Colloid Interface Sci.*, vol. 128-130, pp. 37–46, 2006, http://dx.doi.org/10.1016/j.cis.2006.11.007.

[46] S. Ma, Y. Qian, and S. Kawashima, "Performance-based study on the rheological and hardened properties of blended cement mortars incorporating palygorskite clays and carbon nanotubes," *Constr. Build. Mater.*, vol. 171, pp. 663–671, 2018, http://dx.doi.org/10.1016/j.conbuildmat.2018.03.121.

[47] N. Mohamadian, M. Z. Ramhormozi, D. A. Wood, and R. Ashena, "Reinforcement of oil and gas wellbore cements with a methyl methacrylate/carbon-nanotube polymer nanocomposite additive," *Cement Concr. Compos.*, vol. 114, pp. 103763, 2020, http://dx.doi.org/10.1016/j.cemconcomp.2020.103763.

[48] A. Yahia, "Effect of solid concentration and shear rate on shear-thickening response of high-performance cement suspensions," *Constr. Build. Mater.*, vol. 53, pp. 517–521, 2014, http://dx.doi.org/10.1016/j.conbuildmat.2013.10.078.

[49] J. Hot, H. Bessaies-Bey, C. Brumaud, M. Duc, C. Castella, and N. Roussel, "Adsorbing polymers and viscosity of cement pastes," *Cement Concr. Res.*, vol. 63, pp. 12–19, 2014., http://dx.doi.org/10.1016/j.cemconres.2014.04.005.

[50] M. Tafesse and H. K. Kim, "The role of carbon nanotube on hydration kinetics and shrinkage of cement composite," *Compos., Part B Eng.*, vol. 169, pp. 55–64, 2019, http://dx.doi.org/10.1016/j.compositesb.2019.04.004.

[51] R. K. Abu Al-Rub, A. I. Ashour, and B. M. Tyson, "On the aspect ratio effect of multi-walled carbon nanotube reinforcements on the mechanical properties of cementitious nanocomposites," *Constr. Build. Mater.*, vol. 35, pp. 647–655, 2012, http://dx.doi.org/10.1016/j.conbuildmat.2012.04.086.

[52] P. R. Matos, R. Pilar, C. A. Casagrande, P. J. P. Gleize, and F. Pelisser, "Comparison between methods for determining the yield stress of cement pastes," *J. Braz. Soc. Mech. Sci. Eng.*, vol. 42, no. 1, pp. 24, Jan 2020, http://dx.doi.org/10.1007/s40430-019-2111-2.

[53] A. J. N. MacLeod, A. Fehervari, W. P. Gates, E. O. Garcez, L. P. Aldridge, and F. Collins, "Enhancing fresh properties and strength of concrete with a pre-dispersed carbon nanotube liquid admixture," *Constr. Build. Mater.*, vol. 247, pp. 118524, 2020, http://dx.doi.org/10.1016/j.conbuildmat.2020.118524.

[54] M. O. Mohsen, R. Taha, A. Abu Taqa, and A. Shaat, "Optimum carbon nanotubes' content for improving flexural and compressive strength of cement paste," *Constr. Build. Mater.*, vol. 150, pp. 395–403, 2017, http://dx.doi.org/10.1016/j.conbuildmat.2017.06.020.

[55] O. A. Mendoza Reales, Y. P. Arias Jaramillo, J. C. Ochoa Botero, C. A. Delgado, J. H. Quintero, and R. D. Toledo Fo., "Influence of MWCNT/surfactant dispersions on the rheology of Portland cement pastes," *Cement Concr. Res.*, vol. 107, pp. 101–109, 2018, http://dx.doi.org/10.1016/j.cemconres.2018.02.020.

[56] B. M. Tyson, R. K. Abu Al-Rub, A. Yazdanbakhsh, and Z. Grasley, "Carbon nanotubes and carbon nanofibers for enhancing the mechanical properties of nanocomposite cementitious materials," *J. Mater. Civ. Eng.*, vol. 23, no. 7, pp. 1028–1035, 2011, http://dx.doi.org/10.1061/(ASCE)MT.1943-5533.0000266.

[57] C. A. Casagrande, L. F. Jochem, L. Onghero, P. Ricardo de Matos, W. L. Repette, and P. J. P. Gleize, "Effect of partial substitution of superplasticizer by silanes in Portland cement pastes," *J. Build. Eng.*, vol. 29, pp. 2019, 2020, http://dx.doi.org/10.1016/j.jobe.2020.101226.

[58] A. Sobolkina et al., "Dispersion of carbon nanotubes and its influence on the mechanical properties of the cement matrix," *Cement Concr. Compos.*, vol. 34, no. 10, pp. 1104–1113, 2012, http://dx.doi.org/10.1016/j.cemconcomp.2012.07.008.

[59] K. Pietrak and T. Wiśniewski, "A review of models for effective thermal conductivity of composite materials," *J. Power Technol.*, vol. 95, no. 1, pp. 14–24, 2015.

[60] Y. Xu, G. Ray, and B. Abdel-Magid, "Thermal behavior of single-walled carbon nanotube polymer-matrix composites," *Compos., Part A Appl. Sci. Manuf.*, vol. 37, no. 1, pp. 114–121, 2006., http://dx.doi.org/10.1016/j.compositesa.2005.04.009.

[61] A. Bejan and A. D. Kraus, *Heat Transfer Handbook*, 1st ed. New Jersey: Wiley-Interscience, 2003.

# IBRACON Structures and Materials Journal
## Revista IBRACON de Estruturas e Materiais

ORIGINAL ARTICLE

# Development and validation of an ultrasound imaging software for nondestructive evaluation of concrete pavements

*Desenvolvimento e validação de um software de formação de imagem de ultrassom para avaliação estrutural não-destrutiva de pavimentos de concreto*

Henrique Luiz de Lima Seiffert[a]  (iD)
José Tadeu Balbo[a]  (iD)

[a]Universidade de São Paulo – USP, Escola Politécnica, Departamento de Engenharia de Transportes, São Paulo, SP, Brasil

**Abstract:** A Synthetic Aperture Focusing Technique-based ultrasound imaging software was developed and validated in this work. The software development process was discussed in detail. For validation, Jointed Plain Concrete Pavements were imaged with the evaluated software and a software assumed to yield standard images. The quality of the standard and evaluated images were analyzed and compared. The backwalls and dowels were recognizable in the standard and evaluated images. The thickness estimates obtained with each software was the same. The characteristics of objects and artifacts were explained in terms of the technology's fundamentals and its implementations' characteristics. The evaluated software resulted, therefore, in images of similar quality to the standard software's images from a practical standpoint. The herein developed software was then validated for research on nondestructive evaluation of concrete pavements and can be used for testing and development of performance-improving signal and image processing techniques.

**Keywords:** concrete pavements, nondestructive evaluation, ultrasound imaging.

**Resumo:** Um software de formação de imagem de ultrassom baseado na Synthetic Aperture Focusing Technique foi desenvolvido e validado neste trabalho. O desenvolvimento do software foi discutido em detalhes. Para validação, Pavimentos de Concreto Simples foram imageados com o software avaliado e um software que resulta em imagens consideradas referência. A qualidade das imagens avaliadas e referências foram analisadas e comparadas. As backwalls e a barras metálicas eram reconhecíveis nas imagens avaliadas e referências. As estimativas de espessura obtidas com os dois softwares eram iguais. As características dos objetos e artefatos nas imagens foram explicadas em termos dos fundamentos da tecnologia e das características de suas implementações. O software avaliado resultou, portanto, em imagens de qualidade similar àquelas do software referência para fins práticos. O software desenvolvido aqui foi, logo, validado e poderá ser utilizado para pesquisa sobre avaliação estrutural não-destrutiva de pavimentos de concreto e para teste e desenvolvimento de técnicas de processamento de sinais e imagens para melhorar o desempenho da tecnologia.

**Palavras-chave:** pavimentos de concreto, avaliação estrutural não-destrutiva, imagem de ultrassom.

## 1 INTRODUCTION

To select a method for nondestructive evaluation (NDE) of a given concrete structure, the penetration depth, resolution, signal-to-noise ratio (SNR), and application record of prospective methods should be taken into consideration [1]. Based on this, a good method for Jointed Plain Concrete Pavement (JPCP) NDE would be ultrasound imaging (UI) with the Synthetic Aperture Focusing Technique (SAFT).

The SAFT is an UI algorithm that tackles resolution and noise-related issues hindering conventional concrete UI and offers a better compromise among SNR, resolution, and penetration depth [2], [3]. SAFT UI has been successfully used to recognize steel bars, ducts, delamination, air voids, and cracks in concrete pavements [4]–[7] and other concrete structures [8]–[10].

Nevertheless, JPCP NDE with SAFT UI has been hindered by efficiency and accuracy-related issues [11]. It could be bolstered, therefore, with signal and image processing techniques that improve its efficiency and accuracy [12]–[14]. The development and application of such techniques both require, however, a validated and extensible SAFT UI software; that is, a software that outputs good-quality images within the SAFT's limitations at any time and where those techniques could eventually be plugged in.

A SAFT UI software with these characteristics was developed and validated in this work. The software development process was presented in detail. JPCPs were imaged with the herein developed software and the SAFT UI software accompanying the data acquisition device used in this work. The quality of their images was evaluated from a practical standpoint, and the similarities and differences in image quality were used to validate the herein developed software assuming that the other one yields standard images. The characteristics of the objects and artifacts in the images were discussed to explain image quality and differences between the software.

As previously mentioned, the development of such solutions is requisite for employing or developing performance-improving techniques and therefore, to make the most of the technology for a given application. This work's discussion on image characteristics and their relationship to the algorithm's fundamentals and its implementation's characteristics should be relevant for developing and validation similar solutions for any application. Nevertheless, a general framework for validating such solutions is not presented in this work.

The SAFT is reviewed in the next section. The herein developed software is presented subsequently. The validation process and its results are presented and discussed next, followed by this work's conclusions.

## 2 SYNTHETIC APERTURE FOCUSING TECHNIQUE

The SAFT processes $I$ signals $g_i(t)$, $i=1,2,3,...,I$, acquired in the pulse-echo or pitch-catch inspection of a concrete volume of interest and outputs an image $f(x,y)$ of this volume. To this purpose, the inspected volume is first represented as $I$ rectangular grids $f_i(x,y)$ (reconstruction grid) with rectangular grid elements $P(x,y)$ (Figure 1).
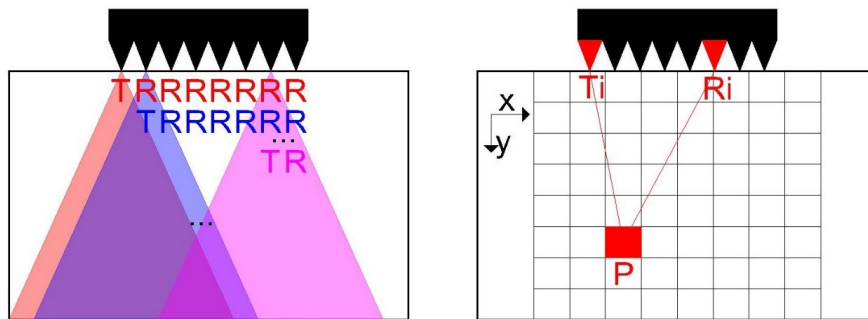


**Figure 1.** Data acquisition device's operation mode (left) and geometry assumed for ultrasound imaging (right).

The signals $g_i(t)$ contain the pressure amplitude of reflected waves (and other waves) as a function of time. The SAFT first maps this time-domain information into space. In the mapping process, the amplitude of $g_i(t)$ at a time instant $t^*$, $g_i(t^*)$, is ascribed to a grid element $P(x,y)$ of $f_i(x,y)$ with Equations 1 and 2. Equation 2 assumes that an ultrasound wave was transmitted into the concrete at $T_i(x_T,y_T)$, reflected at $P(x,y)$, and then sensed at $R_i(x_R,y_R)$ in $t^*$ time units, where $T_i$ and $R_i$ are the positions of the transducers at transmission and reception mode, respectively. It also assumes ray-like wave propagation, constant propagation speed $c$, and specular reflection at $P(x,y)$. $t_d$ is the system's delay. After every $P(x,y)$ of every $f_i(x,y)$ had a pressure amplitude ascribed to it, the $f_i(x,y)$ are summed up with Equation 3 to obtain $f(x,y)$ [3], [15].

$$f_i(x,y) = g_i(t^*) \tag{1}$$

$$t^* = t_d + c^{-1}\left[\sqrt{(x_T - x)^2 + (y_T - y)^2} + \sqrt{(x_R - x)^2 + (y_R - y)^2}\right] \tag{2}$$

$$f(x,y) = \sum_{i=1}^{I} f_i(x,y) \tag{3}$$

The SAFT yields higher-quality images because the best achievable resolution is achieved everywhere in the image plane [15] and reflecting objects, e.g. backwall, steel bars, and defects, are enhanced, whereas noise, including structural noise, is reduced [2], [3]. In Equation 3, the amplitudes of different signals mapped to the same position are superimposed. If these amplitudes are in phase, as expected for reflecting objects, then there will be constructive interference among them and enhancement of such objects in $f(x,y)$. The opposite takes place for the background noise, since noise components in different signals are generally not in phase [2], [16]–[18]. Therefore, SNR and resolution are enhanced [2], [3], [19].

Nevertheless, from a practical standpoint, image quality might be hindered by the SAFT's assumptions. The pulse velocity $c$ is not constant across the image plane since concrete is a dispersive medium [3]; hence, objects might be shown with wrong shape or position in $f(x,y)$ [20]. The implications of attenuation are disregarded; hence, the brightness of objects in $f(x,y)$ might not be proportional to their elastic properties [13]. Consequently, objects might not be shown as expected and their recognition might be hindered despite the SNR and resolution enhancements.

Moreover, every signal component is assumed a one-time reflected wave. Therefore, artifacts might arise from phenomena such as multiple reflections [9] and surface waves [13], [21] that make up the signals but are disregarded. Further artifacts might arise from mode conversion [3] and acoustic shadowing [4]. Acoustic shadowing occurs when objects of interest behind reflecting objects (e.g. steel bars) are not shown in $f(x,y)$ because not enough energy was transmitted across these objects [20].

## 3 SOFTWARE DEVELOPMENT

The SAFT was implemented in MATLAB R2015a (MathWorks, Natick, USA) with some amendments. The width of the grids $f_i(x,y)$ should be approximately the distance between the outermost transducers and their depth should be more than the inspected structure's thickness. The size of our $f(x,y)$ and $f_i(x,y)$ were 500 by 500 mm. The dimensions of the grid elements $P(x,y)$ should be proportional to inspection system's sampling frequency [22]. The size of our $P(x,y)$ were 1 by 1 mm.

The transducers positions $T_i(x_T, y_T)$ and $R_i(x_R, y_R)$ for each $g_i(t)$ should be known with precision. The data acquisition device used in this work was an array with fixed elements and known operation mode; therefore, $T_i$ and $R_i$ were easily determined from the device's characteristics. As the transducers are on the structure's surface, it was assumed that $y_T = y_R = 0$. The value of $c$ should be assumed or estimated with testing or signal processing. The $c$ value estimated by the data acquisition device from the arrival time of surface waves was used in this work [14]. The values of $t^*$ determined from Equation 2 are real but the values of $t$ are integer multiples of the sampling period. The floor function was selected to determine the sample of $g_i(t)$ corresponding to $t^*$. The signals were not rectified, to preserve the phase information used in Equation 3 [23], and were not pre-processed either.

The SAFT assumes in Equation 2 that the entire concrete volume was insonified by every $T_i$ [17]. Since this is not true, the windowing function $w_i(x,y)$ in Equation 4 [12] was used to consider the volume portion that was insonified by each $T_i$. Essentially, $w_i(x,y)$ weights the amplitudes mapped to $f_i(x,y)$ assuming a beam spreading function. Equation 5 was used instead of Equation 3.

$$w_i = \frac{(y - y_T)}{\sqrt{(x_T - x)^2 + (y_T - y)^2}} \frac{(y - y_R)}{\sqrt{(x_R - x)^2 + (y_R - y)^2}} \tag{4}$$

$$f(x,y) = \sum_{i=1}^{N} f_i(x,y) w_i(x,y) \tag{5}$$

Additionally, the upper envelope of each column of $f(x, y)$ was determined with the Hilbert transform and taken as its new values [12]. $f(x, y)$ was then transformed into a grayscale image, outputted, and displayed with a color scheme where pixel brightness is proportional to color warmness. Though the signals were not processed prior to mapping and $f(x, y)$ was not processed after transformation with performance-improving techniques, modules for this could be easily added to the software.

## 4 SOFTWARE VALIDATION

### 4.1 Data acquisition

The JPCP test section (TS) and the concrete slab (CS) imitating doweled regions of JPCPs in Figure 2 were both imaged in this work. TS comprised 250 mm-thick concrete slabs, was built in 1999, and, according to visual inspections [24], was in sound condition at data acquisition. Its as-built thickness was measured with coring right after data acquisition. The CS was 190mm thick (in design and after construction) and had three 25 mm steel bars inserted 54, 74, and 94 mm deep. It was built in laboratory in 2019; dowel positioning was ensured by tying the dowels to trusses and the trusses to the forms. The TS' and CS' concrete mixes are presented in Table 1.
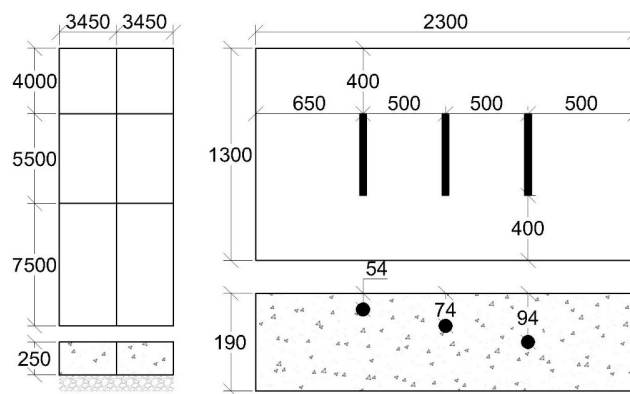


**Figure 2.** TS' (left) and CS' (right) designs (Units: mm.)

**Table 1.** TS' and CS' concrete mixes.

| Component | Proportion in TS (kg/m³) | Proportion in CS (kg/m³) |
|---|---|---|
| Cement | 383 | 375 |
| Sand | 638 | 807 |
| Gravel | 1215 | 1126 |
| Water | 172 | 175 |
| Plasticizer | 1.34 | 2.06 |

Data was acquired on six points on the TS in 2018 and nine points on the CS in 2019. The TS' points were on plain regions. The CS' points were three over each dowel's axis. The number of points was deemed sufficient since this work aimed to validate the software for research purposes and the scenarios of interest were restricted to plain and doweled regions of sound JPCPs. A larger and more diverse set of points should be used to validate similar software for practical purposes or for a large set of scenarios. A practical obstacle for increasing the number and diversity of points for any purpose is the fact that a structure's as-built characteristics must be known with precision for validation.

The data acquisition process was the same for every point. The area where the data acquisition device would be placed was swept free of debris and a point was marked with a construction pencil. The device was positioned centered on the point and data acquisition was carried out. A coupling layer or surface preparation was not required. The acquired data was labelled, stored in the device, and eventually transferred to a personal computer for processing.

ACSYS' A1040 MIRA was the data acquisition device. It comprises a 4-by-12 array of transducers operated as a 1-by-12 one. Its transducers are 30 mm apart and transmit 50 kHz shear-horizontal waves. Its operation mode is illustrated in Figure 1. Each transducer, except the rightmost one, is operated in transmission ($_T$) once, while the transducers to its right are in reception

mode ($_R$). The transducer $_T$ is switched from left to right to sweep the concrete volume beneath the device. A signal $g_i(t)$ is acquired for each $_T$-$_R$ pair. $I = 66$ signals are acquired on each point then. The device also estimates the pulse velocity c in the inspected concrete volume with the time-of-flight of surface waves [14].

## 4.2 Validation procedure

The TS' and CS' data were inputted to the herein developed software and the SAFT UI software accompanying the data acquisition device. The latter was assumed to result in standard images since it was developed for practical purposes. Its images are hereafter called standard images, while the images obtained with the software being validated are called evaluated images.

The herein developed software was evaluated by comparing the quality of its images to the standard ones. The images were analyzed from a practical standpoint. A good-quality image was assumed to be one where the backwall and dowel were recognizable and positioned correctly. An object was assumed recognizable if it was shown with the expected shape and brightness and around their expected positions. Artifacts were expected and considered in the analysis. The TS' and CS' thicknesses were measured from the images by taking the vertical position of the backwall's brightest pixel as the thickness estimate [11], [14] and considered in the analysis.

The differences in image quality were used to infer differences between the software; namely, to enumerate potential issues with the evaluated software and signal and image processing techniques potentially used by the standard software but not by the evaluated one. The information presented above and in the literature was considered for this purpose.

## 5 RESULTS AND DISCUSSION

The TS' standard and evaluated images in Figure 3 both show a backwall and multiple-reflection artifacts. The backwalls are the 200-250 mm deep objects. The backwall was recognizable in both images because it was a bright and wide object at depths roughly the concrete element's as-built thickness (240.50 mm). Its brightness is due to the slab-base course interface's large reflection coefficient, and its width is due to the interface being sensed by every $_T$-$_R$ pair. The standard image's backwall seems larger than the evaluated image's one because the former is presumably saturated.
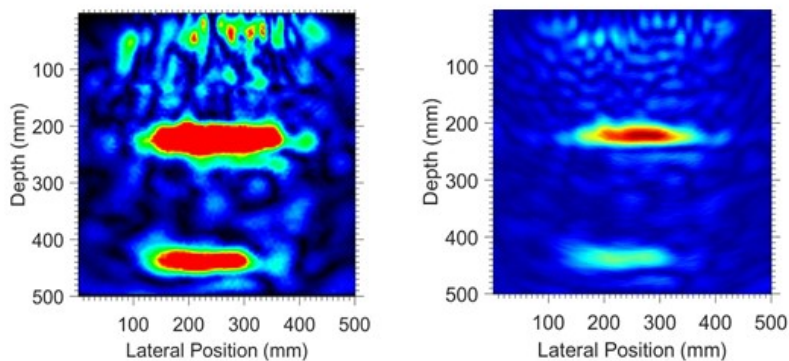


**Figure 3.** Standard (left) and evaluated (right) images of a TS' point.

The multiple-reflection artifacts are the 425-475 mm deep objects (Figure 3). As the SAFT does not recognize multiple reflections, the waves bouncing between backwall and surface (multiple reflections) are computed as reflections at ever deeper backwalls and represented as mirror images of the backwall. The mirror images are not carbon copies of the backwall due to attenuation.

The CS' standard images in Figures 4-6 show a dowel, a backwall, and multiple-reflection artifacts, and its evaluated images shown a dowel, a backwall, surface-waves artifacts and multiple-reflection artifacts. The backwall was recognizable in every image. The multiple-reflection artifacts comprise mirror images of the backwall and dowel.

The dowel is bright, round, and at the expected position in the evaluated images and bright and at the expected position, but not round, in the standard ones (Figures 4-6). The dowels were nevertheless recognizable in every image. The shape information on the mirror images in the standard images were used to recognize the dowels. Artifacts, if well understood, might therefore provide some information on the inspected structure.
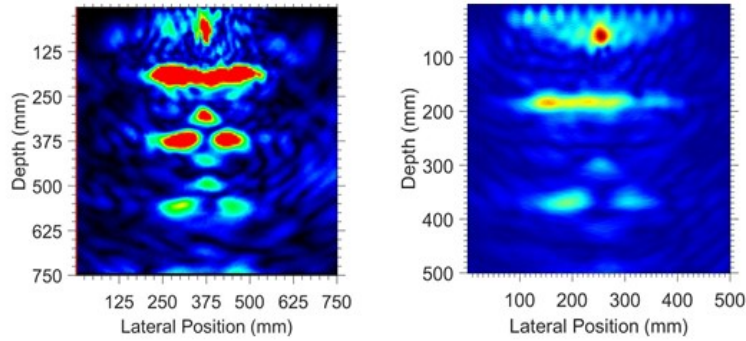
**Figure 4.** Standard (left) and evaluated (right) images of a CS' point over the 54 mm-deep dowel.
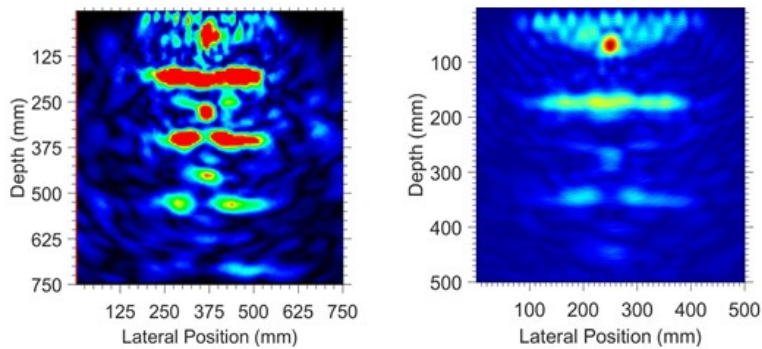


**Figure 5.** Standard (left) and evaluated (right) images of a CS' point over the 74 mm-deep dowel.
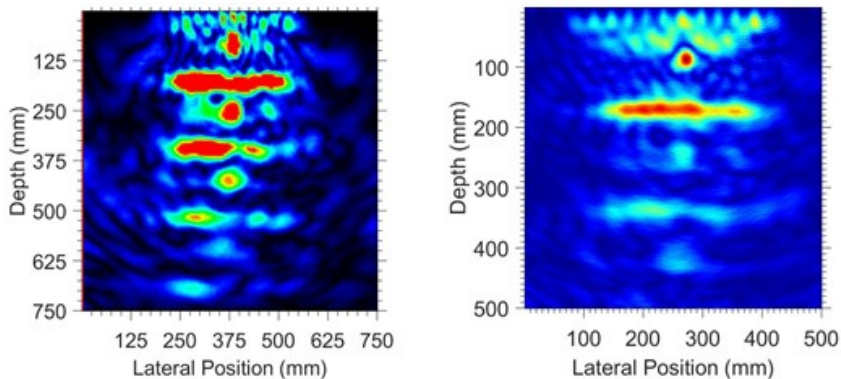


**Figure 6.** Standard (left) and evaluated (right) images of a CS' point over the 94 mm-deep dowel.

The backwalls should be shown brighter than the dowels since the slab-base course interface's reflection coefficient is larger than the slab-dowel's coefficient. Attenuation prevented this in the evaluation images in Figures 4-6. The $_T$-backwall path is larger than the $_T$-dowel path. Hence, the waves striking the backwall have smaller intensity, and the waves reflected at the backwall might have smaller intensity despite the backwall's larger reflection coefficient. In addition, the waves reflected at the backwall are attenuated to a greater degree on their way to $_R$. As a result of this and the fact that attenuation has not been compensated in the evaluated software, the dowels are shown brighter than the backwall in the evaluated images.

The dowels and backwalls have similar brightness in the standard images in Figures 4-6 due to saturation and presumably attenuation compensation. The multiple-reflection artifacts in the standard images are brighter and wider in Figures 3-6 for the same reasons.

The surface-waves artifacts are shown above the dowels in the evaluated images in Figures 4-6. As the SAFT does not recognize surface waves, it computes the waves travelling on the concrete structure's surface from $_T$ to $_R$ as reflected waves in the inspected volume's interior, resulting in those artifacts. The surface waves are unavoidable. The brightness distribution in Figure 3 occluded them. The standard software has presumably filtered them out as the artifacts are not presented in the standard images in Figures 4-6.

The TS and CS were roughly 220 mm and 170 mm thick respectively according to Figures 3-6. As the same thickness measure was obtained with the standard and evaluated images, the evaluated software does not result in gross quantitative errors for the inspected scenarios. The thickness estimates' inaccuracy was due to the $_c$ estimates' inaccuracy. The $_c$ estimate's accuracy was disregarded for this work.

The standard and evaluated images obtained for the other points are presented in Figures 7-11. The observations above are therefore true for all standard and evaluated images obtained int this work. Mode-conversion artifacts were not observed in this work because shear-horizontal waves are not mode converted. Acoustic shadowing was not observed in this work either, despite being reported for similar scenarios [4].
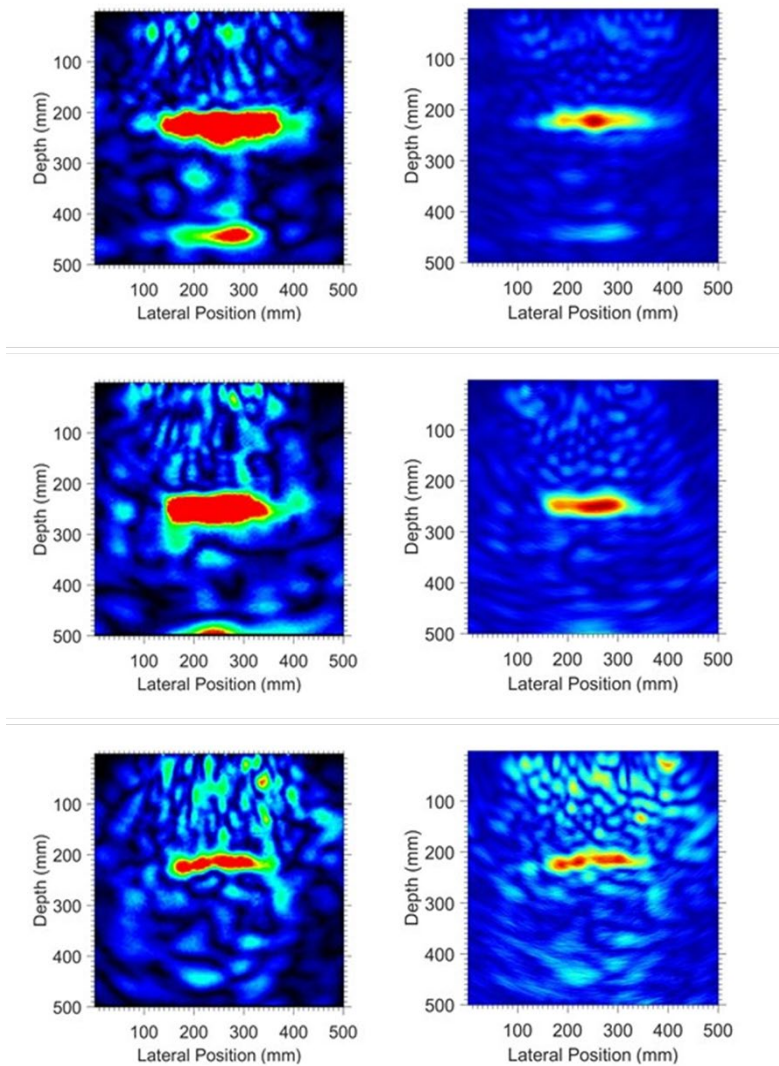


**Figure 7.** Standard (left) and evaluated (right) images of the other TS' points (Part 1).
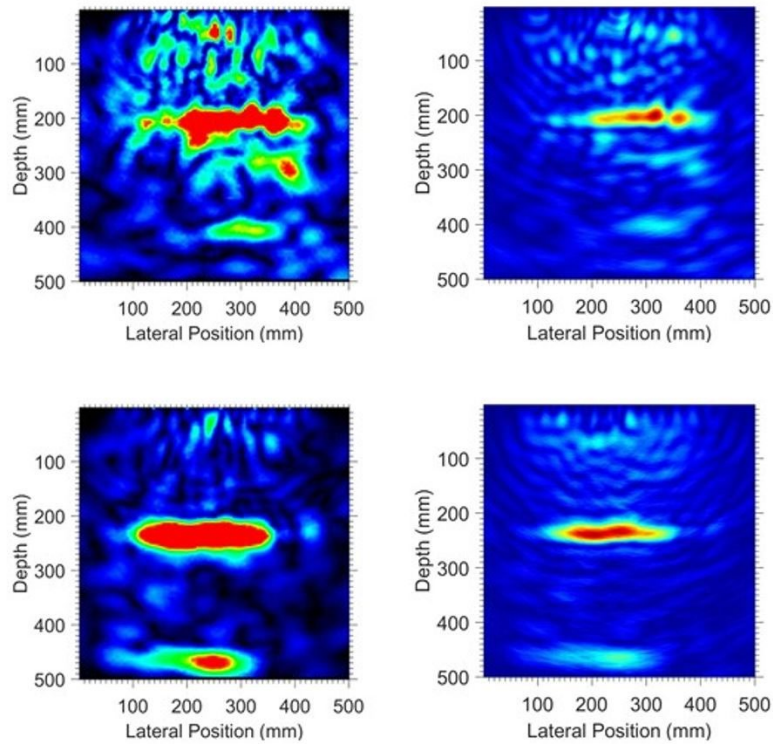
**Figure 8.** Standard (left) and evaluated (right) images of the other TS' points (Part 2).



**Figure 9.** Standard (left) and evaluated (right) images of the other CS' points over the 54 mm-deep dowel.

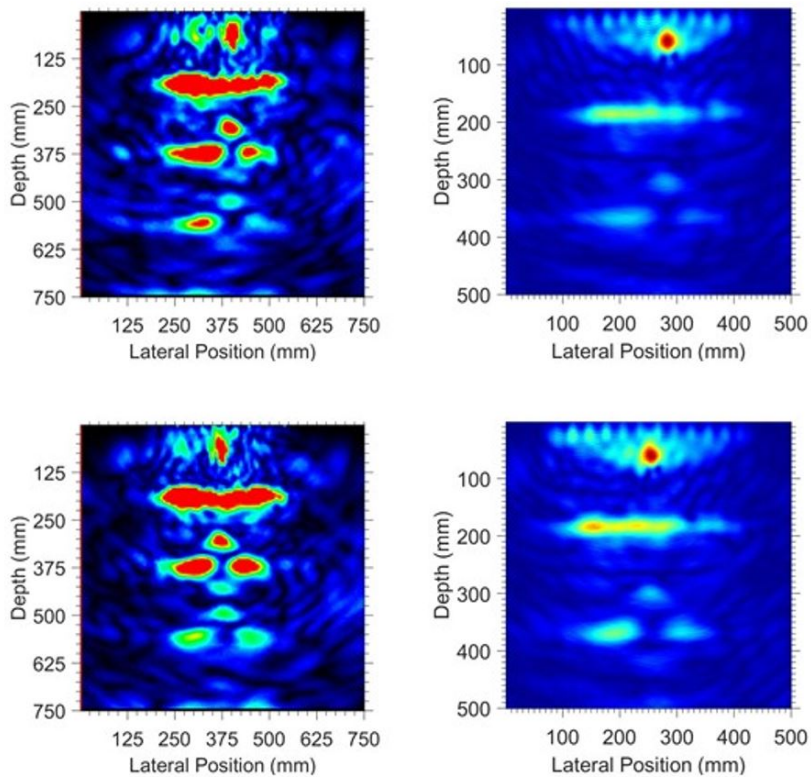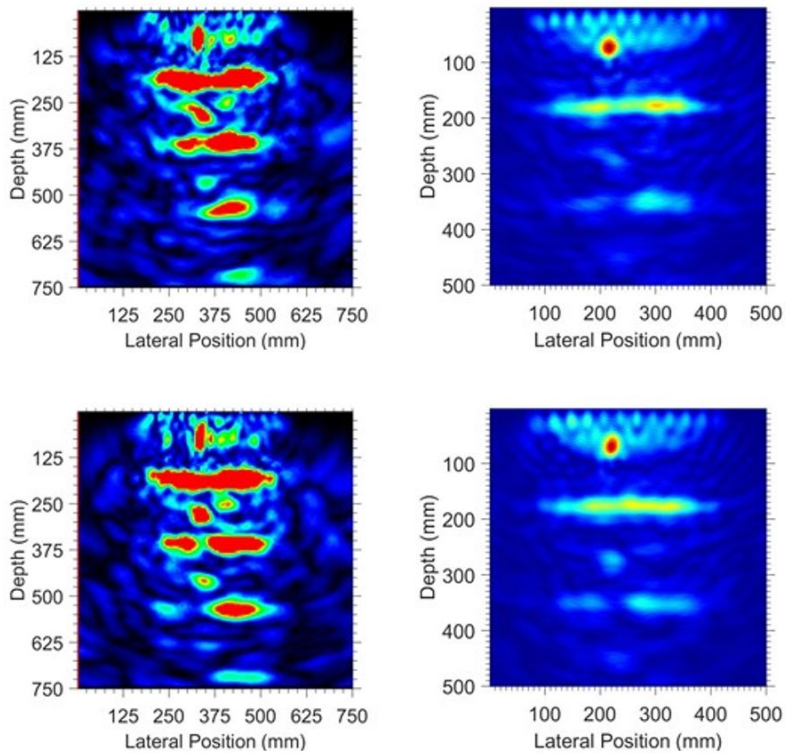Rev. IBRACON Estrut. Mater., vol. 14, no. 5, e14511, 2021

8/11

**Figure 10.** Standard (left) and evaluated (right) images of the other CS' points over the 74 mm-deep dowel.
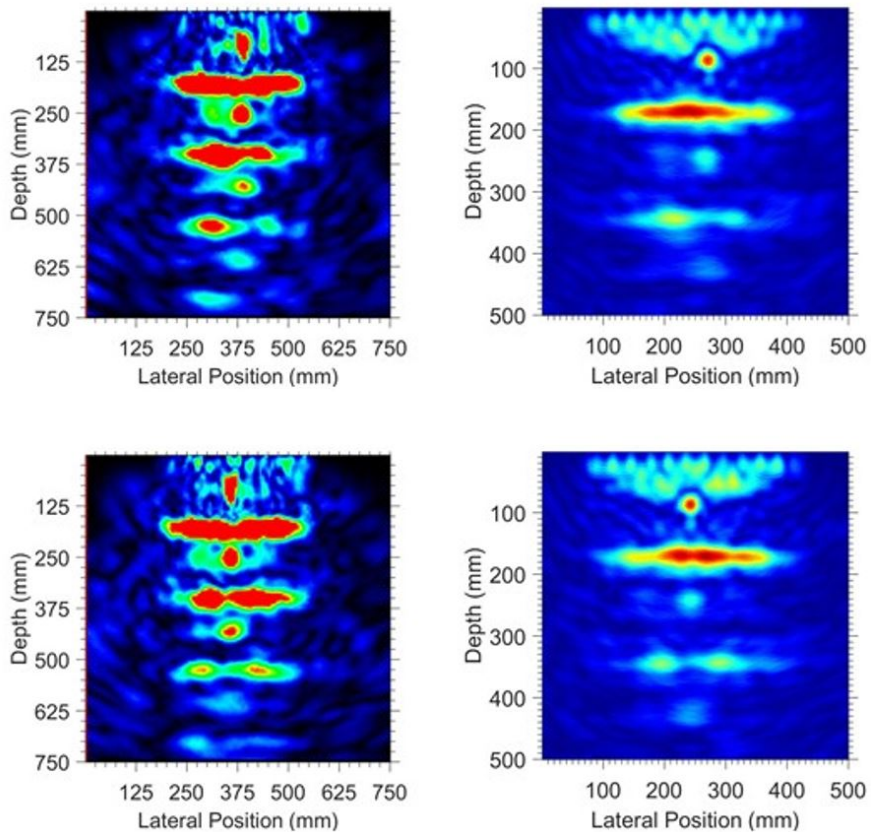
**Figure 11.** Standard (left) and evaluated (right) images of the other CS' points over the 94 mm-deep dowel.

# 6 CONCLUSIONS

A SAFT UI software for JPCP NDE was developed and validated in this work. The SAFT's fundamentals were reviewed and every step required to implement the SAFT was discussed. The validation was carried out by comparing the JPCP images obtained with the herein developed software to the ones obtained with a software assumed to yield standard images. The backwalls and dowels (steel bars) were recognizable in both evaluated and standard images. The characteristic of these objects and artifacts in both images were discussed and considered in the validation. The thickness estimated from the evaluated and standard images were the same. Therefore, from a practical standpoint, the quality of the images obtained with the herein developed software and the standard one was essentially the same and no gross quantitative errors were observed in the evaluated images. The differences between the evaluated and standard images were presumably due to further signal and image processing steps in the standard software and not due to errors in the evaluated software. The herein developed software was therefore validated for JPCP NDE, though restricted to the scenarios represented by the inspected structures. The software can nevertheless be used for testing and development of solutions to tackle SAFT UI's issues.

## LIST OF SYMBOLS

$c$ : Pulse velocity.

$f_i(x,y)$, $f(x,y)$ : Reconstruction grid or image.

$g(t)$, $g_i(t)$ : Time-domain signal.

$P(x,y)$ : Reconstruction grid element or pixel.

$R_i(x_R,y_R)$ : Position of transducer in reception mode.

$T_i(x_T,y_T)$ : Position of transducer in transmission mode.

$t_d$ : System's time delay.

$w_i(x,y)$ : Windowing function.

## LIST OF ABBREVIATIONS

CS: Concrete Specimen
NDE: Nondestructive Evaluation
JPCP: Jointed Plain Concrete Pavement
SAFT: Synthetic Aperture Focusing Technique
SNR: Signal-to-Noise Ratio
TS: Test Section
UI: Ultrasound Imaging

## CITATIONS

[1] D. M. McCann and M. C. Forde, "Review of NDT methods in the assessment of concrete and masonry structures," *NDT Int.*, vol. 34, no. 2, pp. 71–84, Mar 2001, http://dx.doi.org/10.1016/S0963-8695(00)00032-3.

[2] S. R. Doctor, T. E. Hall, and L. D. Reid, "SAFT: the evolution of a signal processing technology for ultrasonic testing," *NDT Int.*, vol. 19, no. 3, pp. 163–167, Jun 1986, http://dx.doi.org/10.1016/0308-9126(86)90105-7.

[3] M. Schickert, M. Krause, and W. Müller, "Ultrasonic imaging of concrete elements using reconstruction by synthetic aperture focusing technique," *J. Mater. Civ. Eng.*, vol. 15, no. 3, pp. 235–246, Jun 2003, http://dx.doi.org/10.1061/(ASCE)0899-1561(2003)15:3(235).

[4] K. Hoegh, L. Khazanovich, and H. T. Yu, "ultrasonic tomography for evaluation of concrete pavements," *Transp. Res. Rec.*, vol. 2232, no. 1, pp. 85–94, Jan 2011, http://dx.doi.org/10.3141/2232-09.

[5] K. Hoegh, L. Khazanovich, B. J. Worel, and H. T. Yu, "Detection of subsurface joint deterioration: blind test comparison of ultrasound array technology with conventional nondestructive methods," *Transp. Res. Rec.*, vol. 2367, no. 1, pp. 3–12, Jan 2013, http://dx.doi.org/10.3141/2367-01.

[6] L. S. Salles, J. T. Balbo, and L. Khazanovich, "Non-destructive ultrasonic tomography for concrete pavement evaluation: signal processing and image analysis of crucial parameters," *Rev. IBRACON Estrut. Mater.*, vol. 10, no. 6, pp. 1182–1191, Nov 2017, http://dx.doi.org/10.1590/s1983-41952017000600004.

[7] L. S. de Salles, L. Khazanovich, and J. T. Balbo, "Non-destructive evaluation of crack initiation and propagation in continuously reinforced concrete pavements," *Transp. Res. Rec.*, vol. 2673, no. 3, pp. 375–385, Mar 2019, http://dx.doi.org/10.1177/0361198119833672.

[8]  M. Krause, F. Mielentz, B. Milman, W. Müller, V. Schmitz, and H. Wiggenhauser, "Ultrasonic imaging of concrete members using an array system," *NDT Int.*, vol. 34, no. 6, pp. 403–408, Sep 2001, http://dx.doi.org/10.1016/S0963-8695(01)00007-X.

[9]  P. Shokouhi, J. Wolf, and H. Wiggenhauser, "Detection of delamination in concrete bridge decks by joint amplitude and phase analysis of ultrasonic array measurements," *J. Bridge Eng.*, vol. 19, no. 3, pp. 04013005, Mar 2014, http://dx.doi.org/10.1061/(ASCE)BE.1943-5592.0000513.

[10]  H. Choi, J. Bittner, and J. S. Popovics, "Comparison of ultrasonic imaging techniques for full-scale reinforced concrete," *Transp. Res. Rec.*, vol. 2592, no. 1, pp. 126–135, Jan 2016, http://dx.doi.org/10.3141/2592-14.

[11]  H. L. L. Seiffert, "Assessment of the accuracy of an ultrasound imaging system for the measurement of the thickness of pavements' concrete slabs," M.S. thesis, Univ. São Paulo, São Paulo, 2019.

[12]  K. Hoegh and L. Khazanovich, "Extended synthetic aperture focusing technique for ultrasonic imaging of concrete," *NDT Int.*, vol. 74, pp. 33–42, Sep 2015, http://dx.doi.org/10.1016/j.ndteint.2015.05.001.

[13]  J. Bittner and J. Popovics, "Ultrasonic analysis modifications for imaging of concrete infrastructure," in *2017 IEEE International Ultrasonics Symposium (IUS)*, Washington, DC, Sep. 2017, pp. 1, https://doi.org/10.1109/ULTSYM.2017.8091747.

[14]  J. A. Bittner, A. Spalvier, and J. S. Popovics, "Internal imaging of concrete elements," *Concr. Int.*, vol. 40, no. 4, pp. 57–63, Jan 2018.

[15]  J. A. Jensen, S. I. Nikolov, K. L. Gammelmark, and M. H. Pedersen, "Synthetic aperture ultrasound imaging," *Ultrasonics*, vol. 44, pp. e5–e15, Dec 2006., http://dx.doi.org/10.1016/j.ultras.2006.07.017.

[16]  M. Spies and H. Rieder, "Synthetic aperture focusing of ultrasonic inspection data to enhance the probability of detection of defects in strongly attenuating materials," *NDT Int.*, vol. 43, no. 5, pp. 425–431, Jul 2010., http://dx.doi.org/10.1016/j.ndteint.2010.04.002.

[17]  M. Spies, H. Rieder, A. Dillhöfer, V. Schmitz, and W. Müller, "Synthetic aperture focusing and time-of-flight diffraction ultrasonic imaging: past and present," *J. Nondestruct. Eval.*, vol. 31, no. 4, pp. 310–323, Dec 2012., http://dx.doi.org/10.1007/s10921-012-0150-z.

[18]  J. Prager, J. Kitze, C. Acheroy, D. Brackrock, G. Brekow, and M. Kreutzbruck, "SAFT and TOFD: a comparative study of two defect sizing techniques on a reactor pressure vessel mock-up," *J. Nondestruct. Eval.*, vol. 32, no. 1, pp. 1–13, Mar 2013., http://dx.doi.org/10.1007/s10921-012-0153-9.

[19]  V. Schmitz, S. Chakhlov, and W. Müller, "Experiences with synthetic aperture focusing technique in the field," *Ultrasonics*, vol. 38, no. 1–8, pp. 731–738, Mar 2000. http://dx.doi.org/10.1016/S0041-624X(99)00219-X.

[20]  S. H. Contreras Ortiz, T. Chiu, and M. D. Fox, "Ultrasound image enhancement: a review," *Biomed. Signal Process. Control*, vol. 7, no. 5, pp. 419–428, Sep 2012, http://dx.doi.org/10.1016/j.bspc.2012.02.002.

[21]  H. L. L. Seiffert and J. T. Balbo, "Suppression of surface waves with the ensemble empirical mode decomposition to enhance ultrasound images of reinforced concrete elements," *NDT Int.*, vol. 116, pp. 102329, Dec 2020, http://dx.doi.org/10.1016/j.ndteint.2020.102329.

[22]  X. Guan, J. He, and E. M. Rasselkorde, "A time-domain synthetic aperture ultrasound imaging method for material flaw quantification with validations on small-scale artificial and natural flaws," *Ultrasonics*, vol. 56, pp. 487–496, Feb 2015, http://dx.doi.org/10.1016/j.ultras.2014.09.018.

[23]  S. Kramer, "Ultrasonic weld defect sizing using the synthetic aperture focusing technique," in *Review of Progress in Quantitative Nondestructive Evaluation*, D. O. Thompson and D. E. Chimenti, Eds. Boston, MA: Springer US, 1989, pp. 1995–2002. http://dx.doi.org/10.1007/978-1-4613-0817-1_253.

[24]  J. T. Balbo, *Pavimentos de Concreto*. São Paulo: Oficina de Textos, 2009.

# IBRACON Structures and Materials Journal
## Revista IBRACON de Estruturas e Materiais

ORIGINAL ARTICLE

# Assessment of the effect of changes in consolidation conditions in the advance of the carbonation front in cementitious matrix composites

*Avaliação do efeito da alteração nas condições de adensamento no avanço da frente de carbonatação em compósitos de matriz cimentícia*

Ruan Gustavo Rezende Silva[a] 

Aldo Giuntini de Magalhães[a] 

Christopher Augusto Campos[a] 

Ivair Ramos Silva[b] 

[a]Universidade Federal de Minas Gerais – UFMG, Escola de Engenharia, Departamento de Engenharia de Materiais e Construção Civil, Belo Horizonte, MG, Brasil

[b]Universidade Federal de Ouro Preto – UFOP, Departamento de Estatística, Ouro Preto, MG, Brasil

**Abstract:** Carbonation is one of the main deleterious effects of reinforced concrete structures, as it creates a favorable condition for the reinforcement depassivation and, thus, facilitates the onset of the corrosive process. The phenomenon is directly influenced by the material void's structure, which is affected by the consolidation of the mass in the fresh state, subject evaluated in this study. For this purpose, samples were made using two water to cement ratios and defining two different consolidation methods. Compressive strength tests were carried out for the mechanical characterization of the specimens, in addition to accelerated carbonation tests, monitoring the progress of the carbonated thickness using the phenolphthalein colorimetric indicator, during 98 days. Microstructural differences were evaluated by scanning electron microscopy (SEM). The results indicate that the lower the workability of the mixture, the greater the impacts on the compressive strength of the material, resulting from failures in the consolidation stage. Nevertheless, another behavior is observed when evaluating this effect in the advancement of the carbonation front, indicating that the voids structure of the material should not be evaluated only according to its volume, but also in terms of the pattern of its distribution, its morphology and its connectivity.

**Keywords:** cementitious composites, durability, carbonation, consolidation.

**Resumo:** A carbonatação é um dos principais efeitos deletérios das estruturas de concreto armado, por criar uma condição favorável à despassivação das armaduras e, assim, facilitar o início do processo corrosivo. O fenômeno é diretamente influenciado pela estrutura de vazios do material que, por sua vez, é afetada pelo adensamento da massa no estado fresco, variável avaliada nesse trabalho. Para tanto, foram moldados corpos de prova utilizando-se duas relações água/cimento e definindo-se dois padrões distintos de compactação das misturas. Foram realizados ensaios de resistência à compressão, para caracterização mecânica das amostras, e ensaios de carbonatação acelerada, fazendo-se o acompanhamento do avanço da espessura carbonatada por meio do indicador colorimétrico de fenolftaleína, durante 98 dias. Diferenças microestruturais foram avaliadas por meio de microscopia eletrônica de varredura (MEV). Os resultados indicam que quanto menor a trabalhabilidade da mistura, maiores serão os impactos na resistência à compressão do material, decorrentes de falhas na etapa de adensamento. Apesar disso, outro comportamento é observado ao avaliar esse efeito no avanço da frente de carbonatação, indicando que a estrutura de vazios do material não deve ser avaliada apenas em função do seu volume, mas também quanto ao padrão de sua distribuição, sua morfologia e conectividade.

**Palavras-chave:** compósitos cimentícios, durabilidade, carbonatação, adensamento.

## INTRODUCTION

An important factor to be considered while designing reinforced concrete structures projects is their expected life span. Normative requirements, such as the maximum water/cement ratio to be used in the mixture, the minimum cover of the reinforcement and the minimum consumption of cement, are prescribed according to a certain class of environmental aggressiveness, aiming to guarantee their durability. These criteria aim to control the flow of fluids through the concrete void structure, preventing its degradation by aggressive external agents, such as chlorides, sulfates and acid gases.

According to Figueiredo [1] and Cascudo and Carasek [2], the main acid gases present in the atmosphere in contact with the surface of the structural elements are carbon dioxide ($CO_2$), sulfur dioxide ($SO_2$) and hydrogen sulfide ($H_2S$), responsible for neutralizing the pH of the composite interstitial liquid phase, in a process known as carbonation or neutralization of concrete [3]. As a result of this phenomenon, concrete, which initially is a very alkaline medium, with a pH close to 13, can reach pH values between 8 and 9 [4], [5].

After its diffusion and dissolution in the liquid phase present in the pores of the cement matrix composite, $CO_2$ reacts with the products of the dissolution of calcium hydroxide [$Ca(OH)_2$], from the hydration of cement, forming calcium carbonate ($CaCO_3$). Carbonation can also happen with the participation of other compounds, such as calcium silicate hydrate (CSH) and with non-hydrated silicates: tricalcium silicate ($C_3S$) and dicalcium silicate ($C_2S$) [5]–[7].

The carbonation front advances from the surface to the interior of the structure and, upon reaching the reinforced concrete, causes its depassivation, leaving it susceptible to corrosion. According to Cascudo and Carasek [2] and Neville [8], the pH range below which the passivation layer cannot be maintained is between 11.5 and 11.8, whereas favorable conditions for triggering the corrosion of the steel occur when its pH drops below a limit value around 9 [9]. Since the first studies carried out by Hamada [3], Meyer [10] and other contemporaries, still in the 1960s, carbonation is considered by the entire technical-scientific community as one of the main harmful effects of reinforced concrete structures, due to the creation of favorable conditions for steel corrosion to start.

Carbonation is a slow process, whose forward velocity decreases with time, a fact, due to the lasting process of hydration of Portland cement and the reduction of concrete permeability, since the formed carbonates lead to clogging of the pores, making it difficult for the $CO_2$ to pass. Although there are complex models that seek to estimate carbonated depth as time-related, a well-known and accepted model is represented by Equation 1, derived from Fick's First Law of Diffusion.

$$e_{CO_2} = k \cdot \sqrt{t} \tag{1}$$

where $e_{CO2}$ is the carbonated thickness, $k$ is a carbonation coefficient, related to $CO_2$ diffusivity, and $t$ is the exposure time.

The k coefficient and, therefore, the speed of $CO_2$ penetration, is influenced both by external factors related to the exposure conditions, such as the $CO_2$ content of the environment, the relative humidity and the temperature, as well as the characteristics of the cementitious composite, such as, for example, the water/cement ratio of the mixture, the mass consolidation in the fresh state, the presence of additives and admixtures and the consumption and type of cement. Such parameters are capable of producing variations, alone or together, in the pH value (alkaline reserve) of the composite and in the formed pore system.

According to Neville and Brooks [11], the voids present in the hardened concrete are composed of bubbles of trapped air or spaces left by the mass excess water outlet. The trapped air can be removed during the stage of concrete consolidation in the fresh state, while the space left by the water outlet is directly related to the water/cement ratio of the mixture. By reducing voids, concrete becomes denser and less permeable, and, consequently, more resistant and durable.

According to ACI 309R-05 [12], the consolidation must be compatible with the mixture and with the conditions of the structural element being produced. The guide presents manual and mechanical methods for carrying out consolidation, mentioning, for example, the use of rods and vibration, and highlights that in certain situations it may be necessary to combine more than one of these alternatives. Not only consolidation lack, but also excess, presents itself as a problem, either due to the prolonged time or the high energy used. Al-Khalaf and Yousif [13] evaluated the impact of the degree of compaction of the

mixture, represented by the vibration time, on the compressive strength of concrete specimens and concluded that there is an optimum time that leads to the greatest resistance. Short compaction times lead to voids in the material and longer times cause instability in the mixture due to excessive vibration, and both effects are responsible for decreases in resistance.

Gonen and Yazicioglu [14], working with samples with different porosity levels, generated by variations in the stage of consolidation of the mixtures, observed a reduction of the mechanical resistance and an increase of the carbonation depth in the samples with worse levels of consolidation (greater porosities). Besides that, they observed that even a small compaction of the mass can promote an increase in the compressive strength and that the consolidation is more important in terms of durability. Gao et al. [15], using chloride ion permeability tests, found a decrease in the long-term durability of cementitious composites caused by excessive consolidation. The authors found that this excess causes the segregation of the mixture components and facilitates the entry of aggressive agents.

Despite being an important step for the material to achieve the expected performance, there are few studies in the literature that specifically evaluate this step and that quantify the impact of this variable on the properties of cementitious composites. In view of this, the present work evaluated the influence of the consolidation and the water/cement ratio (w/c) of the mixture in the advance of the carbonation front.

## MATERIALS AND METHODS

The present study was carried out in cylindrical mortar specimens of dimensions (5 x 10) cm, molded using Portland cement CPV-ARI (High Initial Resistance), potable water and four granulometric fractions of sand, following the mixing procedures described in NBR 7215 [16]. Two water/cement ratios were used to mold the specimens, with two consolidation patterns being defined for each of them, for further evaluation of the effect caused in the advance of the carbonation front.

For statistical analysis of the data generated with the experiment, two-way analysis of variance (ANOVA) and the Tukey´s MSD multiple comparison method were used.

## Cement

Portland cement of high initial strength (CPV-ARI) was used due to its lower number of supplementary cementitious materials, since the replacement of clinker by carbonate material is limited to 10% by NBR 16697 [17], reducing the number of variables that could cause changes in the results obtained. The physical and chemical characterizations of the cement used can be seen in Tables 1 and 2.

**Table 1.** Physical characterizations of the cement used.

| Test | | Results | Limits NBR 16697 [17] |
|---|---|---|---|
| Fineness/Surface area ($cm^2$/g) | | 4767 | $\geq 3000$ |
| Initial setting time (min) | | 121 | $\geq 60$ |
| Final setting time (min) | | 176 | $\leq 600$ |
| Compressive strength (MPa) | 1 day | 29.2 | $\geq 14.0$ |
| | 3 days | 41.4 | $\geq 24.0$ |
| | 7 days | 46.1 | $\geq 34.0$ |
| | 28 days | 54.4 | - |

**Table 2.** Chemical characterizations of the cement used.

| Chemical determination | Normative Reference | Cement used (%) | Limits NBR 16697 [17] (%) |
|---|---|---|---|
| Calcium oxide (CaO) | NBR 14656 | 63.83 | - |
| Silicon Oxide ($SiO_2$) | NBR 14656 | 19.19 | - |
| Aluminum Oxide ($Al_2O_3$) | NBR 14656 | 4.91 | - |
| Iron oxide ($Fe_2O_3$) | NBR 14656 | 3.03 | - |
| Magnesium oxide (MgO) | NBR 14656 | 0.71 | $\leq 6.5$ |
| Sulfur Trioxide ($SO_3$) | NBR 14656 | 2.97 | $\leq 4.5$ |
| Carbon dioxide ($CO_2$) | NBR NM 20 | 2.95 | $\leq 5.5$ |
| Potassium oxide ($K_2O$) | NBR 14656 | 0.73 | - |
| Loss on ignition 1000 °C (PF) | NBR NM 18 | 3.92 | $\leq 6.5$ |
| Insoluble residue (RI) | NBR NM 15 | 0.97 | $\leq 3.5$ |

## Sands

The sand used in the manufacture of the tested specimens was supplied by the São Paulo Institute of Technological Research (IPT), meeting the criteria established by NBR 7214 [18], being divided into four granulometric fractions (coarse, medium coarse, medium fine and fine).

## Preparation of the specimens

The cement matrix composites used in the tests were produced taking as a reference the recommendations specified in NBR 7215 [16]. The amount of water, defined for each of the mixtures, varied according to the maximum water/cement ratio expected for the environmental aggressiveness classes I and III established in NBR 6118 [19]. The quantities of materials used in each mortar can be seen in Table 3.

**Table 3.** Quantity of materials in each mixture.

| Material | Mixing mass (g) | |
|---|---|---|
| | w/c ratio = 0.55 | w/c ratio = 0.65 |
| Cement Portland CPV-ARI | 624.0 ± 0.4 | 624.0 ± 0.4 |
| Water | 343.2 ± 0.2 | 405.6 ± 0.2 |
| Coarse fraction sand | 468.0 ± 0.3 | 468.0 ± 0.3 |
| Medium coarse fraction sand | 468.0 ± 0.3 | 468.0 ± 0.3 |
| Medium fine fraction sand | 468.0 ± 0.3 | 468.0 ± 0.3 |
| Fine fraction sand | 468.0 ± 0.3 | 468.0 ± 0.3 |

Initially, the normal consistency index of the mortars used in this work was determined, according to the procedures described in Annex B of NBR 7215 [16]. For each water/cement ratio adopted, the workability of the mass in the fresh state was determined, in order to verify the influence of water in the mixture and adapt the molding procedures for each one.

The filling of the forms and the consolidation of the mass was carried out in two different ways for each of the mixtures produced, in order to evaluate its effect on the advance of the carbonation front. The variation in the consistency of the mixtures, obtained according to the variation in the water/cement ratio used, caused different procedures to be used for each mixture.

For the mixtures produced with a w/c ratio equal to 0.55, half of the molded specimens were compacted on a vibrating table, filling the form in two layers, using 15 seconds of vibration for the first layer and 5 seconds for the second (pattern A). The other half was consolidated by the impact of a rubber hammer on the side of the mold, with filling also in two layers, with 3 blows on the side for the first layer and 2 blows for the second (pattern B).

Likewise, half of the specimens molded with the mixture produced with the w/c ratio equal to 0.65 were compacted on a vibrating table, with two layers of filling. In this case, however, 7 seconds of vibration were applied to the first layer and 3 seconds to the second (pattern C). The other half was consolidated by the impact of a rubber hammer, the filling, this time, being made in a single layer, being applied 3 blows in the completely filled form (pattern D).

Table 4 presents the information related to each consolidation pattern. It was tried, through standards A and C, to produce a better consolidation condition than standards B and D, which were purposely defined to evaluate the influence of this variable in the process of advancing the carbonation front of cementitious composites analyzed.

**Table 4.** Consolidation patterns used.

| w/c ratio | Consolidation pattern | Number of layers | Consolidation type | Vibration time / Number of blows | |
|---|---|---|---|---|---|
| | | | | 1ª layer | 2ª layer |
| 0.55 | A | 2 | Vibration | 15 seconds | 5 seconds |
| | B | 2 | Blows | 3 blows | 2 blows |
| 0.65 | C | 2 | Vibration | 7 seconds | 3 seconds |
| | D | 1 | Blows | 3 blows | - |

After deformation, the specimens were submitted to a curing stage. To determine the compressive strength, the specimens were submerged in water saturated with lime until the date of the test, as recommended by NBR 7215 [16]. In the case of the accelerated carbonation test, the specimens were submerged in water for a period of 28 days, as recommended by ISO 1920-12 [20].

For each test, corresponding to a dosing and consolidation condition, three cylindrical specimens were molded, in dimensions (5 x 10) cm. The evaluation of the advance of the carbonation front in the samples was carried out at the ages of 0, 28, 56, 70 and 98 days. The evaluation of the compressive strength of specimens was performed at the ages of 3, 7 and 28 days.

**Preconditioning conditions**

Preconditioning was carried out at a stage subsequent to curing, where the specimens were subjected to procedures that sought to regulate their moisture before being stored in the carbonation chamber. It is an important step, because if this regularization is not done, the samples can start the accelerated carbonation process under different saturation conditions, thus causing undue changes in the results due to the different times that each one would take to reach balance with pre-established conditions inside the chamber [4], [21].

In previous studies, a reduction in the superficial alkalinity of the specimens kept in contact with air for short periods of time was observed [22]. Thus, an attempt was made to establish a procedure for the preconditioning step that would avoid exposing the specimens to the air, after the end of the submerged cure.

The preconditioning adopted in this work, carried out over 7 days, was divided into two stages. The first step consisted of drying the samples in a vacuum oven, with an internal temperature adjusted to 35°C, for 5 days. In this period there was a reduction in the humidity of the specimens to levels close to those defined for the storage of the same in the carbonation chamber, without remaining in contact with gases of any nature. Subsequently, in a second stage, the samples were packaged and kept in plastic film for a further 2 days in a laboratory environment, so that a more uniform distribution of moisture would occur in its interior.

In this way, the preconditioning used prevented the onset of uncontrolled carbonation in the specimens, before entering the chamber for the accelerated carbonation test (Figure 1).



**Figure 1.** Stages of the precondition adopted: 1ª Stage - vacuum oven (A) and 2ª Stage – Samples packaged in a plastic film (B).

**Accelerated carbonation**

As carbonation in the natural environment happens slowly, the specimens were placed in an accelerated carbonation chamber, model Thermo Scientific SteriCult $CO_2$, with favorable conditions to increase the speed of the process, by controlling the variables that influence it, specifically the $CO_2$ concentration, temperature and relative humidity. In this work, the recommendations of the international standard ISO 1920-12 [20] for hot climates were adopted, which establishes as a test conditions a $CO_2$ concentration equal to $(3.0 \pm 0.5)$ %, a temperature of $(27 \pm 2)$ °C and a relative humidity of $(65 \pm 5)$ %.

The monitoring of the advance of the carbonated thickness was carried out by the colorimetric method, by spraying a solution of phenolphthalein on the surface of the samples. The phenolphthalein solution was prepared as specified by ISO 1920-12 [20], with 1 g of powdered phenolphthalein dissolved in 70 ml of ethanol and 30 ml of deionized water.

For each of the five carbonation ages evaluated (0, 28, 56, 70 and 98 days, whose counting starts after the end of the preconditioning stage), three specimens of each analyzed condition were cut transversely in half of their height, one of the halves being used to evaluate the carbonated thickness through the sprinkling of phenolphthalein solution on the exposed surface. Subsequently, the other half was sawn lengthwise, along the height, to obtain another surface for the evaluation of the carbonation front, also by the colorimetric method (Figure 2). The carbonation depth was read in 16 points, using a digital caliper, with an accuracy of ± 0.05 mm.
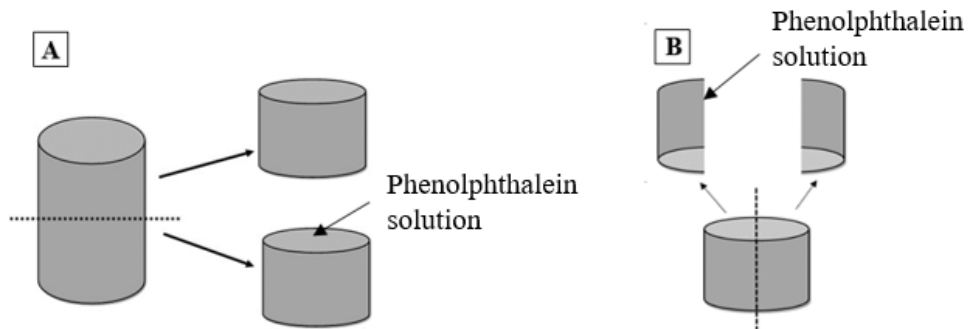


**Figure 2.** Cutting pattern of samples for measuring carbonated thickness after spraying phenolphthalein solution: transversal cut (A) and longitudinal (B).

## Scanning electron microscopy (SEM)

For the study of the composite microstructure under the four conditions evaluated in this work, the scanning electron microscopy (SEM) technique was used. The equipment used for the test was the FEG - Quanta 200 FEI Scanning Electron Microscope.

Analyses were performed for specimens submitted to accelerated carbonation for 98 days. The samples were extracted from a cross section of a specimen of each consolidation condition, with dimensions approximately (20 x 25 x 3) mm. Each of these samples involved both an outer region of the specimens, already carbonated in greater intensity, and an internal region, where carbonation had not yet been detected by the colorimetric method used. Magnifications were performed 40 times to 20,000 times in the samples, generating images using secondary electrons (SE).

## RESULTS AND DISCUSSIONS

The results of the tests, performed as detailed in the previous topic, will be presented below.

## Normal consistency index

The consistency indexes obtained for the two mixtures evaluated in this research, with w/c ratios equals to 0.55 and 0.65, were (219 ± 1) mm and (288 ± 2) mm, respectively. The results proved that the use of less content of water in the mixture causes a drop in the workability of the mass in the fresh state.

## Compressive strength

The average values of compressive strength, observed at each age, for the four conditions analyzed, can be seen in the graph of Figure 3 and Table 5. The uncertainties of the results presented correspond to the mean absolute deviation (MAD) of the individual results obtained. Table 5 also presents the percentage difference in the compressive strength related to the influence from the variation in the consolidation pattern and the variation of the w/c ratio.
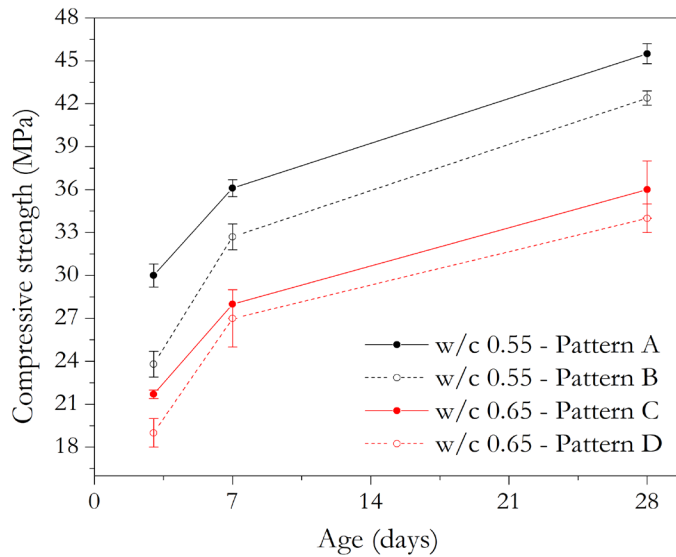
Rev. IBRACON Estrut. Mater., vol. 14, no. 5, e14512, 2021

6/12

**Figure 3.** Average compressive strength.

**Table 5.** Average compressive strength.

| w/c ratio | Consolidation | Compressive strength (MPa) | | | | | | | | |
|---|---|---|---|---|---|---|---|---|---|---|
| | | 3 days | Dif. 1 | Dif. 2 | 7 days | Dif. 1 | Dif. 2 | 28 days | Dif. 1 | Dif. 2 |
| 0.55 | Pattern A | 30.0 ± 0.8 | - | - | 36.1 ± 0.6 | - | - | 45.5 ± 0.7 | - | - |
| | Pattern B | 23.8 ± 0.9 | -21% | - | 32.7 ± 0.9 | -9% | - | 42.4 ± 0.5 | -7% | - |
| 0.65 | Pattern C | 21.7 ± 0.3 | - | -28% | 28 ± 1 | - | -22% | 36 ± 2 | - | -21% |
| | Pattern D | 19 ± 1 | -12% | -20% | 27 ± 2 | -4% | -17% | 34 ± 1 | -6% | -20% |

Notes: Dif. 1 is the percentage difference which refers to the influence of the consolidation pattern (comparison between A-B and C-D patterns). Dif. 2 is the percentage difference which refers to the influence of the w/c ratio (comparison between A-C and B-D patterns).

As expected, the influence of both the water/cement ratio and the specified consolidation pattern is observed, however, there are differences in behavior over time. The mixtures produced with a w/c ratio equal to 0.65, regardless of the consolidation pattern, showed results of compressive strength always below the mixtures produced with w/c ratio equal to 0.55, these being 28% smaller at 3 days and 21% lower at 28 days, for mixtures with A and C consolidation patterns, showing a reduction in the difference in compressive strength between the mixtures at older ages. As for the less dense mixtures (patterns B and D), there was no great influence on the age of rupture of the specimens in the percentage in which the D condition was below the B condition, with this difference always remaining around 20%.

When only the influence of the consolidation in the mixtures with the same water/cement ratio was evaluated, it appears that the inferior condition of consolidation caused, in all cases, a decrease in the compressive strengths. The influence of the established consolidation condition was more present, however, in the younger ages and in the mix with the lowest water-cement ratio (w/c equal to 0.55). As this mixture presented less workability, it requires a more energetic process to eliminate voids. The results indicate that the lower the consistency index of the mixture, the greater the impacts resulting from failures in the consolidation stage.

It is interesting to note that the harmful effect caused by the unfavorable consolidation conditions introduced in this study, has been mitigated over time, by the advancement of cement hydration in the composite matrix.

The hypothesis test for comparing the four conditions, and between ages, using two-way ANOVA, confirmed that these two factors are significant (under any level of significance greater than 0.01) to explain the variability of compressive strength. The comparisons, two by two, between the four conditions, showed that, except for the comparison between C and D, all conditions have different mean resistances. The level of global significance used for comparisons two by two was 0.05.

**Carbonation front advance**

Figure 4 shows the advance of the carbonation front in cylindrical specimens, after 0, 28, 56, 70 and 98 days of exposure to the $CO_2$-rich atmosphere of the carbonation chamber. The measurement shown below each image provides the average value of the carbonated thickness, calculated from 16 measurements taken. The uncertainties of the results presented correspond to the mean absolute deviation (MAD) of the individual results obtained.
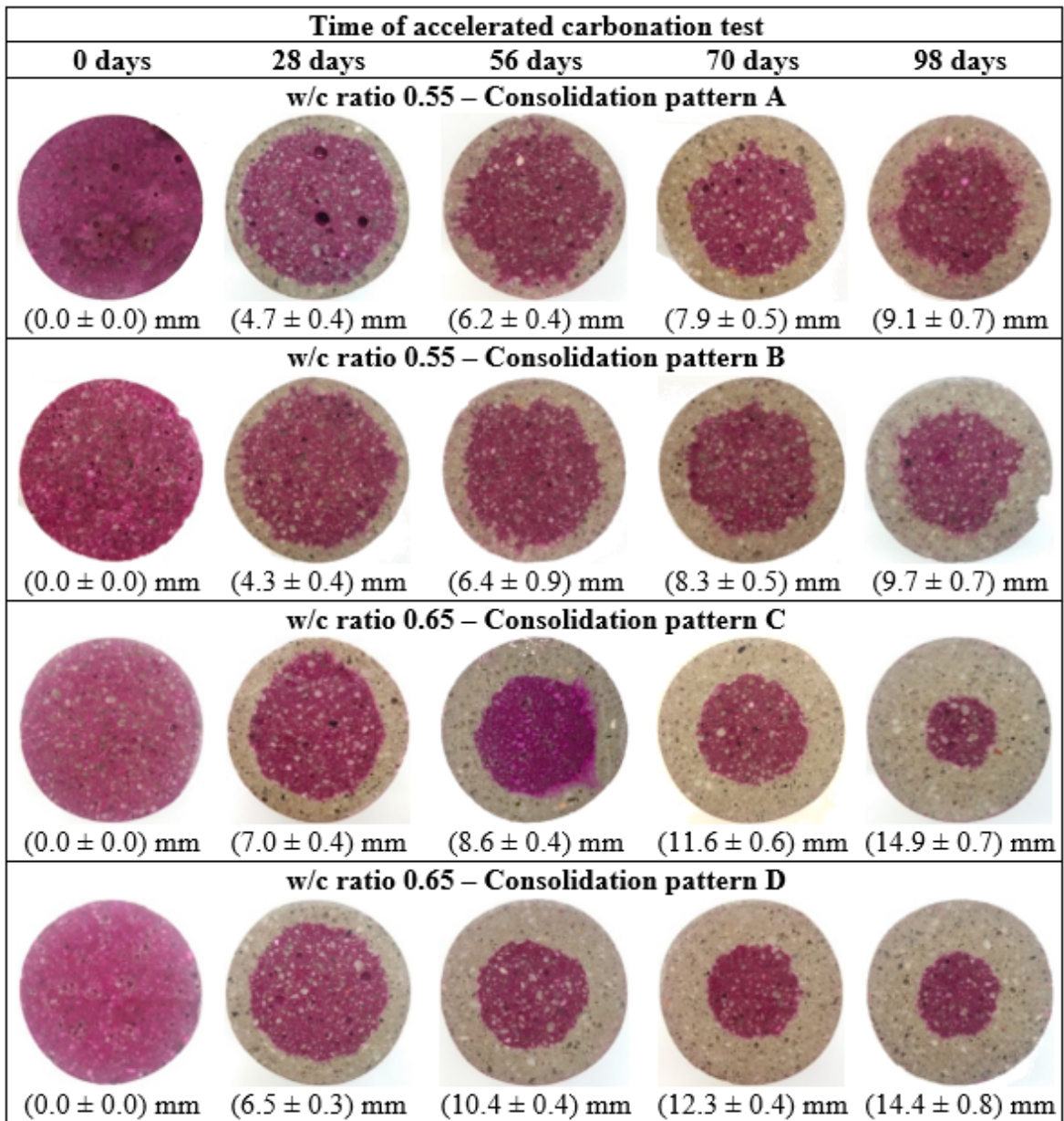


| Time of accelerated carbonation test | | | | |
|---|---|---|---|---|
| **0 days** | **28 days** | **56 days** | **70 days** | **98 days** |
| w/c ratio 0.55 – Consolidation pattern A | | | | |
| (0.0 ± 0.0) mm | (4.7 ± 0.4) mm | (6.2 ± 0.4) mm | (7.9 ± 0.5) mm | (9.1 ± 0.7) mm |
| w/c ratio 0.55 – Consolidation pattern B | | | | |
| (0.0 ± 0.0) mm | (4.3 ± 0.4) mm | (6.4 ± 0.9) mm | (8.3 ± 0.5) mm | (9.7 ± 0.7) mm |
| w/c ratio 0.65 – Consolidation pattern C | | | | |
| (0.0 ± 0.0) mm | (7.0 ± 0.4) mm | (8.6 ± 0.4) mm | (11.6 ± 0.6) mm | (14.9 ± 0.7) mm |
| w/c ratio 0.65 – Consolidation pattern D | | | | |
| (0.0 ± 0.0) mm | (6.5 ± 0.3) mm | (10.4 ± 0.4) mm | (12.3 ± 0.4) mm | (14.4 ± 0.8) mm |

**Figure 4.** Monitoring the progress of the carbonation front by colorimetric pH indicator.

From the average value of the carbonated thickness of each sample, shown in Figure 4, and based on Equation 1, it was possible to determine the value of the diffusion coefficient (k), for each of the analyzed mixtures and consolidation conditions. The values obtained are shown in Table 6. Table 6 also presents the percentage difference in the diffusion coefficient related to the influence from the variation in the consolidation pattern and the variation of the w/c ratio.

Rev. IBRACON Estrut. Mater., vol. 14, no. 5, e14512, 2021

8/12

**Table 6.** Diffusion coefficients obtained for each mixture and consolidation condition analyzed.

| w/c ratio | Consolidation pattern | k (mm.days$^{-1/2}$) | Dif. 1 | Dif. 2 | Model | r$^2$ |
|---|---|---|---|---|---|---|
| 0.55 | Pattern A | 0.90257 | - | - | $e_C = 0.90257 \cdot \sqrt{t}$ | 0.99078 |
| | Pattern B | 0.93696 | +3.8% | - | $e_C = 0.93696 \cdot \sqrt{t}$ | 0.97921 |
| 0.65 | Pattern C | 1.37283 | - | +52% | $e_C = 1.37283 \cdot \sqrt{t}$ | 0.96323 |
| | Pattern D | 1.41938 | +3.4% | +51% | $e_C = 1.41938 \cdot \sqrt{t}$ | 0.98935 |

Notes: Dif. 1 is the percentage difference which refers to the influence of the consolidation pattern (comparison between A-B and C-D patterns). Dif. 2 is the percentage difference which refers to the influence of the w/c ratio (comparison between A-C and B-D patterns).

Figure 5 shows the graphs of the adjusted functions, as well as the average values obtained by measuring the advance of the carbonation front along the accelerated carbonation test.
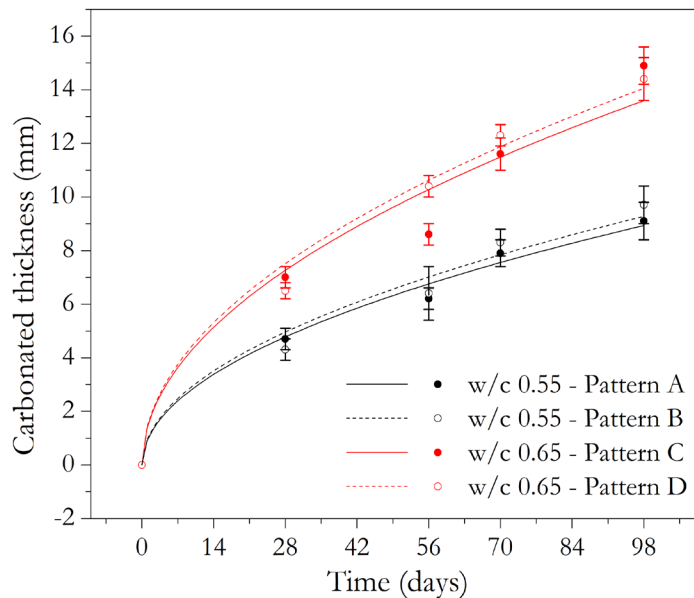


**Figure 5.** Advance of carbonation front in the samples submitted to the accelerated carbonation test.

There is a great improvement in the performance of the cementitious composite, regarding the advance of the carbonation front, produced by the reduction of the water/cement ratio. The diffusivity constant value obtained for samples with w/c ratio of 0.65 was approximately 50% higher than for those that were molded with a ratio of 0.55.

It is also noteworthy that the model used to describe the advance of the carbonation front, provided by Equation 1, was adequate for the conditions analyzed, given that the correlation coefficient (r$^2$) of all adjustments was close to 1.

The hypothesis test for comparing the four conditions, and between ages, using two-way ANOVA, confirmed that these two factors are significant (under any level of significance greater than 0.01) to explain the advance of the carbonation front. The comparisons, two by two, between the four conditions, showed that, except for the comparison between A and B, all conditions have different mean carbonated thickness. The level of global significance used for comparisons two by two was 0.05.

It should be noted that what was measured in this work was only the region where the hydrogen potential of the cementitious material was reduced to levels capable of being detected by the pH colorimetric indicator, and not the presence of carbonic acid ($H_2CO_3$) reactions with the mortar alkali.

**Scanning electron microscopy (SEM)**

Through the images generated by the SEM, the microstructure of the samples was evaluated, which allowed some differences to be verified between the four conditions analyzed here and also the differences between the carbonated and non-carbonated regions of the samples.

Figure 6 shows the images generated by SEM for the four consolidation conditions under study with a magnification of 40 times, where the presence of larger pores is observed in the samples with worse consolidation conditions (patterns B and D) when compared to the better dense features (patterns A and C). However, in the images obtained with a magnification of 5,000 times, shown in Figure 7, there is a greater presence of pores, due to the change in consolidation conditions, only for samples produced with a w/c ratio equal to 0.55. For samples produced with a ratio of w/c equal to 0.65, it is possible to state only that their void volume is much higher than those observed in samples with w/c equal to 0.55, regardless of the consolidation condition. It can also be said that, only by observing the images (C) and (D) of Figure 7, it is not possible to state that the change in the consolidation process caused a significant variation in the voids volume of the analyzed samples. These findings corroborate to validate the analyses made previously based on the results obtained from compressive strength and resistance to the advance of the carbonation front.
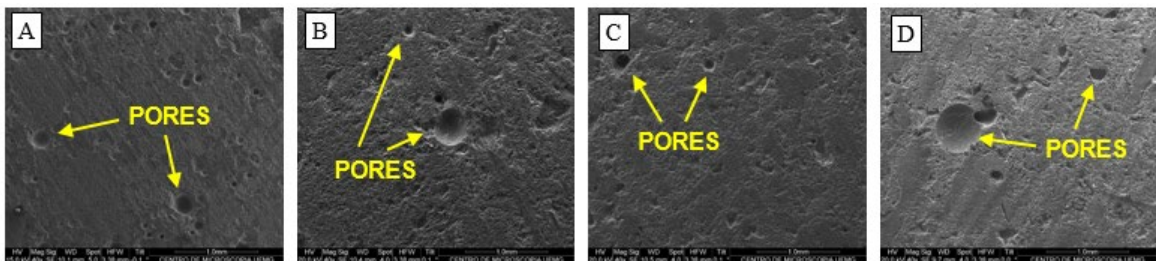


**Figure 6.** Images generated by SEM (SE) with a magnification of 40 times for the four consolidation conditions: w/c 0.55 – pattern A (A), w/c 0.55 – pattern B (B), w/c 0.65 – pattern C (C) e w/c 0.65 – pattern D (D).
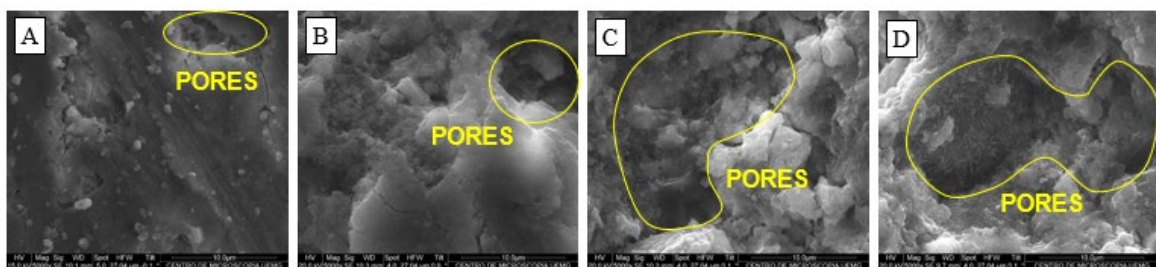


**Figure 7.** Images generated by SEM (SE) with a magnification of 5,000 times for the four consolidation conditions: w/c 0.55 – pattern A (A), w/c 0.55 – pattern B (B), w/c 0.65 – pattern C (C) e w/c 0.65 – pattern D (D).

Figure 8 shows the images obtained on the SEM for the consolidation condition B, with a magnification of 20,000 times, for the carbonated and non-carbonated regions of the sample. The images show the occurrence of carbonation reactions, since the products of this reaction can be observed in the carbonated zone of the sample. In this region, it is possible to visualize the precipitation of small crystals, typical of calcium carbonates, aggregated on larger smooth surfaces, characteristic of calcium hydroxide. In the image of the non-carbonated region, the smooth surface of the calcium hydroxide remains without the presence of such incrustations.
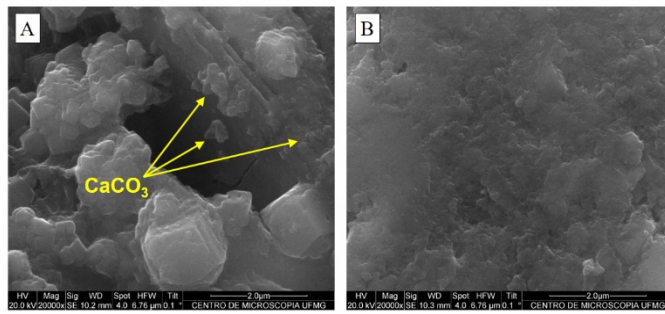
**Figure 8.** Images generated by SEM (SE) with a magnification of 20,000 times, for the carbonated (A) and non-carbonated (B) regions.

## CONCLUSIONS

The results obtained show the influence of voids on the properties of cementitious composites. The increase in the proportion of water in the mixture and/or the reduction in the quality of the consolidation altered the void structure of the material and, consequently, produced effects on the evaluated properties. The impact on the empty structure of the material must, however, be analyzed not only in terms of the variation caused in its volume, but also in the pattern of its distribution, in its morphology and in its connectivity.

The statistical treatment of the experimental data generated, using two-way analysis of variance (ANOVA) and the Tukey´s HSD multiple comparison method, for comparison between the four conditions under study, and between ages, confirmed that such factors are significant (under any significance level greater than 0.01) to explain the variability of compressive strength. The influence of the established consolidation condition was more present, however, in the younger ages and in the mix with the lowest water-cement ratio (w/c equal to 0.55). The results indicate that the lower the workability of the mixture, the greater the impacts on the compressive strength of the material, resulting from failures in the consolidation stage. The comparisons, two by two, between the four conditions, showed that, except for the comparison between C and D, all conditions have different mean resistances. The level of global significance used for comparisons two by two was 0.05. The images obtained by SEM, with an increase of 5,000, corroborate for the validation of such analyses.

It was also observed that the harmful effect on the compressive strength caused by the unfavorable consolidation conditions introduced in this study, was mitigated over time, by the advance of cement hydration in the composite matrix.

Statistical tests indicated that there was no evidence that patterns A and B generated different averages for the carbonation progress. This result shows that despite the reduction in compressive strength observed in pattern B in relation to pattern A, indicating an increase in the volume of voids incorporated in the samples due to differences in the consolidation process, there was no increase in the connectivity of its open porosity. The other comparisons of average carbonation between standards were all significant at an overall significance level of 0.05. This demonstrates that the consolidation pattern D, despite not producing a significant variation in the volume of voids capable of causing a variation in the compressive strength tests, as seen in the images (C) and (D) of Figure 7, made its pore network more connected, favoring the advancement of the carbonation front.

## ACKNOWLEDGEMENTS

## REFERENCES

[1] E. P. Figueiredo, "Efeitos da carbonatação e de cloretos no concreto," in *Concreto: Ensino, Pesquisa e Realizações*, G. C. Isaia, Ed., São Paulo: IBRACON, 2005, vol. 2, ch. 27, pp. 829–855.

[2] O. Cascudo and H. Carasek, "Ação da carbonatação no concreto," in *Concreto: Ensino, Pesquisa e Realizações*, G. C. Isaia, Ed., São Paulo: IBRACON, 2011, vol. 1, ch. 24, pp. 849–885.

[3]   M. Hamada, "Neutralization of concrete and corrosion of reinforcing steel: properties of cement paste and concrete," in *Proc. Fifth Int. Symp. Chem. Cem.*, Tokio, Part III, vol. III, Dec. 1969, pp. 343–369.

[4]   C. Pauletti, "Estimativa da carbonatação natural de materiais cimentícios a partir de ensaios acelerados e de modelos de predição," Ph.D. dissertation, Esc. Eng., UFRGS, Porto Alegre, RS, 2009.

[5]   B. Šavija and M. Lukovic, "Carbonation of cement paste: understanding, challenges, and opportunities," *Constr. Build. Mater.*, vol. 117, pp. 285–301, Aug 2016, http://dx.doi.org/10.1016/j.conbuildmat.2016.04.138.

[6]   V. G. Papadakis, C. G. Vayenas, and M. N. Fardis, "A reaction engineering approach to the problem of concrete carbonation," *AIChE J.*, vol. 35, no. 10, pp. 1639–1650, Oct 1989, http://dx.doi.org/10.1002/aic.690351008.

[7]   V. Shah, K. Scrivener, B. Bhattacharjee, and S. Bishnoi, "Changes in microstructure characteristics of cement paste on carbonation," *Cement Concr. Res.*, vol. 109, pp. 184–197, Apr 2018, http://dx.doi.org/10.1016/j.cemconres.2018.04.016.

[8]   A. M. Neville, *Propriedades do Concreto*, R. A. Cremonini, Transl., 5. ed. Porto Alegre: Bookman, 2016.

[9]   H. Pourbaix, *Atlas of Electrochemical Equilibria in Aqueous Solutions.* Oxford: Pergamon Press, 1966.

[10]  A. Meyer, "Investigations on the carbonation of concrete," in *Proc. Fifth Int. Symp. Chem. Cem.*, Tokio, Part III, vol. III, Dec. 1969, pp. 394–401.

[11]  A. M. Neville and J. J. Brooks, *Tecnologia do Concreto*, 2. ed. Porto Alegre: Bookman, 2013.

[12]  American Concrete Institute, *Guide for Consolidation of Concrete*, ACI 309R-05, 2005.

[13]  M. N. Al-Khalaf and M. H. A. Yousif, "Effect of revibration on the stability and compactibility of concrete," *Cement Concr. Res.*, vol. 15, no. 5, pp. 842–848, 1985, http://dx.doi.org/10.1016/0008-8846(85)90151-6.

[14]  T. Gonen and S. Yazicioglu, "The influence of compaction pores on sorptivity and carbonation of concrete," *Constr. Build. Mater.*, vol. 21, no. 5, pp. 1040–1045, 2007, http://dx.doi.org/10.1016/j.conbuildmat.2006.02.010.

[15]  X. Gao, J. Zhang, and Y. Su, "Influence of vibration-induced segregation on mechanical property and chloride ion permeability of concrete with variable rheological performance," *Constr. Build. Mater.*, vol. 194, pp. 32–41, 2019, http://dx.doi.org/10.1016/j.conbuildmat.2018.11.019.

[16]  Associação Brasileira de Normas Técnicas, *Cimento Portland – Determinação da Resistência à Compressão,* NBR 7215, 2019.

[17]  Associação Brasileira de Normas Técnicas, *Cimento Portland – Requisitos*, NBR 16697, 2018.

[18]  Associação Brasileira de Normas Técnicas, *Areia Normal para Ensaio de Cimento – Especificação*, NBR 7214, 2015.

[19]  Associação Brasileira de Normas Técnicas, *Projetos de Estruturas de Concreto – Procedimento*, NBR 6118, 2014.

[20]  International Organization For Standardization, *Testing of Concrete - Part 12: Determination of the Carbonation Resistance of Concrete – Accelerated Carbonation Method*, ISO 1920-12, 2015.

[21]  F. G. Silva, P. Helene, P. Castro-Borges, and J. B. L. Liborio, "Sources of variations when comparing concrete carbonation results," *J. Mater. Civ. Eng.*, vol. 21, no. 7, pp. 333–342, Jun 2009, http://dx.doi.org/10.1061/(asce)0899-1561(2009)21:7(333).

[22]  P. C. Cordeiro, R. G. R. Silva, L. A. B. A. Ferreira, A. G. Magalhães, F. C. França, and E. V. M. Carrasco, "Estudo comparativo entre diferentes tipos de cura e sua influência no avanço da carbonatação em compósitos cimentícios," in *59° CBC – IBRACON*, Bento Gonçalves, RS, Oct.-Nov., 2017.